Tesi di Dottorato di LUCA CATALANO
Matricola 821469

POLITECNICO
MILANO 1863

**DIPARTIMENTO
DI
CHIMICA, MATERIALI
E INGEGNERIA CHIMICA
"Giulio Natta"**

TOWARDS ENGINEERING OF SOLID-STATE SUPRAMOLECULAR ROTORS *VIA* HALOGEN BONDING

**Dottorato di Ricerca in Chimica
Industriale e Ingegneria Chimica
(CII)**

**PhD in Industrial Chemistry and
Chemical Engineering**

XXIX ciclo
2013 - 2016

Coordinatore: prof. Alessio Frassoldati
Tutore: prof. Attilio Citterio
Relatore: prof. Pierangelo Metrangolo

INDEX

Abstract

Halogen bonding (XB), namely any interaction involving halogen atoms as electrophilic species, is attracting an ever-increasing interest thanks to its unique physico-chemical properties, specifically its strength, directionality, and tunability. All these features make the halogen bond a precious structural tool for the design and synthesis of novel functional materials with new and exciting properties.

My PhD project was devoted to study this rather peculiar non-covalent interaction and expand its frontiers from fundamental aspects towards engineering a new class of functional materials. Specifically my work has been focusing on the two following research strands:

- Studying halogen bonding at a fundamental level by focusing on new tools for its identification and characterization. To reach this goal we built libraries of halogen-bonded complexes, and coupled standard characterization techniques (thermal analysis and XRD measurements) with new experimental approaches to characterize the complexes. In particular, we employed Attenuated Total Reflection Far-IR spectroscopy and solid-state NMR techniques (^{15}N and ^{13}C) to search for diagnostic features of the XB occurrence and geometrical features thereof. Furthermore, we complemented experimental data analysis with theoretical calculations to rationalize our findings.

- Engineering amphidynamic cocrystals based on halogen bonding and studying the effect of the nature and strength of the XB on the dynamics of these systems. Firstly, we synthesized the molecular building blocks through conventional organic synthesis, then we obtained the crystalline supramolecular rotors by co-crystallization, and finally we fully characterized the obtained species, focusing on crystal structures and internal dynamics. To do so, we used variable temperature (VT) single crystal XRD and solid state NMR (^{1}H spin-lattice relaxation and ^{2}H quadrupolar echo) experiments. Finally, we compared the kinetics and thermodynamics related to the rotators motion in isostructural supramolecular rotors to see the effect of the XB strength on the rotators dynamic performances.

Aims

The main aim of my PhD research activity was two-fold:

- To find new tools for the identification of XB in solids by taking advantage of non-routine techniques, specifically far-IR spectroscopy and solid-state NMR analysis (^{15}N and ^{13}C). The idea behind this research strand is to provide alternative effective methods for XB characterization when standard techniques, such as single crystal X-ray difraction, are not available.

- The design, synthesis, and charaterization of new solid-state supramolecular rotors based on halogen bonding. We have envisioned the potential application of XB not only as driving force of the supramolecular assembly but also as main structural tool in the rotor systems, acting as axle of rotation. The results of this PhD thesis pave the way towards new design principles in the field of amphydynamic multi-component cocrystals.

CHAPTER 1

INTRODUCTION

1.1 Halogen bonding in crystals

Molecular crystals are supramolecules "par excellence"[1] as they are macroscopic objects composed by millions of molecules periodically disposed and held together by non-covalent interactions. An isolated molecule of such a system has peculiar physical and chemical properties, but the whole solid can have totally different features depending on the chemical nature of its molecular building blocks and their spatial disposition. Crystal engineering deals with designing new materials by assembling molecules or ionic species into a desired architecture (please see also the Appendix).[2] In order to achieve this goal it is fundamental to build the system with target supramolecular interactions, which can drive the crystallization in a predictable way.
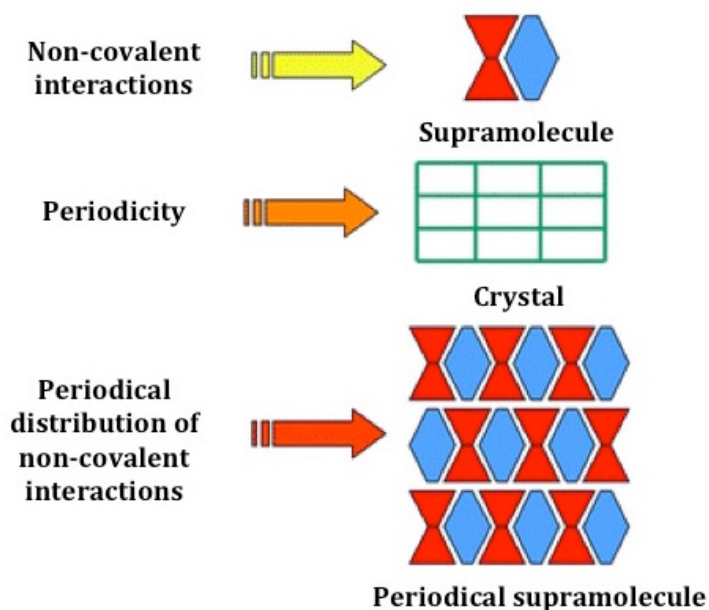
Scheme 1.1 The final properties of a molecular crystal, in the above schematic example a cocrystal, arise from those of the starting molecular building blocks and strongly depend on the periodical distribution of the non-covalent interactions within the crystalline lattice. [2]

The formation of a crystal is probably the most striking example of self-assembly and intermolecular recognition. These phenomena can be controlled

by a careful design of specific supramolecular synthons[3]. These could be based on a wide variety of non-covalent interactions, such as Coulombic interactions, van der Waals forces, π-π interactions, hydrogen bonding and so on. Among them halogen bond (XB) based supramolecular synthons proved to be very efficient to build new crystalline materials.[4,5] In this section we will focus on the key role of halogen bonding in crystal engineering by describing its physicochemical properties and geometrical features, which make XB an ideal candidate in designing smart and functional materials with desired crystal structures.

XB, defined as any attractive interactions between an halogen, acting as an electrophilic species, and an electron-rich moiety[6-8], has been known since the last two centuries; as the first ever-reported example of halogen bonded complex was synthesized by J. J. Colin in Gay-Lussac laboratories in 1814.[9] From that moment only small and unrelated fragments of knowledge on XB had been collected[10-13] untill 1950's structural work made by Hassel and then by Bent, who first tried to rationalize the subject.[14,15] But it is only in the last two decades that systematic studies on XB have been carried out and XB has become an ever growing hot topic, see figure 1.1.
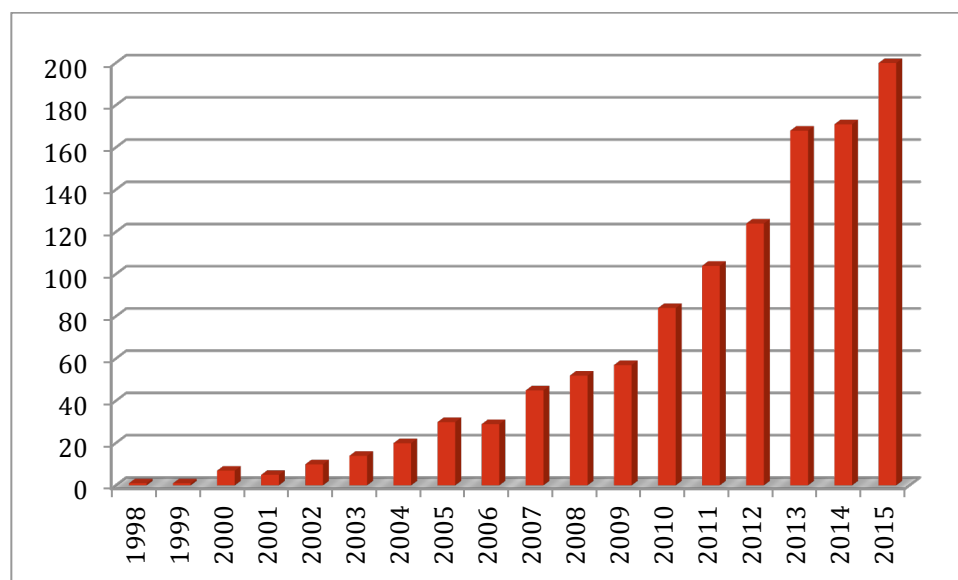
Figure 1.1 Papers per year citing "halogen-bonding" in title and/or abstract (source: Scifinder 2016).

This increasing interest in non-covalent interactions has been a direct consequence of the "paradigm shift"[2] from a molecular view to a supramolecular approach to Chemistry.

XB is often taken into account in designing new crystals thanks to its unique properties, such as selectivity, strength and directionality.[16] It shows similar behaviour as hydrogen bonds, starting from the electrophilic nature of both halogens and hydrogens involved in the interactions, and can compete with them.[17-19] Interestingly they can also coexist by showing complete orthogonality, even in biological systems.[20] On the other hand XB and hydrogen bond differ in various aspects: first of all the steric hindrance of halogens in comparison with hydrogen atoms; secondly the greater tunability of XB strength by simply changing the XB donor (usually Br, Cl or I) compared with hydrogen bond.[21] Thus the flexibility of this interaction makes it a precious tool in designing new crystalline architectures. Thanks to their flexibility, XB tectons[22] could be successfully used in developing functional materials, spanning all branches of Science, *e.g.* new drugs, magnetic and conductive materials, photoresponsive materials, porous solids, luminescent devices and so on.[23,24]

Although molecular halogens and interhalogens give rise to numerous XB based complexes, which paved the way to fundamental studies of this interaction[25-27] and are still attracting interesting studies[28] as well as polyhalide anions[29,30] and complexes where the nucleophilic halogen is bound to atoms different from carbon (S, P, N…),[31,32] in this work we will focus on carbon bound halogens, on which I have been focusing during my graduate studies.

1.1.1 XB features

In 2013 IUPAC proposed the following XB definition: "A halogen bond occurs when there is evidence of a net attractive interaction between an electrophilic region associated with a halogen atom in a molecular entity and a nucleophilic region in another, or the same, molecular entity".[33]
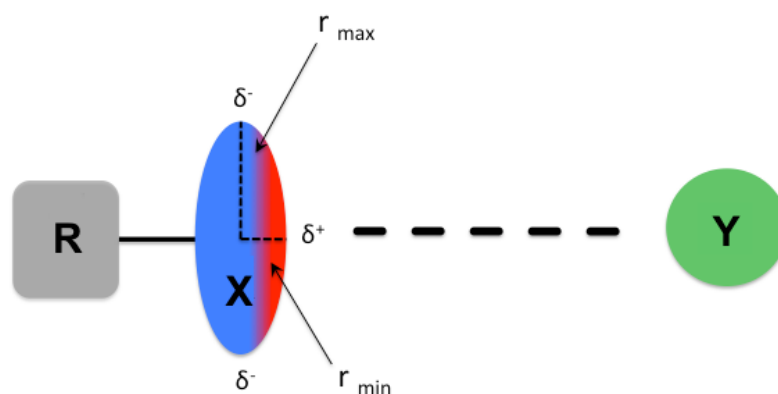
R = C, N, Halogen...   Y = N, O, S, P, Halide...
X = I, Br, Cl, F

Figure 1.2 Schematic representation of XB. XB acceptors (Y) are electron rich moieties, which can be neutral or charged species. XB donors (X) are halogens bound to various molecular entities (R). It is shown the polar flattening effect, which gives rise to ellispoid geometry of the electron density distribution around the halogens. Due to this anisotropic distribution XB donors show a region of positive electrostatic potential (the σ-hole, in red) opposite to the covalent bond R-X and a negative electrostatic potential (in blue) at the equatorial region.

Halogens, as strongly electronegative elements, are usually considered negatively polarized species. However, when involved in XB, they can act as electrophilic moieties. This contradictory behaviour has been well rationalized by the extensive work of P. Politzer and co-workers, the σ-hole theory.[34,35] XB occurrence is directly related to anisotropic electron density distribution around halogen atoms. In halogens covalently bound with electron withdrawing species it is possible to observe a region of positive electrostatic potential, the σ-hole, opposite to the covalent bond itself.[36] In these conditions the halogens can be geometrically described by an ellipsoid model with the minimum radius in correspondence of the covalent bond axis and the maximum radius orthogonal to it, this effect is known as polar flattening.[37,38] These results are clearly consistent with the directionality of XB, which implies the approach of the

electron rich species along the extended C-X bond axis, forming *ca.* 180° C-X•••Y angle.[3]

Going down the 17th group of the periodic table there is a clear enhancement of the σ-hole along the C-X axis, fixing the covalently bound carbon moiety. This is bright evidence that polarizability of the halogens plays a key role in determining the increase of the electron positive potential. Until short time ago in halocarbon the electrostatic potential around F was considered negative all around the atom and F was not listed between the possible halogen bond donors.[34] Nowadays it is accepted that even F can display the σ-hole, when it is bound to particularly strong electron withdrawing groups.[40] Moving from F to Cl, Br and I, the size of the electropositive crown along the covalent C-X bond grows directly with halogens polarizability. XB strenght is directly proportional with the magnitude of the σ-hole, in agreement with experimental findings which show the strongest interactions for C-I⋯D XBs.[41] For example the σ-hole on the two bromine atoms of 1,4-dibromotetrafluorobenzene has a theoretical electrostatic potential of +139 kJ/mol calculated in vacuum, definitely weaker than the one calculated on the two I of 1,4 diiodotetrafluorobenzene, which have a value of +162 kJ/mol.[42]

In halo-organic compounds the extent of the positive electrostatic potential region on the XB donor halogens is also related to the hybridization of the carbon directly bound to the halogens, following the trend $Csp^3<Csp^2<Csp$.[30] Csp-I moieties resulting very strong halogen bond donors as revealed by Le Questel *et al.* CCDC (Cambridge Crystallographic Data Center) survey. 96% of Csp-I iodoorganic compounds in the CCDC database are halogen bonded with O, N, S, Se or π system, while this result falls to 58% for Csp^2-I and 31% for Csp^3.[43] The σ-hole magnitude also depends on the presence of electron withdrawing groups on the molecular fragment covalently bound to the halogens, which can polarize their electron density distribution.

Playing with these three parameters (nature of halogen, hybridization of the C bounded to X and functionalization of the carbon skeleton) can dramatically change the extent of the electropositive crown on the halogens, affecting XB

strength, which can varies from 5-200 kJ/mol.[44] This makes XB an extremely tuneable interaction compared with other non-covalent interactions, *e.g.* hydrogen bond, and particularly useful in designing new crystal architectures; that is why XB is such a precious tool for crystal engineering.
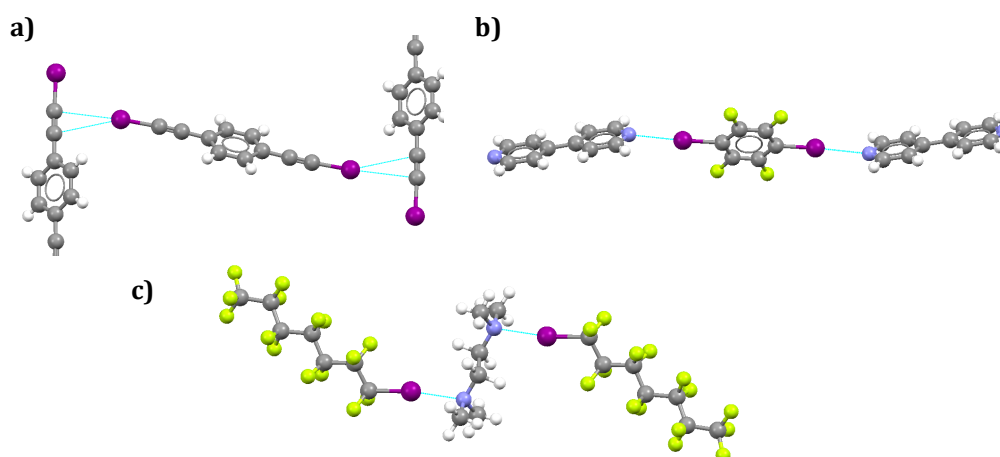
Figure 1.3 a) Halogen bond C-I···π electrons of the covalent triple bond in 1,4-bis(iodoethynyl)benzene crystal structure.[49] b) XB between Iodine and heteroaromatic nitrogen, showing approximately co-planarity of the aromatic planes in 1:1 co-crystal of 4,4'-bipyridyl and 1,4-diidotetrafluorobenzene.[46] c) XB between perfluoroiodoeptane and N,N,N',N'-tetremetylethylenediamine, showing a tetrahedral arrangement.[45] Color code: C, grey; I, magenta; F, green; H, white; N, cyan.

Halogen bond interactions involving n-type electrons are extremely linear with a C-X···D angle of approximately 180°. Short XB tends to move closer to ideal linearity. These observations are valid for I, Br and Cl interacting with Lewis bases sites, such as N, O, S and so on.[8] This kind of XB is preferentially oriented along the axis of the donated lone pair of the electron rich species. Thus, XB forms tetrahedral arrangement with ether, thioether and amines.[45] In R-X···D, where D is an heteroaromatic nitrogen, R-X moiety is *ca.* co-planar with aromatic ring planes with R-X···N angles of approximately 120°.[46] Carbonyl and sulfoxide groups form trigonal planar arrangements working as mono- or bidentate XB acceptors.[47,48] In systems where 2 adjacent carbonyl groups or heteroaromatic

nitrogens are present, bifurcated halogen bonds are also possible as shown by Ji *et al.*[48]

When π electrons are involved in XB, R-X is orthogonally oriented with respect to the plane of aromatic systems or to the double/triple bond of the olephinic XB acceptors.[49,50]
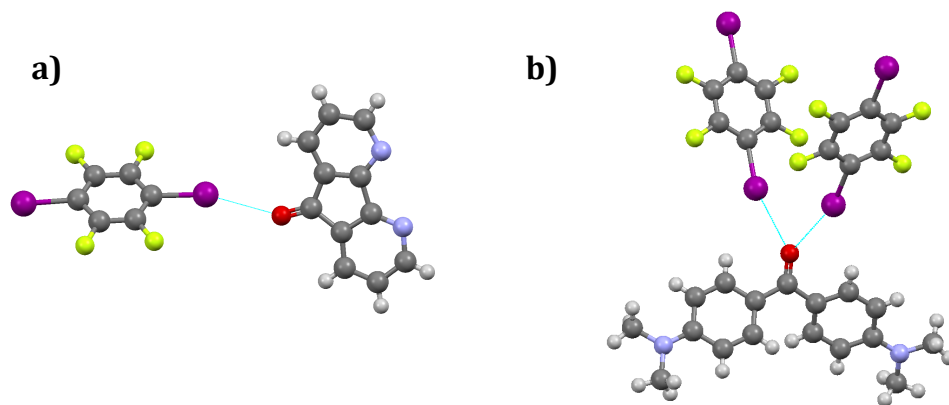
Figure 1.4 a) Monodentate C-I···O halogen bond between 1,4-diiodotetrafluorobenzene and 4,5-diazafluoren-9-one, forming a trigonal planar geometry.[47] b) A carbonyl group working as bidentate XB acceptor in the co-crystal of 4,4'-bis(dimethylamino)-benzophenone and 1,4-diiodotetrafluorobenzene.[48] Color code: O, red; for the other elements see figure 1.3.

Halogen bond has certainly similar characteristics compared to hydrogen bond. For sure the electrophilic nature of both the interactions is the main common feature between them. But what makes XB a special tool in designing new crystal architectures are the differences from HB.[21] In particular the great tunability of XB strenght, depending on the halogen involved in the interaction, the substituent on the carbon skeleton and the hybridization of the carbon covalently bound to the halogen, and its linearity make XB a precious non-covalent interaction in designing supramolecular crystalline materials.

In a system where both XB and HB supramolecular synthons are present, three are the possible scenarios: competition, cooperativity and orthogonality. The occurrence of one of the aforementioned scenario depends on several

factors including the relative strength of the interactions involved and the geometry of the molecular species taken into account.

Friščić *et al.* showed in 2012 an interesting example, where the concept of competition between XB and HB is stressed by the comparable strength of the two non-covalent interactions involved in the studied system. Mixing 1,4-diiodotetrafluorobenzene and methyldiphenylphosphine oxide leads to two different stoichiometric variations of their co-crystals. The formation of the supramolecular architecture of 1:1 co-crystal is driven by C-I⋯O and C-I⋯π XBs. But in the 2:1 crystalline adducts the dominant non-covalent interactions are HBs, which establish an HB network identical to that found in pure phosphine, see scheme 1.2. In the latter complex XB between 1,4-diiodotetrafluorobenzene aromatic π-electrons is still present as a secondary interaction.[51]
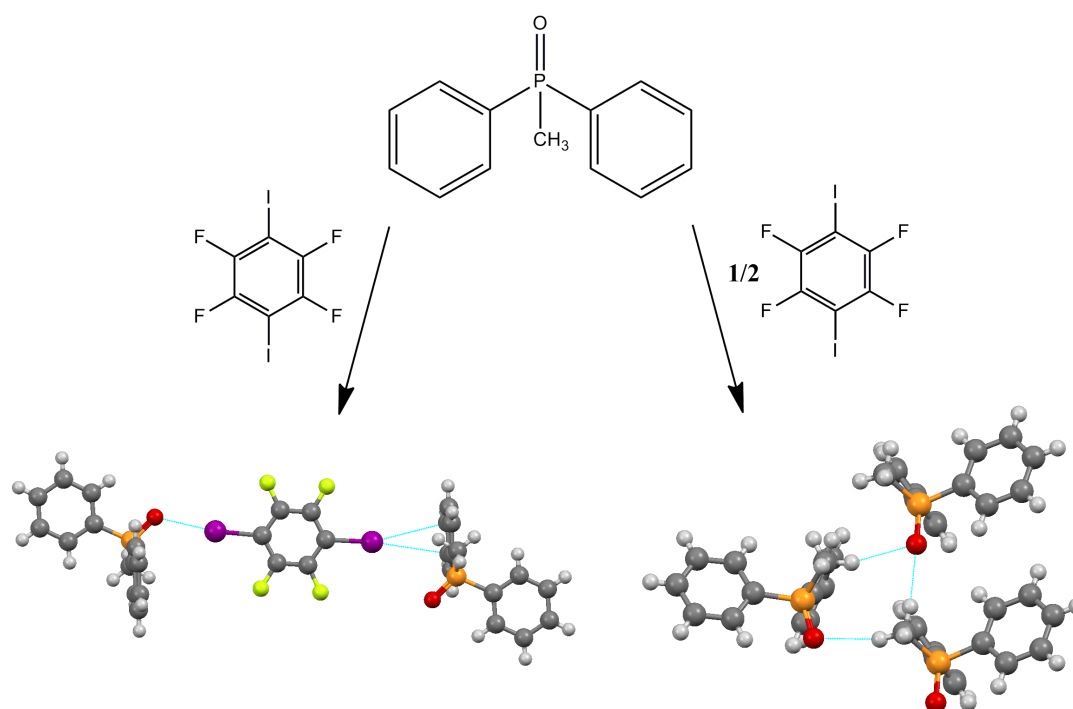
Scheme 1.2 Changing the molar ratio of methyldiphenylphosphine oxide and 1,4-diiodotetrafluorobenzene leads to dramatically changes in the final supramolecular architecture of the complexes, which differ in the dominant structure-directing interaction. On the left XB is the main driving force of the supramolecular assembly. On the right HB is the main actor in the formation of the adduct.[51] Color code: P, orange; for the others elements see figures 1.3 and 1.4.

In molecules, which can be combined *via* different intermolecular forces, the competition between them is not the only observable effect. Cooperativity is another important feature of non-covalent interactions. Cooperation between XB and HB has been studied in several computational studies for simple prototypical systems.[52-54] Experimental evidences of XB and HB cooperation came from anion recognition studies in solution.[55-57] For several anion receptors the proof of XB and HB formation has been given by means of XRD analysis.[58]

XB and HB can also feature orthogonality and can be energetically independent as shown by computational and statistical studies by Voth *et al* in 2009.[20] Electrophilic hydrogens can interact with the negatively polarized equatorial belt of the halogens involved in XB. These conditions are common in a wide variety of protein-ligand systems and can be useful in designing site-specific halogenated species, which can interact with biological receptors without disrupting their main structures. Experimental evidences of orthogonal XB and HB in biomimetical complexes were found by Takemura *et al.* and Vasylyeva *et al.* in their recent papers.[59,60] In the latter work N-methylacetamide, used as peptide bond model, self-assembles with a series of halogen bond donors, showing the occurrence of orthogonal XB and HB on the amidic carbonyl, see Figure 1.5.
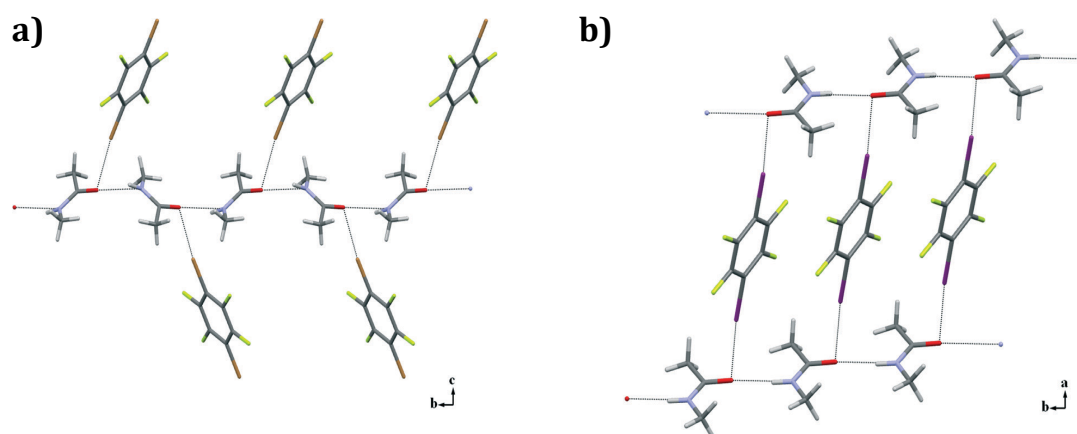
Figure 1.5 N-methylacetamide carbonyl featuring orthogonal XB and HB with two different XB donors, (a) 1,4-dibromotetrafluorobenzene and (b) 1,4-diiodotetrafluorobenzene.[60]

Halogens can form halogen-halogen contacts. This kind of interactions are mainly divided in two categories (type I and type II) depending on their geometries, see scheme 1.3. The different geometrical parameters of the two types of contact find an explanation in the different chemical nature of the interactions.
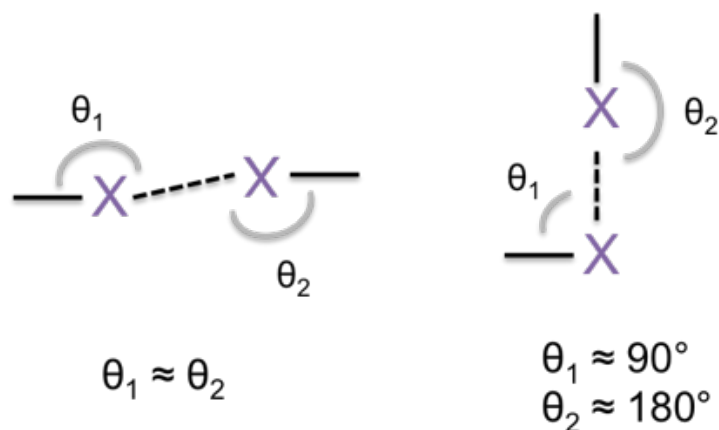
Scheme 1.3 The two different types of halogen-halogen contacts. It is clear from the scheme above that the difference between them lies in the geometry of the final complexes. On the left type I contact and on the right type II.

Type II halogen-halogen contacts are XB interactions, as they involve the approach of the electrophilic region of a halogen to the nucleophilic region of another one. This is possible thanks to the anisotropically distributed electron density around the halogen atoms (polar flattening, see figure 1.2). Type I contacts are Van der Waals in nature. Two halogens interacting via type I contact tend to minimize the reciprocal repulsion by interfacing the neutral regions of their electrostatic potential surfaces.[61]

Halogen bonding has unique physico-chemical features, which make it a precious tool in designing new crystalline architecture with tailored properties. XB-based supramolecular synthons proved to be extremely efficient in predicting and controlling self-assembly and recognition phenomena in solid state and recently the interest of XB in liquid phase too has grown. Its applications wide spread in all the branches of Science, from pharmaceuticals to energy materials. The increasing number of papers dedicated to this non-

covalent interaction is the clear evidence that XB still remains a research hot topic. The future perspectives of XB lie in materials chemistry, pursuing new and unexplored applications; nowadays XB as crystal engineering tool is used in an ever growing number of new different fields, *e.g.* solid state supramolecular machines, photoactuators, solar panels, biomaterials and so on.[62-65]

XB is a critical structural tool in the hands of the crystal engineers to predict and fine tune crystalline supramolecular self-assembly and hence creating new functional materials with unprecedented properties.

1.1.2 XB detection in crystals

Single crystal X-ray analysis is the most used technique in the identification of XB occurrence in crystalline systems. It can give detailed information on the geometrical features of molecules and their arrangement in crystalline lattices, including intermolecular interactions.[66-68] Since Hassel's work on Br_2 and dioxane,[69] it played a key role in the structural characterization of halogen bonded crystalline adducts. Powder X-ray diffraction and others X-Ray techniques, *e.g.* Small Angle X-ray Scattering, SAXS, were also used to study halogen bonded supramolecular species.[70,71]

By single crystal X-ray diffraction it is possible to collect important pieces of information on the main structural features of XB, namely the XB-donor/XB-acceptor distances and the R-X⋯D angle. Taking into account steric hindrances and the overall crystalline packing, the shorter is the distance and the more linear is the angle, the stronger is the XB non-covalent interaction. A useful way to express the X⋯D distance is using the Normalized Contact, defined as the ratio D_{xd} /(rX_X + rD_d), where D_{xd} is the experimental distance between the XB-donor atoms X and the XB-acceptor atom D and rX_X and rD_d are the corresponding vdW radius for the XB-donor and vdW radius, or Pauling ionic radius, for the neutral or anionic XB acceptor respectively. The Normalized Contact allows the comparison of contacts of chemically different interacting sites.

Vibrational spectroscopy is also a powerful technique to assess the presence of XB both in liquid and solid phase. In particular the observation of specific vibrational shifts and peaks intensity increase associated to the formation of

halogen bonded adducts both in FTIR (Mid-IR region) and Raman spectroscopies is a well established XB detection method.[71-74]

Also NMR techniques (*e.g.* [19]F, ^{13}C, ^{15}N, [127]I), both in crystals and in solutions, can be useful methods for the characterization of XB. Studying chemical shifts and coupling constants involving halogens it is possible to identify XB and access to information regarding its association constants and geometry.[75-79]

1.2 Crystalline molecular rotors

1.2.1 Artificial molecular machines

Starting from 1990's there has been a growing interest in artificial molecular machines, which has driven the creativity, imagination and experimental efforts of many chemists in designing new systems displaying triggered mechanical motions of their molecular-level subcomponents to perform specific tasks.[80] Their design and synthesis has been such a great scientific challenge that the founders of the field, namely Jean-Pierre Sauvage, J. Fraser Stoddart and Bernard L. Feringa, have been awarded with the 2016 Nobel Prize in Chemistry for the development of molecular-level machines.
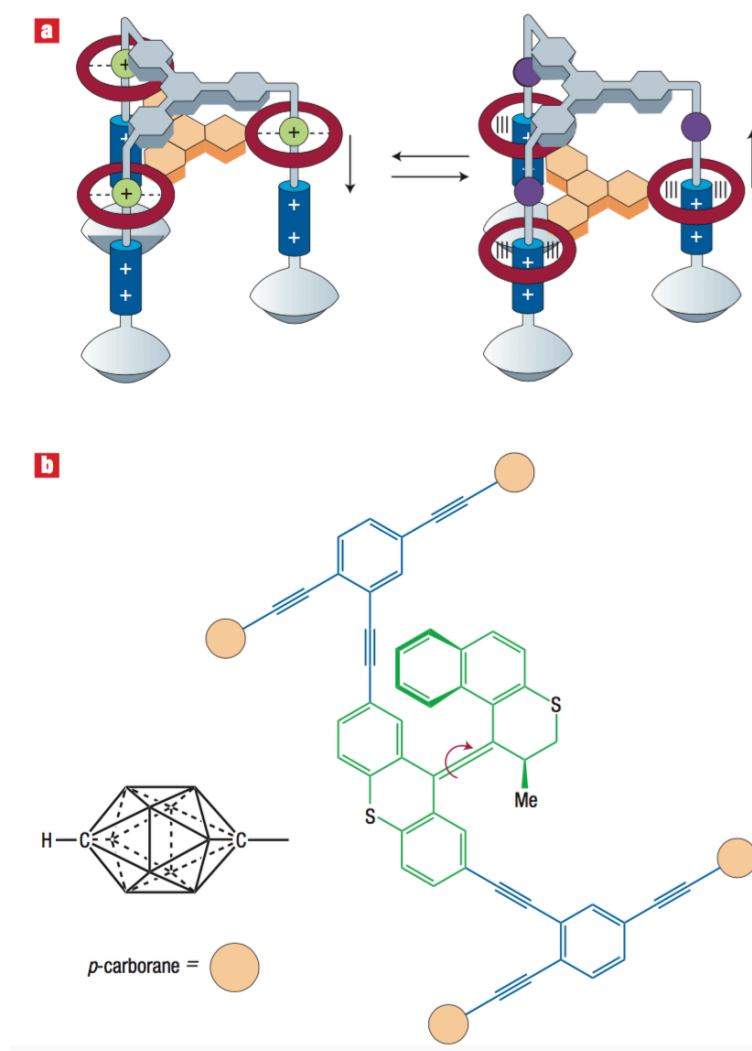
Figure 1.6 Two examples of molecular machines. (a) A pH-triggered molecular elevator and (b) a light-driven nanocar.[83,87,89]

Synthetic molecular machines are generally conceived by taking inspiration from simple macroscopic objects such as bearings, springs, ratchets, wheels, pawls, gears *etc.* which are assembled together through covalent or non-covalent bonds to form molecular motors,[81,82] elevators,[83] brakes,[84] shuttles[85], pumps,[86] or nanocars,[87,88] just to cite few examples.

Although mechanical motions of these molecular machines resemble those of their macroscopic counterparts, there is a substantial difference lying in the mechanisms at the basis of their functioning. Specifically the machines we are dealing with in our everyday life are mainly based on Newtonian mechanics and deterministic theories; this means that inertia and frictional forces play the key

roles in controlling macroscopic motions. On the other hand molecular-level machines are based on quantum mechanics and statistical thermodynamics; in this different scenario thermal energy, namely Brownian motion, must be taken into account to properly design and build such systems. Thus the analogy of modes of operation and structural appearance between macroscopic and molecular machines does not imply that molecules can perform similar functions at the nanoscale.[90]
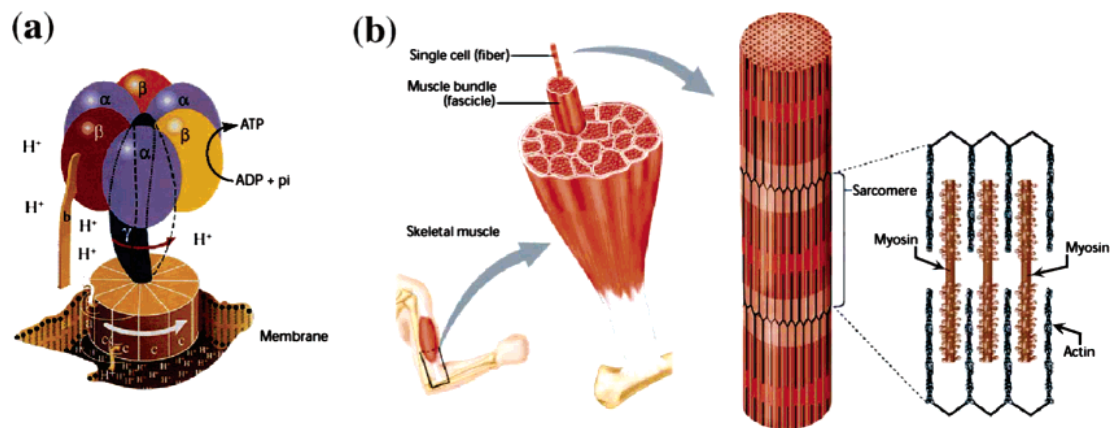
Figure 1.7 Biological molecular motors. (a) ATP synthase, three stage rotary motor membrane-supported. (b) The hierarchical structure of human skeletal muscles, showing the collective work of nano-scale linear molecular machines translated in macroscopic functions, thanks to their highly ordered spatial arrangement.[90]

Being Nature our best teacher, it gives us hints on how to properly design functional machines at molecular level, Figure 1.7. ATP synthase is a classical example of autonomous and discrete molecular motor. Specifically it is a three-stage rotary motor chemically fuelled, which is able to convert energy in highly specific functions, *e.g.* ATP synthesis *via* rotational catalysis.[91] Another molecular machines designing principle is lying in the intimate structure of skeletal muscles, made up of a huge number of nanoscopic linear motors (myosin moving along actin filaments) hierarchically assembled to collectively translate molecular-level motion into macroscopic contractions.[92] In both biological systems above described molecular machines are constantly kept far from thermodynamic equilibrium to overcome Brownian fluctuations. This is the inescapable condition to generate work without breaking the Second Law of

Thermodynamics; any attempt in this direction is like "tilting at windmills", as stated by Anthony P. Davis in 1998.[93]

In the last decades few elegant examples of artificial molecular machines doing work through dissipative processes, either as discrete and autonomous or hierarchically aggregated collective motors, have been proposed. They generally exploit their tasks in solution, soft matter or at the surface.[94-99] We are still far from designing artificial molecular motors in bulky crystalline materials, but there is an increasing interest in reaching this goal, due to the potential application of crystalline artificial machines as functional materials.

Apart from dissipative machinery there are also other strategies that take advantage of Brownian fluctuations within crystal lattices to trigger functions, like sensing or optoelctronics properties as described in the next section.

1.2.2 Amphidynamic crystals

As stated above in the last decades major efforts have been devoted to the synthesis of artificial molecular machines performing their tasks in solution and elegant examples of such systems have been well studied and characterized. However in recent years there has been a shift from individual machines working in solution to functional systems working in denser environments such as functionalized surfaces and bulk crystalline materials. This different approach takes inspiration from biological machines, which are generally complex and hierarchically disposed multi-component systems performing multiple tasks in dense media, *e.g.* cell membrane, and it is pushed by the potential materials applications of solid-state systems.[100]

Amphidynamic crystals are defined as crystalline aggregated possessing moving components (molecules, ions or molecular fragments) within their anisotropic structures. They represent an intriguing new class of materials, which brings together the high phase order typical of crystals and the motility of liquid systems, and they are likely to possess properties different from those of these two states of aggregation (figure 1.8). The inner motion in amphidynamic systems has been envisioned as a fundamental requirement for the development

of solid-state molecular machines, due to the vast gamut of still unexplored macroscopic properties accessible by taking advantage of the ordered anisotropic disposition of the moving components and the hypothetical tune of their dynamics.[101]
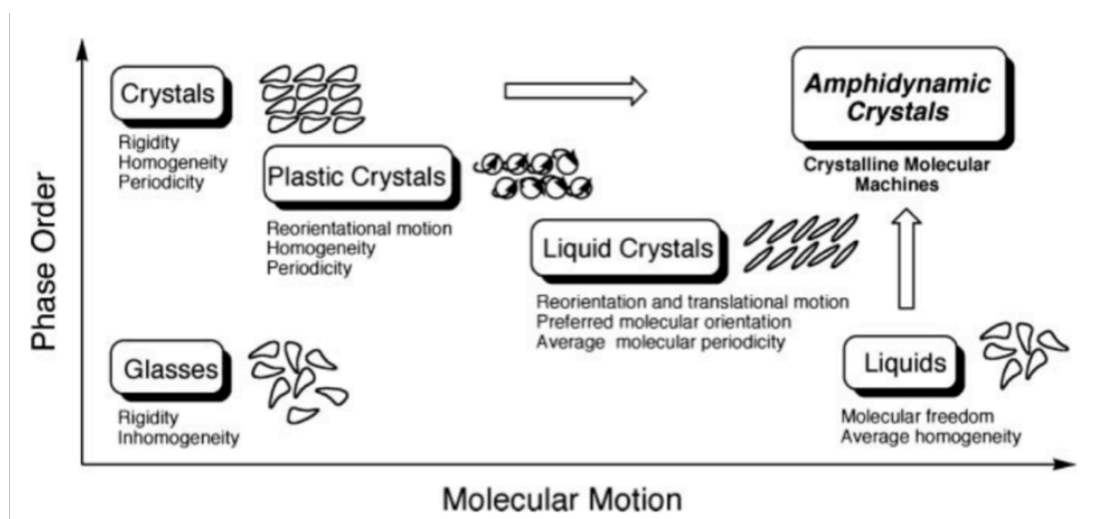
Figure 1.8 Phase Order *vs.* Molecular Motion showing how amphidynamic crystals possess the motility freedom of liquids together with the extreme order of crystalline materials.[101]

To properly design amphidynamic crystals there are three design principles to be followed:

- Free volume around the moving elements;
- The fragments undergoing motion must be volume-conserving, *e.g.* a rotating cylinder along its longer axle, which does not require any change in the surrounding space;
- Correlated motions, namely all the moving parts must interchanging in the occupancy of common spaces to avoid as much as possible steric hindrances obstructing their dynamics.

All these rules are gathered from macroscopic analogues of molecular-level machines and from biological systems, such as bacterial flagellum or ATP synthase. Given these structural design principles Brownian molecular rotors, namely amphidinamic systems where moving components follow rotary motion

trajectories, are the simplest models of amphidynamic crystal achievable and several examples have been given in literature.[102] The general and trivial scheme of such a system is shown below, see scheme 1.4.
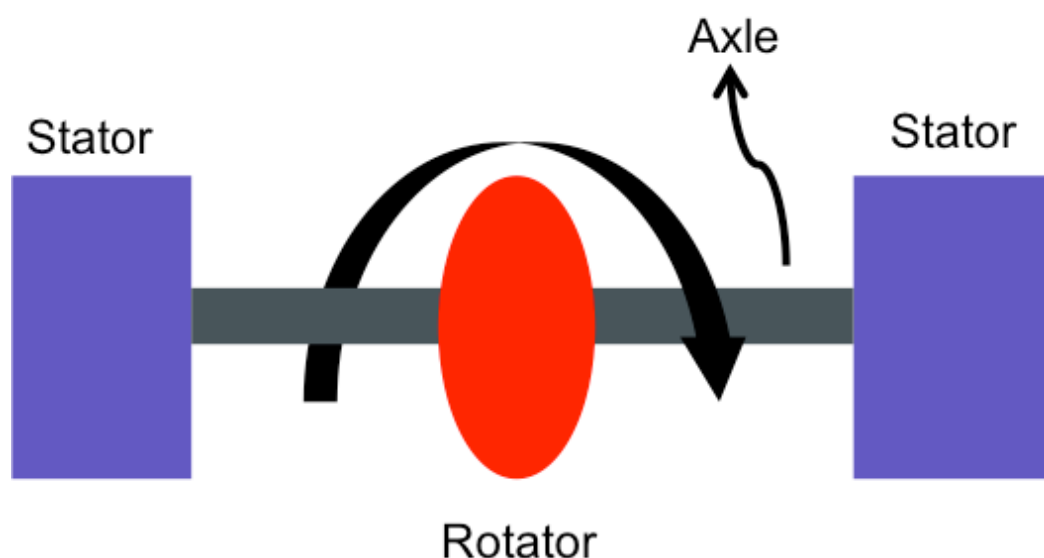

Scheme 1.4 Main components of a typical molecular/supramolecular rotor.

A molecular rotor is composed by few simple components. The stator is working as static reference system for the rotation. The anisotropic axle of rotation can be either covalent or non-covalent in nature; hence we refer to molecular or supramolecular rotors, respectively. The rotator is the moving component undergoing Brownian fluctuations.

Excellent examples of amphidynamic materials have been conceived from single component molecular crystals, forming the so-called molecular gyroscopes and compasses. By carefully design stators and rotators it is possible to finely tune the relaxation rates of the extended crystalline solids.[102] In particular more hindered stators and volume-conserving moving components can result in improving dynamics of the final amphidynamic system. M. A. Garcia-Garibay has been actively working in the design, synthesis and characterization of single component amphidynamic crystals based on triphenylmethane or trypticene derivatives working as stators connected *via* acetylene linkages to a wide variety of rotators shedding lights on the structure-

related inner dynamics of amphidynamic crystals and their possible applications, figure 1.9.[102-107]
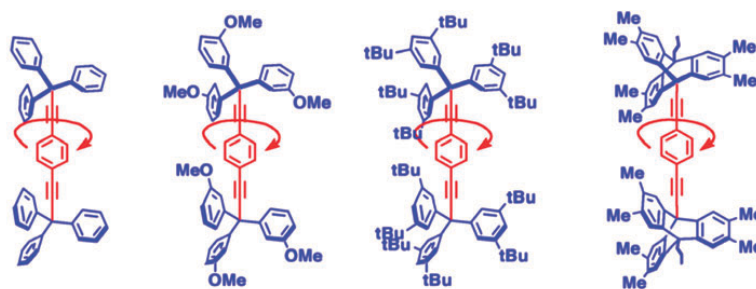
Figure 1.9 Examples of molecular gyroscopes based on phenyl rotators. The stators are highlighted in blue and the rotators are highlighted in red.[102]

The step forward in the development of amphidynamic crystals is constituted by the design and synthesis of multi-component complexes (*e.g.* solid solutions, co-crystals), because it is expected that more components could bring to higher functional complexity if compared to the isolated starting building blocks.[108,109] What is more the different functions could be triggered by different stimuli.[102]

Tuning the anisotropic reorientation dynamics of ordered rotators through external stimuli, *e.g.* light, external electrical field or temperature,[110-113] gives the opportunity to control vectorial properties of matter, such as birefringence or ferroelectrics properties. For example Akutagawa and coworkers demonstrated that it is possible by applying an external electrical field to control the polarity of a ferroelectric amphidynamic crystal, where the rotor owns a permanent dipole. This was done with the supramolecular complex based on charge-assisted hydrogen bonds of (dibenzo[18]crown6)(*m*-fluoroanilinium$^+$) cation mixed with [Ni(dmit)$_2$]$^-$ working as counterion (dmit = 2-thioxo-1,3-dithiole-4,5-dithiolate). The rotational dynamics of *m*-FAni$^+$, acting as rotator, within the close packed crystal structure was successfully controlled by an external electric field which tuned the reorientation of the dipolar rotator thus enabling the control over the polarity of the crystals, as shown in figure 1.10.
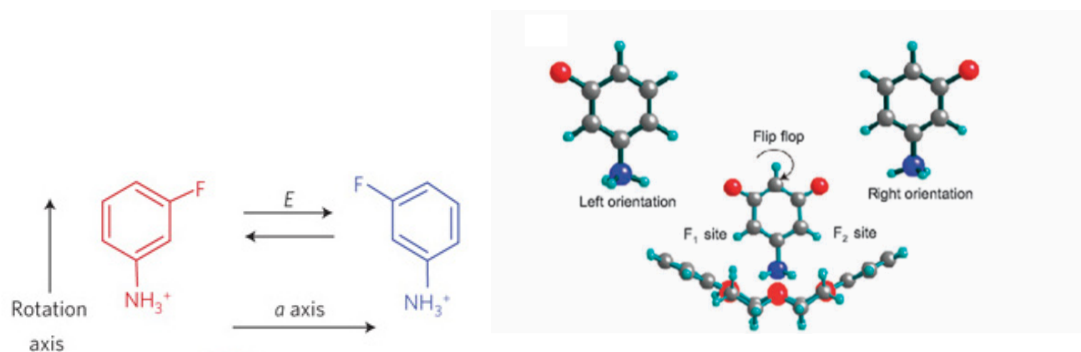
Figure 1.10 Anisotropic reorientation of the anilinium cation through an external electrical field (E) and the rotator flip flop motion around the axle lying along the C-NH$_3^+$ covalent bond.[113]

Crystalline porous materials are another suitable platform for the development of amphidynamic crystals thanks to the highly ordered disposition of their sub-components and the presence of free volumes, which can give rise to virtually not hampered motion of the rotators. These materials are prepared through a great variety of different procedures taking advantage of covalent chemistry, coordination bonds and supramolecular approaches. The first examples of this peculiar class of compounds have been mesoporous organosilica materials possessing aromatic linkers undergoing Brownian fluctuations around anisotropic axles, see figure 1.11. Then metal organic and fully organic frameworks and molecular porous crystals have been extensively studied both structurally and dynamically.[114-116]
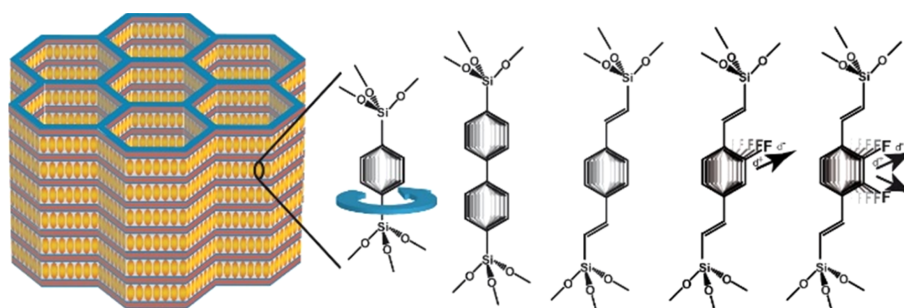
Figure 1.11 Periodic mesoporous orgonosilicas and possible linkers, working as molecular rotators.[113]

As porous materials they possess cavities accessible to molecular guests. The host-guest complexes can be designed to show tunable dynamics of the rotators depending on the chemical nature and steric hindrance of the guests; thus constituting prototypical sensing devices. For example this has been

demonstrated by A. Comotti *et al.* for porous molecular crystals of 4,4'-bis(sulfophenylethynyl)benzene n-pentylammonium organic salt whose crystal structure shows permanent porosity, see figure 1.12. The phenyl rotators of the apohost are characterized by relaxation rates of *ca.* 10^8 Hz and rotation E_a of 4.7 kcal/mol at room temperature; once exposed to iodine vapours, even at very low molecular halogen pressure, the dynamics drastically decreases (rotation frequency = 10^4 Hz) and E_a increases up to 10.5 kcal/mol due to the presence of the guest molecules. Absorption/desorption of molecular iodine can switch on and off the rotator dynamics, making porous amphidynamic materials promising candidates for sensing and pollutant management.[117]
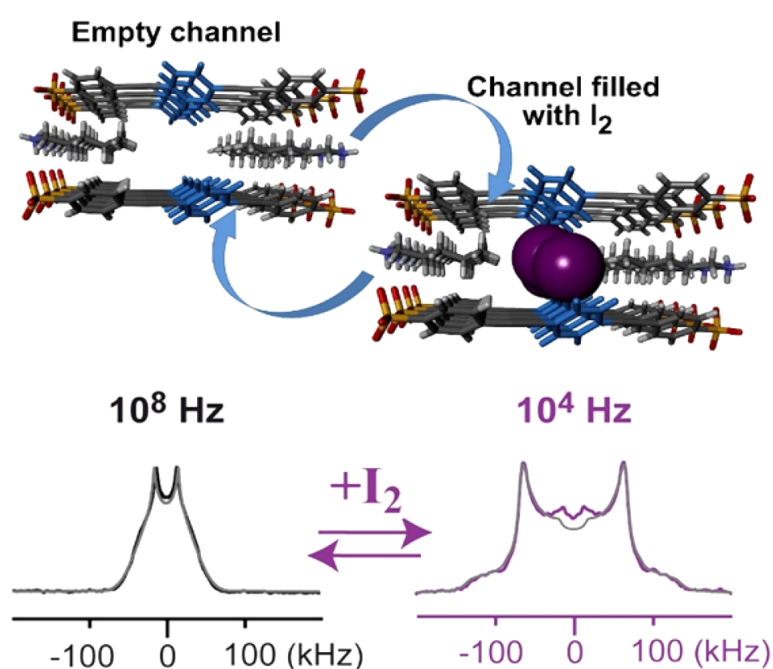
Figure 1.12 Absorption/desorption of molecular iodine in a porous amphidynamic organic molecular crystals and the effect of the guest molecules on the phenyl rotator (highlighted in blue) dynamics at 295 K.[117]

There is still plenty of room for further studies related to amphidynamic crystals. Exploiting a supramolecular approach for their design and synthesis is a future challenge to obtain new materials with better yields and performances. Non-covalent interactions, *e.g.* hydrogen bond, halogen bond among others, can play a critical role to precisely engineer amphidynamic crystals structures and to tune rotators dynamics, as recencly reported by several groups.[118,119]

References:

1 J. D. Dunitz, *Pure Appl. Chem.*, 1991, **63**, 2, 177.

2 D. Braga, *ChemComm*, 2003, 2751.

3 G. R. Desiraju, *Angew. Chem. Int. Ed.*, 1995, **34**, 21, 2311.

4 P. Metrangolo and G. Resnati, *Chem. Eur. J.*, 2001, **7**,12, 2511.

5 P. Metrangolo and G. Resnati, *Cryst. Growth Des.*, 2012, **12**, 5835.

6 G. Cavallo, P. Metrangolo, R. Milani, T. Pilati, A. Priimagi, G. Resnati and G. Terraneo, *Chem. Rev.*, 2016, **116**, 2478.

7 M. Fourmigué, *Curr. Opin. Solid State Mat. Sci.*, 2009, **13**, 36.

8 P. Politzer, J. S. Murray and T. Clark, *PhysChemChemPhys*, 2010, **12**, 7748.

9 J. J. Colin, *Ann. Chi.*, 1814, **91**, 52.

10 F. Guthrie, *J. Chem. Soc.*, 1863, **16**, 239.

11 S. M. Jörgensen , *J. Prakt. Chem.*, 1870, **2**, 347.

12 O. Roussopoulos, *Ber.*, 1883, **16**, 202.

13 I. Remsen and J. F. Norris, *Am. Chem. J.*, 1896 , **18**, 90.

14 O. Hassel, *Science*, 1970, **170**, 497.

15 H. A. Bent, *Chem. Rev.*, 1968, **68**, 587.

16 R. B. Walsh, C. W. Padgett, P. Metrangolo, G. Resnati, T. W. Hanks and W. T. Pennington, *Cryst. Growth Des.*, 2001, **1**, 2, 165.

17 P. Metrangolo and G. Resnati, *Science*, 2008, **321**, 918.

18 C. B. Aackeröy, J. Desper, B. A. Helfrich, P. Metrangolo, T. Pilati, G. Resnati and A. Stavenazzi, *ChemComm*, 2007, 4236.

19 A. C. Legon, *Struct. Bond.*, 2008, **126**, 17.

20 A. R. Voth, P. Khuu, K. Oishi and P. Shing Ho, *Nature Chem.*, 2009, **1**, 74.

21 A. Mukherjee, S. Tothadi and G. R. Desiraju, *Acc. Chem. Res.*, 2014, **47**, 2514.

22 M. Simard, D. Su and J. D. Wuest, *J. Am. Chem. Soc.*, 1991, **113**, 12, 4696.

23 P. Metrangolo,F. Meyer,T. Pilati,G. Resnati and G. Terraneo, A*ngew. Chem. Int. Ed.*, 2008, **47**, 6114.

24 J. D. Wuest, *Nature Chem.*, 2012, **4**, 74.

25 E. K. Plyler and R. S. Mulliken, *J. Am. Chem. Soc.*, **81**, 823.

26 J. Yarwood and W. B. Pearson, *J. Am. Chem. Soc.,* 1968, **90**, 594.

27 C. K. Prout and B. Kamenar, *Crystal structures of electron-donor-acceptor complexes.* In *Molecular complexes*, ed. R. Foster, Elek, London, 1973, pp. 151-207.

28 A. C. Legon, *Angew. Chem. Int. Ed.*, 1999, **38**, 2686.

29 J. A. Blake, F. A. Devillanova, R. O. Gould, W. S. Li, V. Lippolis, S. Parson, C. Radek and M. Schroder, *Chem. Soc. Rev.*, 1998, **27**, 195.

30 M. Fourmigué, *Struct. Bond.*, 2008, **126**, 181.

31 W. W. Du Mont and F. Ruthe, *Coord. Chem. Rev.*, 1999, **189**, 101.

32 K. Raatikainen and K. Rissanen, *CrystEngComm*, 2011, **13,** 6972.

33 G. R. Desiraju, P. Shing Ho, L. Kloo, A. C. Legon, R. Marquardt, P. Metrangolo, P. Politzer, G. Resnati and K. Rissanen, *Pure Appl. Chem.*, 2013, **85**, 8, 1771.

34 T. Clark, M. Hennemann, J. S. Murray and P. Politzer, *J. Mol. Model.*, 2007, **13**, 291.

35 P. Politzer, P. Lane, M. C. Concha, Y. Ma and J. S. Murray, *J. Mol. Model.*, 2007, **13**, 305.

36 F. F. Awwadi, R. D. Willet, K. A. Peterson and B. Twamley, *Chem. Eur. J.*, 2006, **12**, 8952.

37 S. C. Nyburg and J. T. Szymansky, *ChemComm*, 1968, 669.

38 S. C. Nyburg and C. H. Faerman, *Acta Cryst.*, 1985, **B41**, 274.

39 J. P. M. Lommerse, A. J. Stone, R. Taylor and F. H. Allen, *J. Am. Chem. Soc.*, 1996, **118**, 3108.

40 P. Metrangolo, J. S. Murray, T. Pilati, P. Politzer, G. Resnati and G. Terraneo, *CrystEngComm*, 2011, **13**, 6593.

41 R. Walsh, C. W. Padgett, P. Metrangolo, G. Resnati, T. W. Hanks and W. T. Pennigton, *Cryst. Growth Des.*, 2001, **1**, 2, 165.

42 C. B. Aackeröy, C. K. Wijethunga and J. Desper, *J. Mol. Struct.*, 2014, **1072**, 20.

43 J.-Y. Le Questel, C. Laurence and J. Graton, *CrystEngComm*, 2013, **15**, 3212.

44 P. Metrangolo, H. Neukirch, T. Pilati and G. Resnati, *Acc. Chem. Res.*, 2005, **38**, 386.

45 F. Fontana, A. Forni, P. Metrangolo, W. Panzeri, T. Pilati and G. Resnati, *Supramol. Chem.*, 2002, **14**, 47.

46 M. T. Messina, P. Metrangolo, W. Panzeri, T. Pilati and G. Resnati, *Tetrahedron*, 2001, **57**, 8543.

47 B. Ji, W. Wang, D. Deng and Y. Zhang, *Cryst. Growth Des.*, 2011, **11**, 3622.

48   J. L. Syssa-Magalé, K. Boubekeur and B. Schöllhorn, *J. Mol. Struct.*, 2005, **737**, 103.

49 A.-L. Barres, A. El-Ghayoury, L. V. Zorina, E. Canadelli, P. Auban-Senzier and P. Batail, *ChemComm*, 2008, 2194.

50 S. V. Rosokha and J. K. Kochi, *Struct. Bond.*, 2008, **126**, 137.

51 S. Y. Oh, C. W. Nickels, F. Garcia, W. Jones and T. Friščić, *CrystEngComm*, 2012, **14**, 6110.

52 Q. Li, Q. Li, W. Li, J. Cheng, B. Gong and J. Sun, *ChemPhysChem*, 2008, **9**, 15, 2265.

53 Q. Zhao, D. Feng and J. Hao, *J. Mol. Model.*, 2011, **17**, 2817.

54 B. Jing, Q. Li, R. Li, B. Gong, Z. Liu, W. Ji, J. Cheng and J. Sun, *Comp. Theor. Chem.*, 2011, **963**, 417.

55 M. G. Chudzinski, C. A. McClary and M. S. Taylor, *J. Am. Chem. Soc.*, 2011, **133**, 27, 10559.

56 F. Zapata, A. Caballero, P. Molina, I. Alkorta and J. Elguero, *J. Am. Chem. Soc.*, 2014, **79**, 15, 6959.

57 M. J. Langton, S. W. Robinson, I. Marques, V. Felix and P. D. Beer, *Nature Chem.*, 2014, **6**, 1039.

58 S. W. Robinson, C. L Mustoe, N. G. White, A. Brown, A. L. Thompson, P. Kennepohl and P. D. Beer, *J. Am. Chem. Soc.*, 2015, **137**, 1, 499.

59 A. Takemura, L. J. MacAllister, S. Hart, N. E. Pridmore, P. B. Karadov, A. C. Whitwood and D. W. Bruce, *Chem. Eur. J.*, 2014, **20**, 6721.

60 V. Vasylyeva, S. K. Nayak, G. Terraneo, G. Cavallo, P. Metrangolo and G. Resnati, *CrystEngComm*, 2014, **16**, 8102.

61 A. Mukherjee, S. Tothadi and G. R. Desiraju, *Acc. Chem. Res.*, 2014, **47**, 2514.

62 L. Catalano, S. Pérez-Estrada, T. Pilati, G. Terraneo, G. Resnati, P. Metrangolo and M. Garcia-Garibay, *J. Am. Chem. Soc.*, 2015, **137**, 49, 15386.

63 A. Abate, M. Saliba, D. J. Hollman, S. D. Stranks, K. Wojciechowski, R. Avolio, G. Grancini, A. Petrozza, and H. J. Snaith, *Nano Lett.*, 2014, **14**, 6, 3247.

64 A. Vargas-Jentzsch, D. Emery, J. Mareda, S. K. Nayak, P. Metrangolo, G. Resnati, N. Sakai and S. Matile, *Nat. Commun.*, 2012, **3**, 905.

65 A. Bertolani, L. Pirrie, L. Stefan, N. Houbenov, J. S. Haataja, L. Catalano, G. Terraneo, G. Giancane, L. Valli, R. Milani, O. Ikkala, G. Resnati and P. Metrangolo, *Nat. Commun.*, 2015, **6**, 7574.

66 C. Guardigli, R. Liantonio, M. L. Mele, P. Metrangolo, G. Resnati and T. Pilati, *Supra. Chem.*, 2003, **15**, 3, 177.

67 D. D. Burton, F. Fontana, P. Metrangolo, T. Pilati and G. Resnati, *Tetrahedron Lett.*, 2003, **44**, 4, 645.

68 K. B. Dillon and T. C. Waddington, *Nature*, 1971, **230**, 15, 158.

69 O. Hassel and J. Hvoslef, *Acta Chem. Scand.*, 1954, **8**, 5, 873.

70 M. Baldrighi, D. Bartesaghi, G. Cavallo, M. R. Chierotti, R. Gobetto, R.; P. Metrangolo, T. Pilati, G. Resnati and G. Terraneo, *CrystEngComm*, 2014, **16**, 26, 5897.

71 N. Houbenov, R. Milani, M. Poutanen, J. Haataja, V. Dichiarante, J. Sainio, J. Ruokolainen, G. Resnati, P. Metrangolo, O. Ikkala, *Nat. Commun.*, 2014, **5**, 4043.

72 A. Priimagi, G. Cavallo, A. Forni, M. Gorynsztejn-Leben, M. Kaivola, P. Metrangolo, R. Milani, A. Shishido, T. Pilati, G. Resnati and G. Terraneo, *Adv. Funct. Mater.*, 2012, **22**, 2572.

73 M. T. Messina, P. Metrangolo, W. Navarrini, S. Radice, G. Resnati and G. Zerbi, *J. Mol. Struct.,* 2000, **524**, 87.

74 M. Erdélyi, *Chem. Soc. Rev.*, 2012, **41**, 3547.

75 P. Metrangolo, W. Panzeri, F. Recupero and G. Resnati, *J. Fluor. Chem.*, 2002, **114**, 1, 27.

76 R. Glaser, N. J. Chen, H. Wu, N. Knotts and M. Kaupp, *J. Am. Chem. Soc.*, 2004, **126**, 13, 4412.

77 M. Weinegarth, N. Raouafi, B. Jouvelet, L. Duma, G. Bodehausen, K. Boujlel, B. Schollhorn and P. Tekeley, *Chem. Commun.*, 2008, **45**, 5981.

78 M. G. Sanwar, B. Dragisic, L. J. Salsberg, C. Gouliaras and M. S. Taylor, *J. Am. Chem. Soc.*, 2010, **132**, 5, 1646.

79 D. L. Bryce and J. Viger-Gravel, *Top. Curr. Chem.*, 2015, **358**, 183.

80 V. Balzani, A. Credi and M. Venturi, *NanoToday*, **2**, 18.

81 T. R. Kelly, H. De Silva and R. A. Silva, *Nature*, 1999, **401**, 150.

82 N. Koumura, E.M. Geertsema, A. Meetsma and B.L. Feringa, *J. Am. Chem. Soc.*, 2000, **122**, 12005.

83 J. D. Badjic, V. Balzani, A. Credi, S. Silvi and J. F. Stoddart, *Science*, 2004, **303**, 1845.

84 T. R. Kelly, M. C. Bowyer, K. V. Bhasckar, D. Bebbington, A. Garcia, F. Lang, M. H. Kim, and M. P. Jette, *J. Am. Chem. Soc.*, 1994, **116**, 3657.

85 P. L. Anelli, N. Spencer, J. F. Stoddart, *J. Am. Chem. Soc.*, 1991, **113**, 5131.

86 C. Cheng, P. R. McGonigal, S. T. Schneebeli, N. A. Vermeulen, C. Ke, J. F. Stoddart, *Nat. Nanotech.*, 2015, **10**, 547.

87 J.-F. Morin, Y. Shirai, J. M. Tour, *Org. Lett.*, 2006, **8**, 1713.

88 T. Kudernac, N. Ruangsupapichat, M. Parschau, B. Maciá, N. Katsonis, S. R. Harutyunyan, K.-H. Herst and B. Feringa, *Nature*, 2011, **479**, 208.

89   W. R. Browne, B. L. Feringa, *Nat. Nanotech.*, 2006, **1**, 25.

90 T.-A. H. Khuong, J. E. Nuñez, C. E. Godinez and M. A. Garcia-Garibay, *Acc. Chem. Res.*, 2006, **39**, 413.

91 H. Noji, R. Yasuda, M. Yoshida and K. Kinosita Jr., *Nature*, 1997, **386**, 299.

92 I. Rayment, W. R. Rypniewski, K. Schmidt-Base, R. Smith, D. R. Tomchick, M. M. Benning, D. A. Winkelmann, G. Wesenberg and H. M. Holden, *Science*, 1993, **261**, 50.

93 A. P. Davis, *Angew. Chem. Int. Ed.*, 1998, **37**, 909.

94 S. Erbas-Cakmak, D. Leigh, C. T. Mcternan and A. L. Nussbaumer, *Chem. Rev.*, 2015, **115**, 10081.

95 G. Ragazzon, M. Baroncini, S. Silvi, M. Venturi and A. Credi, *Nat. Nanotech.*, 2015, **10**, 70.

96 B. S. L. Collins, J. C. M. Kistemaker, E. Otten and B. L. Feringa, *Nature Chem.*, 2016, **8**, 860.

97 M. R. Wilson, J. Solà, A. Carlone, S. M. Goldup, N. Lebrasseur and D. Leigh, *Nature*, 2016, **534**, 235.

98 R.A. van Delden, M.K.J. ter Wiel, M.M. Pollard, J. Vicario, N. Koumura and B.L. Feringa, *Nature*, **437**, 1337.

99 R. Eelkema, M. M. Pollard, J. Vicario, N. Katsonis, B. Serrano Ramon, C. W. M. Bastiaansen, D.J. Broer, and B.L. Feringa, *Nature*, 2006, **440**, 163.

100 S. D. Karlen, H. Reyes, R. E. Taylor, S. I. Khan, M. F. Hawthorne and M. A. Garcia-Garibay, *Proc. Natl. Acad. Sci.*, 2010, **107**, 14973.

101 M. A. Garcia-Garibay, *Proc. Natl. Acad. Sci.*, 2005, **102**, 10771.

102 C. S. Vogelsberg and M. A. Garcia-Garibay, *Acc. Chem. Res.*, 2012, **41**, 1892.

103 Z. Dominguez, H. Dang, M. J. Strouse and M. A. Garcia-Garibay, *J. Am. Chem. Soc.*, 2002, **124**, 7719

104 Z. Dominguez, T.-A. V. Khuong, H. Dang, C. N. Sanrame, J. E. Nuñez and M. A. Garcia-Garibay, *J. Am. Chem. Soc.*, 2003, **125**, 8827.

105 R. D. Horansky, L. I. Clarke, E. B. Winston, J. C. Price, S. D. Karlen, P. D. Jarowski, R. Santillan and M. A. Garcia-Garibay, *Phys. Rev. B*, 2006, **74**, 054306.

106 X. Jiang, B. Rodríguez-Molina, N. Nazarian and M. Garcia-Garibay, *J. Am. Chem. Soc.*, 2014, **136**, 8871.

107 X. Jiang, Z. J. O'Brien, S. Yang, L. H. Lai, J. Buenaflor, C. Tan, S. I. Khan, K. N. Houk and M. A. Garcia-Garibay, *J. Am. Chem. Soc.*, 2016, **138**, 4650.

108 H. Deng, C. J. Doonan, H. Furukawa, R. B. Ferreira, J. Towne, C. B. Knobler, B. Wang and O. M. Yaghi, *Science*, 2010, **327**, 846.

109 M. Inukai, T. Fukushima, Y. Hijikata, N. Ogiwara, S. Horike and S. Kitagawa, J. Am. Chem. Soc., 2015, **137**, 12183.

110 O. Satu, *Nature Chem.*, 2016, **8**, 644.

111 P. Commins and M. A. Garcia-Garibay, *J. Org. Chem.*, 2014, **79**, 1611.

112 W. Setaka and K. Yamaguchi, *Proc. Natl. Acad. Sci.*, 2012, **109**, 9271.

113 T. Akutagawa, H. Koshinaka, D. Sato, S. Takeda, S.-I. Noro, H. Takahashi, R. Kumai, Y. Tokura and T. Nakamura, *Nature Mater.*, 2009, **8**, 342.

114 A. Comotti, S. Bracco and P. Sozzani, *Acc. Chem. Res.*, 2016, **49**, 1701.

115 S. L. Gould, D. Tranchemontagne, O. M. Yaghi and M. A. Garcia-Garibay, *J. Am. Chem. Soc.*, 2008, **130**, 3246.

116 X. Jiang, H.-B. Duan, S. I. Khan and M. A. Garcia-Garibay, *ACS Cent. Sci.*, 2016, **2**, 608.

117 A. Comotti, S. Bracco, A. Yamamoto, M. Beretta, T. Hirukawa, N. Tohnai, M. Miyata and P. Sozzani, *J. Am. Chem. Soc.*, 2014, **136**, 618.

118 C. Lemouchi, C. S. Vogelsberg, L. Zorina, S. Simonov, P. Batail, S. Brown and M. A. Garcia-Garibay, *J. Am. Chem. Soc.*, 2011, **133**, 6371.

119 Q.-C. Zhang, F.-T. Zu, H.-M. Hao, H. Xu, H.-X. Zhao, L.-S. Long, R.-B. Huang and L. S. Zheng, *Angew. Chem. Int. Ed.*, 2013, **52**, 12602.

CHAPTER 2

Spectroscopic Investigations of

Halogen-Bonded complexes

2.1 Far-IR spectroscopy as diagnostic tool of XB involving aromatic donors[1]

2.1.1 Introduction

In recent years the use of halogen bond (XB) is going beyond the boundaries of crystal engineering and it is rising as a precious tool in designing new functional supramolecular materials, *e.g.* liquid crystals, photoresponive materials, engineered peptides, polymers and so on.[2,3] The confinement of such systems in a single phase (crystal, amorphous, liquid…) is generally difficult, that is why they are defined as soft matter, whose structural characterization and information related to XB formation are not easily achievable with routinary techniques. Thus, there is the need to find out new fast and easy-accessible methods for the identification of XB in supramolecular species.

Starting from Mulliken's work on charge-transfer complexes of I_2 interacting with pyridine derivatives and benzene through "charge-transfer interactions",[4] later on identified as early examples of halogen bond, there have been several far-IR spectroscopic studies involving molecular halogens and interhalogens and various electron-rich species.[5] These studies revealed few diagnostic features of XB occurrence, such as peaks intensity increase and red-shift of the vibrational bands of the covalent bonds involving XB donors moieties. These evidences were associated with a partial charge flux form the XB acceptor sites to the positively polarized halogens, confirming the charge-transfer nature of this non-covalent interaction.[6-8] Same results were obtained by studying halogen-bonded complexes involving simple haloperfluoroalkanes, *e.g.* CF_3I, by means of high-resolution techniques and using harsh experimental conditions, such as the use of cryo-matrices.[9-14]

To the best of our knowledge these distinct vibrational fingerprints have not been observed so far in supramolecular species where aromatic XB donors are involved, even if these building blocks are widely used in the design and

synthesis of new halogen-bonded species. The lack on far-IR assignment for aromatic halogenated compounds and their halogen-bonded complexes is mainly due to low frequencies (< 400 cm^{-1}) and weak intensities of the vibrations involving halogens (X = Br and I), which are not detectable with routine laboratory instrumentations, even if some rare cases of theoretical assignments have been recently discussed in the literature.[15,16] However thanks to new standard instruments the detection limit of vibrational spectroscopy is moving to lower frequencies allowing the exploration of the far-IR region and hence C-X vibrations. Thus we envisaged far-IR spectroscopy as a promising technique for a fast and easy-accessible detection method of XB involving aromatic donors. To demonstrate this hypothesis we studied the far-IR features of prototypical halogen-bonded complexes incorporating haloperfluoroaromatic XB donors.

2.1.2 Results and discussion

To prove the potential of far-IR spectroscopy in revealing the occurrence of XB involving aromatic moieties, we build a series of six halogen-bonded adducts, based on very simple XB donor supramolecular synthons designed to minimize any possible interference to XB formation or modification of its features. To simplify at the maximum crystal packing requirements monodentate XB donors, such as iodopentafluorobenzene (IPFB) and bromopentafluorobenzene (BPFB) , were preferred to multi-dentate systems to favour the formation of discrete either dimeric or trimeric supramolecular complexes.

1   $R_1 = R_2 = R_3 = R_4 = R_5 = H$; X = I
2   $R_2 = CH_3$; $R_1 = R_3 = R_4 = R_5 = H$; X = I
3   $R_3 = CH_3$; $R_1 = R_2 = R_4 = R_5 = H$; X = I
4   $R_2 = R_4 = CH_3$; $R_1 = R_3 = R_5 = H$; X = I
5   $R_1 = R_2 = R_3 = R_4 = R_5 = H$; X = Br
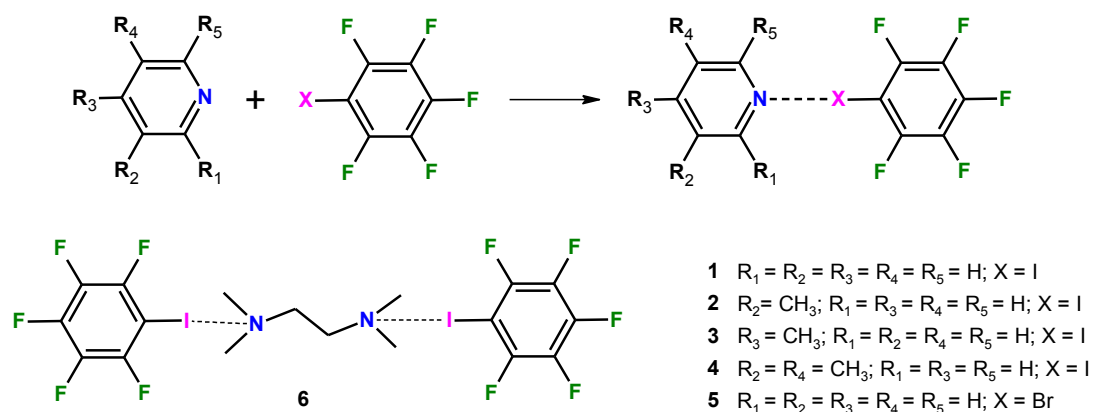
Scheme 2.1 The synthesized dimeric (**1**-**5**) and trimeric (**6**) halogen-bonded complexes.

Pyridine, 3-methylpyridine, 4-methylpyridine, and 3,5-dimethylpyridine were chosen as XB acceptors, along with tetramethylethylenediamine (TMEDA) as an example of an aliphatic acceptor (Scheme 1). Single crystal X-ray structures of the obtained adducts **1**–**6** confirmed that the X···N halogen bonds (X = I, Br) were, by far, the most important interactions in the crystals. Being other interactions relatively long, *i.e.* weak, the studied IR characteristics are indicative of the inherent features of the halogen bonds rather than of halogen bonds heavily perturbed by crystal packing effects.

Table 2.1 Experimental melting points of the starting compounds and the final products. Onset temperatures are given.

Compound	m.p (°C)	m (mg)	Δm.p.$_a$ (°C)	Δm.p.$_d$ (°C)
Pyridine	-40.0	13.3	-	-
3-methylpyridine	-26.0	23.0	-	-
4-methylpyridine	-6.0	25.0	-	-
3,5-dimethylpyridine	-9.0	13.3	-	-
TMEDA	-60.0	12.9	-	-
Iodopentafluorobenzene	-15.0	23.0	-	-
Bromopentafluorobenzene	-30.0	21.6	-	-
1	18.5	26.1	68.5	40.5
2	28.0	13.0	54	43
3	27.0	15.0	33	42
4	52.0	12.0	61	67
5	-22.5	15.3	17.5	7.5
6	50.0	14.2	109	72

Δm.p.$_a$: difference between m.p. of the mixture with respect to the halogen bond acceptor; **Δm.p.$_d$**: difference between m.p. of the mixture with respect to the halogen bond donor.

The six halogen-bonded cocrystals were synthesized by direct mixing of the liquid starting materials in either 1:1 (**1**, **2**, **3**, **4**, and **5**) and 1:2 (**6**) molar ratios, taking into account the pairing of the respective halogen-bond donor and acceptor sites. Crystallization of **2**–**4** and **6** occurred during blending, while **1** and **5** remained liquids at room temperature. The formation of new, discrete

adducts and the absence of remaining starting compounds were confirmed by differential scanning calorimetry (DSC) measurements, see Table 2.1. New single melting and crystallization peaks were obtained, which differed from the starting compounds. In particular, while all starting compounds melted at temperatures below 0 °C (from −60 to −6 °C), all of the iodinated cocrystals melted well above 0 °C, from +18 to +53 °C. Cocrystal **5**, instead, melted at −22 °C, which finds justification in the lower strength of the halogen bond given by BrPFB.[17,18]

Table 2.2 Halogen bond distances in **1**, **2**, **3**, **4**, **5** and **6**.

Compounds	X···Y	X···Y/Å
1	I···N	2.783
2	I···N	2.728
3	I···N	2.806[a]
4	I···N	2.831[b]
		2.841[c]
6	I···N	2.765
5	Br···N	2.882

[a] CCDC: LEZQAJ; [b] CCDC: LEZPUC; [c] CCDC: LEZPUC01

The structures of the obtained halogen-bonded cocrystals were determined via single crystal X-ray diffraction analysis. Cocrystals **1** (m.p.: +18 °C) and **5** (m.p.: −22 °C) were generated and analysed *in situ* by means of an optical heating and crystallization device (OHCD)[19] in order to obtain single crystals suitable for X-ray diffraction. The structures of cocrystals **3** and **4** were already reported in the Cambridge Structural Database[20] (Refcodes: LEZQAJ and LEZPUC, LEZPUC01, respectively)[21] The structures of both polymorphs of **4** (LEZPUC, LEZPUC01) were obtained at 298 K and 150 K, respectively. All other cocrystal structures have never been reported before. Expectedly, the self-assembly of the starting compounds into dimers **1**–**5** and trimer **6** is driven by short X···N (X = I, Br) contacts, as shown in Figure 2.2 and Table 2.2. The I···N distance is in the range of 2.728(2)–2.841(9) Å, corresponding roughly to a 20% reduction in the sum of the vdW radii for I and N (3.50 Å).[22] The Br···N distance found in **5** was 2.882(2) Å, which corresponds to a 15% reduction in the sum of the vdW radii for Br and N (3.40 Å).[22] All crystal structures adopt the same monoclinic space group (P21/c and P21/n), showing strong similarities in their packing.
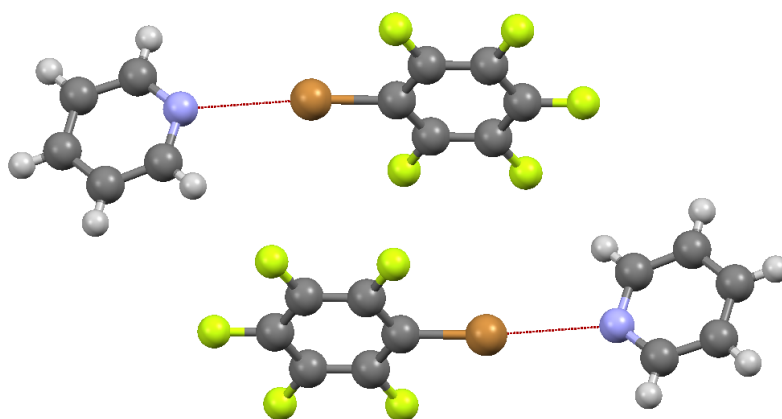
Figure 2.1 Supramolecular dimers within the crystal structure of **5**. In red dashed line the N⋯Br interaction is highlighted. Colour code: C, grey; H, light grey; N, blue; F, yellow; Br, orange.

Once confirmed the formation of all the XB-based cocrystals, all the starting materials and products were investigated by means of IR spectroscopy, in particular in the far-IR region at room temperature, to ascertain the effect of XB on the normal modes of vibrations of the molecular fragments involving the electrophilic halogens. To correctly identify the normal modes of vibration involved in the halogen bond formation an accurate assignment of the corresponding vibrational bands was essential. Therefore we performed a detailed vibrational analysis in the gas phase by density functional theory (DFT) calculations of the optimized geometries of the above mentioned supramolecular adducts (for further details please refer to experimental section 5.1.5).
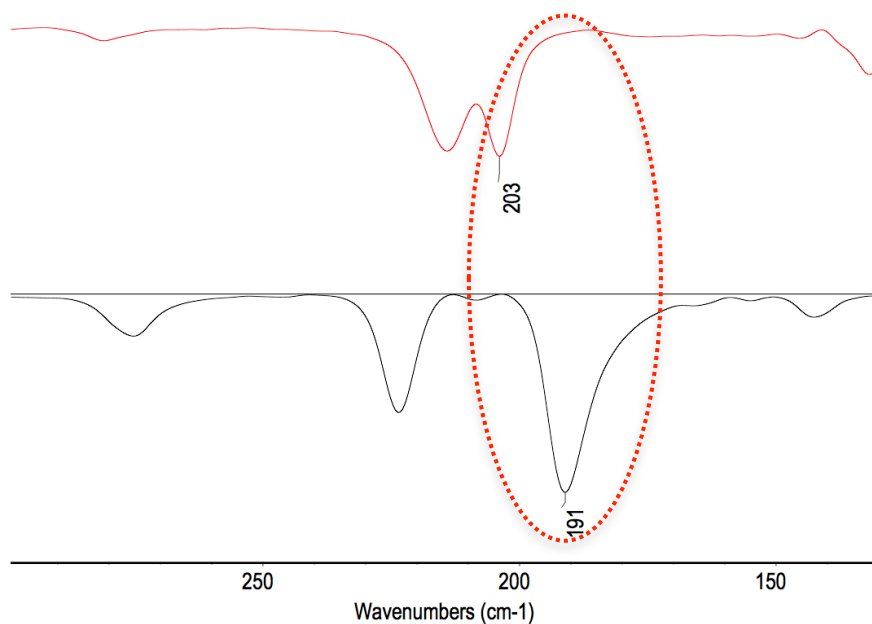
Figure 2.2 Normalized Far-IR spectra of IPFB (red) and **4** (black). Passing from iodopentafluorobenzene to the adduct, there are a clear red-shift and intensity increase of in plane C-I stretching band (highlighted by red dashed line).

Four vibrations involving halogen atom in IPFB were allocated in the far-IR region as out of plane C-I bending at 80 cm^{-1}, in-plane C-I bending at 132 cm^{-1}, in-plane C-I stretching at 204 cm^{-1} and ring wagging at 212 cm^{-1}. The latter three are in a very good accordance with the experimental ATR-FTIR spectroscopic measurements (132 cm^{-1}, 204 cm^{-1} and 214 cm^{-1}), whereas the out of plane C-I bending falls just outside our experimental range. Furthermore, the DFT calculations suggest a noticeable shift of the named vibrational modes should occur upon the halogen bond formation. Whereas red shifts of around 15 cm^{-1} are predicted for the C-I stretching vibration, the C-I bending are expected to contrary shift to higher wavenumbers by approximately the same amount. . Indeed, we observed clear shifts in the far-IR region of the experimental spectra of the cocrystals involving IPFB, *i.e.* **1**–**4** and **6** (Table 2.3). In particular, the in-plane C–I stretching vibration of pure IPFB shifted from 204 cm^{-1} to 193 cm^{-1} in **1** and up to 188 cm^{-1} in **2** and **6**, as shown in the example in figure 2.2. N. F. Cheetham and A. D. E. Pullin previously reported similar redshifts for trivial aliphatic molecular moieties.[9]

Table 2.3 Experimental (exp.) and calculated (calc.) values of selected far-IR vibration bands associated to the C–X bond in pure compounds and related cocrystals. The calculated intensity increase is the ratio between the C–X stretching band and the C–F out of plane wagging mode in both the cocrystals and the pure compounds. For the calculation of the experimental intensity increase please refer to the experimental section 5.1.5.

Compounds	In-plane F$_5$Phe-X bending (cm^{-1})		In-plane F$_5$Phe-X stretching (cm^{-1})		ΔI[a] (%)	ΔI[b] (%)
	Exp.	Calc.	Exp.	Calc.		
IPFB	132	132	203	204	-	-
BrPFB	155	155	242	243	-	-
1	140	151	193	192	7	28
2	146	147	188	191	36	51
3	143	148	192	191	41,5	59
4	143	146	191	190	25	33
5	155	168	241	236	0	0
6	*	139	188	189	21	7

[a] Calculated intensity increase. [b] Experimental intensity increase. * Very low intensity to be detected.

The observed redshift is perfectly consistent with the weakening and lengthening of the C–I bond[23] upon halogen bonding with pyridine nitrogen.[24] Moreover we also observed a remarkable intensity increase in the same vibration band of IPFB when involved in cocrystals, see Figure 2.2. This intensity increase was also reproduced by DFT calculations (Table 2.3) and may find an explanation in the intrinsic charge-transfer nature of the halogen bond.[3] In fact, according to Torii *et al.*,[25] the intensity increase of IR vibrations occurs in halogen-bonded cocrystals as a consequence of the intermolecular charge flux from the electron donor to the acceptor counterpart, thus affecting the dipole moment derivative of the C–I stretching mode. This leads to an increase in IR intensity,[26] since the latter is proportional to the square of the dipole moment derivative with respect to the normal mode of vibration.

The C-I bending vibration of IPFB shows an apparent shift of *ca*. 10 cm^{-1} in its complexes. Expectedly, the displacement of the ring wagging vibrations is less pronounced but still noticeable coinciding with our DFT calculations.

TMEDA was introduced in the series to make a comparison between aromatic and aliphatic halogen bond acceptors. For the iodinated series the effects of the halogen bond on the IR spectra are similar for both aromatic (**1**, **2**, **3** and **4**) and aliphatic (**6**) electron donor systems, as they are good Lewis bases and can form robust halogen bonds.

5, the only sample containing bromine as a halogen bond donor (Figure 2.1), shows no appreciable bands shifts or intensity increases. Clearly, the presence of iodine affects the IR spectra of the complexes more than that of bromine; this is in good accordance with the sigma hole theory,[27] which explains the electrostatic nature of the halogen bond. Higher polarizabilty of iodine compared to bromine enhances the electron-positive crown on the electrostatic surface potential of the halogen atom allowing the formation of stronger intermolecular interactions.[28] This is consistent with a general trend of the XB strength, which decreases in the order I > Br > Cl.[29]

All these evidences give clear hints on the successful formation of the charge transfer complexes under participation of N···I halogen bonding. However no signals associated to the normal mode of vibrations of N···I or N···Br non-covalent bonds were detected. This may have two reasons: the vibration lies below the detection limit of our instrumentation, namely <100 cm^{-1}, or/and its intensity is too weak to be detected, both hypotheses being in line with the recently calculated interaction vibrations.[13]

2.1.3 Conclusion

In summary, six cocrystals assembled through the halogen bond were fully characterized via XRD, DSC, and IR analyses. C–X (X = Br and I) normal modes of vibration of haloperfluoroaromatic donors F$_5$Phe-X, directly involved in the intermolecular halogen bond, were assigned by both experimental analysis and *ab initio* theoretical calculations for all of the studied cocrystals. We have demonstrated that the C–I vibration band undergoes a clear redshift and

intensity increase upon occurrence of the halogen bond. This new spectroscopic fingerprint of the halogen bond involving iodoperfluoroaromatics may be developed as a routine tool to detect its occurrence in materials[2] when alternative methods are not available. This is clearly the case for amorphous materials, polymers,[30,31] liquid crystals, and fibrils[32] where more complex and advanced methods, such as Raman spectroscopy[33] and X-ray photoelectron spectroscopy (XPS)[34] have been used. Due to the availability of modern instruments at reasonable cost, far-IR spectroscopy may nowadays be developed as a powerful and sensitive technique for the fast and easy study of intermolecular interactions. IR spectroscopy typically allows for the halogen bond formation to be detected in the solid state by studying normal mode of vibrations indirectly associated to the molecular fragments involved in the XB (vibration of the pyridyl aromatic rings or C-F covalent bonds).[23] The new fingerprint here reported complements these possibilities and affords the first vibrational tool to detect the direct occurrence of the non-covalent interaction *via* changes in the IR features of iodoperfluoroaromatics, common moieties in halogen- bonded molecular materials.

Furthermore, the present study also contributes to the on-going discussion on the nature of the halogen bond demonstrating a charge-transfer contribution in the studied systems evidenced by the band intensity increase associated to the C–I bond.

2.2 XB characterization *via* natural abundance ^{15}N and ^{13}C solid-state NMR spectroscopies[35]

2.2.1 Introduction

As already stated above, XB can be detected by means of various techniques (thermal analysis, X-ray diffraction analysis, vibrational and UV-visible spectroscopies and so on). Among them NMR measurements have been generally employed to shed lights over XB occurrence and its features in solution.[36,37] In particular solution NMR spectroscopy has proven to be a convenient and sensitive tool for establishing the occurrence of XB in supramolecular adducts, for ranking the ability of XB donors and acceptors involved in the interactions, and even for describing thermodynamics and geometric characteristics of the formed adducts.[38-42]

Unlike solution NMR, detailed studies of XB by solid-state NMR (SSNMR) spectroscopy have been carried out only in recent years, although some ^{13}C CPMAS data relating to a complex of 1,4-diazabicyclo[2.2.2]octane and CBr_4 were already reported by Kochi *et al.* in 1987.[43] Recently, efforts have been directed to in-depth, specialized SSNMR analysis, with multinuclear approaches and systematic resort to quantum chemical calculations with DFT-based methods.

XB can be probed by looking at the atoms directly involved in the interaction: the halogen, the carbon covalently bonded to the halogen atom, and the nitrogen (if present). While the acquisition/interpretation of both ^{13}C and ^{15}N spectra is straightforward since it is based on the variation of the chemical shift parameter upon XB formation, the acquisition/interpretation of halogen atom spectra is still challenging. Indeed, $^{35/37}$Cl, $^{79/81}$Br, and ^{127}I are all quadrupolar nuclei (i.e. , I > 1/2) with very high quadrupolar coupling constants. This leads to very broad lines (in the order of tens of MHz) that require a combination of sophisticated hardware and techniques to be acquired, such as very high magnetic fields (up to 21 T), ultrafast MAS (up to 100 kHz), acquisition of several subspectra to be added for collecting the whole signal, and special pulse sequences. On the other hand, David L. Bryce and coworkers have extensively demonstrated that quadrupolar nuclei provide several other interesting parameters in addition to

the chemical shift, such as quadrupolar coupling constants and electric field gradient tensors that add further insights on the halogen environment, and thus the XB.[44-50]

XB acceptors

XB donors
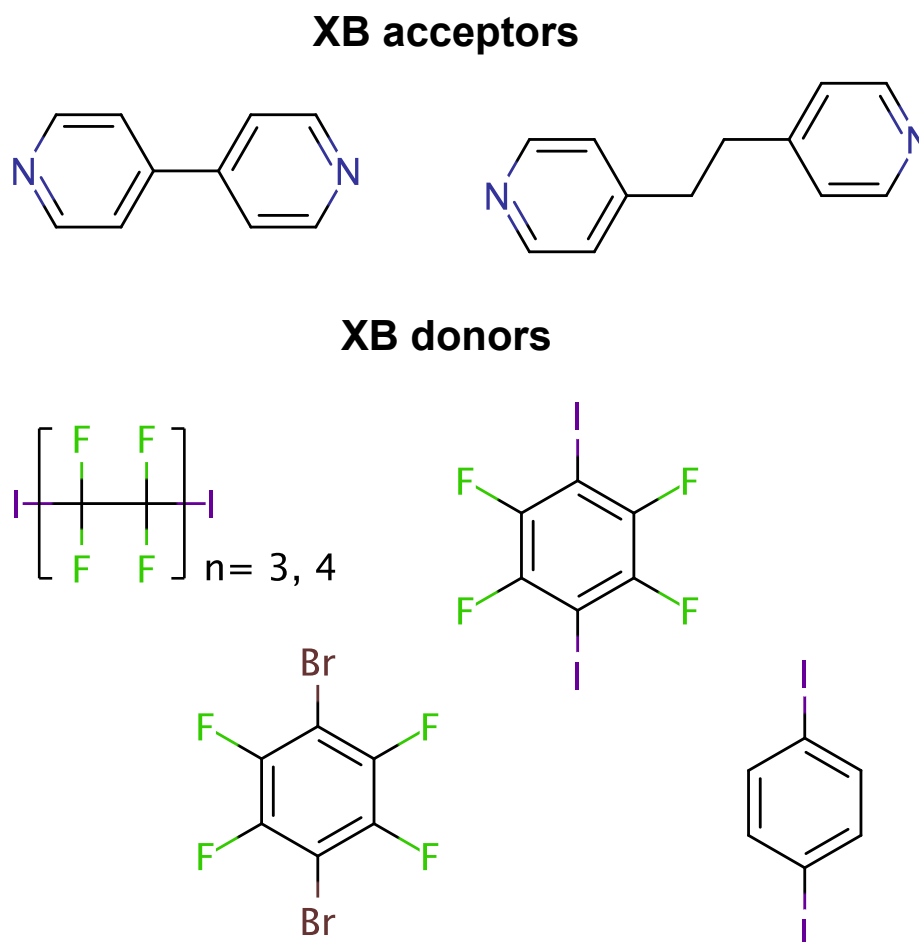
Figure 2.3 Molecular building blocks of the halogen-bonded cocrystals.

Although several articles on SSNMR investigation of XB have already been reported in the last years,[51-60] there is still a need for a multinuclear SSNMR approach in order to find a systematic relationship between the changes in chemical shift of atoms involved in XB and the geometry of the interaction. Indeed, clear and general relationships between NMR parameters and XRD data are not fully reported, yet. For this reason, we performed a complete screening by ^{15}N and ^{13}C SSNMR spectroscopy of different XB donors in two series of X-bonded supramolecular structures, constructed by assembling dipyridyl derivatives and either halobenzenes or haloalkanes (Figure 2.3 Table 2.4).

2.2.2 Results and discussion

Firstly we prepared a series of 10 X-bonded cocrystals by mixing equimolar amount of 4,4'-bipyridine (**1A**) or 1,2-bis(4-pyridyl)ethane (**1B**) with several aliphatic and aromatic XB donors in various solvents (Table 2.4). All the cocrystals were obtained by slow evaporation at room temperature, as shown in detail in the experimental section 5.2.1.

Table 2.4 Obtained halogen-bonded cocrystals.

Compounds	Name
[(**1A**)·(1,4-dibromotetrafluorobenzene)]	**2A**
[(**1A**)·(1,4-diiodobenzene)]	**3A**
[(**1A**)·(1,4-diiodotetrafluorobenzene)]	**4A**
[(**1A**)·(1,8-diiodohexadecafluorooctane)]	**5A**
[(**1A**)·(1,6-diiodododecafluorohexane)]	**6A**
[(**1B**)·(1,4-dibromotetrafluorobenzene)]	**2B**
[(**1B**)·(1,4-diiodobenzene)]	**3B**
[(**1B**)·(1,4-diiodotetrafluorobenzene)]	**4B**
[(**1B**)·(1,8-diiodohexadecafluorooctane)]	**5B**
[(**1B**)·(1,6-diiodododecafluorohexane)]	**6B**

Thermal analysis by DSC confirmed the formation of new chemical species by comparing melting points and degradation temperatures of systems obtained on mixing starting materials with melting points of starting materials (for new cocrystals **3B**, **5B** and **6B**) or of adducts already reported in literature. **2A**, **3A**, **5A**, **6A**, **2B**, **4B**, **5B**, and **6B** pack in the P−1 triclinic space group, **3B** and **4A** crystallize in the monoclinic crystal system in P2$_1$/n and P2$_1$/c space groups, respectively, for further details please refer to Chapter 5 (section 5.2.2). All the X-bonded systems under study were chosen due to their similar 1D supramolecular arrangement and hence their comparable geometry. All the chosen XB-acceptors and donors are ditopic and both their coordination sites are involved in forming halogen-bonded infinite supramolecular 1D chains, as shown in the examples in Figure 2.4. In all structures, XBs tend to be close to

linearity: C–X···N (X = Br, I) angles fall in the range 172.3–177.5°, see Table 2.5. The X···N distances are expressed as normalized contacts (R_{XB}) calculated as the ratio D_{Xn} /(r_X + r_N), where D_{Xn} is the experimental distance between the halogen atoms (X) and the XB-acceptor nitrogen and r_X and r_N are the corresponding vdW radii. The use of R_{XB} allows contacts of chemically different interacting sites to be directly compared.[3]
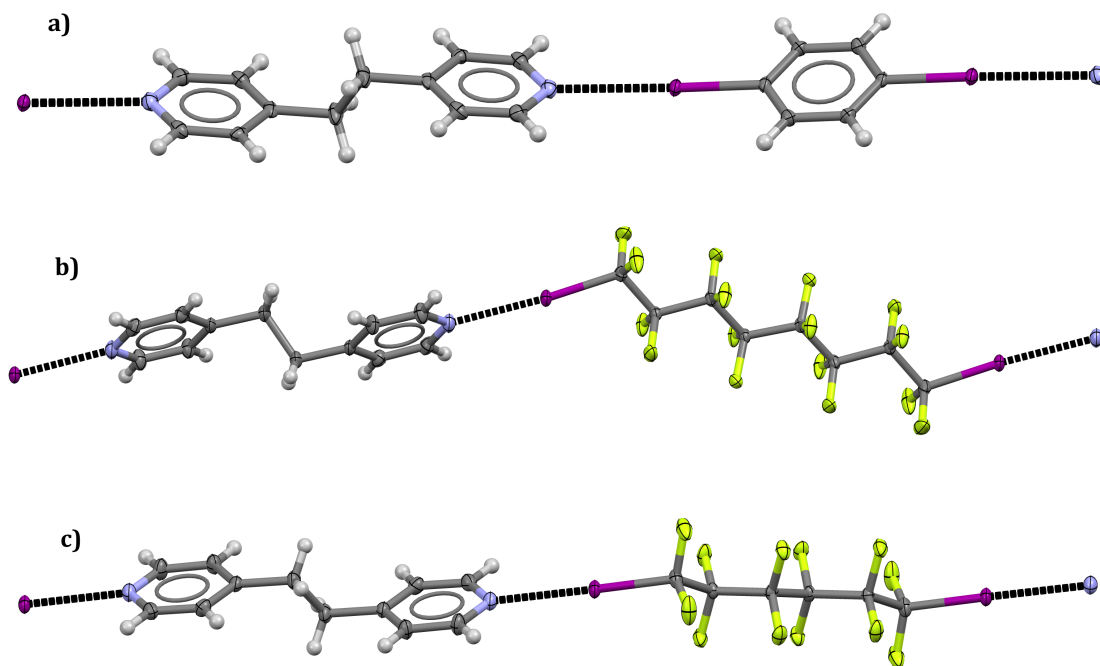
Figure 2.4 Supramolecular infinite chains of **3B**, **5B** and **6B** within their crystal structures. Thermal ellipsoid at 50% of probability. In black dotted line XB is highlighted. Colour code: C, grey; H, light grey; N, blue; F, yellow; I, magenta.

As expected, the shortest, namely the strongest, interactions are those involving iodoperfluorinated XB donors, thanks to the electron-withdrawing effect of the perfluorinated residue, which increases the magnitude of the positive σ-hole on iodine. Except for cocrystals **2A** and **2B**, in all other supramolecular adducts the R_{XB} is shorter for the systems involving **1B** as XB acceptor, due to the higher Lewis base character of **1B** compared to **1A**. Prior to NMR analysis the composition of the bulk crystalline materials was confirmed by comparing experimental and calculated PXRD patterns, see example in figure 2.5 and further details in experimental section 5.2.3.

Table 2.5 Normalized XB contacts (R_{XB}) and C–X···N (X= Br, I) angles ($\theta_{C-X···N}$) for the supramolecular adducts under study.

Cocrystal	R_{XB}	$\theta_{C-X···N}$ (°)
2A	0.85*	177.21 (4)*
	0.88*	176.40 (4)*
3A	0.86	176.1 (1)
4A	0.81	177.3 (1)
5A	0.81	176.7 (2)
6A	0.80	177.5 (6)
2B	0.89	172.3 (3)
3B	0.84	177.41 (6)
4B	0.79	175.8 (3)
5B	0.78	176.3 (1)
6B	0.78	176.97 (6)

* Two crystallographically independent X-bonds.
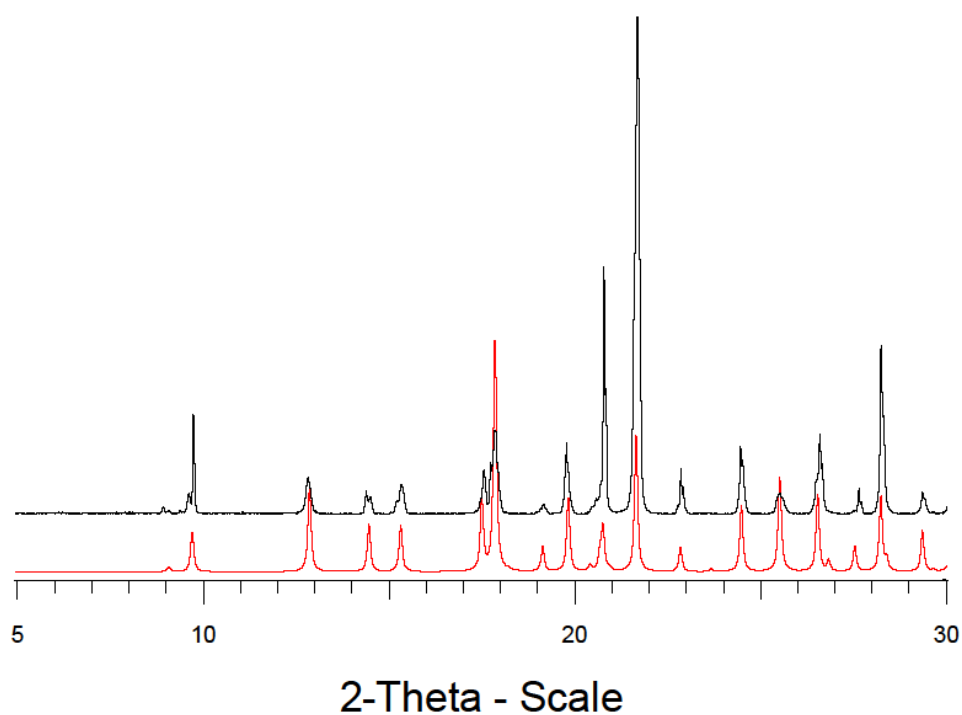
Figure 2.5 Comparison between calculated (red) and experimental (black) powder X-ray diffraction patterns of cocrystal **4A**.

Crystalline powder samples of all cocrystals were then submitted to ^{15}N CPMAS NMR analysis and their spectra are shown in figure 2.6. As it is clear,

48

except for cocrystal **2A**, in both series it can be noted the occurrence of a systematic low-frequency shift in the signal of the pyridyl nitrogen upon cocrystal formation, which is consistent with the lone pair removal for pyridine-like nitrogen atoms.[61] The magnitude of the shift increases going from haloarenes to haloalkanes, and this result is consistent with the measured distance of the XB, that is, R_{XB} (Table 2.6).
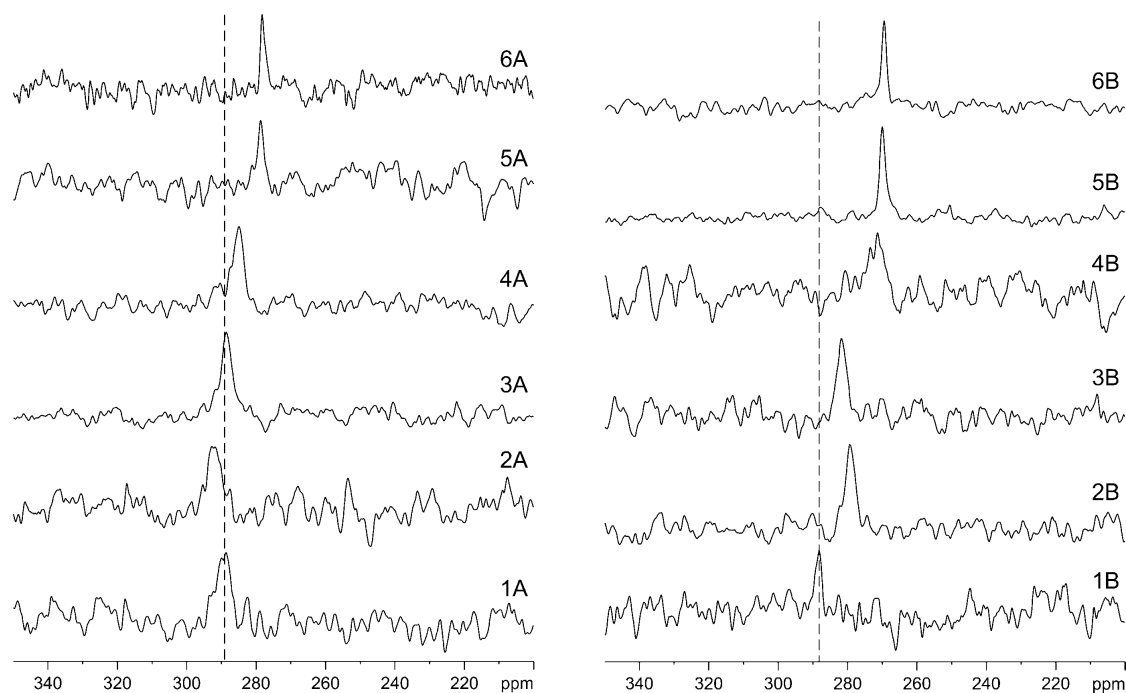
Figure 2.6 [15]N (40.56 MHz) CPMAS spectra of the two series of X-bonded compounds **2 A–6 A**, and **2 B–6 B**, together with starting material **1 A** and **1 B**, recorded at 9 kHz. The vertical dashed line highlights the systematic shift upon XB formation.

Specifically, the strongest N···I attraction occurs in **6B**, for which we observed a shift upon XB formation (δ_{iso} 15N) as high as 19 ppm (Table 3). The other compounds exhibit progressively lower δ_{iso} 15N, affording an overall trend that dictates the strength of the XB donor in the order 1,6-diiodododecafluorohexane >1,8-diiodohexadecafluorooctane>1,4-diiodotetrafluorobenzene >1,4-dibromotetrafluorobenzene > 1,4-diiodobenzene for **1B** series, which is in agreement with the one proposed by Aakeröy *et al.*,[18] but this trend does not hold in the **1A** series because 1,4-diiodobenzene and 1,4-

dibromotetrafluorobenzene are exchanged with each other. We sought to explain such difference in the following ways:

1) **1B** is a better XB acceptor than **1A**, because of the ethyl moiety that increases its basic character. Therefore, in the **1A** series the XB is less strong and, in the absence of a pronounced σ-hole as in the case of 1,4-diiodobenzene and 1,4-dibromotetrafluorobenzene, the XB will be even weaker. Hence, we can infer that other crystal packing effects rather than the XB alone may have an influence on the chemical shifts of **2A** and **3A**, thus altering the donors hierarchy.

2) The unexpected high-frequency shift in **2A** might be one of the reasons that leads 1,4-dibromotetrafluorobenzene to be a worse XB donor than 1,4-diiodobenzene in **1A** series, therefore we explored the changes in the tensor components that occur in the presence of the XB.

Table 2.6 Experimental ^{15}N isotropic chemical shift of dipyridyl nitrogen atoms directly involved in XB.

Compound	$\delta_{iso}{}^{15}N$ (ppm)	$\Delta\delta_{iso}{}^{15}N$ (ppm)[a]	Compound	$\delta_{iso}{}^{15}N$ (ppm)	$\Delta\delta_{iso}{}^{15}N$ (ppm)[a]
1A	289.3	-	**1B**	288.2	-
2A	292.2	−3.0	**2B**	279.3	8.9
3A	288.7	0.6	**3B**	281.7	6.4
4A	285.0	4.3	**4B**	271.4	15.8
5A	278.7	10.5	**5B**	270.0	18.2
6A	278.3	11.0	**6B**	269.4	18.8

[a]Experimental change of the ^{15}N chemical shift upon XB formation, with respect to the corresponding dipyridyl derivative (**1A** or **1B**).

Owing to the very low ^{15}N natural abundance, the ^{15}N chemical shift tensors could not be experimentally obtained, thus they were computed. The results of GIPAW DFT computations are summarized in Table 2.7 together with a comparison with experimental isotropic chemical shifts.

Table 2.7 Calculated[a] nitrogen chemical shift tensors[b] for X-bonded cocrystals herein reported.

	Ω (ppm)	κ	δ_{11} (ppm)[c]	δ_{22} (ppm)[c]	δ_{33} (ppm)[c]	δ_{ave} (ppm)[c]	δ_{iso} (ppm)[d]
1A	659	0.38	629	424	−30	341	314
2A[e]	657	0.38	631	428	−26	344	317
	658	0.38	630	427	−28	343	
3A	645	0.36	628	420	−17	343	313
4A	612	0.40	602	419	−10	337	310
5A	572	0.44	569	409	−3	325	303
6A	577	0.43	573	408	−4	325	303
1B	686	0.36	646	426	−40	344	313
2B	621	0.41	598	416	−23	330	304
3B	614	0.42	593	416	−21	329	306
4B	571	0.43	569	407	−2	324	297
5B	534	0.50	534	401	0	311	295
6B	528	0.49	535	401	7	314	294

[a] PW86PBE-XDM calculation. [b] Chemical shift tensor parameters: span, $\Omega \approx \delta_{11} - \delta_{33}$; skew, $\kappa = 3(\delta_{22} - \delta_{iso})/\Omega$; average of the principal components, $\delta_{ave} = (\delta_{11} + \delta_{22} + \delta_{33})/3$, where $\delta_{11} \geq \delta_{22} \geq \delta_{33}$. [c] All chemical shift tensor components are referenced to liquid NH_3 at 300 K. [d] Experimental isotropic chemical shifts taken from Table 2.6, referenced to liquid NH_3. [e] Two crystallographically independent nitrogen sites.

The experimental δ_{iso} [15]N values are overestimated by the calculations by several ppm, even with the adoption of the XDM method. However, while it should be noted that the challenges associated with this type of chemical calculations are not trivial at all, the overestimation of the SSNMR chemical shifts has been systematically reported in the case of XB.[53,55,56] Consistently with previous results,[53] we observed a reduction in the tensor span upon XB formation; the decrease is in the order of 10% for the **1A** series, and of 20% for the **1B** series. Not surprisingly, the principal components of the chemical shift tensor provide more sensitive information than the isotropic chemical shift. Indeed, the δ_{iso} range for all systems is in the order of 10–20 ppm, while the change in the principal component is much larger, up to 100 ppm. In particular, the component, which changes the most, is the least shielded component, δ_{11}: it varies within the range of 62ppm for **1A** series, and 112 ppm for **1B** series. The

other two components show narrower ranges: the δ_{22} component changes within the range of 20–25 ppm, while the δ_{33} component falls within the range of 27–47ppm respectively for **1A** and **1B** series.

These results are in excellent agreement with those obtained by Facelli and coworkers in a study of the changes of the ^{15}N chemical shift tensor in pyridine upon hydrogen-bond formation.[62] According to Facelli's work, the least shielded component δ_{11} lies in the direction tangential to the aromatic ring. The middle principal component δ_{22} also lies in the plane of the molecule and along the radial direction, while the most shielded component δ_{33} lies in the direction perpendicular to the aromatic ring (Figure 2.7).
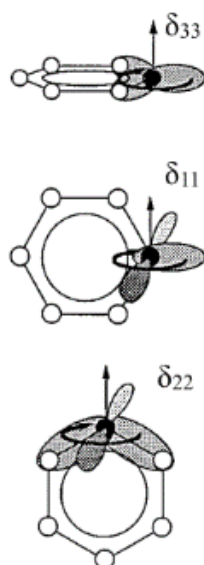
Figure 2.7 Orientation of the principal components of the ^{15}N chemical shift tensor in pyridine. The shaded areas represent the electron orbitals making the largest contribution to the chemical shift tensor components.[63]

The δ_{11} component is dominated by the n–π* (lone-pair) transition, which is the one with the smallest energy gap. The δ_{22} component is dominated by σ_{N-C}– π* transitions. The δ_{33} component is instead dominated by the σ-electronic structure.[63] Furthermore, according to the Ramsey expression of the chemical shift,[64] the paramagnetic term is inversely proportional to the energy gap between the HOMO and LUMO pair of orbitals; hence, following the decreasing trend observed for δ_{11} and δ_{22} values we may speculate that there should be an

increase of the energy difference between orbitals upon XB formation. Such an account may be rationalized as follows; Pinter *et al.* have used accurate DFT calculations to demonstrate that the XB has a non-negligible part of charge transfer character, especially when the halogen and the Lewis base are soft.[65] The same authors pointed out that the observed orbital-interaction stabilization comes from the donation of the lone pair of the halogen bond acceptor to the σ^* orbital of the donor. For these reasons we think that the orbital-interaction stabilization coming from charge transfer enlarges the gap of the nitrogen $n-\pi^*$ and $\sigma_{N-C}-\pi^*$ transition in the X- bonded compound, thus reducing the δ_{11} and δ_{22} values accordingly. This is true for all the compounds herein except for **2A**, which displays a slight increase of the δ_{11}, δ_{22} components. This opposite behavior helps to explain why the δ_{iso} [15]N of the above mentioned compound shifts toward high frequency when compared to that of the **1A** alone; moreover, the trend is confirmed by the computed δ_{ave} [15]N value, which increases with respect to **1A** alone. The accuracy of these accounts should be verified by a thorough DFT study with molecular orbital analysis, including fully relativistic pseudopotentials. However, while the inclusion of relativistic corrections to periodic boundary conditions is still an on-going area of research,[56] an extensive molecular orbital analysis was beyond the scope of our work.

[15]N chemical shifts are a direct source of information about XB surrounding, thus we hypothesized a strong dependence with the XB geometry and strength. This prompted us to examine the experimental correlation between the δ_{iso} [15]N and the normalized distance parameter, R_{XB}. The plot is given in Figure 2.8; a remarkably good linear correlation is observed ($R^2 = 0.9650$) when the X-bonded cocrystals are taken within the same space group (i.e. P-1). The inclusion of the **3B** and **4A** data points, which crystallize, in the same space group (P2$_1$/n and P2$_1$/c), dramatically worsen the relationship ($R^2 = 0.8273$). Difficulties lie in comparing such distinct XB geometries hence such constraints are needed. In addition, we have excluded *a priori* the data relative to **2B** for two reasons: firstly, because it has a significantly different angle of interaction (172.38°), probably due to the geometry of the ethyl moiety; secondly, because it exhibits C-Br bond shortening. The C-X bond shortening upon XB formation is not something unheard of; in fact, Pinter *et al.* have addressed the issue from a

molecular orbital perspective.[65] They have attributed the smaller bond length upon XB formation to a modulating effect of the XB acceptor on the orbital energies of X: since the acceptor is electron rich, thus partially negative, the coordination of the acceptor to X elevates the orbital energies of X. Such perturbation results in a smaller energy mismatch between interacting atomic orbitals of C and X, thus increasing the covalent character of the C-X bond making it stronger (*i.e.* shorter). This phenomenon usually takes place upon increasing the hardness of the Lewis base, and this is exactly what happens when we switch from **2 A** to **2 B**.
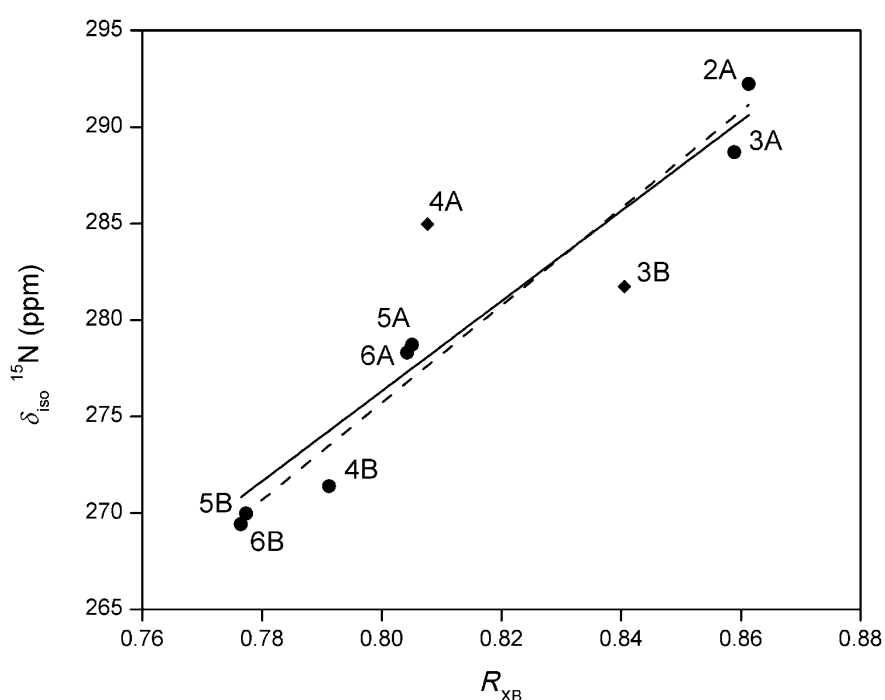
Figure 2.8 Plot of the experimental values of ^{15}N chemical shifts as a function of the corresponding normalized distance parameter. The values are taken from Table 2.6. The diamonds represent the two X-bonded cocrystals the space groups of which are different from the others. The solid line represents the best fit including the latter: δ_{iso} ^{15}N = 233.4 R_{XB} + 89.6, R2 = 0.8273. The dashed line represents the best fit excluding **3B** and **4A** data points: δ_{iso} ^{15}N = 251.9R_{XB}+74.2, R^2=0.9650.

On balance, it can be seen that when the R_{XB} increases, the value of δ_{iso} ^{15}N increases. This is a reasonable trend, as the XB becomes gradually weak, the ^{15}N chemical shift becomes similar to that of the starting material. The experimental

correlation has been reproduced computationally, although the magnitude of the shifts is overestimated (Figure 2.9). To the best of our knowledge, this is the first successful correlation between SSNMR ^{15}N chemical shifts and geometry of the XB.
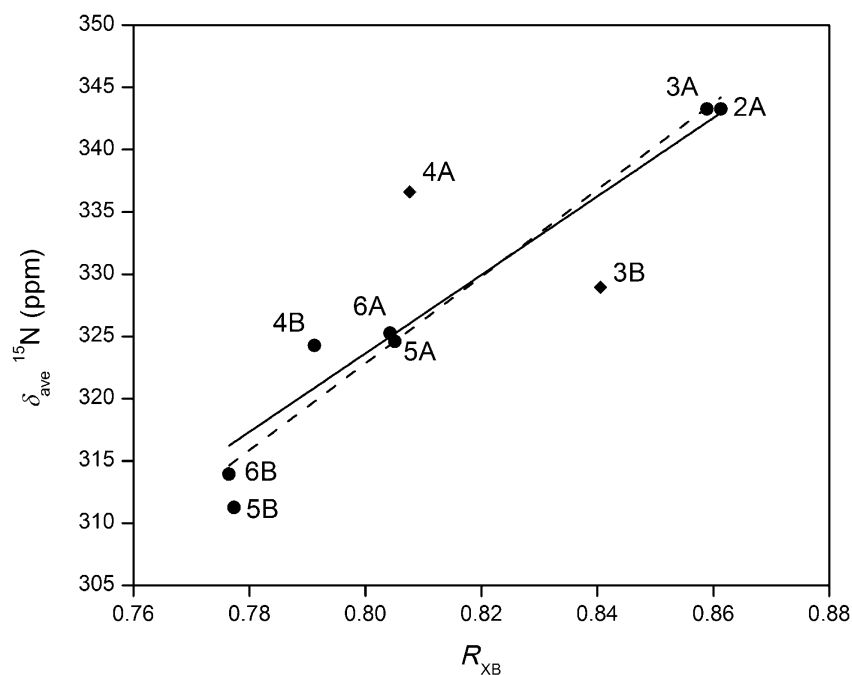
Figure 2.9 Plot of computed values of ^{15}N chemical shifts as a function of the corresponding normalized distance parameter. The values are taken from Table 2.7. The diamonds represent the two X-bonded structures the space groups of which are different from the others. The solid line represents the best fit including the latter: δ_{ave} ^{15}N = 315.2 R_{XB} + 71.5, R^2 = 0.7685. The dashed line represents the best fit excluding **3B** and **4A** data points: δ_{ave} ^{15}N = 348.6R_{XB} +44.0, R^2=0.9552.

We then moved to ^{13}C NQS (non-quaternary suppression) NMR to demonstrate the same correlations by studying a different nucleus.
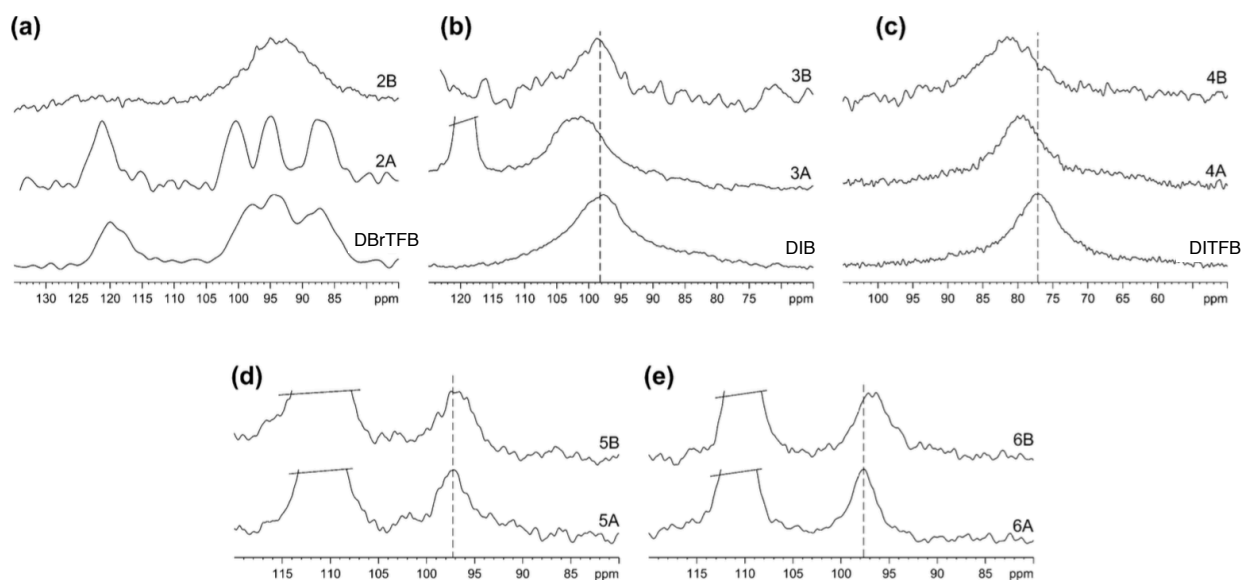
Figure 2.10 Selected regions corresponding to the C-X resonance of the experimental ^{13}C NQS spectra of X-bonded cocrystals recorded at 12 kHz. The vertical lines highlight the systematic high-frequency shift upon XB formation in (b) and (c). The starting materials do not appear in (d) and (e) because they melted inside the rotor. Abbreviations: 1,4-dibromotetrafluorobenzene (DBrTFB), 1,4-diiodobenzene (DIB) and 1,4-diiodotetrafluorobenzene (DITFB).

Figure 2.10 presents the covalently bonded C-X regions of the ^{13}C NQS NMR spectra for compounds **2A–6A**, **2B–6B**. Analogous spectra of the pure starting material are also shown. In order to obtain sensitivity enhancement, when possible we performed NQS experiments with ^{19}F/^{13}C cross polarization (CP) instead of the standard ^{1}H/^{13}C CP, thus improving the signal-to-noise ratio of the C-X signals with a dramatic reduction of the number of scans.

The observed isotropic chemical shifts for the carbon nuclei are given in Table 2.8. The full ^{13}C NQS NMR spectra and chemical shift assignments may be found in the experimental section in Chapter 5 (section 5.2.6). It is well known[55–58] that the ^{13}C resonances of carbons covalently bound to quadrupolar nuclei are broadened or even split due to second-order quadrupolar effects via residual dipolar coupling (RDC). This phenomenon enlarges the error in ^{13}C isotropic chemical shifts measurement. In general, no splitting or asymmetric broadening was observed for the peaks of carbon atoms bound to iodine, while for the carbons bound to bromine we observed the characteristic asymmetric quartet[66]

arising from second-order effects. ^{13}C solid-state NMR chemical shifts of carbon atoms bonded to iodine in both aromatic[55-57] and C(sp)[24,58] XB donors are known to increase upon XB formation. Consistent with these data, the spectra presented in Figure 2.10 clearly show an increase of δ_{iso} [13]C relative to the pure compounds when XB occurs. The chemical shift of carbon directly bound to bromine atom also move to higher frequencies upon XB formation although the extent of the shift is quite modest (about 1 ppm) when compared to the carbon–iodine system. For cocrystals **5A**, **6A**, **5B**, and **6B**, the lack of the starting materials spectra prevents us from observing whether the same trend upholds.

Table 2.8 [13]C Isotropic chemical shifts of C-X corbon atoms.

Compound	δ_{iso} [13]C (ppm)	d_{C-X} (Å)
1,4-dibromotetrafluorobenzene	99.9	1.867
1,4-diiodotetrafluorobenzene	77.0	2.075
1,4-diiodoterafluorobenzene	98.2	2.091
1,6-diiodododecafluorohexane	n/a[a]	n/a[b]
1,8-diiodohexadecafluorooctane	n/a[a]	n/a[b]
2A	100.9[c]	n/a[c]
3A	101.7	2.105
4A	79.6	2.094
5A	97.1	2.162
6A	97.6	2.149
2B	95.9[d]	1.860
3B	99.8	2.112
4B	81.2	2.101
5B	96.7	2.149
6B	96.8	2.157

[a] Not applicable due to low melting temperatures (powder melts inside the rotor). [b] Lack of SCXRD data. [c] Two resonances due to two different carbon sites were expected in 2A. [d] Rough estimate due to unresolved quartet: the real value could be several ppm greater than the listed one.

As for nitrogen chemical shift, we tried to correlate the ^{13}C chemical shifts to the changes of the XB environment by plotting δ_{iso} [13]C values as a function of the corresponding C-I distances, d_{C-I} (Figure 2.11). We observed a reasonable trend

with a remarkable linear correlation (R^2=0.9664), which is consistent with the linear fit between δ_{iso} ^{13}C values and their respective C-I distances reported by Bryce and coworkers.[56] The trend is also in nice agreement with ^{15}N data related to the strength of the different XB donors: stronger XBs are associated with higher shift values. It is worthy to note that this trend comprises both aromatic and aliphatic sp^3 carbons, thus giving a better overview of the ^{13}C SSNMR chemical shifts of halogen-bonded compounds, as well as linking the sparse data already present in the literature.
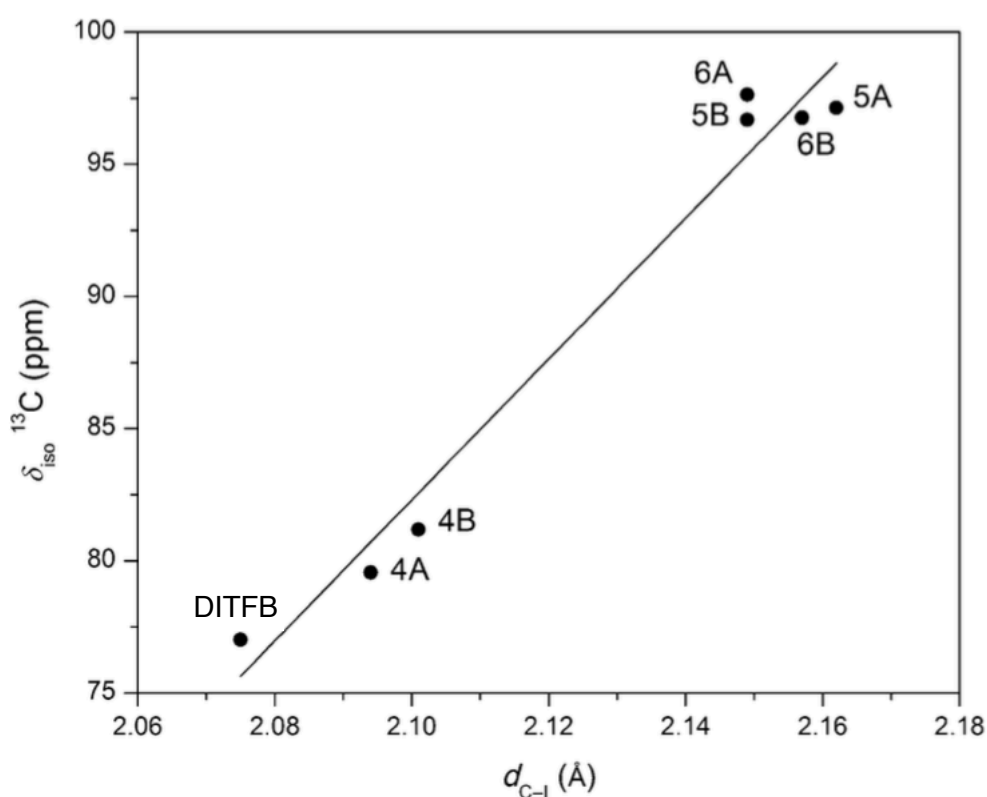
Figure 2.11 δ_{iso} ^{13}C covalently bound to iodine *vs* d_{C-I}. The values are taken from Table 2.8. The best fit is represented by a linear function:

δ_{iso} ^{13}C = 266.5d_{C-I} - 477.3, R2 = 0.9664.

2.2.2 Conclusions

The present contribution demonstrates the ability of SSNMR spectroscopy to directly investigate the XB with an affordable and known technique such as CPMAS. The challenge is to provide a reliable and accurate analysis of the interaction while avoiding the troublesome examination of halogen atoms, which are affected by well-known issues, such as excessive line breadth, extremely expensive hardware, and complicated pulse sequences. We tackled the problem by selecting prototypical 1D X-bonded cocrystals exhibiting various types of C-X···N (X=I, Br) interactions. These cocrystals have been separated in two series based on two different XB acceptors, arranging them in rank order on the basis of their normalized distance parameter, R_{XB}, which is useful to compare distinct interaction geometries. By doing so, we wanted to verify whether this crystallographic trend could be reproduced by means of ^{15}N and ^{13}C SSNMR spectroscopy, thus giving us the chance to test the ability of the technique in quantifying the XB distance.

For both series, the solid-state ^{15}N chemical shifts generally decrease upon XB formation. When the change of chemical shifts is plotted against the corresponding R_{XB} value, a good linear correlation is observed. This experimental trend has been reproduced by GIPAW DFT calculations, even though there is still plenty of room for improvement in the quantum chemical method. For instance, the inclusion of relativistic corrections is desirable in this class of compounds, where the heavy atom effect has significant influence on the chemical shift of nearby atoms. Despite these difficulties, we have successfully determined for the first time the relationship between solid-state ^{15}N chemical shifts and the geometry of the XB.

For cocrystals **2A**–**4A** and **2B**–**4B**, the solid-state ^{13}C chemical shifts generally increase upon XB formation. This trend could not be examined for cocrystals **5A**, **6A**, and **5B**, **6B**, due to the solid–liquid phase transition of the starting materials inside the magnet. Nonetheless, we were able to establish a correlation between the isotropic value of the carbon chemical shifts and the C-I distance: as the chemical shift increases, so does the C-I length. This correlation has

demonstrated to be reliable only within comparable C-X environments, that is, within iodoperfluorobenzene or bromoperfluorobenzene series. Indeed, correlations with the R_{XB} have not been observed experimentally, perhaps due do the many different carbon environments considered.

Overall, this work provides an effective method for the direct detection of the XB by natural abundance ^{15}N SSNMR spectroscopy. The ^{15}N isotropic chemical shifts are diagnostic of the geometry of the XB, and their change upon XB occurrence is generally greater than the change of ^{13}C chemical shifts in a large set of X-bonded systems. Further studies on different XB motifs may extend the use of SSNMR spectroscopy as a first-choice technique when preliminary characterization of XB compounds is required.

References:

1   V. Vasylyeva, L. Catalano, C. Nervi, R. Gobetto, G. Resnati and P. Metrangolo, *CrystEngComm*, 2016, **18**, 2247.

2   A. Priimagi, G. Cavallo, P. Metrangolo and G. Resnati, *Acc. Chem. Res.*, 2013, **43**, 2686.

3   G. Cavallo, P. Metrangolo, R. Milani, T. Pilati, A. Priimagi, G. Resnati and G. Terraneo, *Chem. Rev.*, 2016, **116**, 2478.

4   E. K. Plyler and R. S. Mulliken, *J. Am. Chem. Soc.*, 1959, **81**, 823.

5   J. Yarwood and W. B. Person, *J. Am. Chem. Soc.*, 1968, **90**, 3930.

6   E. E. Ferguson and F. A. Matsen, *J. Phys. Chem.*, 1958, **29**, 105.

7   E. E. Ferguson and F. A. Matsen, *J. Am. Chem. Soc.*, 1960, **82**, 3268.

8   R. F. Lake and H. W. Thompson, *Proc. R. Soc. London, Ser. A*, 1967, **297**, 440.

9   N. F. Cheethaman and A. D. E. Pullin, *Chem. Commun.*, 1967, 233.

10 N. F. Cheethaman, I. J. McNaught and A. D. E. Pullin, *Aust. J. Chem.*, 1974, **27**, 987.

11 A. Mishra and A. D. E. Pullin, *Aust. J. Chem.*, 1971, **24**, 2493.

12 D. Hauchecorne, R. Szostak, W. A. Herrebout and B. J. van der Veken, *ChemPhysChem*, 2009, **10**, 2105.

13 D. Hauchecorne, B. J. van der Veken, A. Moiana and W. A. Herrebout, *Chem. Phys.*, 2010, **374**, 30.

14 N. Nagels, D. Hauchecorne and W. A. Herrebout, *Molecules*, 2013, **18**, 6829.

15 G. R. Hanson, P. Jensen, J. McMutrie, L. Rintou and A. S. Micallef, *Chem. Eur. J.*, 2009, **15**, 4156.

16 D. Hauchecorne, R. Szostak, W. A. Herrebout and B. J. van der Veken, *ChemPhysChem*, 2009, **10**, 2105.

17 P. Politzer, J. S. Murray and T. Clark, *Phys. Chem. Chem. Phys.*, 2010, **12**, 7748.

18 C. B. Aackeröy, M. Baldrighi, J. Desper, P. Metrangolo and G. Resnati, *Chem. Eur. J.*, 2013, **19**, 16240.

19 R. Boese and N. Nussbaumer, *Organic Crystals Chemistry*, Oxford University Press, Oxford, 1994, p. 20.

20 CSD search (ConQuest Version 1.17, 2015).

21 A. Wasilewska, M. Gdaniec and T. Polonski, *CrystEngComm*, 2007, **9**, 203.

22 A. Bondi, *J. Phys. Chem.*, 1964, **68**, 441.

23 M. T. Messina, P. Metrangolo, W. Navarrini, S. Radice, G.Resnati and G. Zerbi, *J. Mol. Struct.*, 2000, **524**, 87.

24 M. Baldrighi, G. Cavallo, M. R. Chierotti, R. Gobetto, P. Metrangolo, T. Pilati, G. Resnati and G. Terraneo, *Mol. Pharmaceutics*, 2013, **10**, 1760.

25 H. Torii, *J. Phys. Chem. B*, 2010, **133**, 034504.

26 H.Torii, *J.Mol.Struct.*, 2014, **1056**, 84.

27 J. S. Murray, P. Lane and P. Politzer *J. Mol. Model.* 2009, **15**, 723.

28 T. Clark, M. Hennemann, J. S. Murray and P. Politzer, *J. Mol. Model.*, 2007, **13**, 291.

29 S. Tsuzuki, T. Uchimaru, A. Wakisaka, A., T. Ono and T. Sonoda, *Phys. Chem. Chem. Phys.* 2013, **15**, 6088.

30 N. Houbenov, R. Milani, M. Poutanen, J. Haataja, V. Dichiarante, J. Sainio, J. Ruokolainen, G. Resnati, P. Metrangolo and O. Ikkala, *Nat. Commun.*, 2014, **5**, 4043.

31 A. Priimagi, G. Cavallo, A. Forni, M. Gorynsztejn-Leben, M. Kaivola, P. Metrangolo, R. Milani, A. Shishido, T. Pilati, G. Resnati and G. Terraneo, *Adv. Funct. Mater.*, 2012, **22**, 2572.

32 A. Bertolani, L. Pirrie, L. Stefan, N. Houbenov, J. S. Haataja, L. Catalano, G. Terraneo, G. Giancane, L. Valli, R. Milani, O. Ikkala, G. Resnati and P. Metrangolo, *Nat. Commun.*, 2015, **6**, 7574.

32 X. Pang, X. R. Zhao, H. Wang, H.-L. Sun and W. J. Jin, *Cryst. Growth Des.*, 2013, **13**, 3739.

34 L. González, N. Gimeno, R. M. Tejedor, V. Polo, M. B. Ros, S. Uriel and J. L. Serrano, *Chem. Mater.*, 2013, **25**, 4503.

35 P. Cerreia Vioglio, L. Catalano, V. Vasylyeva, C. Nervi, M. R. Chierotti, G. Resnati, R. Gobetto and P. Metrangolo, *Chem. Eur. J.*, 2016, **22**, 16819.

36 M. Erdelyi, *Chem. Soc. Rev.*, 2012, **41**, 3547.

37 R. A. Thorson, G. R. Woller, Z. L. Driscoll, B. E. Geiger, C. A. Moss, A. L. Schlapper, E. D. Speetzen, E. Bosch, M. Erdelyi and N. P. Bowling, *Eur. J. Org. Chem.*, 2015, 1685–1695.

38 P. Metrangolo, W. Panzeri, F. Recupero and G. Resnati, *J. Fluorine Chem.*, 2002, **114**, 27.

39 P. D. Rege, O. L. Malkina and N. S. Goroff, *J. Am. Chem. Soc.*, 2002, **124**, 370.

40 S. Libri, N. A. Jasim, R. N. Perutz and L. Brammer, *J. Am. Chem. Soc.*, 2008, **130**, 7842.

41 M. G. Sarwar, B. Dragisic, G. Gouliaras and M. Taylor, *J. Am. Chem. Soc.*, 2010, **132**, 1646.

42 A.-C. C. Carlsson, J. Grafenstein, A. Budnjo, J. L. Laurila, J. Bergquist, A. Karim, R. Kleinmaier, U. Brath and M. Erdelyi, *J. Am. Chem. Soc.*, 2012, **134**, 5706.

43 S. Blackstock, J. Lorand and J. Kochi, *J. Org. Chem.*, 1987, **52**, 1451.

44 C. M. Widdifield and D. L. Bryce, *Phys. Chem. Chem. Phys.*, 2009, **11**, 7120.

45 C. M. Widdifield and D. L. Bryce, *J. Phys. Chem. A*, 2010, **114**, 10810.

46 C. M. Widdifield and D. L. Bryce, *J. Phys. Chem. A*, 2010, **114**, 2102.

47 D. L. Bryce, C. M. Widdifield, R. P. Chapman and R. J. Attrell, in *NMR of Quadrupolar Nuclei in Solid Materials* (Eds.: R. E. Wasylishen, S. E. Ashbrook, S. Wimperis), Wiley, Hoboken, 2012, pp. 321 – 348.

48 F. A. Perras and D. L. Bryce, *Angew. Chem. Int. Ed.*, 2012, **51**, 4227.

49 P. M. J. Szell and D. L. Bryce, in *Annual Reports on NMR Spectroscopy* (Ed.: G. A. Webb), Academic Press, London, 2015, pp. 115 – 162.

50 P. M. J. Szell, D. L. Bryce, *J. Phys. Chem. C*, 2016, **120**, 11121.

51 K. Bouchmella, S. G. Dutremez, B. Alonso, F. Mauri and C. Gervais, *Cryst. Growth Des.*, 2008, **8**, 3941.

52 M. Weingarth, N. Raouafi, B. Jouvelet, L. Duma, G. Bodenhausen, K. Boujlel, B. Schoellhorn and P. Tekely, *Chem. Commun.*, 2008, 5981.

53 J. Viger-Gravel, I. Korobkov and D. L. Bryce, *Cryst. Growth Des.*, 2011, **11**, 4984.

54 R. J. Attrell, C. M. Widdifield, I. Korobkov and D. L. Bryce, *Cryst. Growth Des.* 2012, **12**, 1641.

55 C. M. Widdifield, G. Cavallo, G. A. Facey, T. Pilati, J. Lin, P. Metrangolo, G. Resnati and D. L. Bryce, *Chem. Eur. J.,* 2013, **19**, 11949.

56 J. Viger-Gravel, S. Leclerc, I. Korobkov, D. L. Bryce, *CrystEngComm*, 2013, **15**, 3168.

57 J. Viger-Gravel, S. Leclerc, I. Korobkov and D. L. Bryce, *J. Am. Chem. Soc.*, 2014, **136**, 6929.

58 M. Baldrighi, D. Bartesaghi, G. Cavallo, M. R. Chierotti, R. Gobetto, P. Metrangolo, T. Pilati, G. Resnati and G. Terraneo, *CrystEngComm*, 2014, **16**, 5897.

59 X. Nonappa, M. Lahtinen, E. Kolehmainen, J. Haarala and A. Shevchenko, *Cryst. Growth Des.*, 2013, **13**, 346.

60 J. Viger-Gravel, J. E. Meyer, I. Korobkov and D. L. Bryce, *CrystEngComm*, 2014, **16**, 7285.

61 G. C. Levy, R. L. Lichter, in *Nitrogen-15 Nuclear Magnetic Resonance Spectroscopy*, Wiley, Hoboken, 1979.

62 J. C. Facelli, *Chem. Phys. Lett.*, 2000, **322**, 91.

63 M. S. Solum, K. L. Altmann, M. Strohmeier, D. A. Berges, Y. L. Zhang, J. C. Facelli, R. J. Pugmire and D. M. Grant, *J. Am. Chem. Soc.*, 1997, **119**, 9804.

64 N. F. Ramsey, *Phys. Rev.*, 1950, **78**, 699.

65 B. Pinter, N. Nagels, W. A. Herrebout, and F. De Proft, *Chem. Eur. J.*, 2013, **19**, 519.

66 A. Aliev, K. Harris, R. Harris, S. Carss, and A. Olivieri, *J. Chem. Soc. Faraday Trans.*, 1995, **91**, 3167.

CHAPTER 3

Solid-state supramolecular rotors based on halogen bond

3.1 A new class of amphidynamic crystals based on XB[1]

3.1.1 Introduction

Amphidynamic crystals are materials specifically designed with static and mobile components capable of displaying anisotropic dynamics in the solid-state. There is a growing interest in their study, because it is expected that controlled molecular motion in dense multicomponent assemblies will become a suitable platform for the development of new functional materials and artificial molecular machines.[2]

Over the last few years, molecular designs have taken advantage of structures akin to those of macroscopic compasses and gyroscopes to control rotation in the solid-state. Rotational dynamics in condensed matter has been studied in molecular crystals,[3] inclusion compounds,[4] metal-organic frameworks,[5] porous molecularly ordered silicates,[6] amorphous solids[7] and solid solutions.[8]

An alternative approach would rely on a crystal engineering strategy where stators and rotators, properly selected on the basis of their supramolecular features, could assemble into supramolecular adducts, *i.e.* cocrystals. Benefits of this strategy originate from its intrinsic flexibility and its modular design, in fact thanks to the wide variety of supramolecular synthons available in the crystal engineering toolbox the formation of a small library of active rotator systems with different dynamic performances could be easily achieved and studied.

With that goal in mind, it is possible to take advantage of a wide variety of intermolecular interactions such as hydrogen bonding, coulombic interactions, π-π interactions, van der Waals forces and halogen bonding. Among these, it has been extensively demonstrated that halogen bond is a precious structural tool to build supramolecular systems thanks to its strength, directionality, selectivity and tunability.[9] In addition it has been recently showed that single-component amphidynamic crystals based on bis(1,4-iodoethynyl)bicyclo[2.2.2]octane (BIBCO) display ultra-fast Brownian rotation when self-assembled in crystalline lattices whose structure-directing interaction is iodine-acetylene XB.[10]

For a simple and versatile multicomponent supramolecular rotor design it would be desirable to use structurally simple building blocks that are commercially available. Thus we identified, as commercial starting building blocks, differently fluoro-substituted iodobenzenes (F_nPheI) as promising stators and powerful XB donors, and 1,4-diazabicylo[2.2.2]-octane (DABCO) as a potential rotator, thanks to its D_{3h} symmetry and cylindrical shape,[11] and good XB acceptor[12] (Figure 3.1); we expected the F_nPh–I$\cdots$NR$_3$ XB interaction to drive the crystallization, forming trimeric halogen-bonded adducts.

3.1.2 Results and discussion
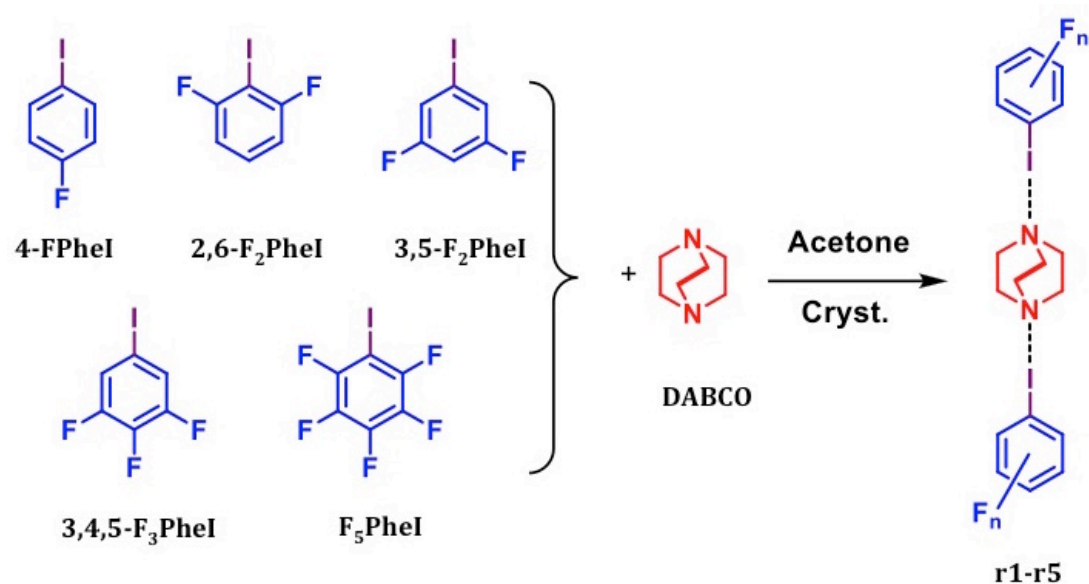
Figure 3.1 Expected self-assembly of fluoro-substituted iodobenzenes (F_nPheI) and DABCO to give cocrystals **r1-r5**.

To verify our hypothesis on the formation of halogen-bonded amphidyanamic crystals, we mixed the chosen haloaromatic compounds (F_nPheI) and DABCO in 2:1 molar ratio in acetone, considering the monotopic nature of the XB donors and ditopic nature of the XB acceptor, as shown in figure 3.1. By slow evaporation of the solvent we were able to obtain good quality crystals in all cases. The first evidence of the formation of new compounds came from the thermal analysis of the bulk crystalline powders obtained, which showed melting

points different from those of the starting materials, as shown in detail in table 3.1.

Table 3.1 Melting points of cocrystals **r1**-**r5** and of pure DABCO.*

Compounds	mp (°C)*
DABCO	156
4-FPheI + DABCO **(r1)**	45-48
2,6-F_2PheI + DABCO (**r2**)	61-63
3,5-F_2PheI + DABCO (**r3**)	71-72
3,4,5-F_3PheI + DABCO (**r4**)	38-41
F_5PheI + DABCO (**r5**)	104-105

* XB donors are all liquids at room temperature.

Hence the crystals were submitted to single crystal X-ray diffraction analysis, which, for all the samples, was carried out at 103 K (for crystallographic tables please refer to experimental section 5.3.1 in Chapter 5). Structural analysis confirmed for compounds **r1**, **r2**, **r4** and **r5** the starting design of the desired XB motif with both the nitrogen atoms of DABCO working as XB acceptors toward the iodine atoms of two different F_nPheI modules, resulting in trimeric complexes (Figure 3.2a).
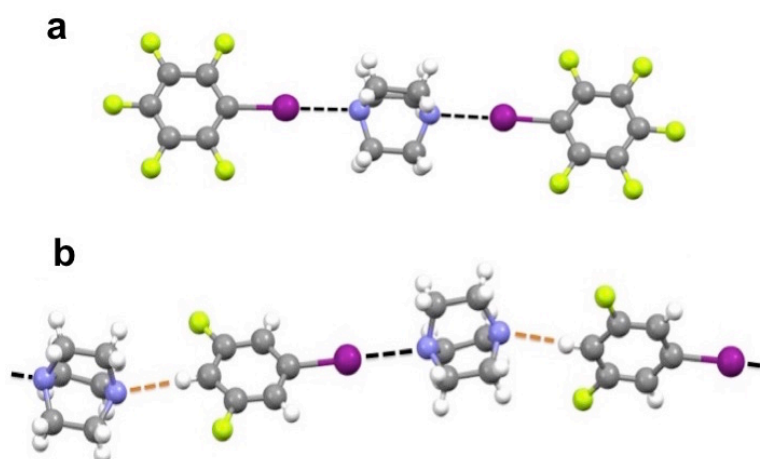
Figure 3.2 a) Illustrative supramolecular trimer in the crystal structure **r5** and b) 1D mixed XB/HB infinite chain in **r3**. XB and HB are represented as black and orange dashed lines, respectively.

In contrast, the structure of complex **r3** consisted of 1D infinite chains in which 3,5-F_2PheI and DABCO alternated as a consequence of the ditopic nature of 3,5-F_2PheI, which also behaved as a H-bond donor through the H-atom in the *para*-position to the iodine atom in the benzene ring; this H-atom interacts with one of the two Lewis base sites of DABCO, namely one nitrogen atom (HB geometrical parameters are as follows: C···N distance 3.348(3) Å and C-H···N angle 176.07(8)°). This hydrogen results particularly acidic, *i.e.* stronger H-bond donor, due to the presence of two adjacent electron withdrawing fluorine atoms (Figure 3.2b).

Halogen bonding interactions in all co-crystals are characterized by short I···N distances and almost linear C-I···N angles, as shown in Table 3.2. The interaction becomes stronger by increasing the degree of fluorination of the stator, and hence the magnitude of the iodine σ-hole.[13] Except XB, and HB in the case of **r3**, and π-π interactions, favoured by the perfluoroaromatic moieties,[14,15] no other relevant interactions are found within the crystalline lattices of the supramolecular adducts.

Table 3.2 . XB geometrical features in **r1-r5** at 103 K.

Cocrystal	N···I (Å)	N···I-C angle (°)
r1	2.971 (4), 2.955 (4)[a]	176.32 (2), 175.51 (2)[a]
r2	2.857 (2), 2.732 (2)[a]	173.86 (8), 179.12 (8)[a]
r3	2.832 (1)	175.19 (4)
r4	2.815 (6)	175.8 (2)
r5	2.713 (1), 2.682 (1), 2.681 (1), 2.701 (1)[a]	177.04 (5), 178.64 (5), 177.96 (5), 177.19 (5)[a]

[a] Indipendent halogen bonds.

The cocrystals were obtained in quantitative yields and, before further investigations, their bulk composition was checked through IR analysis and X-ray powder diffraction measurements by comparing experimental data with calculated diffractograms from single crystal data, an XRPD example in Figure 3.3 and further details in the experimental section 5.3.2 in Chapter 5.
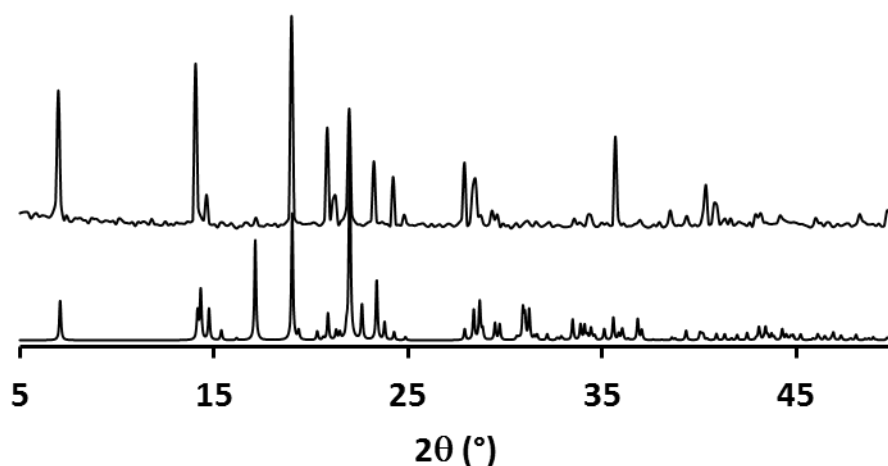
Figure 3.3 Comparison between calculated (bottom) and experimental (top) powder X-ray diffraction patterns of complex **r1**.

To explore the temperature dependence of structural changes and of the dynamics of DABCO in the complexes **r1-r5**, we performed variable-temperature (VT) single-crystal XRD, ^{1}H spin-lattice relaxation T_1 NMR, and wide-line quadrupolar echo ^{2}H NMR analyses. It is known that changes in the size and orientation of the anisotropic thermal parameters may be related to the potential energy that determines dynamic processes in crystals.[16-17] On heating single crystals of the complexes **r1** and **r5** from ~100 K to room temperature, reversible phase transitions without substantial modifications of the crystal packing were recorded. These occurred at ~280 and 230 K, respectively, and they were followed by a direct analysis of the oscillating images of the cocrystals lattices recorded during heating and cooling cycles by SCXRD, which revealed the appearance of new phases at the phase transition temperatures, as show in figure 3.4 for cocrystal **r1**.

For **r5**, XRD data were collected in the range 103–298 K, following five intermediate steps (140, 180, 200, 220, and 250 K). On increasing the temperature of the XRD acquisition, increasing rotational disorder of the DABCO −CH$_2$CH$_2$− alkyl bridges was observed, which has to be expected from a thermally activated rotational process (Figure 3.5 and Figure 3.6). Conversely, the F$_5$PheI module only showed disorder in the plane of the aromatic ring, as it is clear from Figure 3.6. Similar motion and disorder were also observed for the co-crystals **r1**-**r4**.
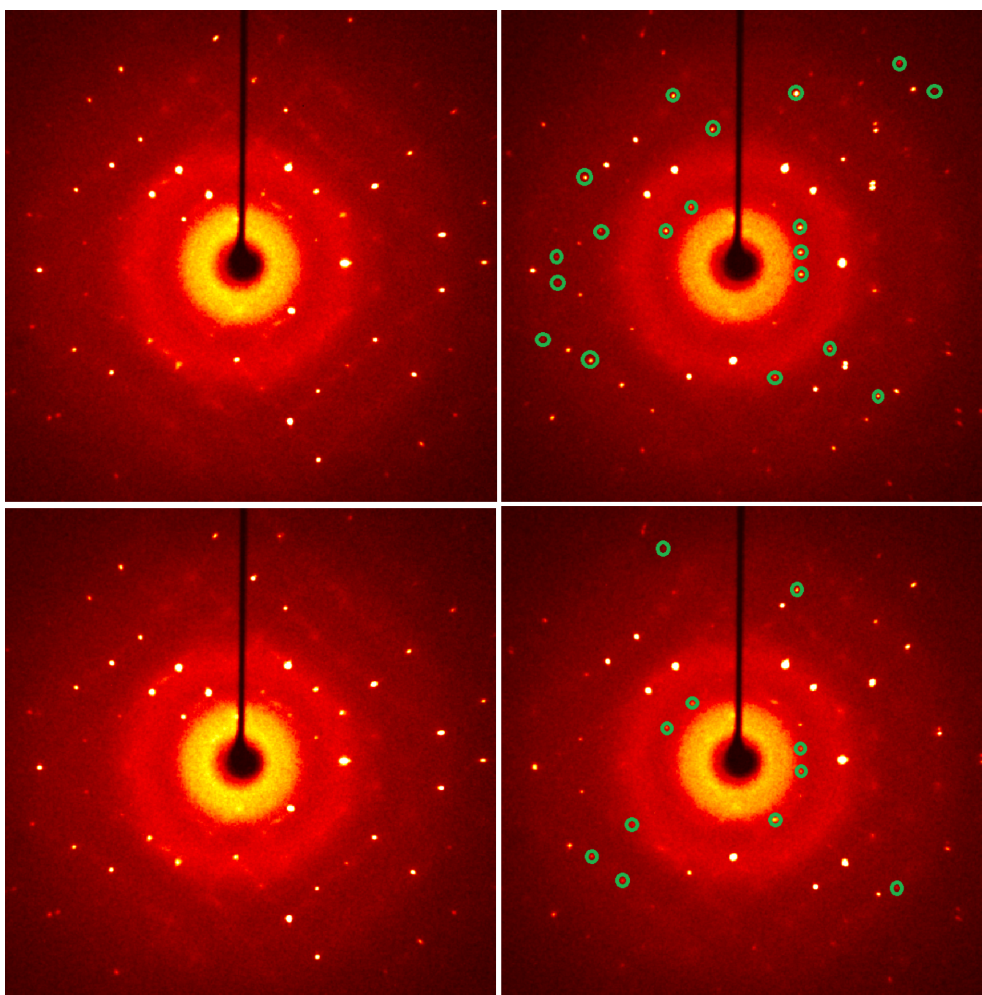
Figure 3.4 Procedure to follow the phase transitions of **r1** and **r5**. Here above four oscillating images of **r1** lattice taken in a cooling-heating cycle around the phase transition temperature. Cooling: top-left at 280K; top-right at 270 K. Heating: bottom-right at 279 K; bottom-left at 280K. Images are dramatically different and the appearance of reflections at 270K (some of them circled in

green), not compatible with the lattice at 280 K, are a clear indication of the phase transition.
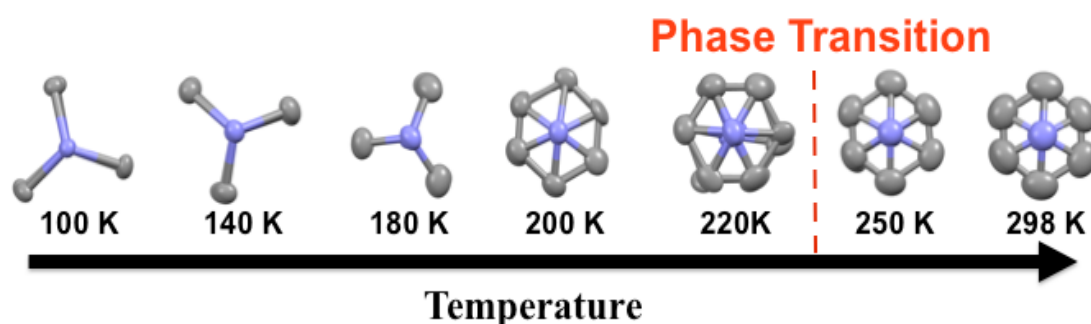
Figure 3.5 Views of DABCO along the N-N axis showing increasing disorder of the alkyl bridges in **r5**, in terms of larger thermal ellipsoids and splitting of the two positions as a function of temperature from 103 K to 140 K, 180 K, 200 K, 220 K, 250 K and 298 K.
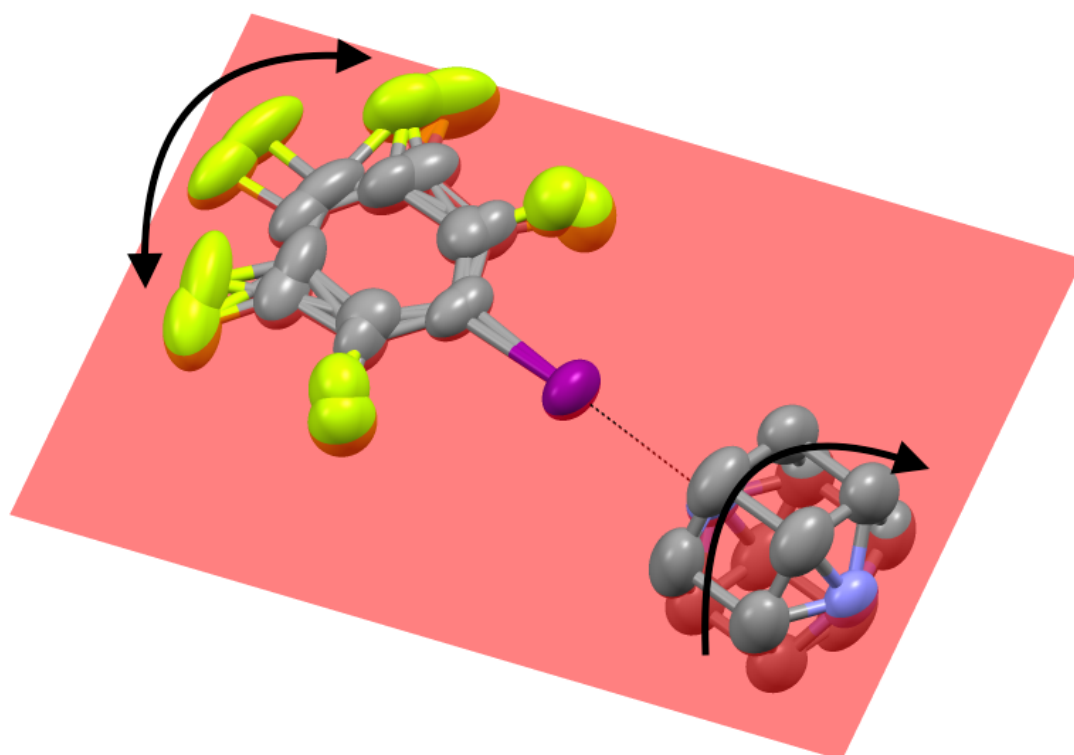
Figure 3.6 Asimmetric unit in **r5** structure at Room Temperature. In red the benzene ring plane is highlighted. Looking at the F_5PheI thermal ellipsoids and atoms splitted positions, it is clear that the benzene derivative thermal motion is confined to one plane, thus the aromatic ring is not rotating as DABCO.

Spin lattice relaxation measurements have been used to document dynamic processes in the vicinity of the Larmor frequency;[18] 300 MHz for ^1H T_1 measurements in this case. The method is well suited for crystalline solids where the main mechanism of relaxation is due to the motion-mediated fluctuation of magnetic fields arising from dipolar coupling among hydrogens. In the case of solid **r1-r5**, DABCO rotation is the predominant thermally activated process with dynamics characterized by a correlation time (τ_c), which follows an Arrhenius-type behaviour (eq. 1). Under these conditions, it is possible to obtain its activation energy (E_a) and pre-exponential factor (τ_0^{-1}) by fitting the T_1 data measured as a function of temperature to the Kubo-Tomita (K-T) relaxation expression (eq. 2), by substituting the τ_c with eq. 1.

$$\tau_c^{-1} = \tau_0^{-1} \exp(-E_a/RT) \qquad \text{(eq. 1)}$$

$$T_1^{-1} = C\,[\tau_c(1+\omega_0^2\,\tau_c^2)^{-1} + 4\tau_c(1+4\,\omega_0^2\,\tau_c^2)^{-1}] \qquad \text{(eq. 2)}$$

$$C = (n/N)(9/40)(\mu_0/4\pi)^2\gamma^4\hbar^2/r^6 \qquad \text{(eq. 3)}$$

Table 3.3 Arrhenius parameters of rotational process of DABCO coming from the K-T fit of the T1 data for all adducts and for pure DABCO.

Crystal	E_a (kcal/mol)	τ_0^{-1} (s^{-1})	C (s^{-2})
DABCO	8.2[a]	1.3×10^{14} [a]	n.a.
r1	4.8	9.9×10^{12}	5.2×10^8
r2	2.7	2.0×10^{12}	7.4×10^8
r3	2.4	1.1×10^{12}	6.5×10^8
r4	2.8	2.3×10^{12}	5.0×10^8
r5	3.6	2.3×10^{12}	7.5×10^8

[a] Reference 19.

The parameter C in eq. 2 and eq. 3 is a constant related to strength of the homonuclear dipolar interactions, which depends on the ratio of the mobile nuclei responsible for the relaxation (n) to the total number of nuclei that need to be relaxed (N), μ_0 is the permeability of free space, γ is the gyromagnetic ratio, $\hbar$ is the reduced plank constant and r is the inter-nuclei distance. C is expected to be similar for all the cocrystals (see Table 3.3). ω_0 is the Larmor frequency.

Good K-T fitting of the experimental data were obtained allowing the determination of the Arrhenius parameters in Table 3.3.

As illustrated in the Figure 3.7 with $\ln(T_1^{-1})$ *vs.* 1000/T(K) plot of the experimental data obtained for cocrystal **r5**, there is a single maximum at *ca.* 195 K with an excellent K-T fit for a single dynamic process with an exceptionally low energy of activation of around 3.6 kcal/mol and a pre-exponential factor τ_o = 2.3×10^{12} s^{-1}. Similar behaviors were obtained also for **2a-d** with activation energies ranging from 2.4 to 4.9 kcal/mol (Table 3.3). Notably, data obtained from cocrystal **r1** showed a discontinuity that correlates with a phase transition that occurs at *ca.* 280 K (Figure 3.8). While it was not possible to fit the experimental data in the high temperature phase due to the small number of experimental points in the proximity of the crystal melting, the dynamics of the low temperature phase was fully characterized with an E_a = 4.9 kcal/mol and τ_o = 9.9×10^{12} s^{-1}. For further details relative to ^{1}H spin-lattice relaxation analysis please refer to Chapter 5 (section 5.3.4).
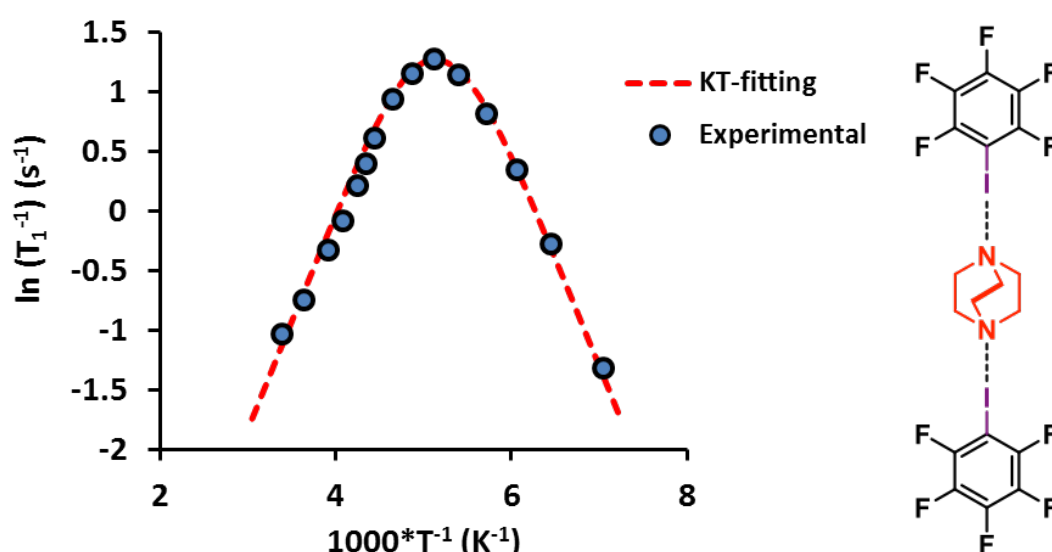
Figure 3.7 ^{1}H spin-lattice relaxation times (^{1}H T_1) measured for **r5** on cooling from 295 K to 141 K at 300 MHz (solid blue circles). The plot $\ln(T_1^{-1})$ vs.1000*T^{-1} shows a maximum at approximately 195 K. The red dotted line corresponds to the Kubo-Tomita fit of the experimental data.
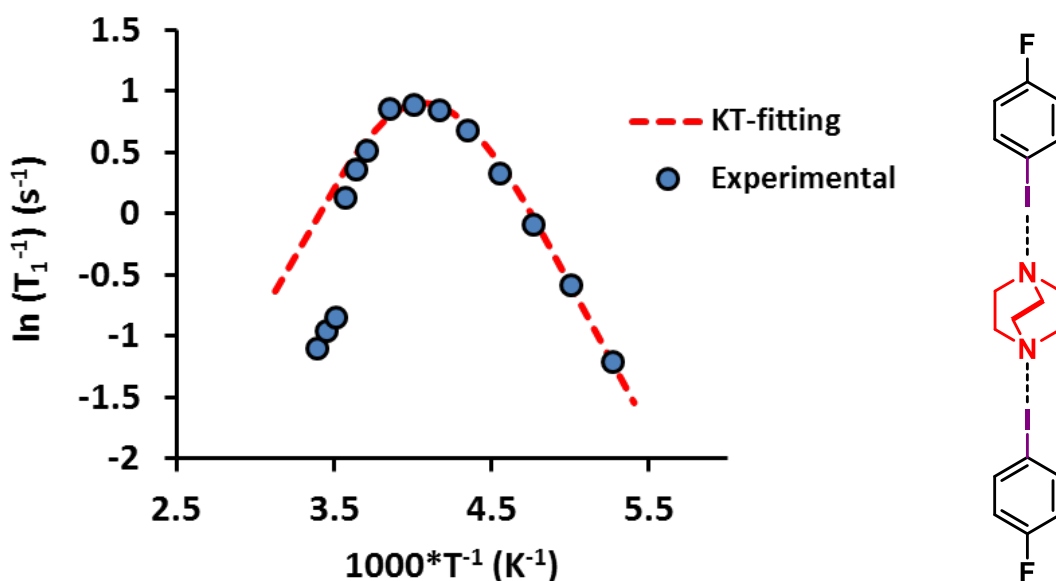
Figure 3.8 ^1H spin-lattice relaxation times (^1H T_1) measured on **r1** from 310 K to 200 K at 300 MHz (solid blue circles). The plot ln (T_1^{-1}) vs $1000T^{-1}$ shows two processes, one occurring close to room temperature and another at low temperature in the range of 280 K – 200 K. The low temperature process displays a maximum that corresponds to the minimum ^1H T_1, at approximately 250 K. The red dotted line corresponds to the Kubo-Tomita fit of the experimental data.

The activation energies measured for cocrystals **r1**-**r5** are considerably lower than the activation energy for rotation reported in the case of pure crystalline DABCO, which has an Ea = 8.2 kcal/mol and τ_o = 1.3x10^{14} s^{-1} (Table 3.3). This may probably be due to the fact that rotator molecules in the reported halogen-bonded cocrystals are partially isolated from neighbouring rotators by the XB-donors F_nPheI, which thus function as bearings and stators (Figure 3.9). The higher activation energy for rotation of pure DABCO may be associated with the closer rotator-rotator distances and steric interactions in the crystal. The pre-exponential factor τ_0^{-1} is related to the frequency of oscillations within the local energy well, and can be associated with an attempt frequency for rotational jumps that is determined both by thermal energy and the size of the activation barrier (-E_a/RT). The attempt frequency corresponds to the rotational exchange frequency that would occur in the absence of a barrier, i.e., when E_a =0. Notably,

the τ_0^{-1} values obtained for the halogen-bonded cocrystals **r1-r5** are comparable to those determined for other amphidynamic crystals with analogous DABCO-based molecular rotators linked to the stators by covalent bonds.[10,20,21] This suggests that the halogen-bonded molecular rotors reported under study may be as efficient as similar rotors based fully on covalent bonds. However, in cocrystal **r3**, it was not possible to discern the different contributions of XB and HB to the rotational dynamics of the supramolecular rotor.
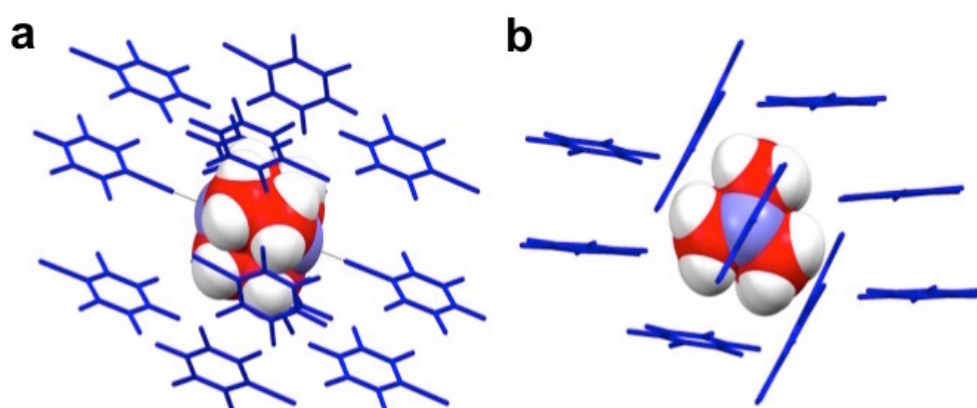
Figure 3.9 a) View along the *b* crystallographic axis. b) View along the N-N molecular axis of the crystal structure of **r5**, showing the isolation of a DABCO rotator (red) by neighboring F_5PheI modules in blue.

To elucidate the trajectories of motion, three supramolecular rotors, **r1**, **r2** and **r5**, were taken as models and their dynamics studied by wide-line quadrupolar echo ^{2}H NMR.[18] The sample co-crystals were prepared by using perdeuterated DABCO obtained by H/D exchange reaction using Raney nickel and D_2O (for the detailed synthesis procedure see experimental section 5.3.5 in Chapter 5).[22] For the three studied systems, the wide-line spectra collected between 140 and 295 K did not show any appreciable changes, in good agreement with the high rotational frequencies expected from the low Ea and high τ_0^{-1} values. The simulated spectra, obtained with Nishikiori's software package,[23] suggested a dynamical process in which DABCO rotates around its N−N axis in the fast-exchange regime. The experimental data coupled with the simulations are consistent with either a 3-site or 6-site potential of the rotator; see example in Figure 3.10 and further details in Chapter 5 (section 5.3.6).
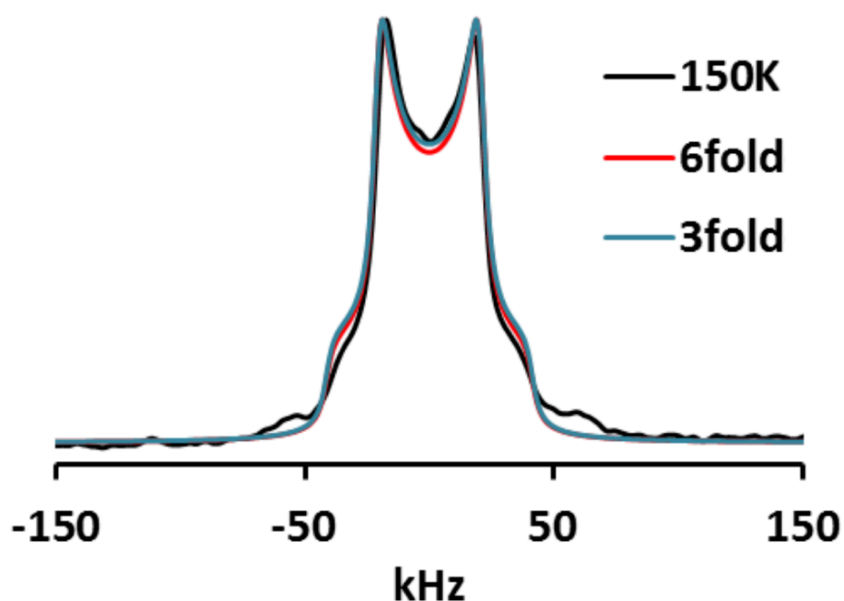
Figure 3.10 Deuterium wide-line spectrum of **r1** collected at 150 K (black line) compared with 3-fold and 6-fold potential simulated spectra (blue and red lines).

3.1.3 Conclusions

In conclusion, a series of two-component amphidynamic co- crystals with very efficient rotational dynamics were readily prepared from simple and commercially available building blocks by taking advantage of a crystal engineering strategy based on the use of XB. The reported systems are the first examples of this new class of materials. Rotational dynamics based on VT ^{1}H T_1 NMR spin–lattice relaxation revealed pre-exponential factors comparable to those found in rotors with covalent rotational axles, suggesting that the XB, and the HB in the specific case of **r3**, constitute new robust axles for molecular rotation and a new design principle in the field of molecular rotors. The discovery of these new crystalline multicomponent systems thus opens up new avenues in the development of new smart materials and molecular machines.

3.2 Entropic and enthalpic effects in isomorphous halogen-bonded ampidynamic cocrystals[24]

3.2.1 Introduction

Based on the assumption that amphidynamic crystals possessing more hindered stators display more efficient dynamics performances, we tried to combine the design principles established with the synthesis of supramolecular rotors **r1**-**r5** with the use of a particularly bulky stator unit, namely a trytil moiety, to prepare new and more efficient supramolecular rotors halogen-bond-based.

The trityl group is a well-known molecular unit in the construction of molecular rotors that is extensively used as a stator.[25-27] We designed the stator units possessing a strong XB donor molecular fragment, namely a X-acetylene moiety (X = Cl, Br and I), which has already proved to form efficient XB motif in amphidynamic crystals, as shown by BIBCO crystals.[10] The desired 3,3,3-triphenyl-1-iodopropyne (TrI), 3,3,3-triphenyl-1-bromopropyne (TrBr) or 3,3,3-triphenyl-1-chloropropyne (TrCl) are easily accessible *via* trivial synthesis procedures (as shown in detail in experimental section 5.4.2).

As for **r1**-**r5**, The Lewis-base diazabicyclo[2.2.2]octane (DABCO) molecule was selected as the XB acceptor because of its average D_{3h} point group symmetry and globular shape, both of which ensure high mobility.[11] Considering the ditopic nature of the DABCO rotator, we envisaged the formation of trimeric (**r6**) and dimeric (**r7**) adducts by cocrystallization (Figure 3.11).

One of the appealing features of the expected cocrystals **r6** and **r7** is that substitution of a single halogen atom in an otherwise identical structure is expected to form isomorphous crystals, with subtle packing differences affecting near neighbour distances, normal modes of vibration and lattice phonons. *A priori*, we expected that geometric changes would have an effect on the activation enthalpy while changes in molecular and lattice vibrations should have an effect on the activation entropy. As described in detail in Section 3.2.2, variable temperature ^2H line shape analysis and ^1H T_1 spin lattice relaxation measurements revealed ultra-fast DABCO rotation in a 6-fold potential with the

two co-crystals having the same activation entropy ($\Delta S^{\neq}$) but clearly distinguishable activation enthalpies ($\Delta H^{\neq}$).
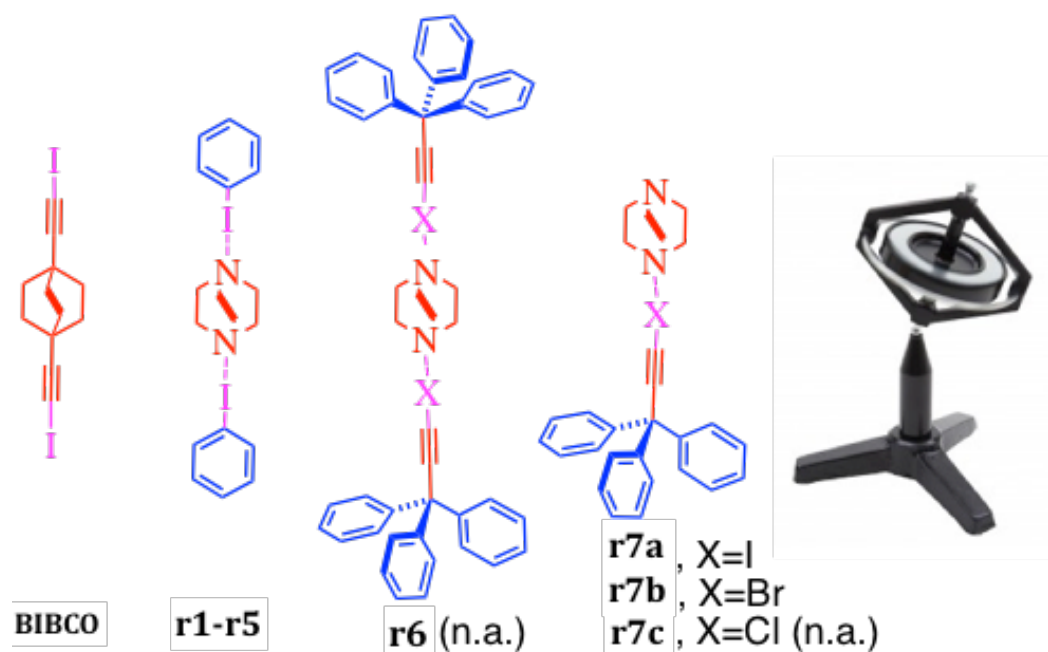
Figure 3.11 Molecular structures of amphidynamic crystals based on halogen bonding and photographic representation of the target system, a spinning top on a tripod. Co-crystals with stator:rotator ratio 2:1 (**r6**) and 1:1 (**r7a**, **r7b** and **r7c**) were the target of this project. Co-crystals **r6** and **r7c** were not obtained.

3.2.2 Results and discussion

Samples of iodo-, bromo- and chloro-tritylacetylene XB donors were prepared as reported in the literature, as it is shown in detail in Chapter 5 (section 5.4.2). Co-crystallizations were carried out by slow evaporation from acetone solutions of the corresponding trityl halide and DABCO. Experiments revealed that supramolecular cocrystals **r6** in which XB donors and acceptors are in 2:1 molar ratio, respectively, are not obtained, perhaps due to geometrical constrains associated with the crystal packing. While several conditions (slow evaporation and liquid assisted grinding) afforded good quality cocrystals containing TrI (**r7a**) or TrBr (**r7b**) and DABCO, no cocrystals were formed with TrCl (**r7c**). The behaviour of TrCl molecule was expected and could be explained by the poor XB donor ability of chlorine atom.[28] It's known that the interaction strength of a XB

contact is strictly correlated to the polarizability of the halogen atom involved in the interaction.[29] Chlorine is less polarizable than iodine or bromine and thus its halogen bond with the "rotating" DABCO is very weak, so weak that is not able to drive the formation of the target cocrystal.

The crystal structures of **r7a** and **r7b** were solved at 100 K and at room temperature, revealing that the two co-crystals are isomorphous and do not undergo phase transition by changing temperature. They both crystallize in the monoclinic space group P2_1/c. It is important that co-crystals are isomorphous from the standpoint of comparing the dynamic performance of DABCO interacting with two XB donors, TrI and TrBr. The crystal structure revealed a supramolecular complex of TrX and DABCO in a 1:1 ratio, where the I- and Br-atoms of TrX and one nitrogen atom of DABCO (C-X$\cdots$NR$_3$) take part in a XB interaction (Figure 3.12). In both supramolecular complexes DABCO sits on top of the TrX in such a way that resembles a macroscopic spinning top on a tripod (Figure 3.11). As expectable the XB interaction in **r7a** was found to be stronger and more directional than in complex **r7b** as demonstrated by shorter N$\cdots$X contacts and N$\cdots$X-C angles closer to the ideal 180° (see Table 3.4).

Table 3.4 XB Geometrical features found in cocrystals **r7a** and **r7b** at two different temperatures. XB distances are expressed as normalized contacts (N$_C$) according to reference 9.

Complex	N$\cdots$X (N$_c$)	N$\cdots$X-C angle (°)
r7a (R.T.)	0.78	175.21 (7)
r7a (100 K)	0.78	173.88 (9)
r7b (R.T.)	0.83	173.73 (8)
r7b (100 K)	0.82	172.17 (6)
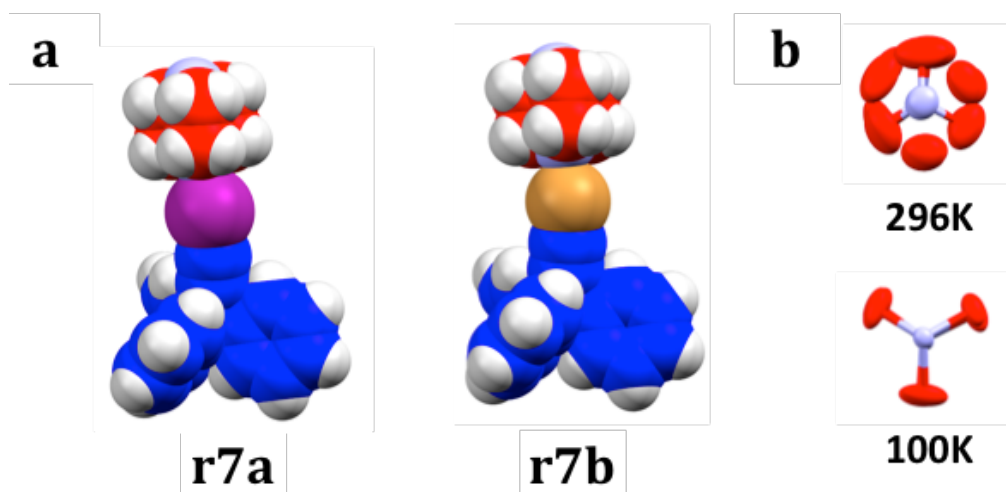
Figure 3.12 a) Structures of supramolecular trimers in cocrystals **r7a** and **r7b** obtained at 100K and b) a top-down view along the N-N axis of dabco within **r7a** crystal lattice at 296K (top) and at 100K (bottom) displaying the presence and absence of disorder, respectively. Color code: stator C, blue; rotator C, red; N, light blue; H, white; I, magenta; Br, orange.

One of the most interesting features in the structure of cocrystals **r7a** and **r7b** is that the molecular structure of DABCO at 100 K does not present disorder, while the structure solved at 298 K requires two positions with occupancies of 69:31 in **r7a** and 62:38 in **r7b** (Figure 3.12b). It is worth noting that the TrX stators are not disordered at these two temperatures. The disorder of DABCO was interpreted and later on confirmed to be dynamic in nature. From analysis of the atomic displacement parameters (ADPs), one can also infer that rotation occurs along the N-N axis of DABCO, as the ADPs display elongations on the plane perpendicular to the rotational axis, as we have already inferred for cocrystals **r1-r5**.

The crystal packings of **r7a** and **r7b** can be described as pairs of columns of DABCO and TrX molecules that propagate in the direction of the *a* axis by translation along the same axis and a 180° rotation along the *b* axis that runs parallel to the column (Figure 3.13). It is interesting to observe that the trityl-halide molecules, within the column and with adjacent columns, are engaged in edge-to-face interactions.[26] Two adjacent columns of DABCO molecules sit in cavities composed of three adjacent trityl-halide columns (Figure 3.13), which

generate some free volume around the rotator. A parameter indirectly related to this free volume is the packing coefficient (C_k), defined as the ratio between the van der Waals volumes of the molecules in the unit cell in relation to the total volume of the unit cell.[2,31] Interestingly, the packing coefficients for **r7a** and **r7b** are exactly the same, C_k = 0.66 at 100 K, which in the context of molecular crystals is quite small (*ca.* C_k = 0.65 - 0.77)[2,31] and comparable to crystalline molecular rotors showing high dynamics (C_k=0.68[33] and 0.69[34,35]).
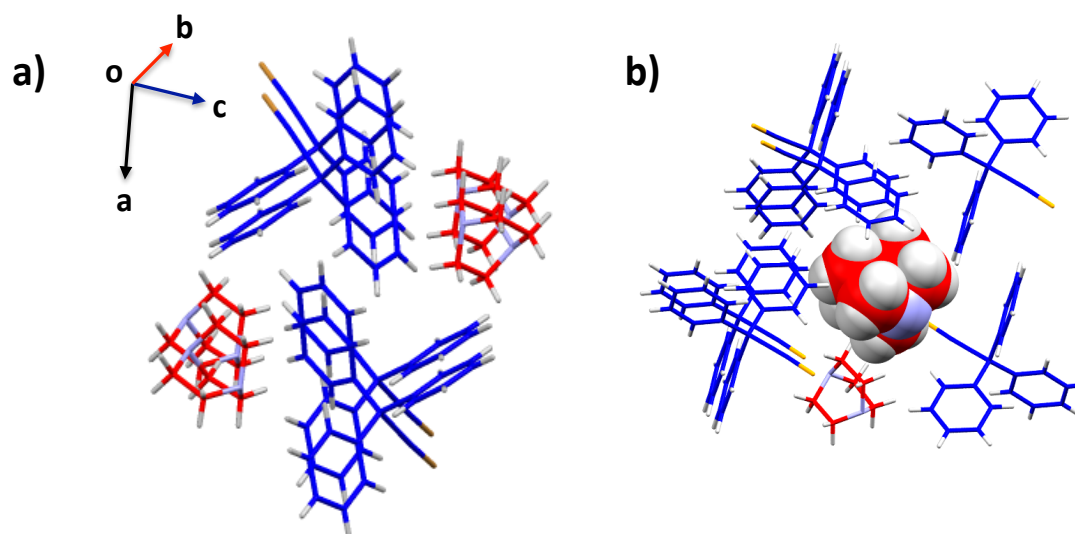
Figure 3.13 a) Columnar arrays of TrBr and DABCO molecules in the structure of cocrystal **r7b** and b) a DABCO rotator in a cavity surrounded by six molecules of TrBr and one DABCO. Color code: please refer to Figure 3.12.

Another sign of the structural and dynamic similarities between the two co-crystals comes from their nearly identical IR spectra (figure 3.14), which provide information related to normal modes and lattice phonons, which may be expected to result in similar rotational dynamics.
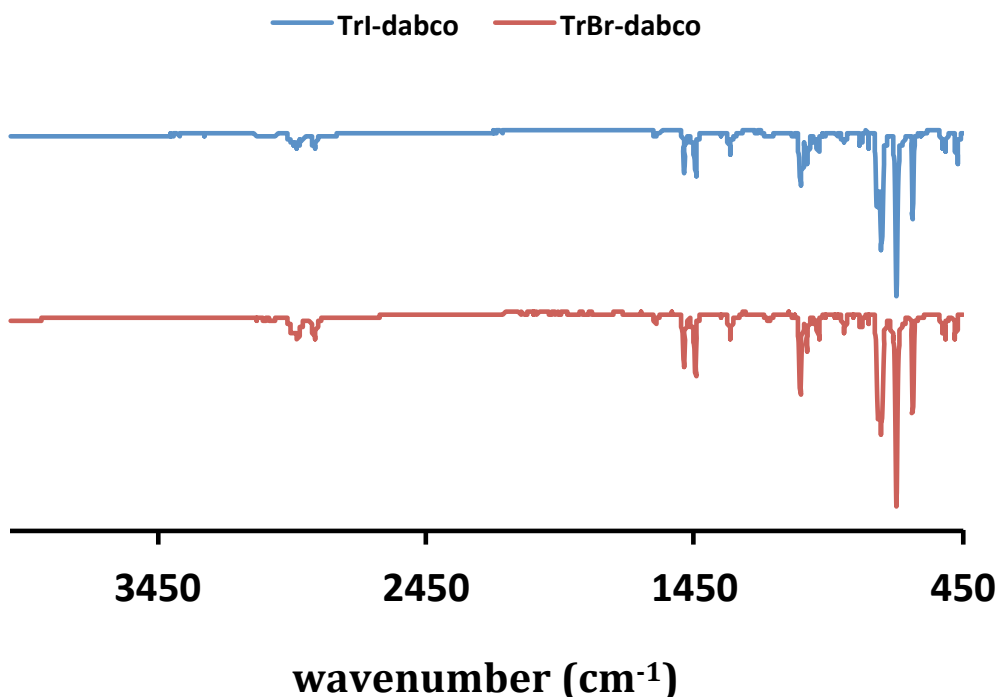
Figure 3.14 Attenuated total reflection (ATR) infrared spectra of cocrystals **r7a** (top) and **r7b** (bottom).

Pure phase crystalline bulk materials of **r7a** and **r7b** were also obtained by liquid-assisted mechanochemical method.[36] The crystalline phases of the bulk materials were analyzed by powder X-ray diffraction analysis, which showed that the patterns of **r7a** and **r7b** matched the calculated patterns from the single crystal X-ray diffraction analyses and were congruent between them (Figure 3.15 and experimental section 5.4.4 in Chapter 5); this confirmed that these materials are isomorphous. The thermal stabilities of both crystalline samples were determined by visual melting point analysis in sealed capillaries, which showed that **r7a** and **r7b** cocrystals melt with decomposition in the ranges of 140 – 146 °C and 157 – 160 °C, respectively.
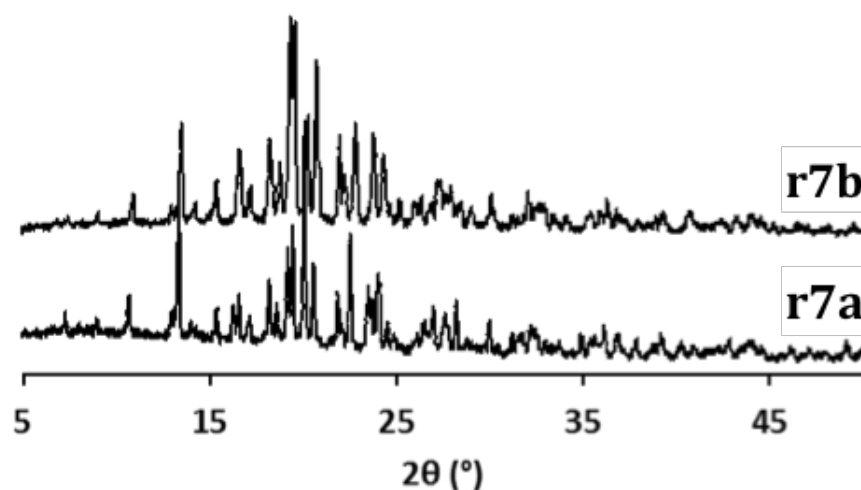
Figure 3.15 Powder X-ray diffraction patterns of samples of cocrystals **r7a** (bottom) and **r7b** (top) obtained by solvent assisted mechanochemical crystallization.

With crystallographic and thermal stability information available we were able to evaluate the dynamic performance of isomorphous co-crystals **r7a** and **r7b**. As a first glance into the dynamics of DABCO, we decided to use quadrupolar-echo ^{2}H NMR, as the line shape of the spectra are sensitive to the magnitude and rate of the angular displacement of the mobile element resulting from the dynamic modulation of electric field gradient (EFG) interaction with the electric quadrupole moment (eQ) in the C-D bond.[18] Simulation of the ^{2}H spectrum provides the site exchange rate and the jump angle.[23] With this in mind, we prepared a sample of **r7b** with isotopically enriched dabco-d_{12} (**r7b**-d_{12}), prepared following the same procedure shown in the previous section. Quadrupolar-echo ^{2}H NMR experiments were recorded at 46.2 MHz and at 296 K, 210 K and 150 K, with the latter being the lowest temperature attainable with our instrument. Comparison of the three spectra showed no significant line-shape differences. All three spectra were satisfactorily simulated using a model that considers either 120° or 60° jump angles (see experimental section 5.3.6 for further details) in the fast exchange limit of 10^8 s^{-1}. This result is in agreement with the dynamic disorder and thermal ellipsoids of the DABCO rotator observed in the single crystal X-ray structure. It should also be pointed out that in the fast exchange regime there is no difference in line shape between three-fold (120°) and six-fold (60°) rotational symmetry orders, as shown in cocrystals **r1**, **r2** and

r5. Notably the sharp central peak in ²H wide-line spectrum collected at 296 K was assigned to isotropic motion of pure DABCO impurities on the surface of **r7b** crystals.
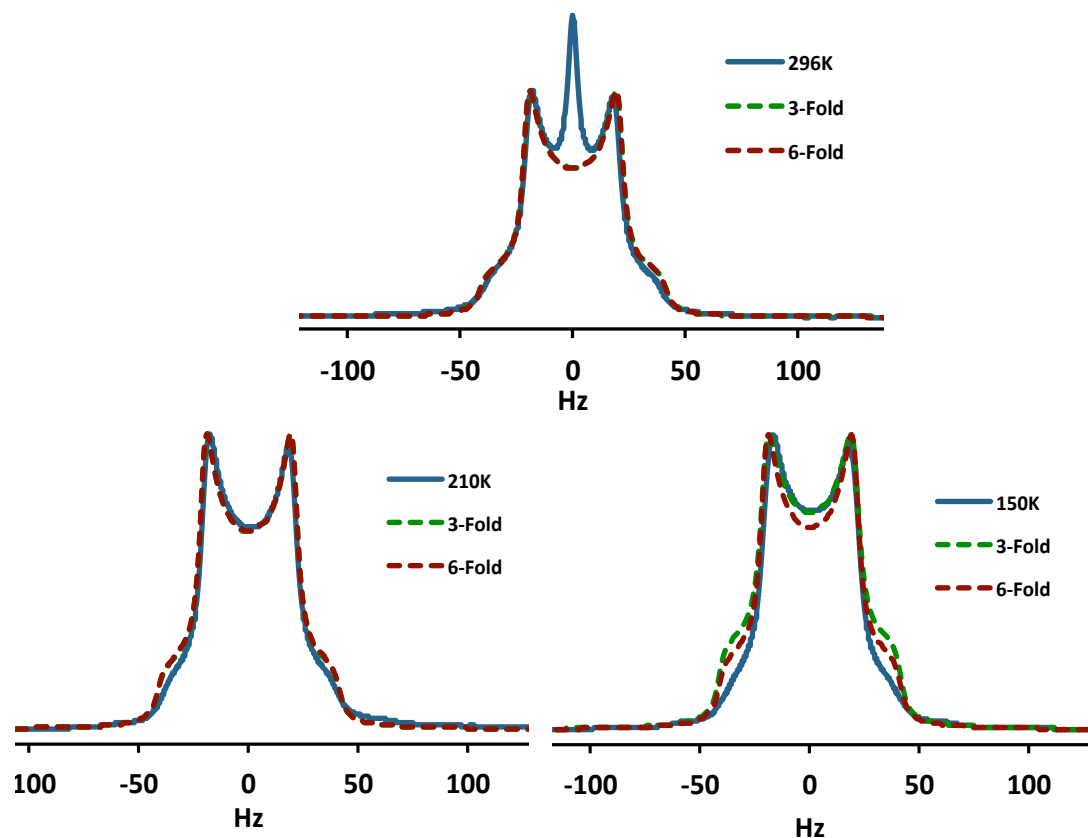
Figure 3.16 Experimental (blue solid lines) and simulated (green and red dashed lines) ²H NMR wide line spectra of **R7b**-*d₁₂* cocrystals recorded at 296 K, 210 K and 150 K at a frequency of 46.07 MHz. The figure shows that at these three temperatures the experimental spectra are reproduced by considering 3-fold (120° jump angle) or 6-fold (60° jump angle) rotational symmetries. Simulations were carried out using the Nishikiosri's program[23] with a β angle of 70°, a quadrupolar coupling constant (QCC) of 170 kHz, a line broadening of 5 kHz and an echo delay of 50 μs.

In order calculate the activation parameters (E_a, τ_0^{-1}, $\Delta H^{\neq}$, $\Delta S^{\neq}$) for the rotation of DABCO rotator in the XB cocrystals, **r7a** and **r7b**, we needed a probe that covers a larger dynamic range. In this scenario, we turned our attention to ¹H spin-lattice relaxation (¹H T_1), as we had already done for supramolecular rotors **r1-r5**.
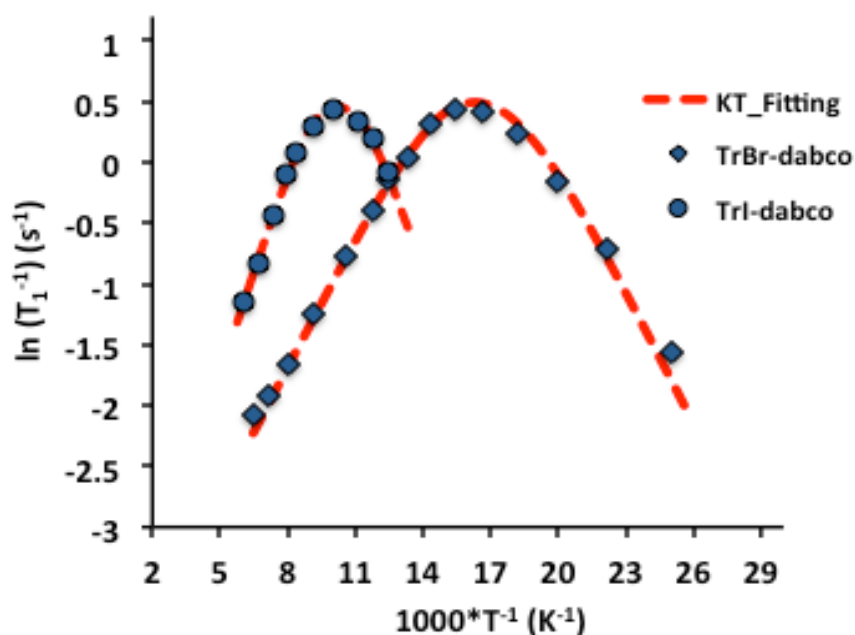
Figure 3.17 ^{1}H T_1 experiments as a function of the temperature plotted as ln (T_1^{-1}) vs $1000*T^{-1}$. ^{1}H T_1 was measured at 359.9 MHz in the range of 80 – 165 K and 40 – 155 K on cocrystals **r7a** (solid circles) and **r7b** (solid diamonds), respectively. ^{1}H T_1 minima occurred at approximately 100 K for **r7a** and 65 K for **r7b**. The red dotted lines correspond to the Kubo-Tomita fittings of the experimental data.

   Using microcrystalline samples of **r7a** and **r7b** we performed variable temperature ^{1}H T^1 experiments at a frequency $v_0 = \omega_0/2\pi$ of 359.9 MHz for proton and a saturation recovery pulse sequence. Individual relaxation curves were properly described by single exponential functions, as shown in detail in the experimental section 5.4.5. Experiments with **r7a** were recorded in the range of 80 K – 165 K with a minimum in T_1 found at 100 K. In the case of **r7b**, ^{1}H T_1 experiments were recorded in the range of 40 K – 155 K presenting a minimum in T_1 at 65 K. Using the activation energy, E_a, pre-exponential factor, τ_0^{-1} and C factor as adjustable parameters, the experimental relaxation data (T_1) as a function of the temperature were adequately described by the Kubo-Tomita equation[37] (eq. 2), as shown in Figure 3.17 and Table 3.5.

Table 3.5 Activation parameters for the rotation of DABCO in cocrystals **r7a** and **r7b**.

Kinetics parameters	r7a	r7b
E_a (kcal/mol)	1.15	0.71
τ_0^{-1} (s^{-1})	1.3×10^{12}	1.2×10^{12}
C (s^{-2})	2.55×10^9	2.6×10^9
$\Delta H^{\neq}$ (kcal/mol)	0.95	0.54
$\Delta S^{\neq}$ (cal/mol K)	-3.0	-3.0

Given the fact that the crystal structures of **r7a** and r**7b** are isomorphous, it is interesting to observe that there are almost no differences in the C constants and pre-exponential factors (τ_0^{-1}), although they have small but clearly distinguishable energy barriers. As expected for structures with the same number of protons involved in the relaxation mechanism, the C constant for both co-crystals has almost the same value, 2.55×10^9 and 2.6×10^9 s^{-2} for **r7a** and **r7b**, respectively (Table 3.5). Related to the frequency of torsional oscillations of the DABCO rotator within its potential energy well, we found that the pre-exponential factors (τ_0^{-1}) are almost the same for the two cocrystals, 1.3×10^{12} and 1.2×10^{12} s^{-1}. This observation is in line with a mechanism where normal modes and lattice phonons combine to produce essentially identical librations, as expected for the isomorphous crystal structures. However, we found an activation energy of $E_a = 0.71$ kcal/mol for **r7b**, which is 38% lower as compared to the $E_a = 1.15$ kcal/mol of **r7a**, with the former being the lowest reported in the field of amphidynamic crystals. We propose that such low activation energies are in line with the low packing coefficients of **r7a** and **r7b** cocrystals, $C_k = 0.66$, which means that the crystals are loosely packed and have enough empty space for the rotation of DABCO. We also noted that the lower energy barrier for the rotation of dabco in **r7b** as compared to that in **r7a**, correlates with the occupancies of the disordered structure of dabco at room temperature, 62:38 and 69:31, respectively, where, as a result of the lower energy barrier, the second position in **r7b** is more populated. We propose that in isomorphous

crystal structures **r7a** and **r7b**, with the only difference being the strength of the C-X$\cdots$NR$_3$ interaction, the small differences in E$_a$ could come from small differences in the cavity of the rotator. As previously noted, the strength of the XB is reflected in the length and directionality of the C-X$\cdots$NR$_3$ interaction, where, as predicted, this distance is shorter in **r7a** than in **r7b** (at 103 K 2.717 Å and 2.773 Å, respectively). As a consequence, we could foresee that the DABCO makes different contacts with the neighboring molecules. We found that, as a result of DABCO being closer to the iodine atom, the close contact interactions of the nitrogen not involved in XB with two hydrogen atoms of two different TrX molecules are longer (2.71 Å, 2.91 Å) as compared to the same in **r7b** (2.68 Å, 2.88 Å) (Figure 3.18). Furthermore, in the more loosely bound cocrystal **r7b** the rotator alkyl chains are closer than those in **r7a**. We found that rotator cavity is larger in **r7b** than in **r7a**, 169.6 Å^3 and 162.8 Å^3, respectively at 100 K. We reasoned that smaller rotator cavity creates a more crowded environment for the rotation of DABCO in **r7a**, thus raising the activation energy.
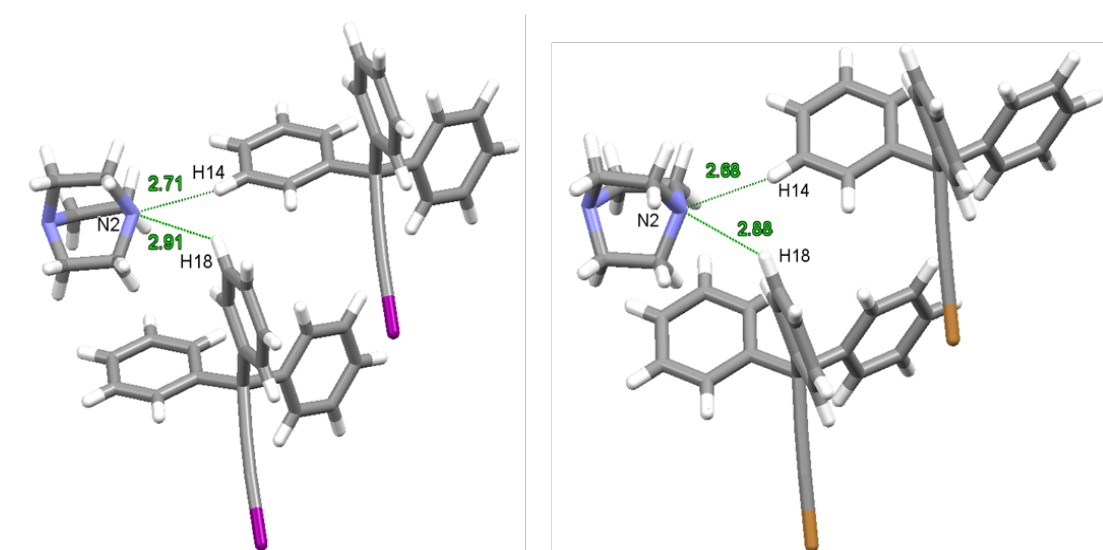
Figure 3.18   Close up of the crystal structures of r7a (left) and r7b (right) where weak hydrogen bonds between the unbound nitrogen and two different aromatic hydrogen atoms are highlighted. Contacts and distances (in Å) are in green. Color code: C, grey; N, light blue; H, white; I, magenta; Br, orange.

The thermodynamic parameters of activation, enthalpy ($\Delta H^{\neq}$) and entropy ($\Delta S^{\neq}$), would reflect these steric interactions. To this end, $\Delta H^{\neq}$ and $\Delta S^{\neq}$ were calculated by fitting the experimental T_1 data to the Kubo-Tomita equation using t_c in the form of the Eyring equation (eq. 4).

$$\tau_c = h/k_B T \exp(-\Delta S^{\neq}/R) \exp(\Delta H^{\neq}/RT) \quad \text{(Eq. 4)}$$

An excellent fit to T_1^{-1} data was obtained with the data presented in Table 3.5. As expected from their similar pre-exponential factor, rotation of DABCO in crystals of **r7a** and **r7b** takes place with the same activation entropy, $\Delta S^{\neq} = -3.0$ cal/mol K. A relatively small but negative value suggests that some organization must occur at the transition state for DABCO to jump from one energy well to the other. On the other hand, we observed that $\Delta H^{\neq}$ in **r7a** is almost twice as large, 0.95 kcal/mol, as that of **r7b**, 0.54 kcal/mol, suggesting that relatively subtle differences in steric interactions are responsible for the higher enthalpic barrier of **r7a**.
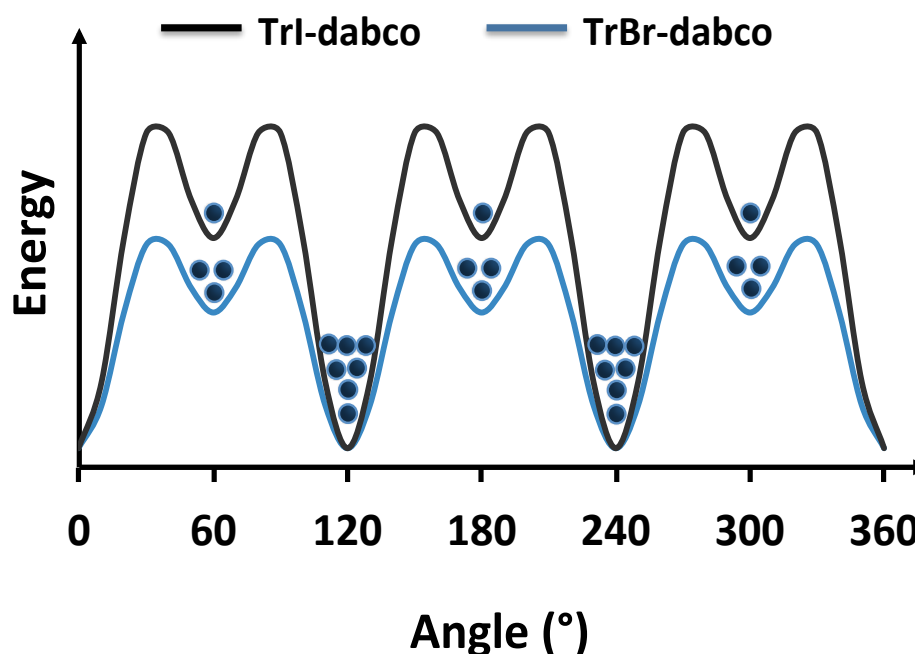
Figure 3.19 Potential energy surface for the rotation of dabco in cocrystals of **r7a** (black trace) and **r7b** (blue trace).

Based on crystallographic data, quadrupolar-echo ^{2}H NMR and activation parameters (E_a, τ_0^{-1}, $\Delta H^{\neq}$ and $\Delta S^{\neq}$) obtained by ^{1}H T_1 relaxometry experiments, we proposed a six-fold potential energy surface with three lowest energy minima. We inferred by crystallographic data that the second equilibrium position observed by X-ray diffraction analysis is of lower activation energy and occurs at a higher potential energy level, which explains why it is the less populated at low temperatures (Figure 3.19). The potential energy surface diagram also shows that the rotational barrier for dabco in **r7b** is lower than in **r7a**.

3.2.3 Conclusions

In conclusion, we have successfully designed and realized two new halogen-bonded supramolecular spinning tops on a tripod, **r7a** and **r7b**, which show isomorphous crystal structures at 100 K and room temperature. In agreement with the strength of the non-covalent interaction, we observed that the C-X$\cdots$NR$_3$ distance is shorter when iodine is present, as in the case of **r7a**, as compared to the case when a bromine atom is involved in XB in **r7b**. Liquid-assisted mechanochemical synthesis allowed us to prepare pure crystalline phase samples of **r7a** and **r7b**, which were evaluated by ^{1}H T_1 relaxometry experiments. We observed a good correlation between their loose crystal packing, C_k = 0.66 at 100 K, and the small barriers of 1.15 and 0.71 kcal/mol, respectively for DABCO rotation in cocrystals **r7a** and **r7b**. It was also shown that pre-exponential factors for DABCO rotation in **r7a** and **r7b** are almost identical with values of (τ_0^{-1}) 1.3 x 10^{12} s^{-2} and 1.3 x 10^{12} s^{-2}, respectively. Taking advantage of isomorphus cocrystals with nearly identical crystal structures with similar normal vibrational modes and lattice phonons we were able to sort out the origin of the enthalpy and entropy of activation. Accordingly, by fitting ^{1}H T_1 data to the Eyring and Kubo-Tomita equations, we unveiled essentially identical negative activation entropies ($\Delta S^{\neq}$ = -3.0 cal/mol K) and clearly distinguishable activation enthalpies. Thus, the enthalpic barrier for DABCO rotation in cocrystal **r7a** ($\Delta H^{\neq}$ = 0.95 kcal/mol) is almost twice as large as that of **r7b** ($\Delta H^{\neq}$ = 0.54 kcal/mol). This difference can be assigned to subtle

differences in their crystal structure which result in a more hindered environment for the DABCO cavity in **r7a**.

References:

1   L. Catalano, S. Pérez-Estrada, G. Terraneo, T. Pilati, G. Resnati, P. Metrangolo and M. A. Garcia-Garibay, *J. Am. Chem. Soc.*, 2015, **137**, 15386.

2   C. S. Vogelsberg and M. A. Garcia-Garibay, *Acc. Chem. Res.*, 2012, **41**, 1892.

3   A. Colin-Molina, S. Pérez-Estrada, A. E. Roa, A. Villagrana-Garcia, S. Hernández-Ortega, M. Rodríguez, S. E. Brown and B. Rodríguez-Molina, *Chem. Commun.*, 2016, **52**, 12833.

4   L. Kobr, K. Zhao, Y. Shen, A. Comotti, S. Bracco, R. K. Shoemaker, P. Sozzani, N. A. Clark, J. C. Price, C. T. Rogers and J. Michl, *J. Am. Chem. Soc.*, 2012, **134**, 10122.

5   A. E. Khudozhitkov, H. Jobic, D. Freude, J. Haase, D. I. Kolokolov and A. G. Stepanov, *J. Phys. Chem. C*, 2016, **120**, 21704.

6   S. Bracco, A. Comotti, P. Valsesia, B. F. Chmelka and P. Sozzani, *Chem. Commun.*, 2008, 4798.

7   Z. J. O'Brien, S. D. Karlen, S. Khan and M. A. Garcia-Garibay, *J. Org. Chem.*, 2010, **75**, 2482.

8   M. Inukai, T. Fukushima, Y. Hijikata, N. Ogiwara, S. Horike and S. Kitagawa, *J. Am. Chem. Soc.*, 2015, **137**, 12183.

9   G. Cavallo, P. Metrangolo, R. Milani, T. Pilati, A. Priimagi, G. Resnati and G. Terraneo, *Chem. Rev.*, 2016, **116**, 2478.

10   C. Lemouchi, C. S. Vogelsberg, L. Zorina, S. Simonov, P. Batail, S. Brown and M. A. Garcia-Garibay, *J. Am. Chem. Soc.*, 2011, **133**, 6371.

11   S. D. Karlen, H. Reyes, R. E. Taylor, S. I. Khan, M. F. Hawthorne and M. A. Garcia-Garibay, *Proc. Natl. Acad. Sci.*, 2010, **107**, 14973.

12   J.-Y. Le Questel, C. Laurence, J. Graton, *CrystEngComm*, 2013, **15**, 3212.

13   P. Politzer, J. S. Murray and T. Clark, *PhysChemChemPhys*, 2013, **15**, 11178.

14   D. M. Cho, S. R. Parkin and M. D. Watson, *Org. Lett.*, 2005, **7**, 1067.

15 O. V. Shishkin, S. V. Shishkina, A. V. Maleev, R. I. Zubatyuk, V. Vasylyeva, K. Merz, *ChemPhysChem*, 2013, **14**, 847.

16 J. D. Dunitz, V. Schomaker, K. N. Trueblood, *J. Phys. Chem.*, 1988, **92**, 856.

17 J. Dunitz, E. F. Maverick, K. N. Trueblood, *Angew. Chem., Int. Ed. Engl.*, 1988, **27**, 880.

18 C. A. Fyfe in *Solid State NMR for Chemists*, 1983, CFC Press: Guelph, Ontario.

19 A. Zussman and S. J. Alexander, *Chem. Phys.*, 1968, **48**, 3534.

20 S. D. Karlen, H. Reyes, R. E. Taylor, S. I. Khan, M. F. Hawthorne and M. Garcia-Garibay, *Proc. Natl. Acad. Sci.*, 2010, **107**, 14973.

21 B. Rodriguez-Molina, S. Pérez-Estrada, M. A. Garcia-Garibay, *J. Am. Chem. Soc.,* 2013, **135**, 10388.

22 J. P. D'innocenzo and T. E. Banach, *J. Am. Chem. Soc.*, 1988, **110**, 971.

23 S. Nishikiori, T. Soma and T. Iwamoto, *J. Inclusion Phenom. Mol. Recogn. Chem.*, 1997, **27**, 233.

24 L. Catalano, S. Pérez-Estrada, H.-H. Wang, A. J.-L. Ayitou, S. Khan, G. Terraneo, P. Metrangolo, S. Brown and M. A. Garcia-Garibay, *J. Am. Chem. Soc.,* 2017, **139**, 843*.*

25 R. Arcos-Ramos, B. Rodriguez-Molina, M. Romero, J. M. Méndez-Stivalet, M. Eugenia Ochoa, P. I. Ramirez-Montes, R. Santillan, M. A. Garcia-Garibay and N. Farfán, *J. Org. Chem.*, 2012, **77**, 6887.

26 A. Stopin and M. A. Garcia-Garibay, *Cryst. Growth Des.*, 2012, **12**, 3792.

27 R. Arcos-Ramos, B. Rodriguez-Molina, E. Gonzalez-Rodriguez, P. I. Ramirez-Montes, M. Eugenia Ochoa, R. Santillan, N. Farfán and M. A. Garcia-Garibay, *RSC Adv.*, 2015, **5**, 55201.

28 T. Clark, M. Hennemann, J. S. Muray and P. Politzer, *J. Mol. Model.*, 2007, **13**, 291.

29 K. E. Riley, J. S. Murray, J. Fanfrlík, J. Řezáč, R. J. Solá, M. C. Concha, F. M. Ramos and P. Politzer, *J. Mol. Model.*, 2011, **17**, 3309.

30 P. Politzer, J. S. Murray, P. Lane and M. C. Concha, *Int. J.Quantum Chem.*, 2009, **109**, 3773.

31 A. I. Kitaigorodsky in *Molecular Crystals and Molecules*, 1973, Academic Press, New York.

32 Z. J. O'Brien, A. Natarajan, A.; S. Kahn, M. A. Garcia-Garibay, *Cryst. Growth. Des.*, 2011, **11**, 2654.

33 T.-A. V. Khuong, G. Zepeda, R. Ruiz, S. I. Khan, M. A. Garcia-Garibay, *Cryst. Growth Des.*, 2004, **4**, 15.

34 C. E. Godinez, G. Zepeda, C. J. Mortko, H. Dang, M. A. Garcia-Garibay, *J. Org. Chem.*, 2004, **69**, 1652.

35 C. E. Godinez, M. A. Garcia-Garibay, *Cryst. Growth Des.*, 2009, **9**, 3124.

36 D. Braga, L. Maini and F. Grepioni, *Chem. Soc. Rev.*, 2013, **42**, 7638.

36 R. Kubo, K. Tomita, *Phys. Soc. Jpn.*, 1954, **9**, 888.

CHAPTER 4

Conclusions

In conclusion, we studied XB-based crystalline systems to explore nature and role of this peculiar non-covalent interaction from its fundamentals to engineering novel supramolecular solid-state machines.

Specifically, we demonstrated that Far-IR spectroscopy may become a fast and easily-accessible tool for the direct investigation of XB involving iodoperfluoroaromatics systems, common moieties in the design of XB-based molecular complexes. Far-IR spectroscopy may represent a valid alternative technique to detect this non-covalent interaction in materials when well-established methods are not available (XRD techniques, NMR, thermal analysis, Raman spectroscopy, *etc.*). This is the case for the study of amorphous compounds, liquid crystals or fibrils. Furthermore, we contributed to the on-going discussion about the physical nature of XB by clearly showing a charge-transfer contribution affecting vibration bands of the cocrystals under study. We also demonstrated that natural abundance ^{15}N solid-state NMR may provide an effective tool for the direct detection of XB. In particular, we found a linear correlation between ^{15}N chemical shifts and R_{xb} values, which paves the way to the quantification XB geometrical features from solid-state NMR experiments. Moreover, we explored the correlation between ^{13}C isotropic chemical shifts and the length of C-I covalent bonds of the XB donors under study. This study points out that solid-state ^{15}N and ^{13}C NMR are first-choice analytical techniques to study materials involving XB when alternative methods are not available. We came up with nice and reliable results with both the reported analytical techniques, however there are some advantages and disadvantages by using these two different diagnostic tools. In particular far-IR spectroscopy has few advantages: it needs just a small quantity of sample for each measurement (even less than 1 mg); it can be done in few minutes; in principle, it can be performed not only on solid-state systems, but also on soft matter and liquids. On the other hand, complex molecular structures, bearing a high number of degrees of freedom, may possess crowded and overlapped far-IR region of the spectra, which could lead to a non-trivial interpretation and assignment of the normal modes of vibration. SSNMR generally needs at least *ca.* 100 mg to be performed, the samples must be solids and the analysis is time-consuming and non-

routinary. Though this spectroscopic tool can give you precious information on the structure and geometry of the supramolecular species under investigation.

Importantly, we realized and fully characterized the first examples of XB-based amphidynamic cocrystals from simple and commercially available starting building blocks by taking advantage of a supramolecular approach. Variable temperature XRD and ^{1}H T_1 relaxometry measurements revealed highly efficient dynamics comparable to those found in rotors build with covalent axles of rotation and shed light over the fundamental role of XB, which works as a new robust rotational axle and hence as new design principle in the field of amphidynamic crystals. In addition, by preparing two isomorphous XB-based amphidynamic cocrystals, we were also able to sort out the origin of enthalpy and entropy of activation of the rotators dynamics. One of these two new amphidynamic systems showed the lowest activation energy of the rotational dynamics ever reported in literature. The discovery of these new crystalline multicomponent systems thus opens up new avenues in the development of new smart materials and molecular machines, *e.g.* sensors, tunable dielectrics, guest-selective supramolecular hosts.[1-3] Future plans about XB-based amphidynamic crystals are focused on addressing the development of specific functional materials to be exploited for practical applications.

In summary, this PhD thesis demonstrates once more the great potential of XB as a precious structural tool in designing and building new crystalline materials opening its new exploitation in the field of molecular rotors.

References:

1   C. S. Vogelsberg and M. A. Garibay, *Chem. Soc. Rev.*, 2012, **41**, 1892.

2   A. Comotti, S. Bracco and P. Sozzani, *Chem. Soc. Rev.*, 2016, **49**, 1701.

3   S. K. Elsaidi, M. H. Mohamed, C. M. Simon, E. Braun, T. Pham, K. A. Forrest, W. Xu, D. Banerjee, B. Space, M. J. Zaworotko and P. K. Thallapy, *Chem. Sci.*, 2017, DOI: 10.1039/C6SC05012C.

CHAPTER 5

Experimental Section

5.1 Far-IR spectroscopy as diagnostic tool of XB involving aromatic donors

5.1.1 Supramolecular synthesis
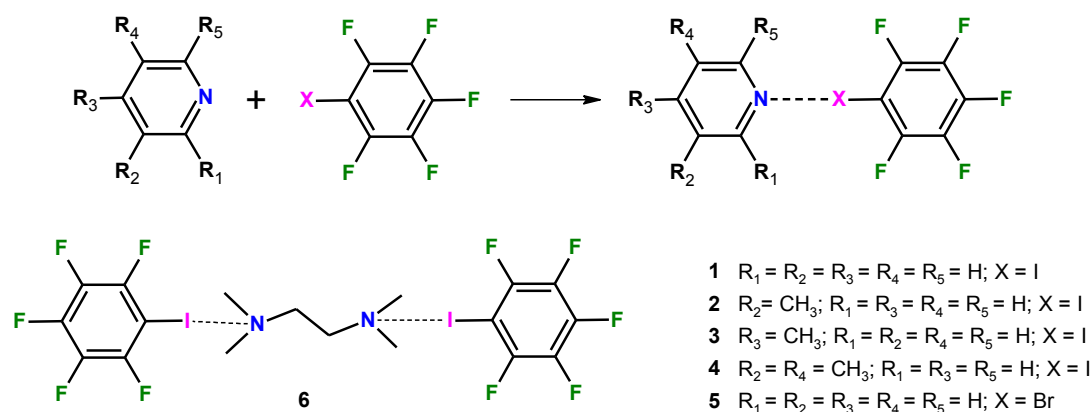
Figure 5.1 Starting materials and cocrystals involved in the study.

Starting materials pyridine, 3-methylpyridine, 4-methylpyridine, 3,5-dimethylpyridine, iodopentafluorobenzene (IPFB) and bromopentafluorobenzene (BrPFB) were purchased from commercial suppliers (Sigma-Aldrich, Apollo Scientific, and ABCR) and used without further purification. The six halogen-bonded cocrystals were synthesized by direct mixing of the liquid starting materials in either 1:1 (**1**, **2**, **3**, **4**, and **5**) and 1:2 (**6**) molar ratios, taking into account the pairing of the respective halogen-bond donor and acceptor sites. The liquid mixtures were stirred for 1h at room temperature. **2**, **3**, **4**, and **6** crystallized during mixing somewhere between 1 - 30 minutes.

5.1.2 Single crystal XRD analysis

1 and **5** were in situ *cryo*-crystallized on the diffractometer in sealed 0.3 mm Lindemann capillaries according to a reported procedure.[1] Suitable crystals of **2**, **3**, **4** and **6** were, instead, chosen directly from the crystallized starting mixtures.

The crystals were diffracted using Mo-Kα radiation (λ= 0.71073 Å) on a Bruker KAPPA APEX II diffractometer with a Bruker KRYOFLEX low temperature device. Cocrystal formation of **3**, **4** and **6** was confirmed by the crystal cell determination and comparison with priviously reported data.[2]

Crystal structures of **1**, **2** and **5** were solved by direct method and refined against F^2 using SHELXL97.[3] Packing diagrams were generated using Mercury.[4] Intermolecular interactions were analyzed with PLATON.[5] The non-hydrogen atoms were refined anisotropically and hydrogen atoms were refined using difference Fourier map or positioned geometrically.

Table 5.1 Selected crystallographic and refinement parameters for cocrystals **1**, **2**, **5** and **6**.

	1	2	5	6
Formula	(C_6F_5I) (C_5H_5N)	(C_6F_5I) (C_6H_7N)	(C_6F_5IBr) (C_5H_5N)	(C_6F_5I) $(C_6H_{16}N_2)$
Formula weight	373.1	387.09	326.1	352.06
Temperature (K)	223 (2)	100(2)	173(2)	100(2)
Space group	$P\,2_1/c$	$P\,2_1/n$	$P\,2_1/c$	$P\,2_1/n$
a (Å)	11.9726(5)	8.0031(4)	8.8544(4)	11.7434(7)
b (Å)	9.2769(4)	12.0310(6)	9.3356(4)	5.8599(3)
c (Å)	11.5812(5)	13.4501(6)	14.0154(6)	16.7329(10)
β (°)	112.372(2)	100.731(2)	101.4780(1)	99.173(2)
Volume (Å^3)	1189.49(9)	1272.40(11)	1135.36(9)	1136.75(11)
Z	4	4	4	4
Density (gcm^{-3})	2.08	2.02	1.91	2.06
μ (mm^{-1})	2.736	2.562	3.666	2.856
F (000)	704	736	632	668
$\theta_{min,\,max}$ (°)	(1.8, 27.5)	(2.3, 25.1)	(2.6, 24.9)	(3.5, 25.0)
$h_{min,\,max}$	(-15, 15)	(-9, 7)	(-10, 10)	(-12, 13)
$k_{min,\,max}$	(-12, 10)	(-14, 14)	(-9, 11)	(-6, 5)
$l_{min,\,max}$	(-15, 14)	(-15, 16)	(-16, 11)	(-18, 19)
No. of refl. measured	9611	6134	5249	5132
No. unique refl.	2731	2257	1994	1999
No of parameter	184	200	163	177
Data compl. (%)	99.3	99.7	99.5	99.6
$R_{\_all}$, $R_{\_obs}$	0.0224, 0.0202	0.017, 0.015	0.019, 0.018	0.019, 0.018
wR_{2_all}, wR_{2_obs}	0.0457, 0.0443	0.036, 0.035	0.049, 0.048	0.038, 0.038
$\Delta\rho_{max,\,min}$ (eÅ^{-3})	0.648, -0.492	0.337, -0.330	0.237, -0.241	0.498,-0.414
G.o.F	1.140	1.022	1.070	1.175

5.1.3 Thermal analysis

DSC analyses were performed using a Mettler Toledo DSC 823e. 12-26 mg of each sample were enclosed in aluminium pans and measured with heating/cooling rates of 5 °C/min.

All the mixtures melted with single peaks at temperatures higher than both pure precursors indicating cocrystal formation, as shown in Table 2.1.

5.1.4 Infrared spectroscopy analysis

IR spectra were obtained using a Nicolet iS50 FTIR spectrometer equipment with attanuated total reflection (ATR) device. For each sample, spectra were collected in the far-IR region (128 scans, 80-400 cm^{-1}) using solid-state substrate beam splitter. All the spectra were measured with a resolution of ±4 cm^{-1} and corrected with the baseline correction tool of the OMNIC® software. The experimental intensity increase was calculated following the equation:

$$\Delta I = (I_{\text{C-I stretch.}} / I_{\text{ref.}})_{\text{cocrystal}} / (I_{\text{C-I stretch.}} / I_{\text{ref.}})_{\text{XB donor pure}}$$

Where $I_{\text{C-I stretch.}}$ is the intensity of the vibration band associated to the symmetric C-I in plane stretching and $I_{\text{ref.}}$ is the intensity of a reference peak, centered at around 310 cm^{-1} , which does not change passing from the starting material to the final adducts. To partially correct peak overlapping, all the spectra were deconvoluted using OMNIC® software tools to calculate the intensities. Partial band overlapping and deconvolution methods may affect intensity measurements, therefore these intensity variations have to be considered indicative. Calculated intensity increase (see section 5.1.5), instead, are not affected by peak overlapping.
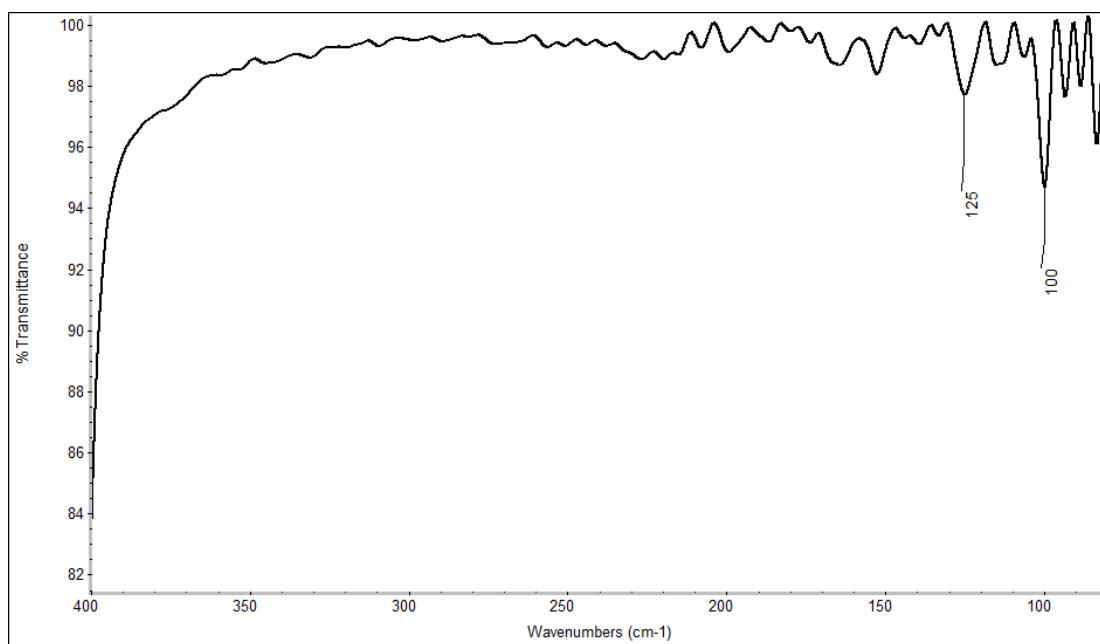
Figure 5.2 Far-IR spectrum of Pyridine from 80 to 400 cm^{-1}.
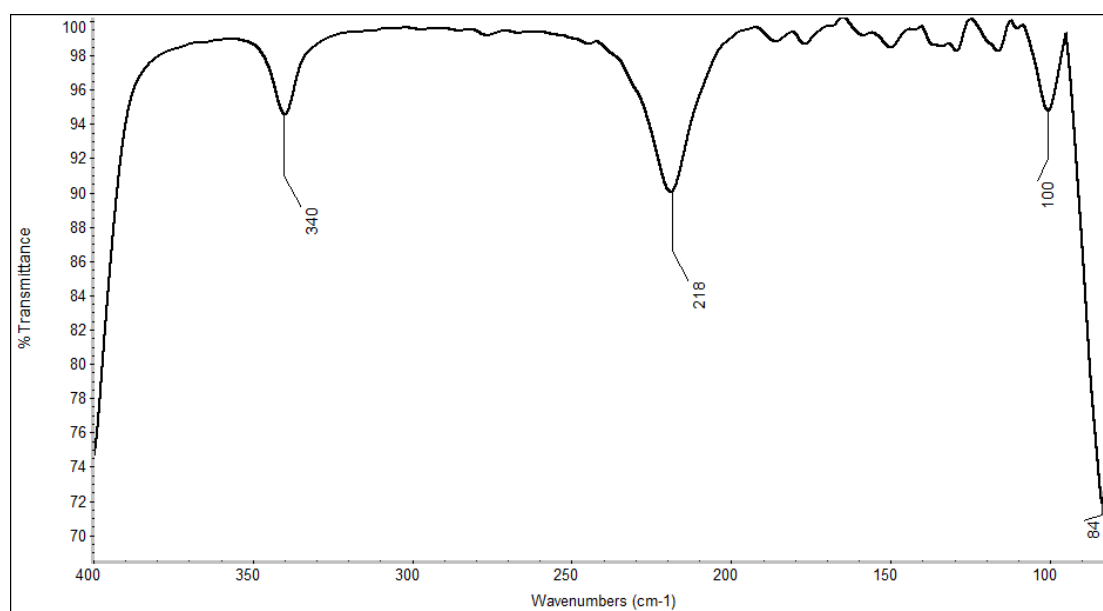
Figure 5.3 Far-IR spectrum of 3-methylpyridine from 80 to 400 cm^{-1}.
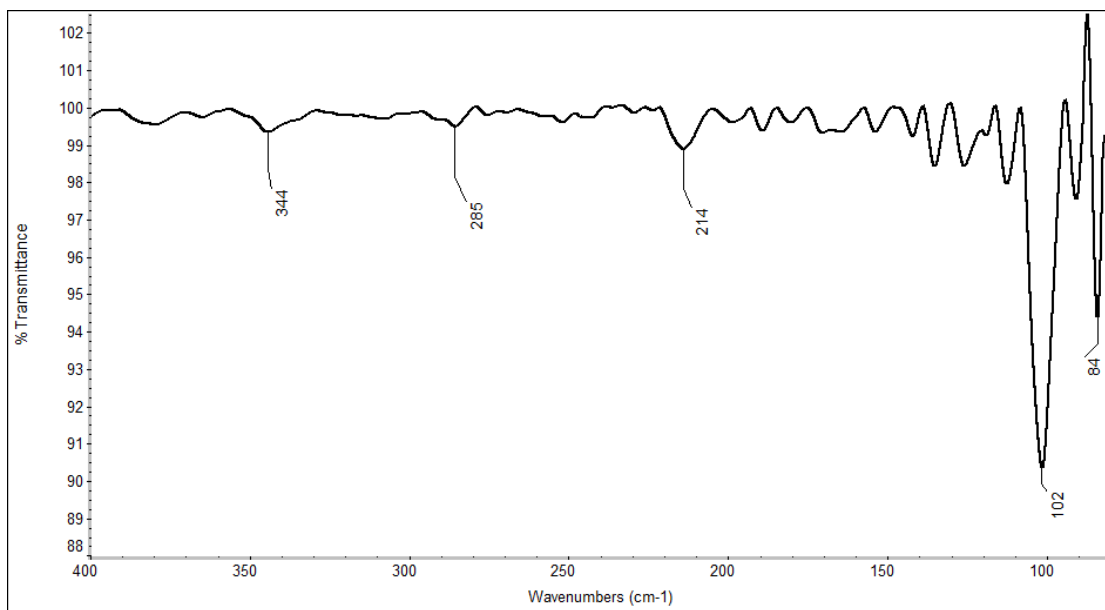
Figure 5.4 Far-IR spectrum of 4-methylpyridine from 80 to 400 cm^{-1}.
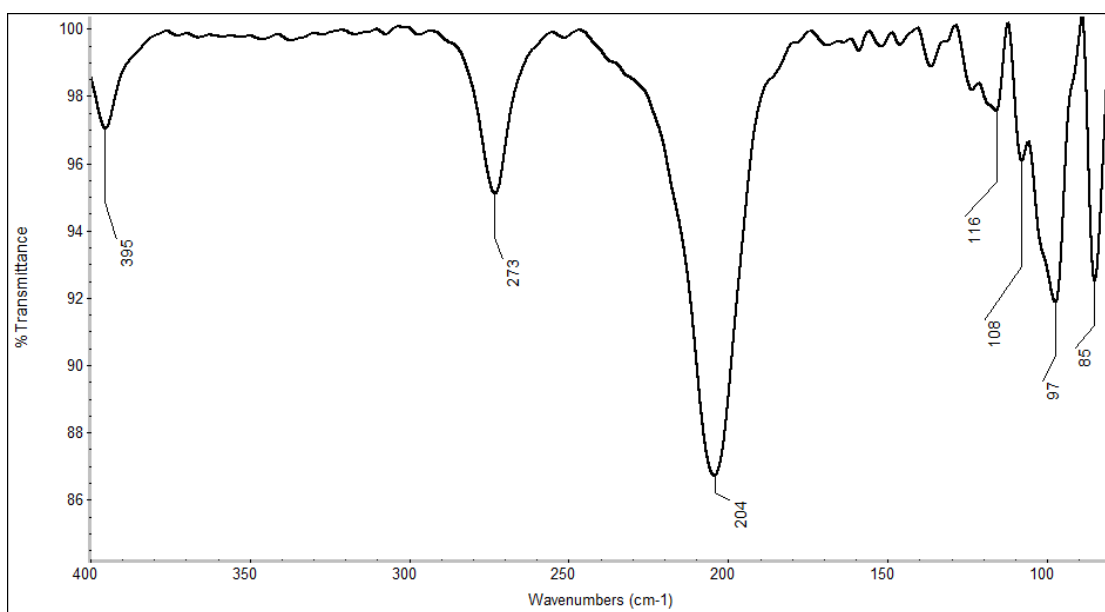
Figure 5.5 Far-IR spectrum of 3,5-dimethylpyridine from 80 to 400 cm^{-1}.
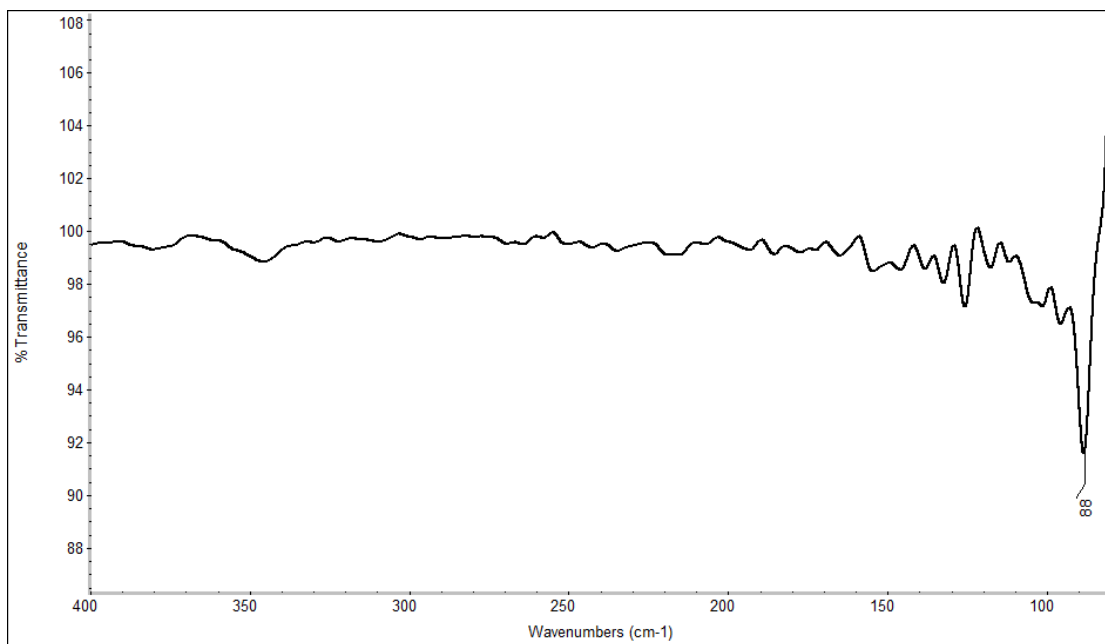
Figure 5.6 Far-IR spectrum of tetramethylethylenediamine from 80 to 400 cm^{-1}.
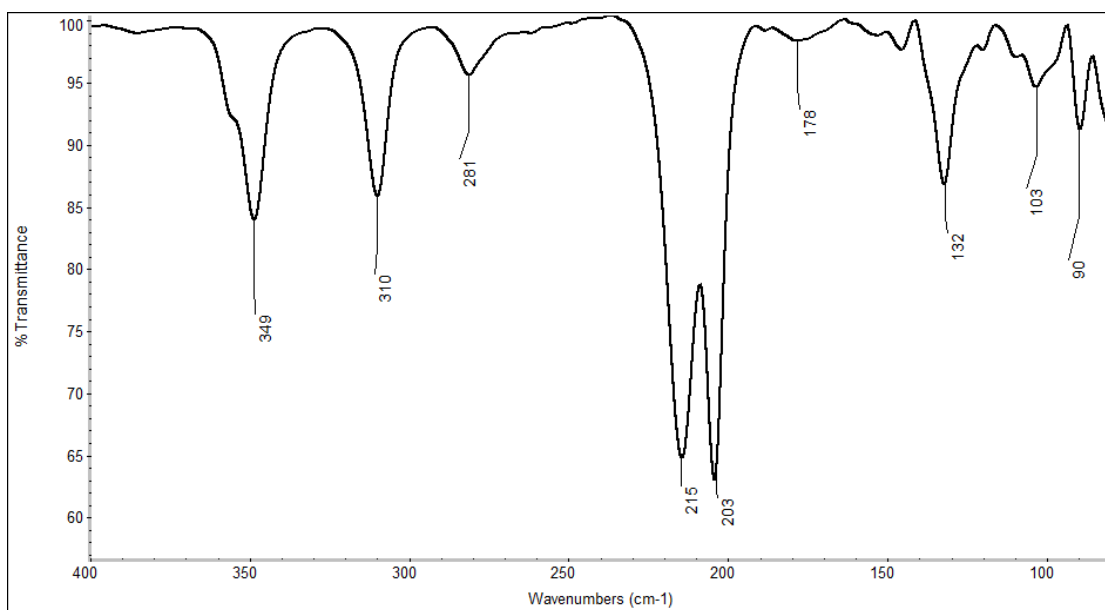
Figure 5.7 Far-IR spectrum of iodopentafluorobenzene from 80 to 400 cm^{-1}.
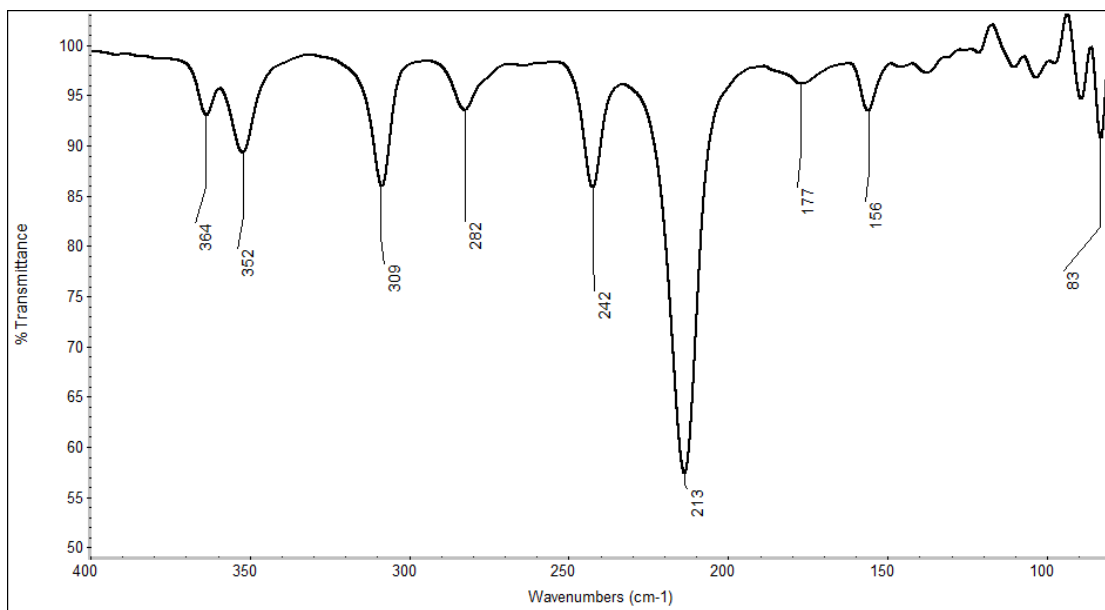
Figure 5.8 Far-IR spectrum of bromopentafluorobenzene from 80 to 400 cm^{-1}.
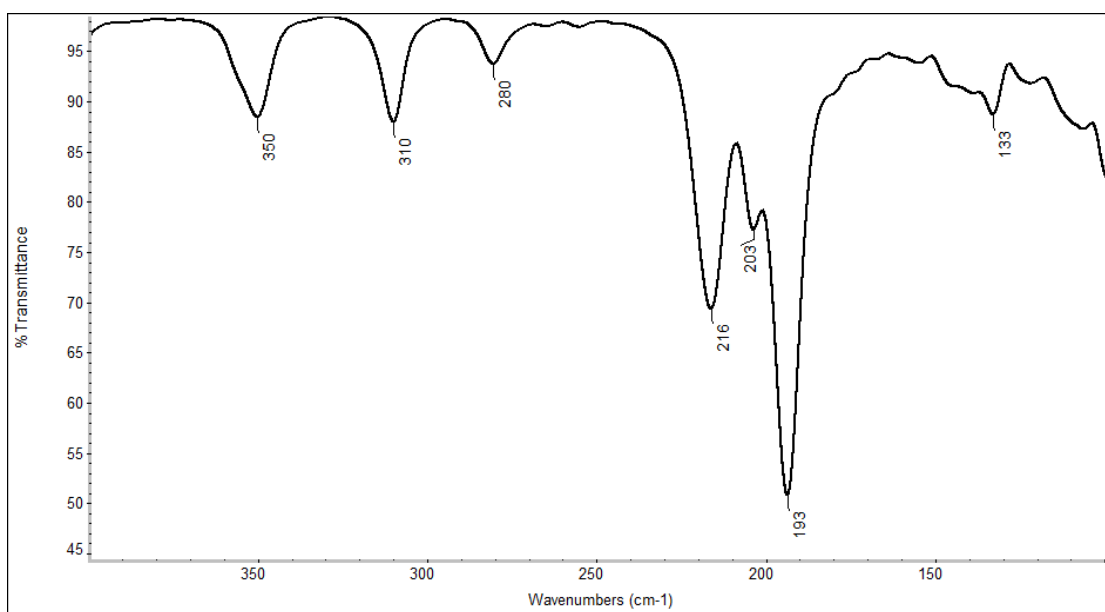
Figure 5.9 Far-IR spectrum of **1** from 80 to 400 cm^{-1}.
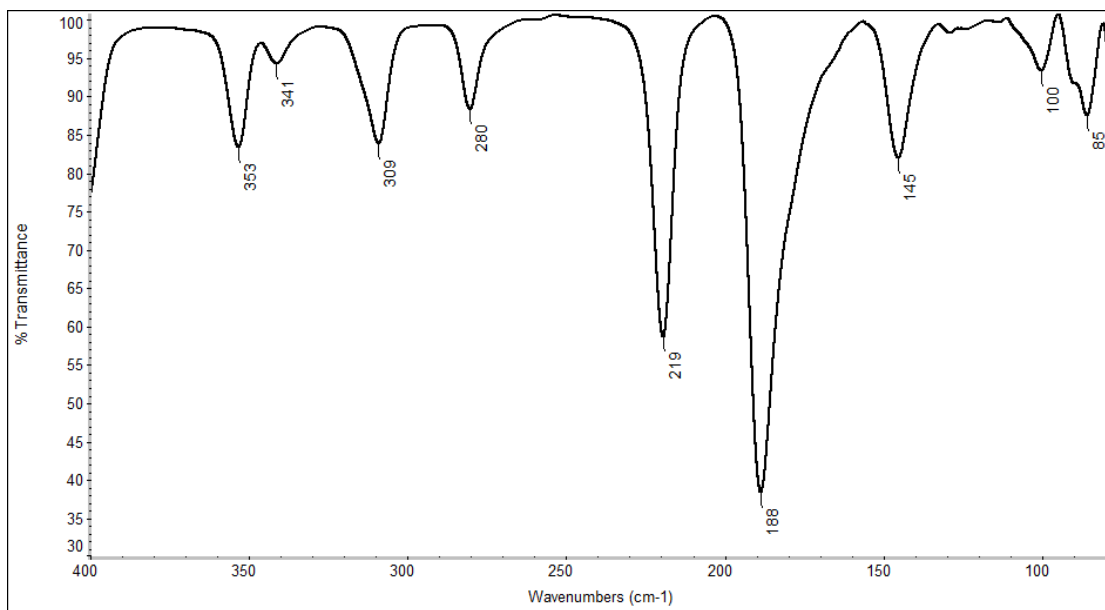
Figure 5.10 Far-IR spectrum of **2** from 80 to 400 cm^{-1}.
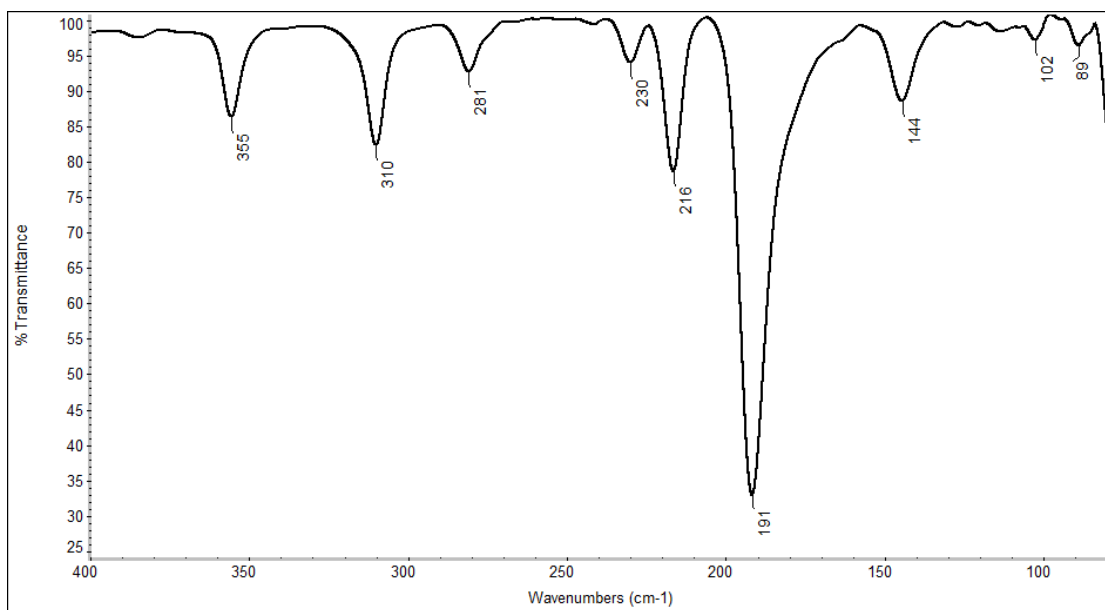
Figure 5.11 Far-IR spectrum of **3** from 80 to 400 cm^{-1}.
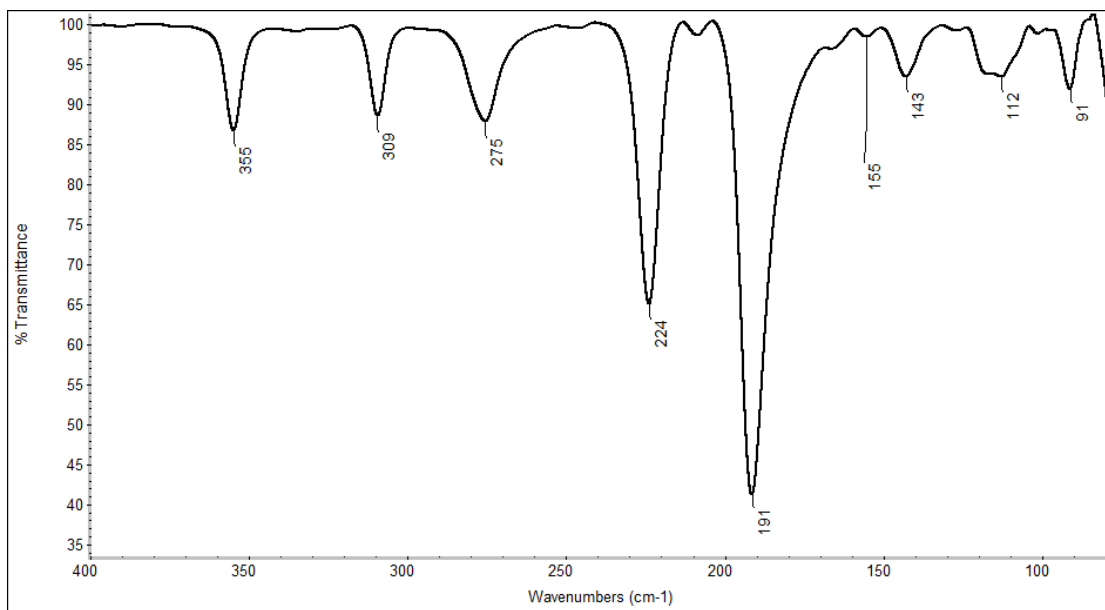
Figure 5.12 Far-IR spectrum of **4** from 80 to 400 cm^{-1}.
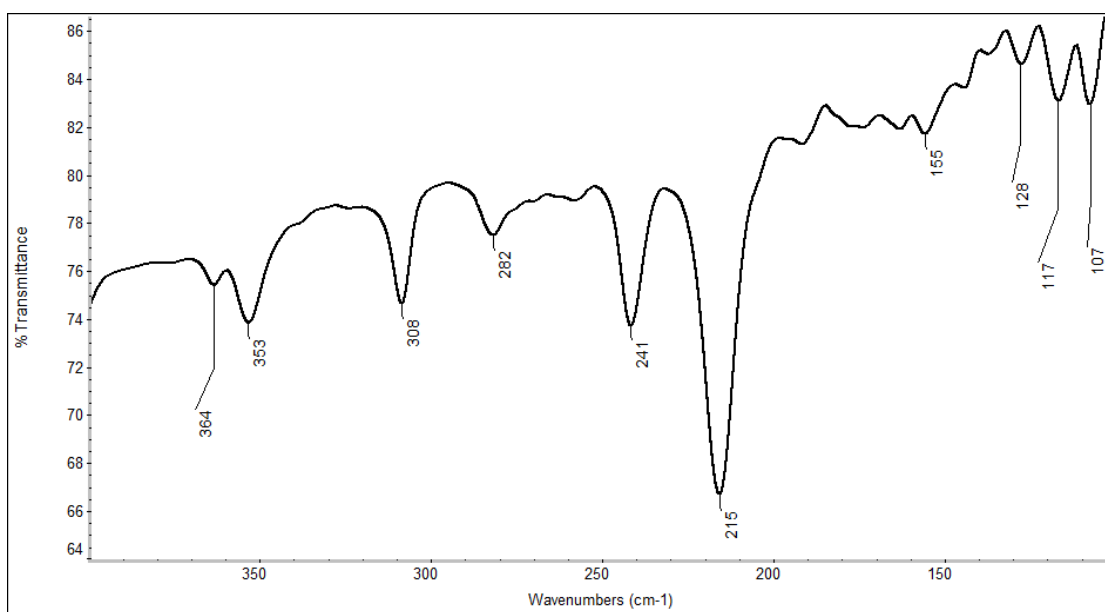
Figure 5.13 Far-IR spectrum of **5** from 80 to 400 cm^{-1}.
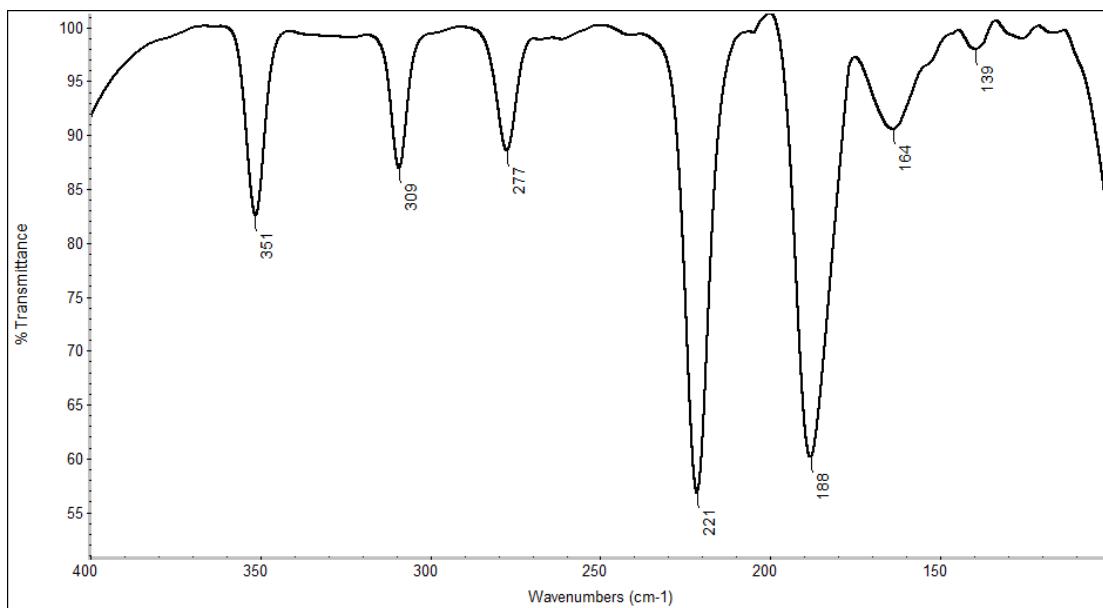
Figure 5.13 Far-IR spectrum of **6** from 80 to 400 cm^{-1}.

5.1.5 Computational analysis
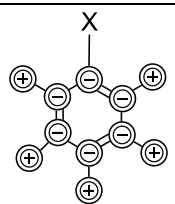
All calculations were performed with the Gaussian 09 (G09) program package[6] employing the density functional theory (DFT) method with Becke's three parameter hybrid functional[7] and Lee-Yang-Parr's gradient-corrected correlation functional (B3LYP).[8] For iodine and bromine atoms the Los Alamos double-ζ (LanL2Dz)[9] basis set and effective core potential, augmented with polarization functions of d symmetry and diffuse functions of p symmetry,[10] were used. The 6-31+G(d,p) basis set was applied for all other atoms. The ground-state geometries of the supramolecular complexes were optimized in the gas phase. This approximation does not take into account some weak interactions of the solid state, which would require a periodic plane-wave computational approach, but the results appear to be in good agreement with the experimental data, probably because in these class of cocrystals the nitrogen-halogen interactions observed within the crystal lattices are very similar in the gas and in the solid state phases. The nature of all stationary points was confirmed by performing a normal-mode analysis, which finally gave the wave numbers of carbon-halogen stretching and bending modes.

For comparison purposes, in Table 5.2 calculations with the set base LanL2DZ (as implemented in Gaussian 09) are also reported.

106

Significant improvements are obtained adopting diffuse and polarization functions, *i.e.* passing from the B3LYP/LanL2DZ to the B3LYP/6-31+G(d,p)-LanL2DZdp basis set. As we focused on the vibrational analysis, counterpoise[11] correction has not been considered. On the other hand, the frequencies of the adduct **2**, computed for the single (1:1) or for the double (2:2) adducts are nearly equivalent in positions and intensities.

Table 5.2 Selected experimental and calculated IR normal modes of vibrations (cm^{-1}) involving halogen bond. The calculated IR vibrations are shown together with their IR intensity and Raman intensity.

	Out of Plane C-X Bending		In plane C-X bending			In plane C-X stretching					
	Calc.a	**Calc.b**	**Exp.**	**Calc.a**	**Calc.b**	**Exp.**	**Calc.a**	**Calc.b**	**Exp.**	**Calc.a**	**Calc.b**
IPFB	80 0.1217 0.0164	80 0.0191 0.0597	132	132 0.2467 2.3042	132 0.2850 0.8032	204	203 1.1451 2.8932	204 0.9615 2.8986	214	205 3.8759 1.1434	212 3.2444 0.1841
BrPFB	88 0.0569 0.0021	90 0.0038 0.0211	155	152 0.0723 2.0896	155 0.1302 0.8445	242	237 0.7576 2.8079	243 0.4251 2.1457	*	205 4.4098 0.5846	212 3.7118 0.1269
1	109 1.7179 2.3910	103 0.4927 0.9563	141	151 0.5846 1.0594	149 0.3099 0.4550	193	185 21.8538 32.4097	192 16.2261 30.3179	216.5	208 3.3296 1.8172	215 3.1765 0.6853
2	110 1.6271 1.9420	104 0.4816 0.8968	146	149 0.5900 1.1592	147 0.3080 0.5127	188	184 23.8546 34.7700	191 17.7118 32.9400	219	208 3.0826 1.7269	215 3.5131 0.8192
2c)	-	104 0.4343 0.9430 106 0.4426 0.9002	146	-	147 0.3962 0.5924 148 0.3258 0.4407	188	-	190 17.1949 29.2215 191 17.9952 32.5548	219	-	215 3.0070 0.5769 216 4.5085 0.9734
3	102 0.7985 0.5821	98 0.1692 0.1725	143	150 0.5300 1.4967	148 0.2922 0.6817	192	184 24.5695 36.5004	191 18.2823 34.5285	216	207 3.4257 0.8829	213 2.7401 0.0922
4	109 1.5691 1.2573	104 0.4436 0.5974	143	147 0.4144 1.1048	146 0.2307 0.4621	191	183 25.9622 37.1966	190 19.2274 35.6561	223.5	208 3.7960 2.0601	215 3.2827 0.7730
6	84 0.9968 0d	83 10.4422 0d	*	137 1.0439 0d	139 0.4451 0d	188	183 24.0720 0d	189 36.8477 0d	221	208 7.2474 0d	215 6.4791 0d
5	107 0.8515 1.2606	106 0.2070 0.4811	155	167 0.2200	168 0.1180 0.6153	241	224 17.8165 53.5201	236 9.4157 29.0803	*	208 4.0193 1.1202	214 3.6991 0.4773

* too low intensity to be detected **a** B3LYP/LanL2DZ; **b** B3LYP/6-31+G(d,p)-LanL2DZdp; **c** This is the **2** adduct 2:2 computed with four molecules (two XB interactions). **d** Raman intensities are zero because symmetry.

5.2 XB characterization *via* natural abundance ^{15}N and ^{13}C solid-state NMR spectroscopies

5.2.1 Supramolecular synthesis

All the starting materials were purchased from Sigma-Aldrich and were used without further purification. At room temperature, equimolar amount of 4,4'-bipyridine (**1A**) or 1,2-bis(4-pyridyl)ethane (**1B**) were dissolved in acetone with 1,8-diiodohexadecafluorooctane, 1,6-diiodododecafluorohexane or 1,4-diiodotetrafluorobenzene. At room temperature, equimolar amounts of either **1A** or **1B** were also dissolved in chloroform with 1,4-dibromotetrafluorobenzene and in dichloromethane with 1,4-diiodobenzene. All the solutions were put in vials and then placed in jars containing paraffin oil and sealed. All of adducts were obtained in the form of good-quality single crystals by slow-evaporation of the solvent. The crystalline products were all washed with cold heptane before further characterization.

5.2.2 Single crystal XRD analysis

The crystals were measured using Mo-Kα radiation (λ= 0.71073 Å) on a Bruker KAPPA APEX II diffractometer with a Bruker KRYOFLEX low temperature device. Formation of cocrystals **2A**, **3A**, **4A**, **5A**, **6A**, **2B**, **4B**, **5B** and **6B** was confirmed by crystal unit cell determination and comparison with previously reported data.[12-18] Crystal structures of the new adducts **3B**, **5B**, and **6B** were solved by direct method and refined against F[2] using SHELXL97.[3] Packing diagrams were generated using Mercury.[4] Intermolecular interactions were analyzed with PLATON.[5] The non-hydrogen atoms were refined anisotropically and hydrogen atoms were positioned geometrically.

Table 5.3 Selected crystallographic and refinement parameters for cocrystals **3B**, **5B** and **6B**.

	3B	5B	6B
Formula	$(C_6H_4I_2)$ $(C_{12}H_{12}N_2)$	$(C_8F_{12}I_2)$ $(C_{12}H_{12}N_2)$	$(C_6F_{12}I_2)$ $(C_{12}H_{12}N_2)$
Formula weight	257.08	419.06	369.05
Temperature (K)	100 (2)	95(2)	100(2)
Space group	$P\,2_1/n$	P-1	P-1
a (Å)	10.7004(5)	5.2033(15)	5.2203(9)
b (Å)	7.4871(4)	9.569(3)	9.7180(16)
c (Å)	11.1161(5)	13.330(4)	11.343(2)
α (°)	90	105.82(15)	97.553(7)
β (°)	100.572(2)	98.156(11)	100.607(16)
γ (°)	90	102.144(10)	101.351(7)
Volume (Å^3)	875.45(8)	610.1(3)	546.10(16)
Z	4	2	2
Density (gcm^{-3})	1.950	2.281	2.244
μ (mm^{-1})	3.590	2.714	2.991
F (000)	488	396	348
No. of refl. measured	8100	4084	5076
No. unique refl.	1546	2052	1935
No of parameters	100	200	178
$R_{\_all}$, $R_{\_obs}$	0.0145, 0.0124	0.0204, 0.0191	0.0140, 0.0130
wR_{2_all}, wR_{2_obs}	0.0339, 0.0323	0.0444, 0.0438	0.0299, 0.0294
$\Delta\rho_{max,\ min}$ (eÅ^{-3})	0.224, -0.436	1.226, -0.672	0.357, -0.298
G.o.F	1.099	1.046	1.050

5.2.3 Powder XRD analysis

A Bruker AXS D8 powder diffractometer was used for all PXRD measurements with experimental parameters as follows: Cu-Ka radiation Cu-Kα = 1.5406 Å; scanning interval : 5–40 2θ. The experimental PXRD patterns and calculated PXRD patterns from single crystal structures were compared to confirm the composition of bulk materials.
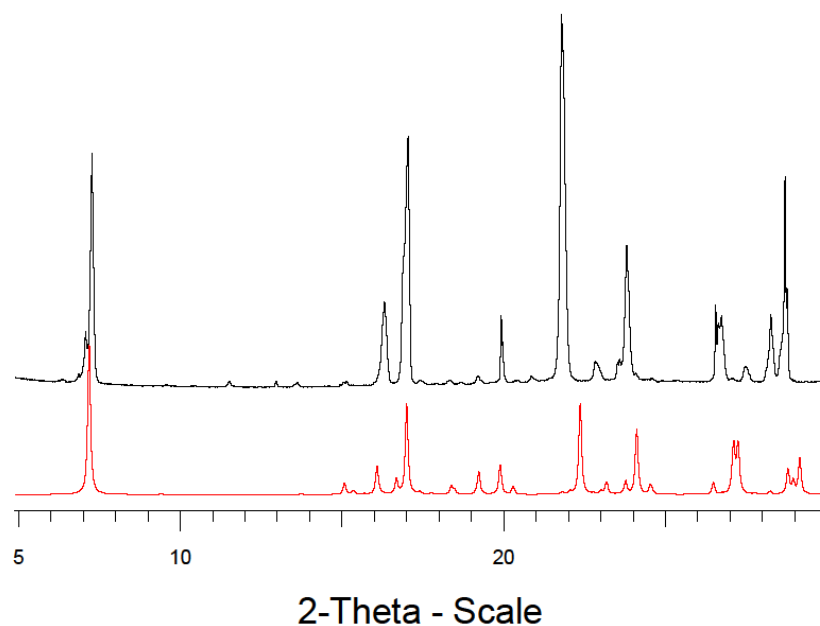
Figure 5.14 Comparison between calculated (red) and experimental (black) powder X-ray diffraction patterns of cocrystal **2A**.
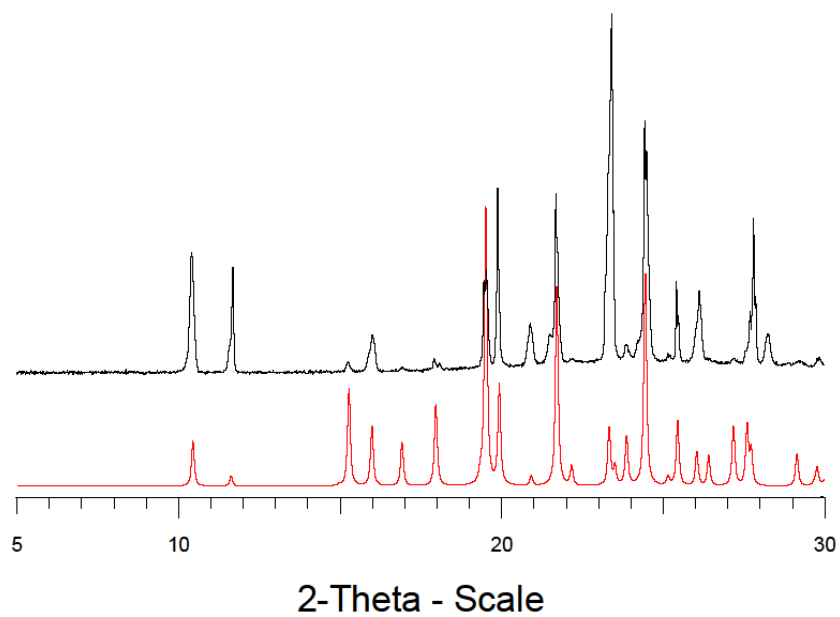
Figure 5.15. Comparison between calculated (red) and experimental (black) powder X-ray iffraction patterns of cocrystal **3A**.
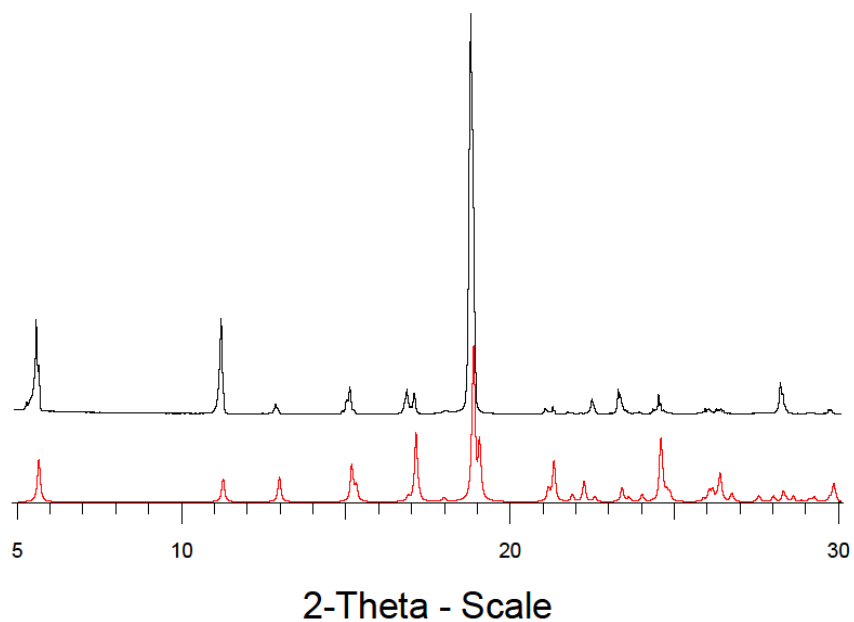
Figure 5.16 Comparison between calculated (red) and experimental (black) powder X-ray diffraction patterns of cocrystal **5A**.
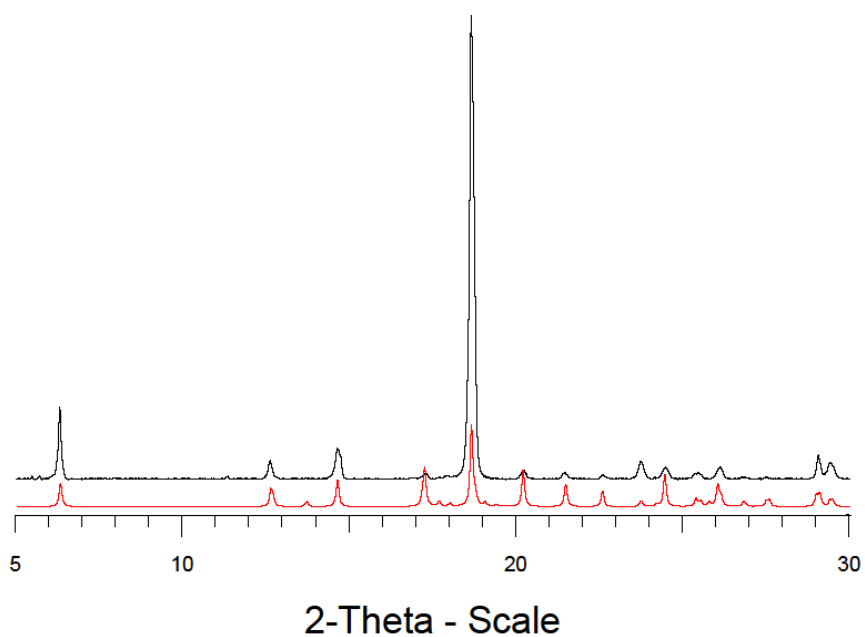
Figure 5.17 Comparison between calculated (red) and experimental (black) powder X-ray diffraction patterns of cocrystal **6A**.
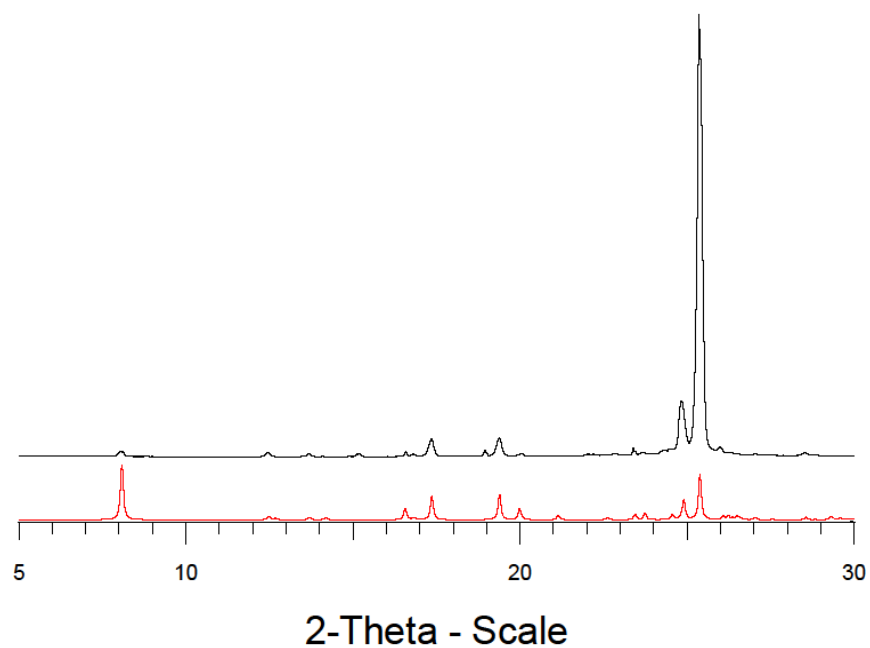
Figure 5.18 Comparison between calculated (red) and experimental (black) powder X-ray diffraction patterns of cocrystal **2B**.
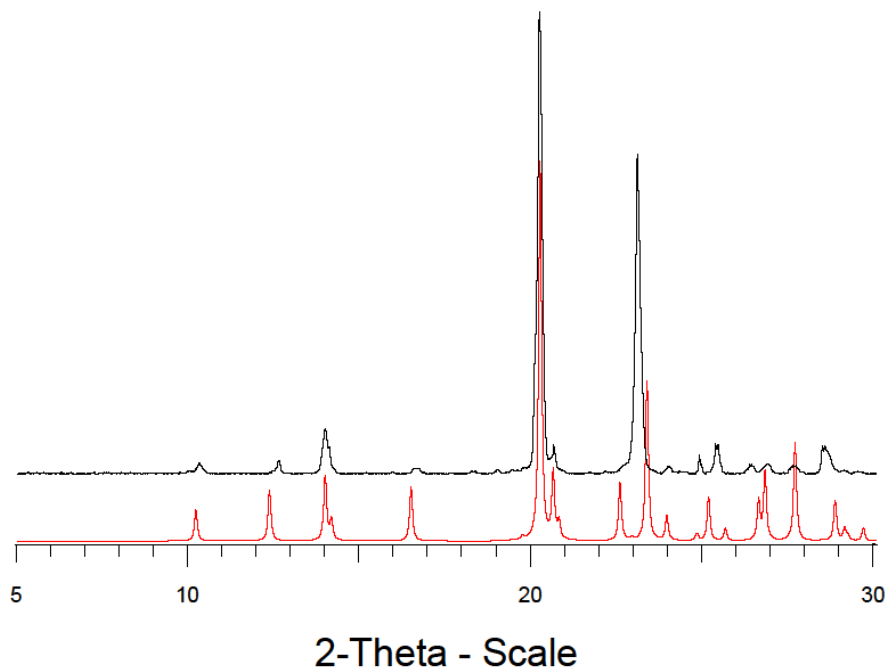
Figure 5.19 Comparison between calculated (red) and experimental (black) powder X-ray diffraction patterns of cocrystal **3B**.
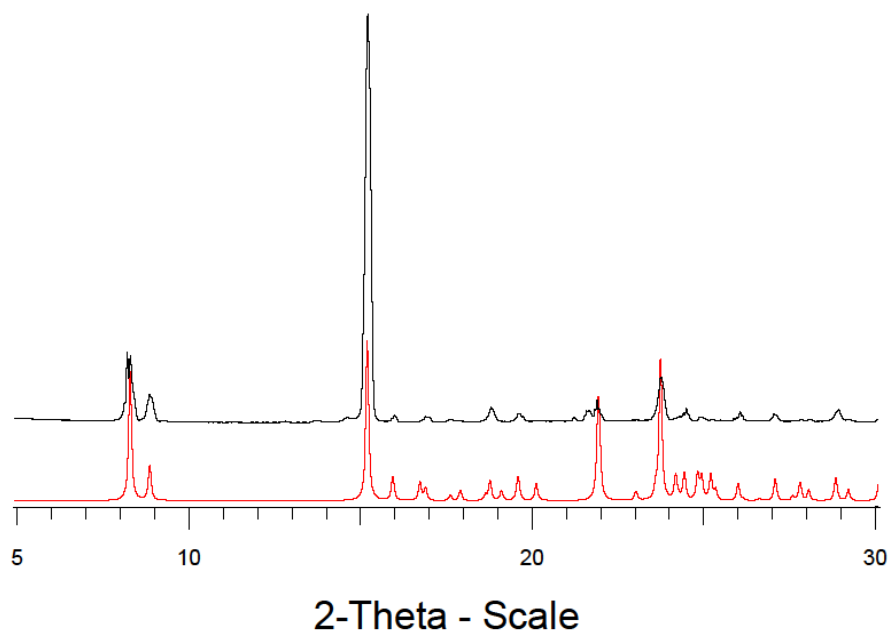
Figure 5.20 Comparison between calculated (red) and experimental (black) powder X-ray diffraction patterns of cocrystal **4B**.

113
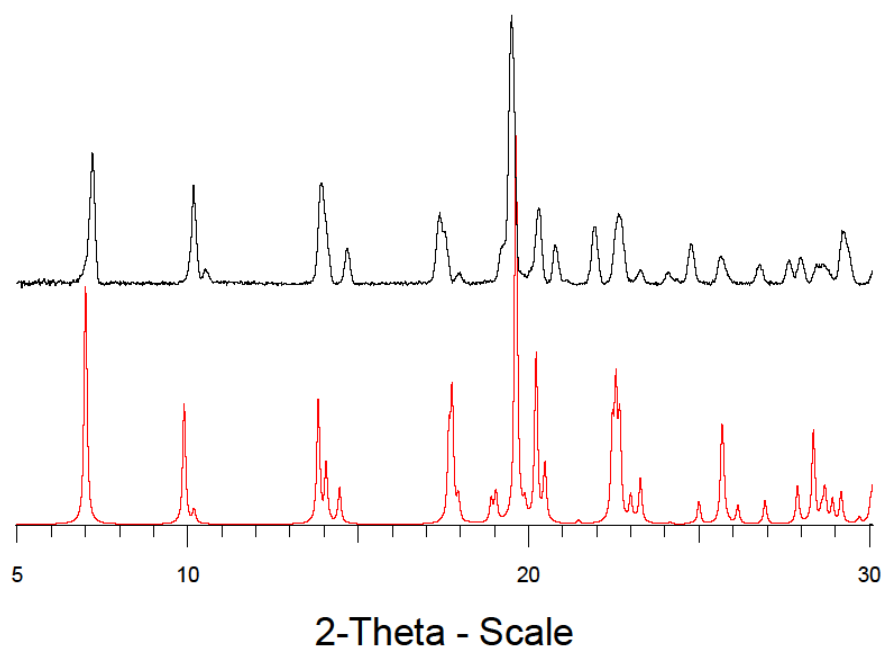
Figure 5.21 Comparison between calculated (red) and experimental (black) powder X-ray diffraction patterns of cocrystal **5B**.
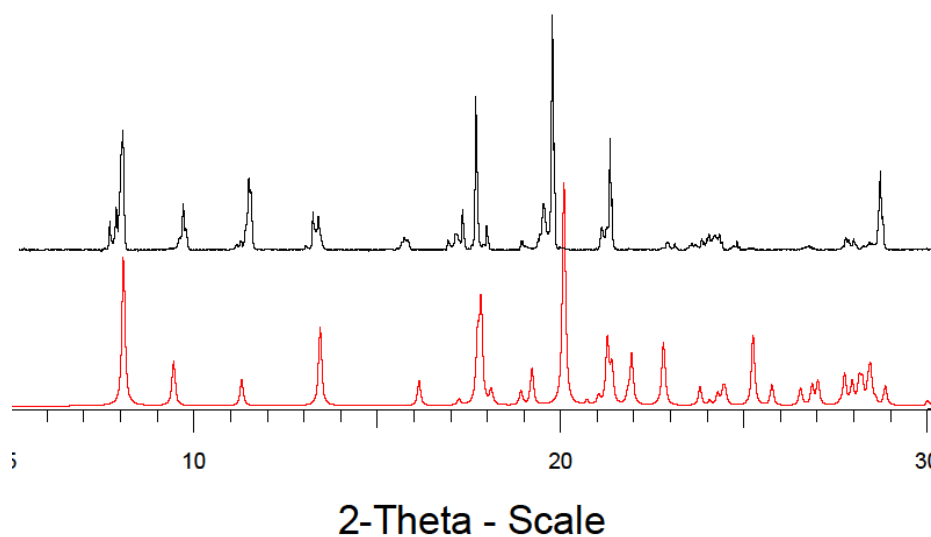
Figure 5.22 Comparison between calculated (red) and experimental (black) powder X-ray diffraction patterns of cocrystal **6B**.

5.2.4 Thermal and Infrared spectroscopy analyses

DSC analyses were performed by using a Mettler Toledo DSC 823e. The samples (2-20 mg of each) were closed in an aluminum pan and measured with heating/cooling rates of 10°C min $^{-1}$.

IR spectra were obtained using a Nicolet iS50 FTIR spectrometer equipment with ATR device. For each compound two different spectra were collected: far IR spectrum (128 scans, 100–1000 cm^{-1}) using solid substrate beam splitter; middle IR (32 scans, 1000–4000 cm^{-1}) with KBr beam splitter. All the spectra were measured with a resolution of 4 cm $^{-1}$ and corrected with the baseline correction tool of the OMNIC® software.

Cocrystal 2A. exp m.p. 109°C (lit. 110/115°C) FT-IR main bands (cm^{-1}): 357, 441, 470, 608, 728, 791, 804, 849, 989, 1059, 1214, 1372, 1400, 1463, 1532, 1586, 3032.

Cocrystal 3A. exp m.p. 148°C FT-IR main bands (cm^{-1}): 217, 269, 443, 587, 607, 732, 785, 798, 951, 988, 1061, 1404, 1475, 1533, 1586, 3085.

Cocrystal 4A. exp m.p. 172°C (lit. 176°C) FT-IR main bands (cm^{-1}): 233, 312, 449, 575, 613, 728, 758, 800, 935, 993, 1059, 1219, 1405, 1454, 1535, 1592, 3029.

Cocrystal 5A. exp m.p. 148°C (lit. 152°C) FT-IR main bands (cm^{-1}): 121, 165, 206, 265, 278, 546, 598, 805, 994, 1055, 1217, 1592.

Cocrystal 6A. exp m.p. 142°C (lit. 146°C) FT-IR main bands (cm^{-1}): 149, 273, 552, 591, 803, 930, 995, 1062, 1212, 1592, 3036.

Cocrystal 2B. exp m.p. 103°C FT-IR main bands (cm^{-1}) : 290, 359, 472, 521, 543, 808, 824, 994, 1068, 1215, 1375, 1412, 1466, 1559, 1595, 3028.

Cocrystal 3B. exp m.p. 142°C FT-IR main bands (cm^{-1}): 215, 268, 520, 545, 785, 822, 953, 993, 1070, 1219, 1412, 1475, 1560, 1600, 3027.

Cocrystal 4B. exp m.p. 197°C (lit. 199°C) FT-IR main bands (cm^{-1}): 217, 230, 298, 312, 421, 525, 541, 568, 749, 819, 868, 1001, 1069, 1218, 1452, 1562, 1601, 3037.

Cocrystal 5B. exp m.p. 121°C FT-IR main bands (cm^{-1}): 132, 166, 207, 271, 541, 822, 1002, 1217, 1601, 3043.

Cocrystal 6B. exp m.p. 93°C FT-IR main bands (cm^{-1}): 150, 199, 209, 275, 541, 591, 822, 933, 1002, 1207, 1602, 3034.

5.2.5 Computational analysis

Periodic lattice calculations were performed by means of Quantum Espresso version 5.1.2.[19] The Generalized Gradient Approximation (GGA) functional PW86PBE,[20,21] with the inclusion of the exchange-hole dipole moment (XDM)[22,23] dispersion correction method for accurate model of the X-bonded interactions was used in all calculations. XDM dispersion energies were computed using the modified version of Quantum Espresso, adopting the appropriate damping parameters for the functional PW86PBE (a_1 = 0.6836 and a_2 = 1.5045).[22] For geometry optimizations, the solid-state crystal structures from either the literature or the present study (*i.e.*, **3B**, **5B,** and **6B**) were considered as starting structures. Calculations were performed with the variable-cell scheme, adopting the Kresse-Joubert Projected Augmented Wave pseudopotentials.[24] A cut-off of 60 Ry was used for structural optimization. The NMR chemical shifts were calculated using an 80 Ry energy cut-off by the GIPAW method.[25] A 60 Ry cut-off for NMR calculations gave unsatisfactory results, but values higher than 80 Ry did not significantly improved the quality of the data. The theoretical absolute magnetic shielding (σ) values were converted into chemical shift scale (δ) by subtracting the shielding values from the experimental absolute shielding value of liquid ammonia at 300 K, 244.6 ppm, given in literature.[26] Additional chemical shift calculation details may be found in Table 5.4. The Brillouin zones were automatically sampled with the Monkhorst-Pack scheme,[27] in a similar approach as previously described.[28] Geometry optimization, phonon and NMR chemical shift calculations for compounds **2A**, **3A**, **4A**, **5A**, **6A**, **2B**, **3B**, **4B**, **5B**, **6B** were performed with a grid mesh of 2×1×1, 2×2×2, 2×2×1, 3×2×1, 2×1×2, 1×2×1, 3×1×1, 3×1×1, and 3×1×1, respectively. For compounds **1A**, and **1B** grid meshes of 2×2×1 and 3×1×2 were respectively used.

Table 5.4 Computed nitrogen magnetic shielding tensors.[a]

Compound	σ_{11}	σ_{22}	σ_{33}	σ_T
1A	-384	-179	275	-96
2A	-386	-183	271	-99
	-385	-182	273	-98
3A	-383	-175	262	-99
4A	-357	-174	255	-92
5A	-324	-164	248	-80
6A	-328	-163	249	-81
1B	-401	-181	285	-99
2B	-353	-171	268	-85
3B	-348	-171	266	-84
4B	-324	-162	247	-80
5B	-289	-156	245	-67
6B	-290	-156	238	-69

[a] Theoretical magnetic shielding tensors were converted to chemical shift tensors with the formula used by Solum et al.[29], that is, $\delta_{ii} = (\sigma_{ref} - \sigma_{ii})$, where σ_{ref} is the experimental absolute shielding of liquid ammonia at 300 K, 244.6 ppm[26], σ_{ii} is the computed tensor component, and δ_{ii} is the chemical shift tensor component.
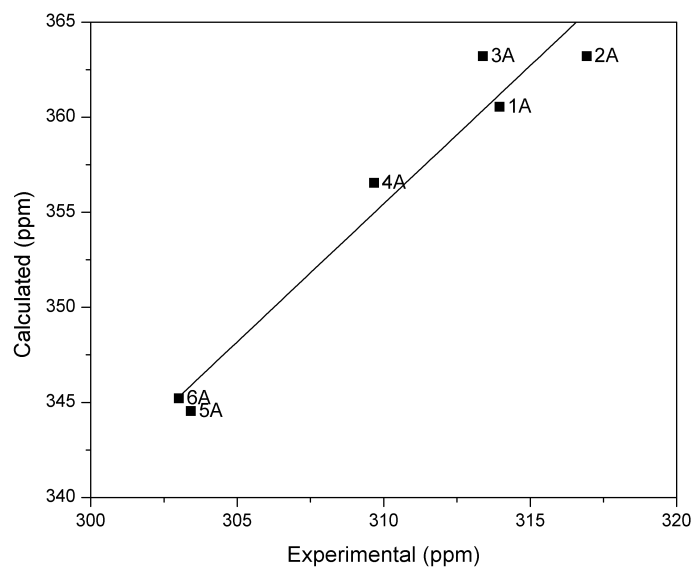
Figure 5.23 Relationship between calculated and experimental ^{15}N chemical shift values for the bipy series. The solid line represent the best fit, δ_{ave} ^{15}N = $1.5\delta_{iso}$ $^{15}N - 94.9$; $R^2 = 0.939$
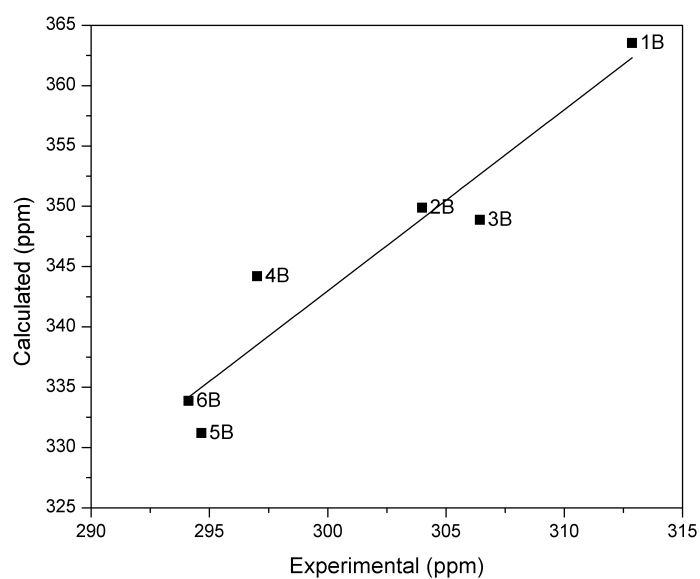
Figure 5.24 Relationship between calculated and experimental ^{15}N chemical shift values for the bipyet series. The solid line represent the best fit, δ_{ave} ^{15}N = $1.5\delta_{iso}$ $^{15}N - 107.4$; $R^2 = 0.887$.

5.2.6 Solid-state NMR analysis

SSNMR measurements were carried out on a Bruker AVANCE II 400 instrument operating at 400.23, 376.55, 100.65 and 40.56 MHz for ^{1}H, ^{19}F, ^{13}C and ^{15}N, respectively. Powdered samples were packed in cylindrical 4 mm zirconia rotors, with sample volume of 80 μL.

^{15}N CPMAS (cross-polarization magic-angle spinning) spectra were recorded at room temperature at the spinning speed of 9 kHz. A ramp cross-polarization pulse sequence[30] was used with contact time of 4 ms, a ^{1}H 90° pulse of 3.80 μs, recycle delays ranging from 5 to 60 s, and 2048–10240 transients. The two pulse phase modulation (TPPM) decoupling scheme[31] was used with a frequency field of 66 kHz. All spectra were acquired with a resolution of 0.5 ppm.

^{13}C non-quaternary suppression (NQS) spectra were collected at room temperature at spinning speed of 12 or 13 kHz, with ^{13}C 180° refocusing pulse of 9.20 μs and dephasing times ranging from 40 to 55 μs. The pulse width and the RF power were finely adjusted for best resolution. ^{1}H/^{13}C ramp cross-polarization pulse sequence was used with contact time of 9 ms, a ^{1}H 90° pulse of 4.00 μs, recycle delays ranging from 5 to 60 s, and 1440–7680 transients. ^{19}F/^{13}C ramp cross-polarization pulse sequence was employed with contact time of 9 ms, a ^{19}F 90° pulse of 3.40 μs, recycle delays ranging from 20 to 60 s, and 256–2304 transients. The ^{19}F/^{13}C Hartmann-Hahn conditions were calibrated on a poly(tetrafluoroethylene) sample. For all samples containing protons a two-pulse phase modulation (TPPM) decoupling scheme was used with frequency field of 62 kHz, while in the case of samples containing fluorine atoms a swept-frequency two-pulse phase modulation (SWf-TPPM) decoupling scheme[32] was used, with frequency field of 74 kHz. ^{13}C and ^{15}N chemical shift scales were referenced to glycine (^{13}C methylene signal at 43.5 ppm) and to $(NH_4)_2SO_4$ (^{15}N ammonium signal at δ = 24.7 ppm with respect to NH_3), respectively as external standards. All NMR data were processed with Bruker TOPSPIN 2.1 software.
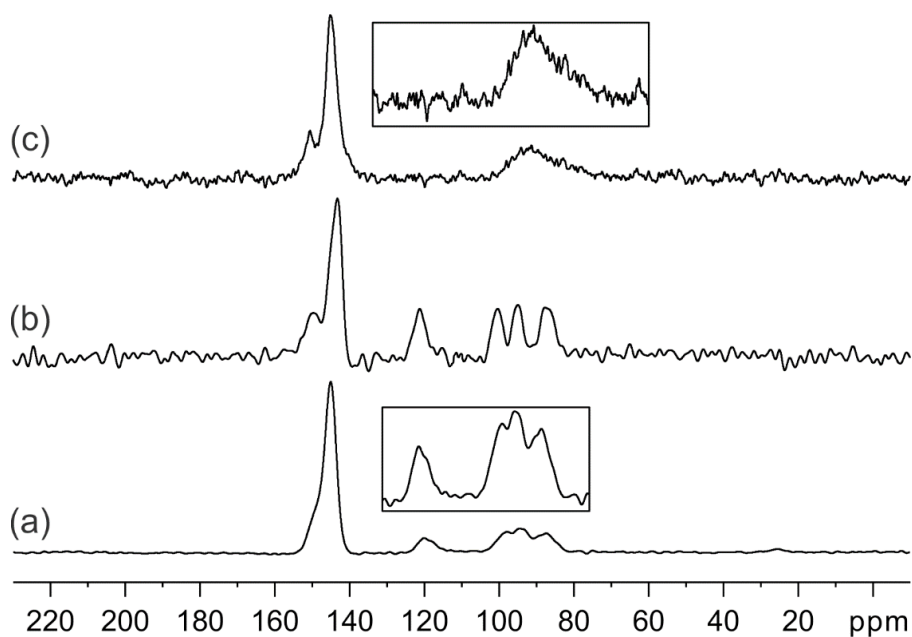
Figure 5.25 Experimental $^{19}F/^{13}C$ NQS spectra for the series of halogen bonded compounds in which the donor is DBrTFB: **2A** (b), and **2B** (c). The DBrTFB spectrum is shown in (a). A detailed account for the C–Br characteristic asymmetric quartet due has been reported elsewhere.[33,34] Insets show vertical expansions. All spectra were acquired at B_0 = 9.4 T and T = room temperature.
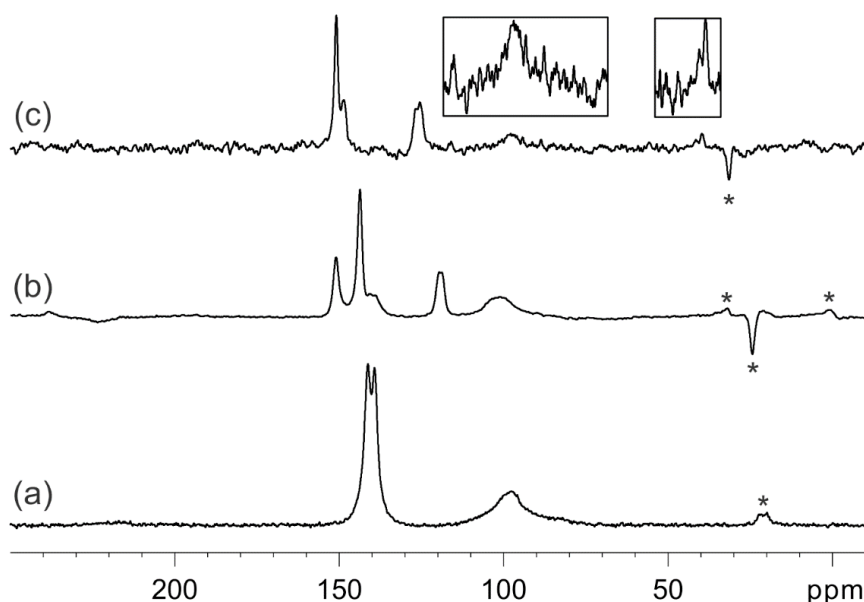
Figure 5.26 Experimental $^{1}H/^{13}C$ NQS spectra for the series of halogen bonded compounds in which the donor is DIB: **3A** (b), and **3B** (c). The spectrum of pure DIB is shown in (a). Insets show vertical expansions, while the asterisks denote minor peaks due to MAS spinning sidebands (12 kHz). All spectra were acquired at B_0 = 9.4 T and T = room temperature.
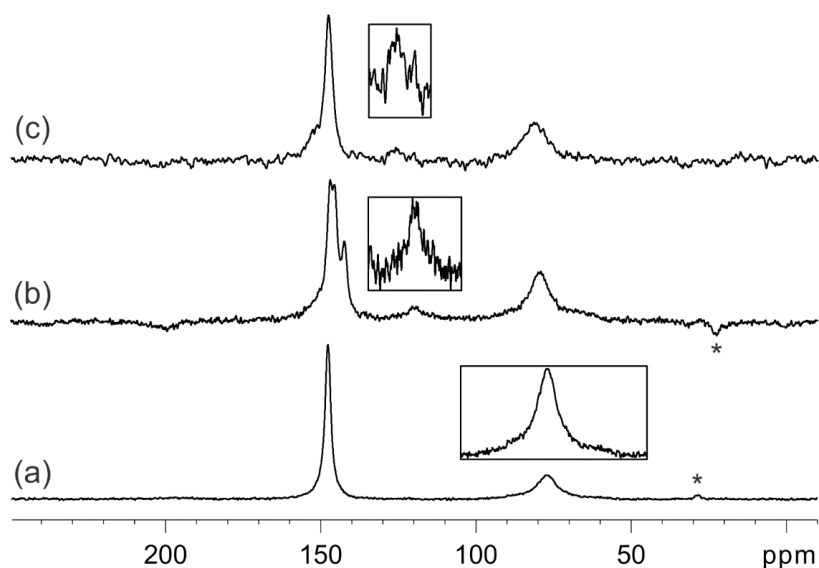
Figure 5.27 Experimental $^{19}F/^{13}C$ NQS spectra for the series of halogen bonded compounds in which the donor is DITFB: **4A** (b), and **4B** (c). The spectrum of pure DITFB is shown in (a). Insets show vertical expansions, while the asterisks denote minor peaks due to MAS spinning sidebands (12 kHz). All spectra were acquired at B_0 = 9.4 T and T = room temperature.
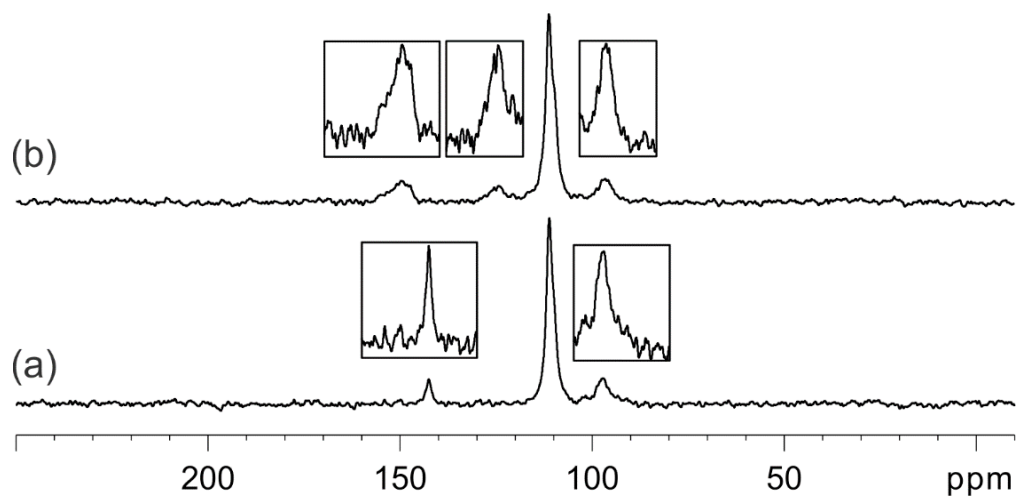
Figure 5.28 Experimental $^{19}F/^{13}C$ NQS spectra for the series of halogen bonded compounds in which the donor is DIHFO: **5A** (a), and **5B** (b). The spectrum of pure DIHFO could not be collected due to solid-liquid transition of the powder inside the magnet. Insets show vertical expansions. Both spectra were acquired at B_0 = 9.4 T and T = room temperature.
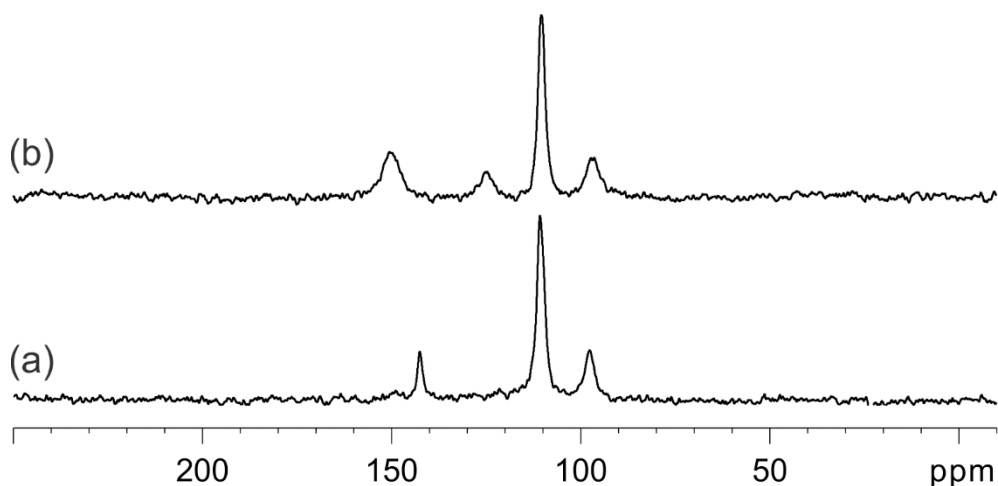
Figure 5.29 Experimental $^{19}F/^{13}C$ NQS spectra for the series of halogen bonded compounds in which the donor is DIDFH: **6A** (a), and **6B** (b). The spectrum of pure DIDFH could not be collected due to solid-liquid transition of the powder inside the magnet. Both spectra were acquired at $B_0 = 9.4$ T and T = room temperature.

^{13}C assigments:

Figure 5.25

^{13}C NMR (100.65 MHz): (a) δ 145.0 (C–F), 120.0 – 87.3 (C–Br); (b) δ 149.6 (C–H, ortho), 143.2 (C–F), 121.2 – 87.0 (C–Br); (c) δ 150.6 (C$_q$), 145.1 (C–F), 91.6 (C–Br).

Figure 5.26

^{13}C NMR (100.65 MHz): (a) δ 141.3 (C–H), 139.3 (C–H), 98.2 (C–I); (b) δ 150.9 (C–H, ortho), 143.7 (C$_q$), 140.8 (C–H, DIB), 139.1 (C–H, DIB), 119.7 (C–H, meta), 118.7 (C–H, meta), 101.7 (C–I); (c) δ 150.9 (C$_q$), 148.6 (C–H), 125.4 (C–H), 97.9 (C–I), 41.5 (CH$_2$).

Figure 5.27

^{13}C NMR (100.65 MHz): (a) δ 147.7 (C–F), 77.0 (C–I); (b) δ 147.0 (C–F), 145.7 (C–F), 142.6 (C$_q$), 120.0 (C–H, meta), 79.6 (C–I); (c) δ 147.7 (C–F), 126.0 (C–H, meta), 81.2 (C–I).

Figure 5.28

^{13}C NMR (100.65 MHz): (a) δ 142.6 (C$_q$), 111.2 (C̲–F), 97.1 (C̲–I); (b) δ 149.5 (C$_q$), 124.2 (C̲–H, meta), 111.2 (C̲–F), 96.7 (C̲–I).

Figure 5.29

^{13}C NMR (100.65 MHz): (a) δ 142.6 (C$_q$), 110.8 (C̲–F), 97.6 (C̲–I); (b) δ 150.2 (C$_q$), 124.9 (C̲–H, meta), 110.4 (C̲–F), 96.8 (C̲–I).

5.3 A new class of amphidynamic crystals based on XB

5.3.1 Cocrystallization and single crystal XRD analysis

The co-crystals were synthesized by directly mixing the iodobenzene derivatives and DABCO in a 2:1 molar ratio, except **r3** with 1:1 molar ratio, in acetone at room temperature. The obtained solutions were put into open vials and left slow evaporating in a closed jar containing mineral oil. For all the products colorless prismatic crystals were obtained. The crystals were measured using Mo-Kα radiation (λ= 0.71073 Å) on a Bruker KAPPA APEX II diffractometer with a Bruker KRYOFLEX low temperature device. The crystal structures were solved by direct method and refined against F^2 using SHELXL97.[3] Packing diagrams were generated using Mercury 3.5.1.[4] The non-hydrogen atoms were refined anisotropically and hydrogen atoms were refined using difference Fourier map or positioned geometrically. The phase transition was measured cooling and heating the systems and measuring the temperature at which changes occur to the diffraction pattern.

Table 5.5 XB features within the cocrystals at room temperature and at 103 K.

	I•••N distance (Å)		C-I•••N angle (°)	
	Room Temperature	103 K	Room Temperature	103 K
2e	2.737 (1)	2.713 (1) 2.682 (1) 2.681 (1) 2.701 (1)	177.05 (6) and 176.32 (6)[a]	177.04 (5) 178.64 (5) 177.96 (5) 177.19 (5)
2a	3.014 (3)	2.971 (4) 2.955 (4)	177.55 (1)	176.32 (2) 175.51 (2)
2b	2.960 (4) 2.781 (3)	2.857 (2) 2.732 (2)	173.86 (1) 178.79 (1)	173.86 (8) 179.12 (8)
2c	2.876 (2) 3.348 (4)[b]	2.832 (1) 3.312 (2)[b]	176.07 (8)	175.19 (4)
2d	2.830 (1)	2.815 (6)	175.60 (1)	175.8 (2)

[a] The two angles refer to two disordered positions of the carbon bound to the iodine atom. [b] The distances refer to C-H•••N hydrogen bond. The reported

distances are between the C and N, because the position of hydrogens is calculated.

Table 5.6 Crystallographic details of **r5** data collections at 7 different temperatures.

Formula	2(C_6F_5I). $C_6H_{12}N_2$	2(C_6F_5I). $C_6H_{12}N_2$	2(C_6F_5I). $C_6H_{12}N_2$	2(C_6F_5I). $C_6H_{12}N_2$	2(C_6F_5I). $C_6H_{12}N_2$	2(C_6F_5I). $C_6H_{12}N_2$	2(C_6F_5I). $C_6H_{12}N_2$
Temp. (K)	297 (2)	250(2)	220(2)	200(2)	180(2)	140(2)	103(2)
System	monoclinic	monoclinic	monoclinic	monoclinic	monoclinic	monoclinic	monoclinic
Space group	$P2_1/c$	$P2_1/c$	Pc	Pc	Pc	Pc	Pc
a (Å)	8.1331(2)	8.1324(3)	8.0881(3)	8.0570(3)	8.0353(4)	7.9746(4))	7.9438(6)
b (Å)	10.6901(3)	10.6494(4)	21.1918(8)	21.1290(7)	21.0755(9))	20.9827(9)	20.923(2)
c (Å)	13.1218(3)	13.0939(5)	13.0834(5)	13.0753(5)	13.0840(6))	13.0699(6)	13.0731(12
α (°)	90.00	90.00	90.00	90.00	90.00	90.00	90.00
β (°)	99.9680(10	99.702(2)	99.594(2)	99.567(2)	99.573(2)	99.5560(10	99.508(6)
γ(°)	90.00	90.00	90.00	90.00	90.00	90.00	90.00
V (Å³)	1130.54(5)	1117.78(7)	2211.15(14	2194.93(14	2184.89(17	2156.62(17	2143.0(3)
Z	2	2	4	4	4	4	4
Collected I_o	25913	23669	108261	56823	40089	38298	110604
Unique I_o	3169	2552	16172	15325	11882	14790	22443
$I_o > 2\sigma(I_o)$	2373	1909	8903	11620	10328	13602	21073
R_{ave}	0.0257	0.0357	0.0421	0.0310	0.0276	0.0255	0.0255
Parameters	272	271	908	772	578	578	578
Restraints	333	321	1565	1037	2	2	2
R_1 [$I_o > 2\sigma(I_o)$]	0.0216	0.0216	0.0372	0.0328	0.0309	0.0259	0.0201
wR_2 (all)	0.0421	0.0421	0.0729	0.0621	0.0650	0.0454	0.0369
G.o.f.	1.036	1.007	0.996	1.016	1.020	1.007	1.019
$\Delta\rho_{min}$ eÅ^{-3}	-0.28	-0.29	-0.54	-0.55	-0.46	-0.41	-0.57
$\Delta\rho_{max}$ eÅ^{-3}	0.22	0.06	0.60	0.08	0.68	0.77	0.79

Table 5.7 Crystallographic details of **r2** data collections at 3 different temperatures.

Formula	2($C_6H_3F_2I$). $C_6H_{12}N_2$	2($C_6H_3F_2I$). $C_6H_{12}N_2$	2($C_6H_3F_2I$). $C_6H_{12}N_2$
Temperature (K)	297 (2)	253(2)	103(2)
System	monoclinic	monoclinic	monoclinic
Space group	$P2_1/n$	$P2_1/n$	$P2_1/n$
a (Å)	6.6497(8)	6.6438(8)	6.6183(10)
b (Å)	31.023(5)	30.796(4)	30.067(5)
c (Å)	10.1247(8)	10.1083(12	10.0093(16)
α (°)	90.00	90.00	90.00
β (°)	95.124(8)	93.656(9)	93.56(2)
γ(°)	90.00	90.00	90.00
V (Å³)	2080.3(5)	2064.0(4)	1987.9(5)

Z	4	4	4
Collected I_o	34482	36509	35159
Unique I_o	3715	5307	6102
$I_o > 2\sigma(I_o)$	2812	4458	5528
R_{ave}	0.0320	0.0267	0.0358
Parameters	236	235	235
Restraints	21	0	0
$R_1 [I_o>2\sigma(I_o)]$	0.0276	0.0301	0.0278
wR_2 (all)	0.0668	0.0776	0.0563
G.o.f.	1.014	1.049	1.187
$\Delta\rho_{min}$ e$Å^{-3}$	-0.53	-1.06	-0.54
$\Delta\rho_{max}$ e$Å^{-3}$	0.46	0.66	0.66

Table 5.8 Crystallographic details of **r3** data collections at 3 different temperatures.

Formula	$C_6H_3F_2I.$ $C_6H_{12}N_2$	$C_6H_3F_2I.$ $C_6H_{12}N_2$	$C_6H_3F_2I.$ $C_6H_{12}N_2$
Temperature (K)	296(2)	233(2)	103(2)
System	monoclinic	monoclinic	monoclinic
Space group	$P2_1/c$	$P2_1/c$	$P2_1/c$
a (Å)	10.7720(10)	10.7352(9)	10.7007(6)
b (Å)	9.7608(8)	9.6627(6)	9.4853(5)
c (Å)	13.4616(12)	13.3970(12)	13.2984(8)
α (°)	90.00	90.00	90.00
β (°)	99.003(6)	99.145(10)	99.438(4)
γ(°)	90.00	90.00	90.00
V (Å³)	1398.0(2)	1372.0(2)	1331.51(13)
Z	4	4	4
Collected I_o	20152	48399	54204
Unique I_o	3198	5229	9283
$I_o > 2\sigma(I_o)$	2270	319	7013
R_{ave}	0.0323	0.0347	0.0355
Parameters	209	163	163
Restraints	21	3	3
$R_1 [I_o>2\sigma(I_o)]$	0.0236	0.0340	0.0271
wR_2 (all)	0.0614	0.0870	0.0581
G.o.f.	1.009	0.992	1.006
$\Delta\rho_{min}$ e$Å^{-3}$	-0.41	-0.45	-0.88
$\Delta\rho_{max}$ e$Å^{-3}$	0.37	0.68	1.28

Table 5.9 Crystallographic details of **r1** data collections at 3 different temperatures.

Formula	2(C$_6$H$_4$FI). C$_6$H$_{12}$N$_2$	2(C$_6$H$_4$FI). C$_6$H$_{12}$N$_2$	2(C$_6$H$_3$F$_2$I). C$_6$H$_{12}$N$_2$
Temperature (K)	297 (2)	270(2)	103(2)
System	monoclinic	triclinic	triclinic
Space group	*C*2/*c*	*P-1*	*P-1*
a (Å)	8.547(2)	6.2187(9)	6.0623(10)
b (Å)	9.334(2)	12.6468(18)	12.477(2)
c (Å)	25.542(6)	13.345(2)	13.206(2)
α (°)	90.00	73.611(9)	74.566(15)
β (°)	94.81(2)	78.799(7)	78.334(9)
γ(°)	90.00	84.086(6)	83.940(10)
V (Å^3)	1998.7(8)	986.4(3)	941.6(3)
Z	4	2	2
Collected I_o	34118	*	51341
Unique I_o	2907	*	8540
$I_o > 2\sigma(I_o)$	2207	*	7423
R_{ave}	0.0830	*	0.0263
Parameters	136	*	217
Restraints	0	*	0
$R_1 [I_o > 2\sigma(I_o)]$	0.0398	*	0.0458
wR_2 (all)	0.1086	*	0.1512
G.o.f.	1.081	*	1.258
$\Delta\rho_{min}$ eÅ^{-3}	-0.982	*	-2.372
$\Delta\rho_{max}$ eÅ^{-3}	1.366	*	2.290

* Structure not refined due to bad quality crystals, high twinning.

Table 5.10 Crystallographic details of **r4** data collections at 2 different temperatures.

Formula	C$_6$H$_2$F$_3$I . C$_6$H$_{12}$N$_2$	C$_6$H$_2$F$_3$I . C$_6$H$_{12}$N$_2$
Temperature (K)	296(2)	100 (2)
System	monoclinic	monoclinic
Space group	*P*2$_1$/*c*	*P*2$_1$/*c*
a (Å)	6.6529(6)	6.5893(7)
b (Å)	20.388(2)	20.2195(19)
c (Å)	8.0414(8)	7.9262(8)
α (°)	90.00	90.00
β (°)	102.832(4)	102.405(5)
γ(°)	90.00	90.00
V (Å^3)	1063.49(18)	1031.37(18)
Z	2	2

Collected I_o	21644	38735
Unique I_o	5676	2893
$I_o > 2\sigma(I_o)$	3684	2773
R_{ave}	0.0262	0.0248
Parameters	155	190
Restraints	0	93
$R_1 [I_o > 2\sigma(I_o)]$	0.0265	0.0548
wR_2 (all)	0.0571	0.1336
G.o.f.	1.005	1.540
$\Delta\rho_{min}$ eÅ^{-3}	-0.845	-1.427
$\Delta\rho_{max}$ eÅ^{-3}	0.610	1.273
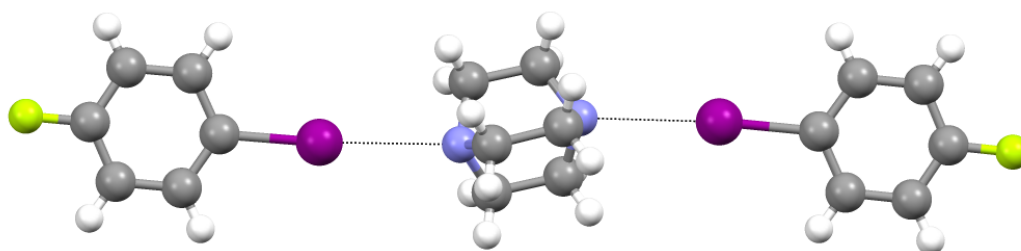
Figure 5.30 Halogen-bonded supramolecular trimers of **r1** crystal lattice at 103 K.
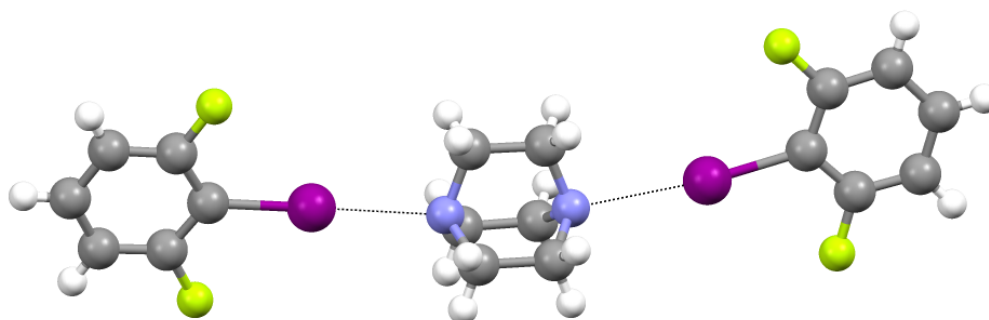
Figure 5.31 Halogen-bonded supramolecular trimers of **r2** crystal lattice at 103 K.
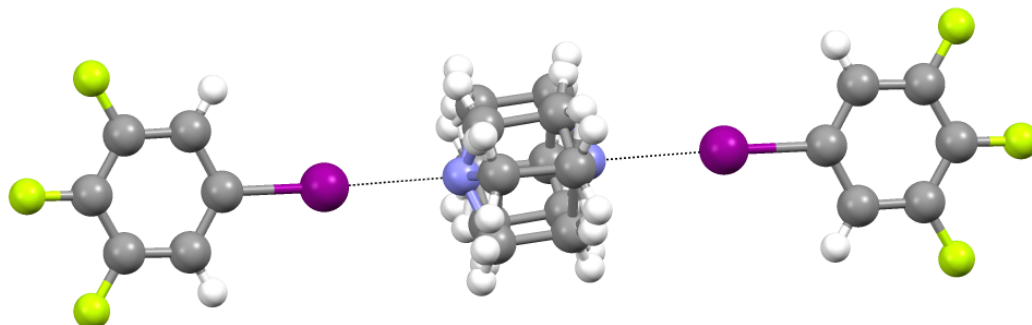
Figure 5.32 Halogen-bonded supramolecular trimers of **r4** crystal lattice at 100 K. As it is clear dabco molecules still display disorded positions at low temperature.

5.3.2 Powder XRD analysis

For all measurements we employed a Panalytical X'Pert PRO automated diffractometer. Analyses were carried out using Cu-Kα = 1.5406 Å radiation. Data were collected at room temperature in the range of 2Θ = 4-50° (step of 0.016°, step time 0.125 s).
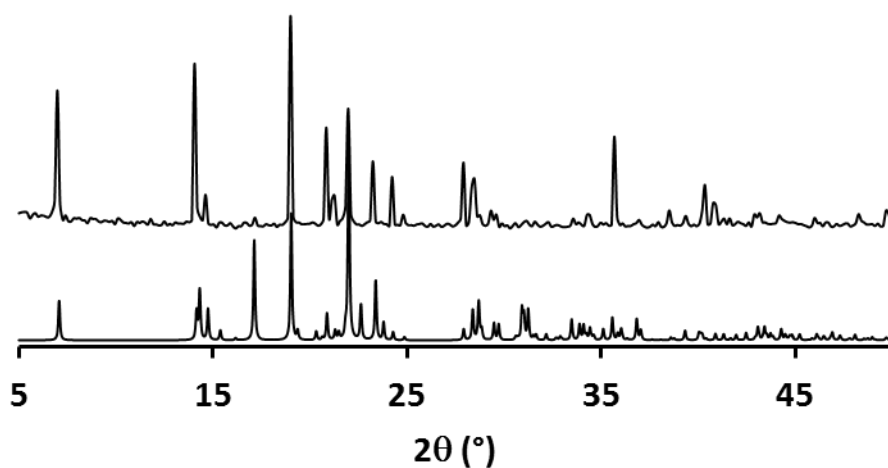
Figure 5.33 Comparison between calculated (bottom) and experimental (top) powder X-ray diffraction patterns of complex **r1**.
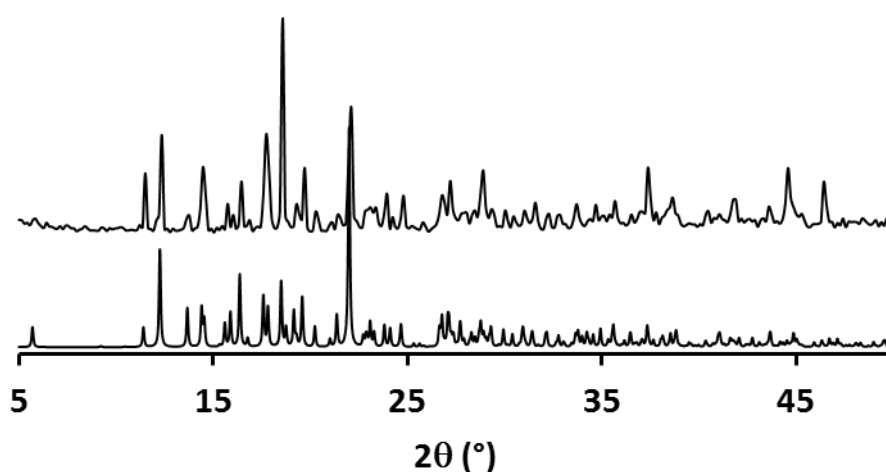
Figure 5.34 Comparison between calculated (bottom) and experimental (top) powder X-ray diffraction patterns of complex **r2**.
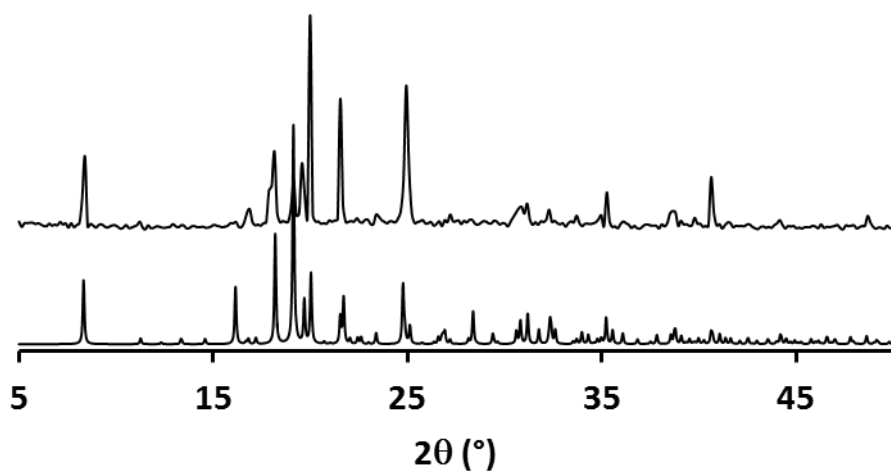
Figure 5.35 Comparison between calculated (bottom) and experimental (top) powder X-ray diffraction patterns of complex **r3.**
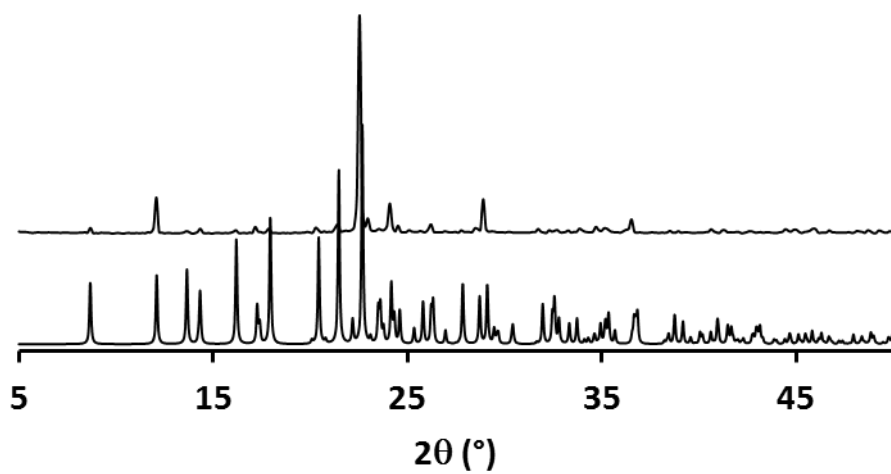
Figure 5.36 Comparison between calculated (bottom) and experimental (top) powder X-ray diffraction patterns of complex **r4**.
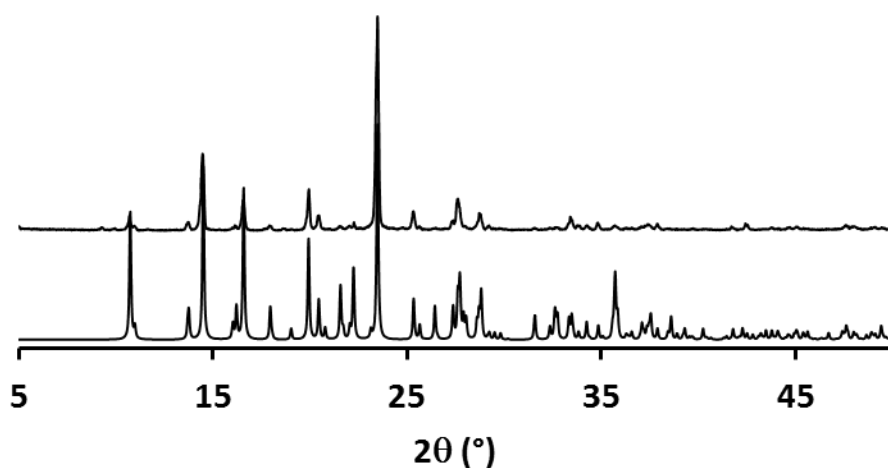
Figure 5.37 Comparison between calculated (bottom) and experimental (top) powder X-ray diffraction patterns of complex **r5**.

5.3.3 Thermal and Infrared spectroscopy analyses

Uncorrected melting points were recorded on a melting point apparatus using sealed glass capillaries.

IR spectra were obtained using a Nicolet iS50 FTIR spectrometer equipment with ATR device. Units are reported in cm^{-1}. For each compound the spectra were collected with the following set up: 32 scans in the region 400-4000 cm^{-1} with KBr beamsplitter. All the spectra have an accuracy of ±4 cm^{-1}.
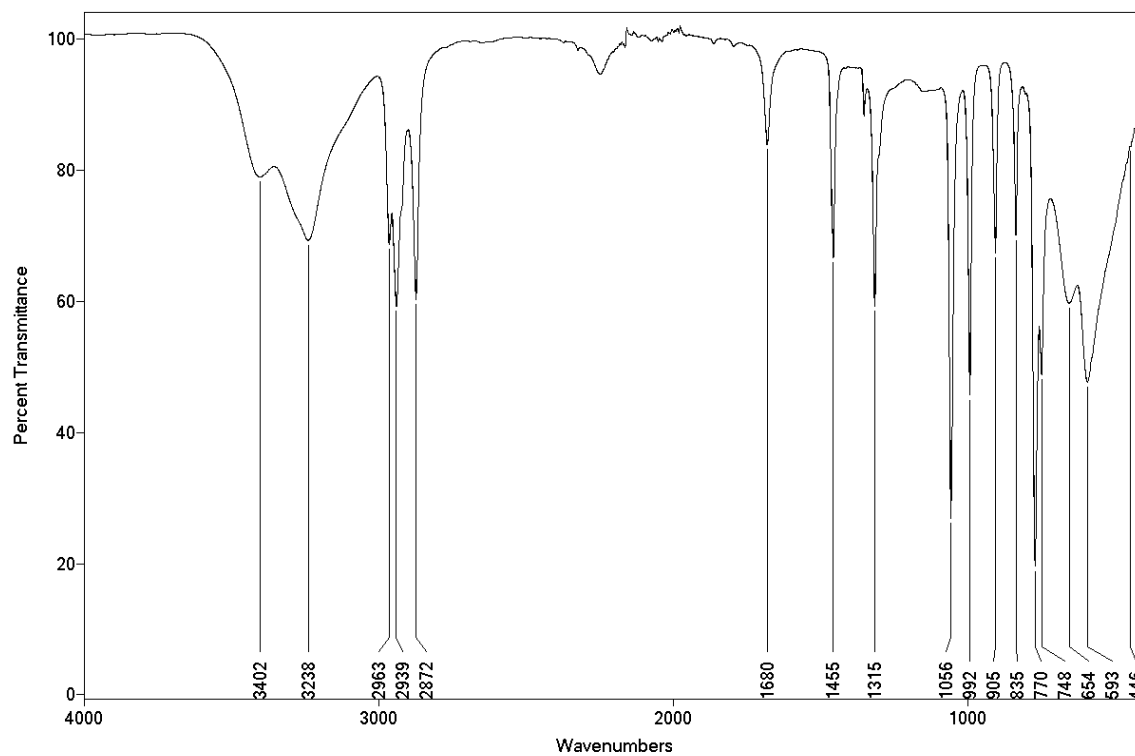
Figure 5.38 DABCO ATR-FTIR spectrum.
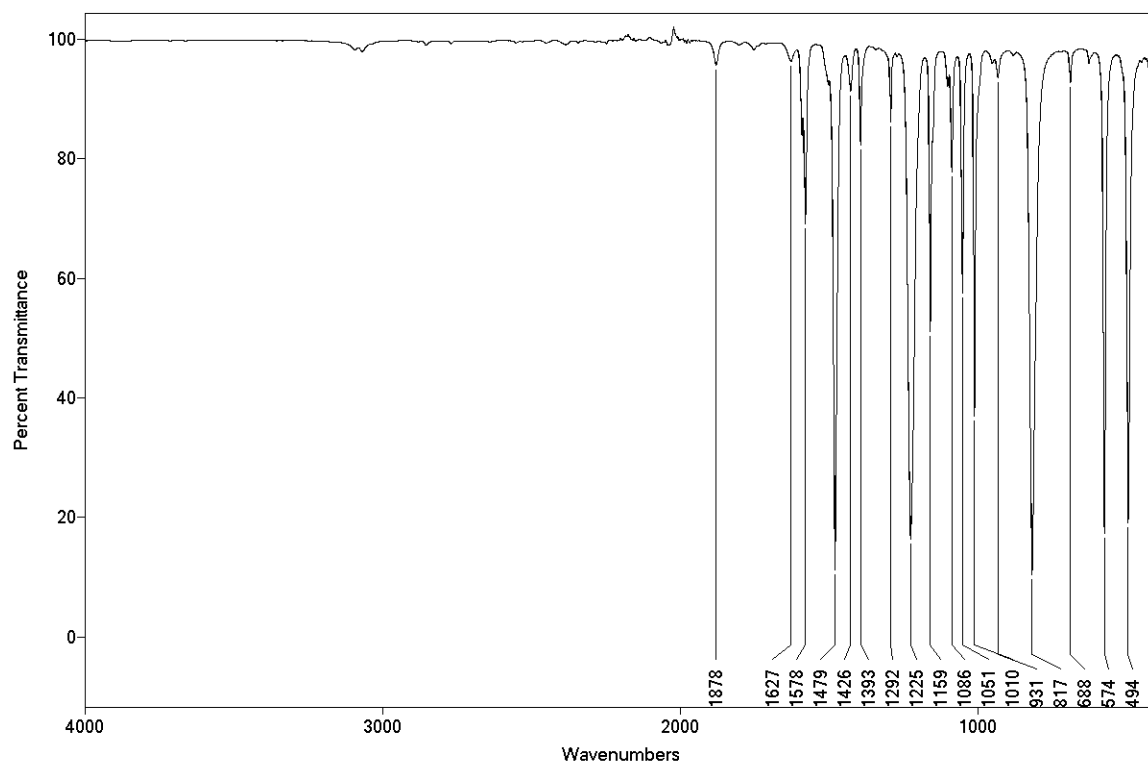
Figure 5.39 *para*-fluoroiodobenzene ATR-FTIR spectrum.
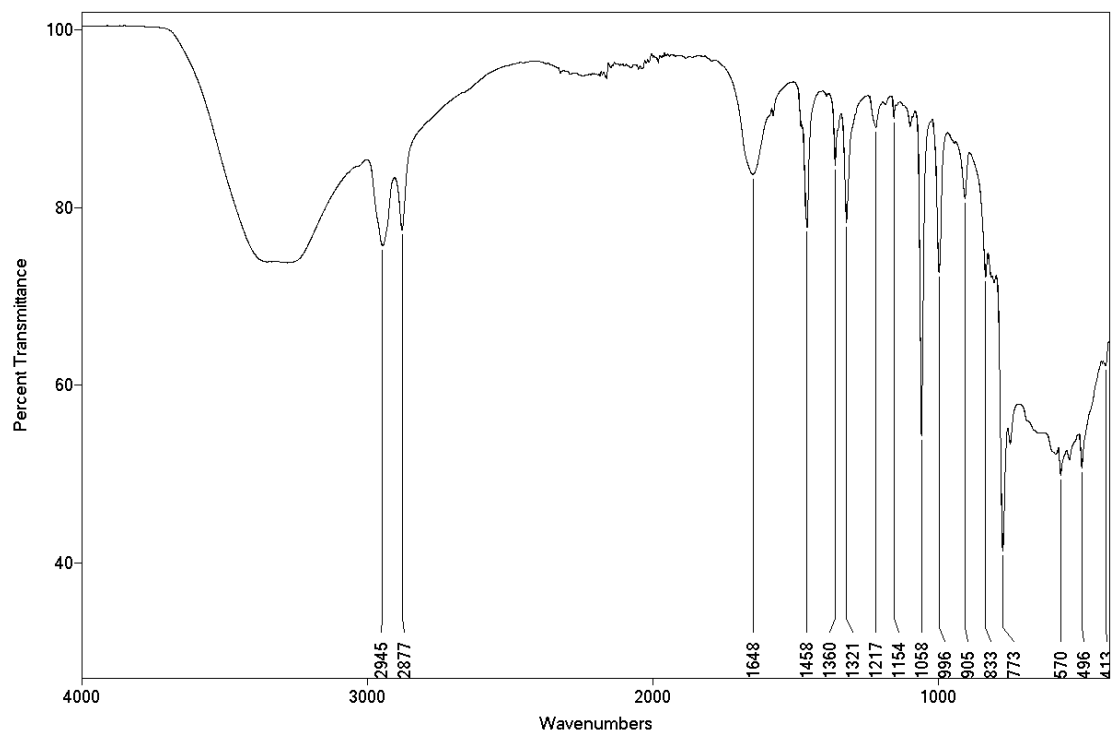
Figure 5.40 Cocrystal of **r1** ATR-FTIR spectrum.
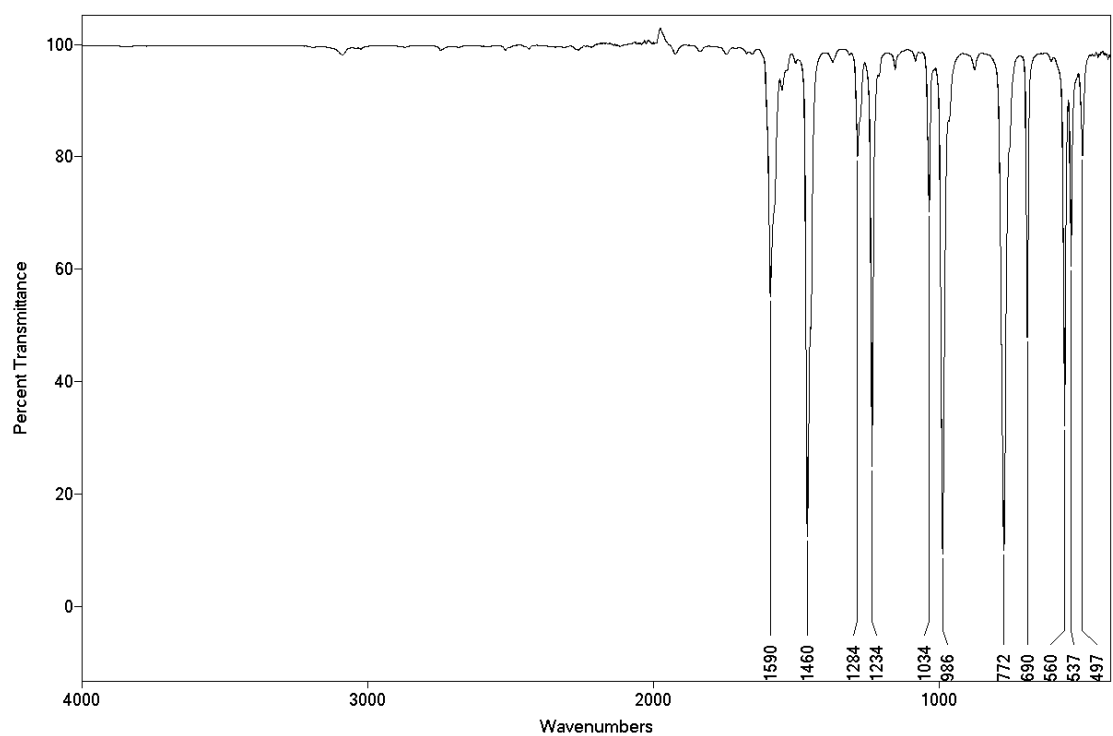
Figure 5.41 2,6-difluoroiodobenzene ATR-FTIR spectrum.
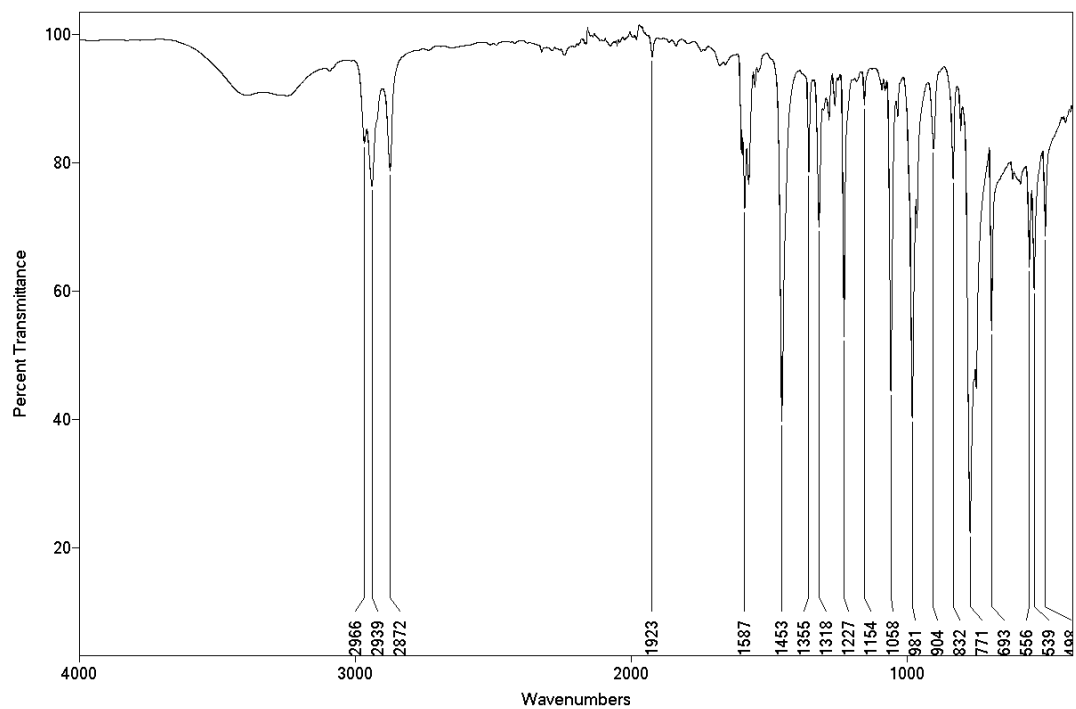
Figure 5.42 Cocrystal of **r2** ATR-FTIR spectrum.
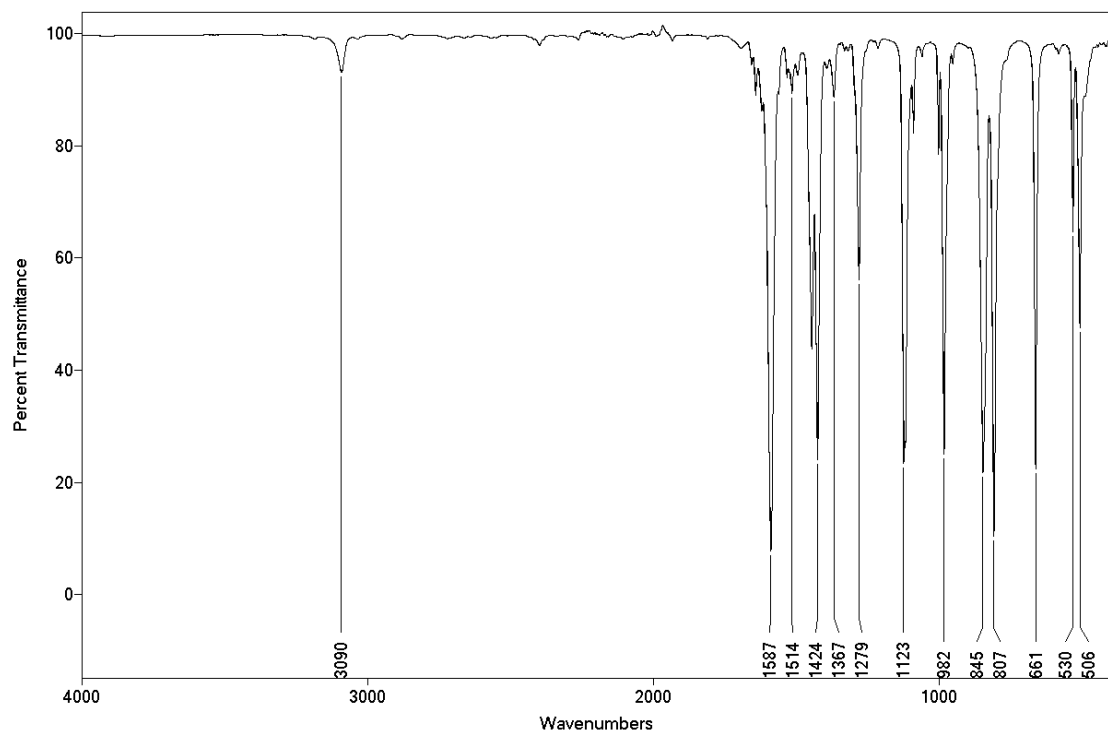
Figure 5.43 2,6-difluoroiodobenzene ATR-FTIR spectrum.
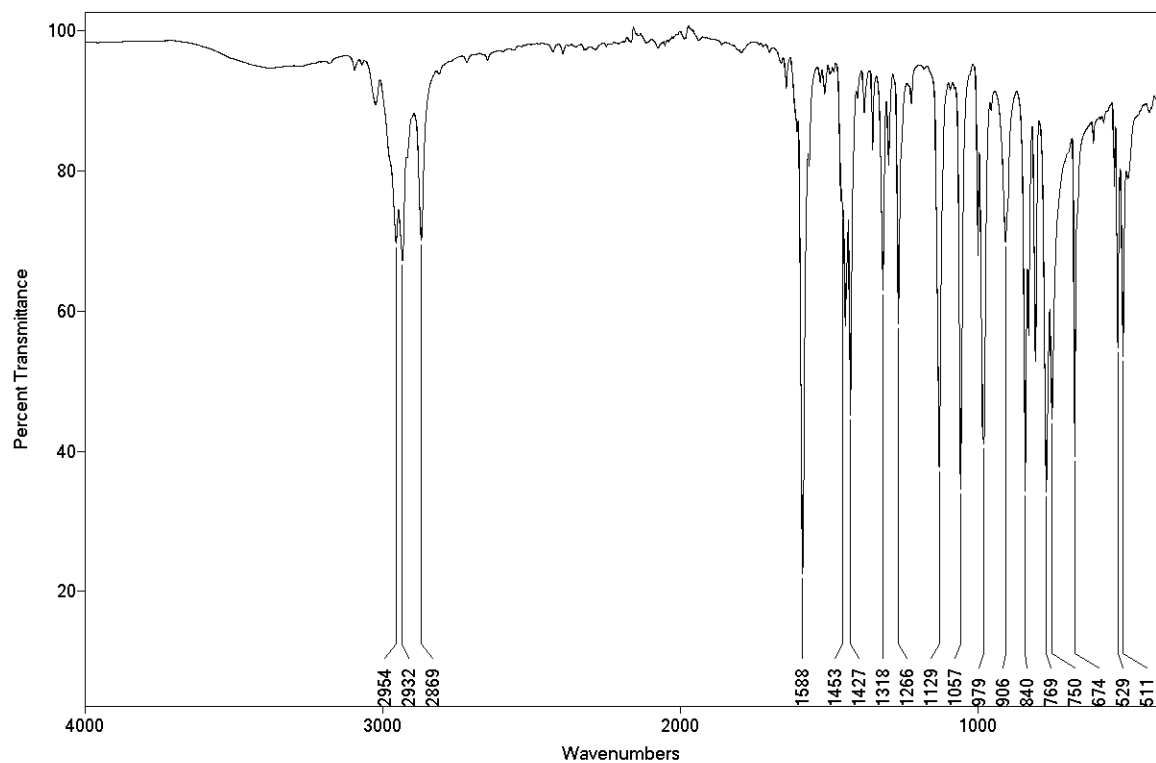
Figure 5.44 Cocrystal of **r3** ATR-FTIR spectrum.
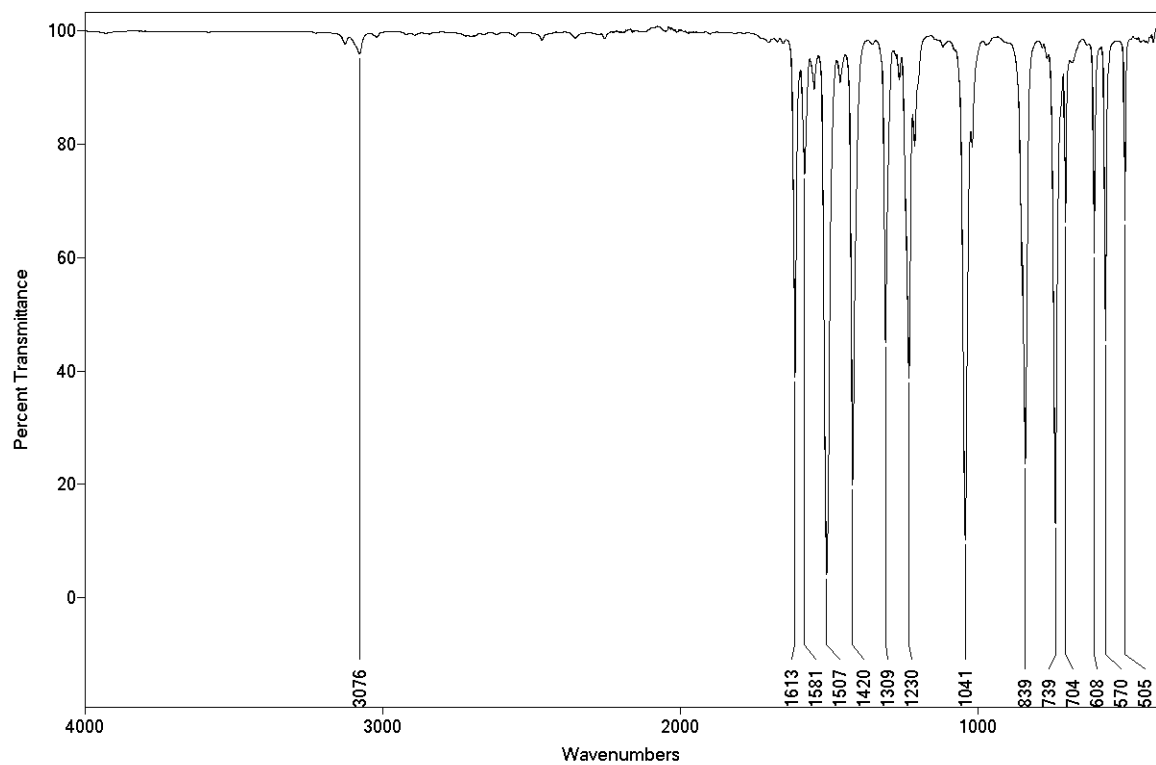
Figure 5.45 3,4,5-trifluoroiodobenzene ATR-FTIR spectrum.
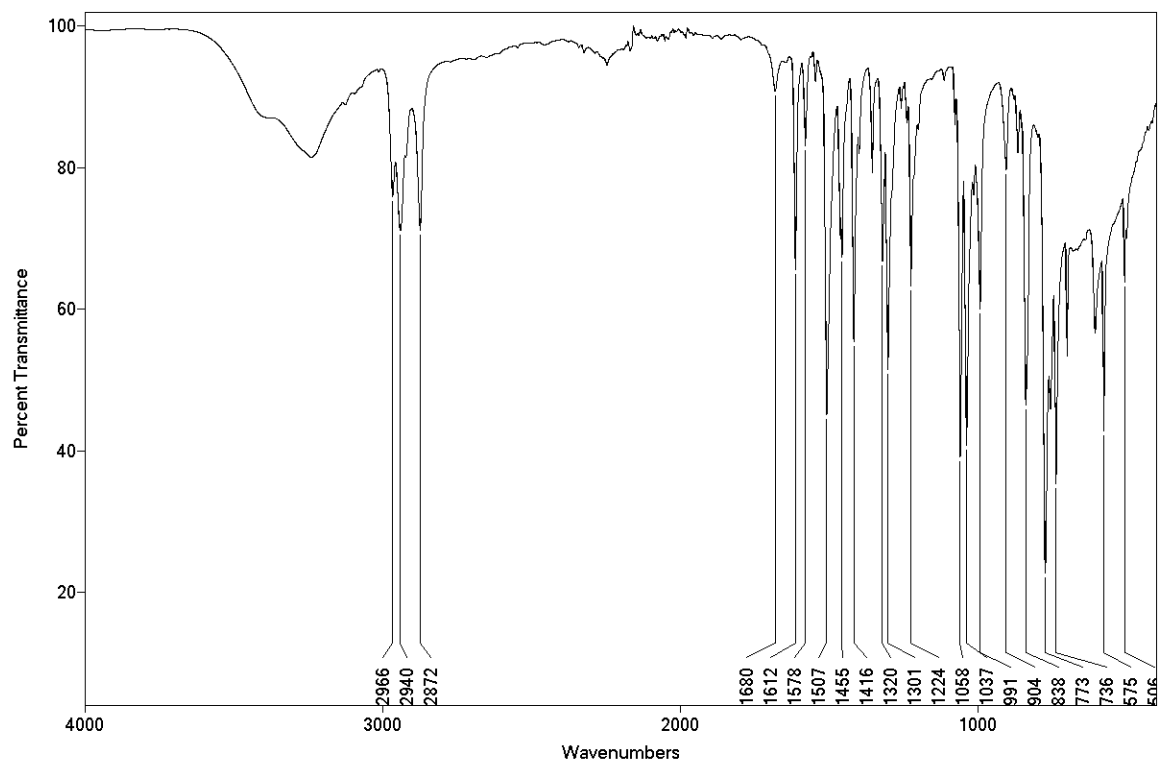
Figure 5.46 Cocrystal of **r4** ATR-FTIR spectrum.
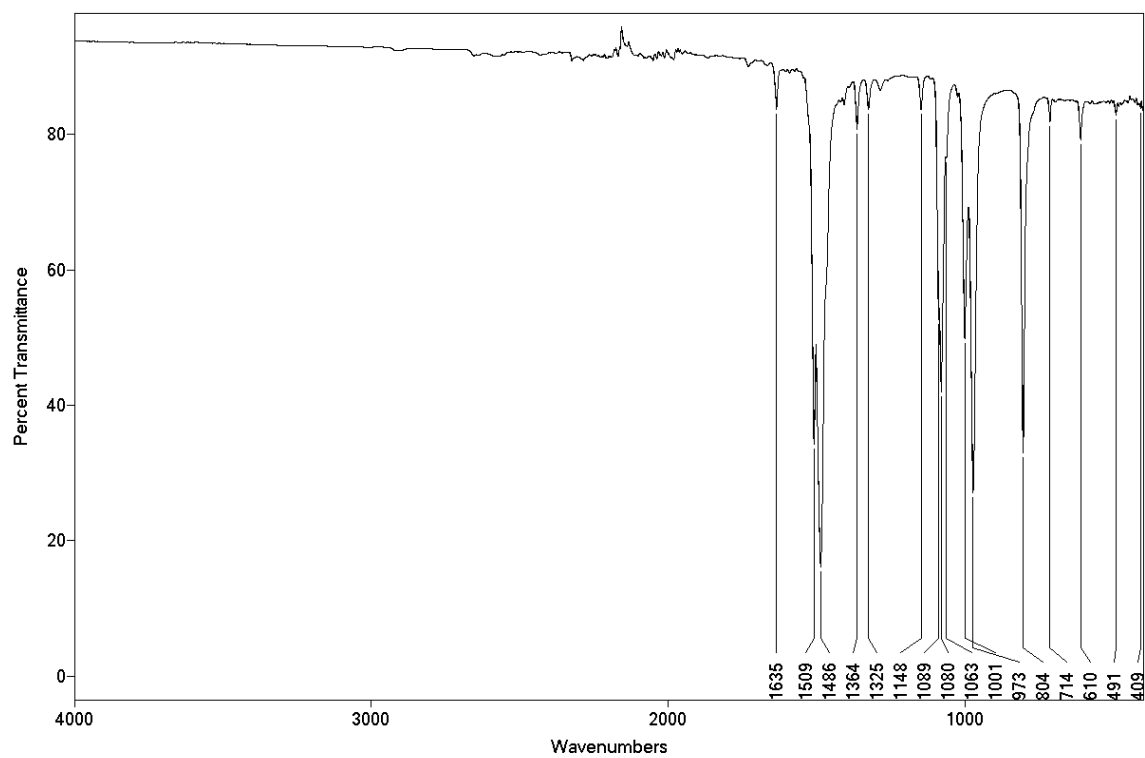
Figure 5.47 Pentafluoroiodobenzene ATR-FTIR spectrum.

136
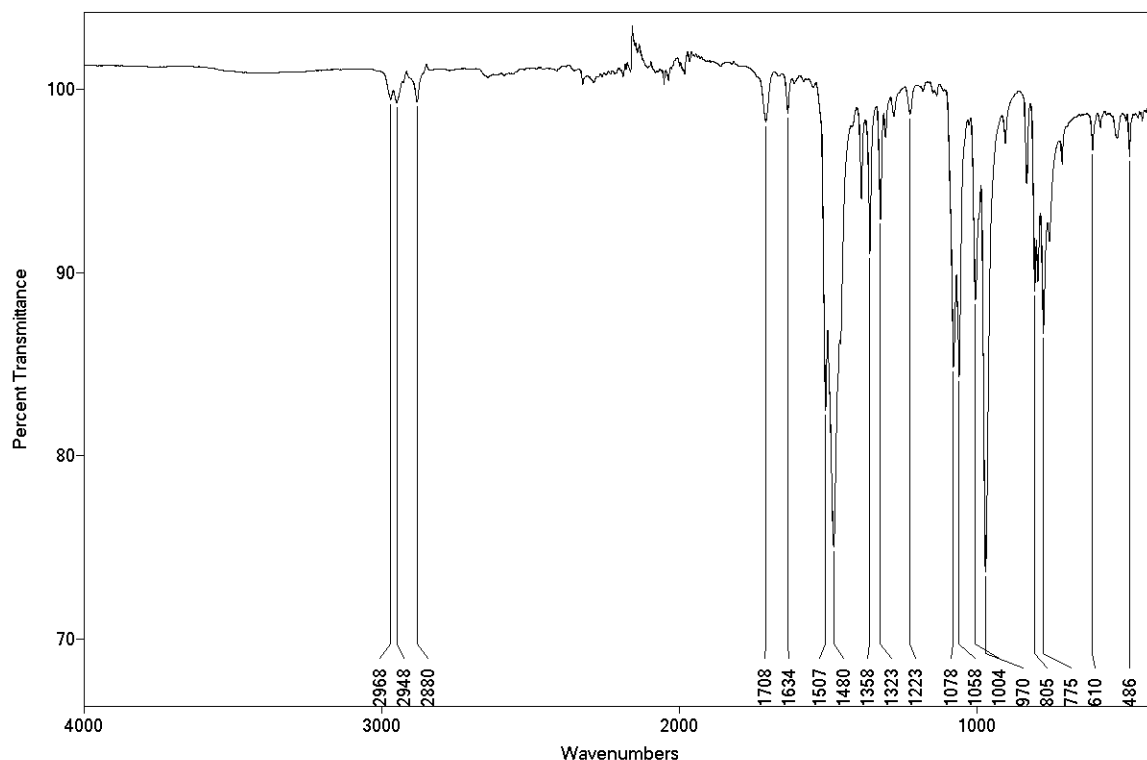
Figure 5.48 Cocrystal of **r5** ATR-FTIR spectrum.

5.3.4 ^{1}H spin-lattice T$_1$ relaxation solid-state NMR analysis

Here an example of the procedure used to collect T$_1$ relaxation data. ^{1}H T$_1$ NMR relaxation was measured on polycrystalline samples of complex **r5** obtained from crystallization of a solution in acetone of pentafluoroiodobenzene and DABCO in a 2:1 molar ratio. The sample was placed inside a borosilicate glass NMR tube between two glass rods and then, prior to sealing under vacuum, the sample was vacuumed-argon backfilled (x2). The experiments were carried out with a static wideline probe using solid-state spectrometer Bruker300 operating at a ^{1}H Larmor frequency of 300 MHz. The saturation recovery sequence used contains a saturation pulse comb followed by a time τ' (τ' values taken from the variable delay list) with a π/2 pulse p1. For each measurement, an acquisition time of 2.0985 ms was used. The ^{1}H spin-lattice relaxation experiments were determined for T = 141 K - 295 K.
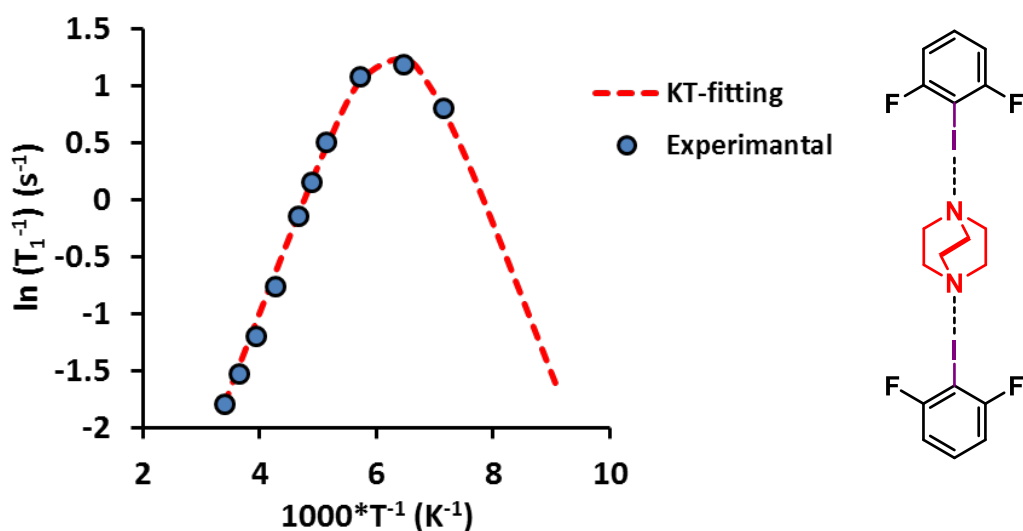
Figure 5.49 ^{1}H spin-lattice relaxation times ([1]H T_1) measured on 2,6-F_2PhI·dabco (**r2**) from 295 K – 145 K at 300 MHz (solid blue circles). The plot ln (T_1^{-1}) *vs* $1000T^{-1}$ shows a strong dependence of [1]H T_1 with the temperature displaying a maximum, that corresponds to the minimum [1]H T_1, at approximately 155 K. The red dotted line corresponds to the Kubo-Tomita fit for the process assuming an Arrhenius behavior with an E_a = 2.65 kcal·mol^{-1} and τ_0^{-1} = 2.0x10^{12} s^{-1}.
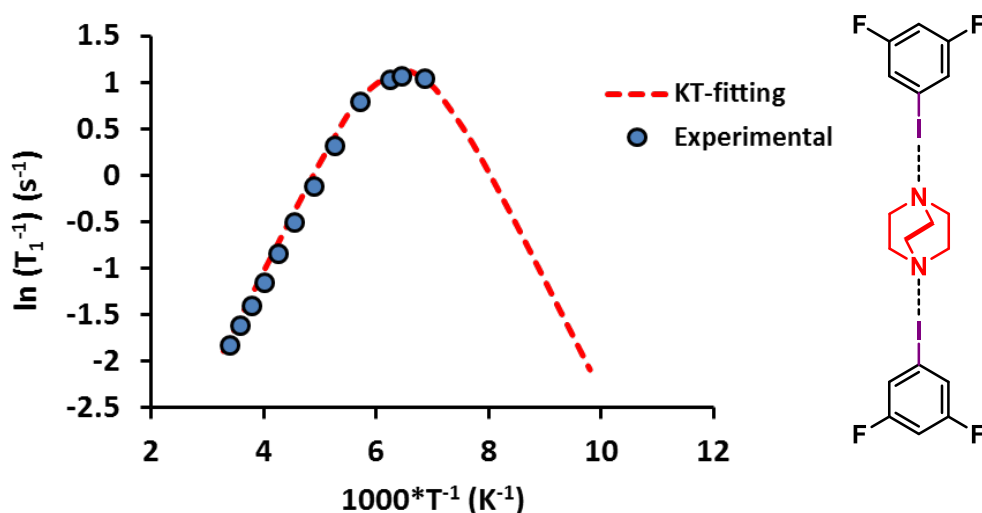
Figure 5.50 ^{1}H spin-lattice relaxation times ([1]H T_1) measured on 3,5-F_2PhI·dabco (**r3**) from 196 K – 146 K at 300 MHz. The plot ln (T_1^{-1}) *vs* $1000T^{-1}$ shows a maximum, that corresponds to the minimum [1]H T_1, at approximately

138

155 K. The red dotted line corresponds to the Kubo-Tomita fit for the process assuming an Arrhenius behavior with an E_a = 2.4 kcal·mol⁻¹ and τ_0^{-1} = 1.1x10¹² s⁻¹
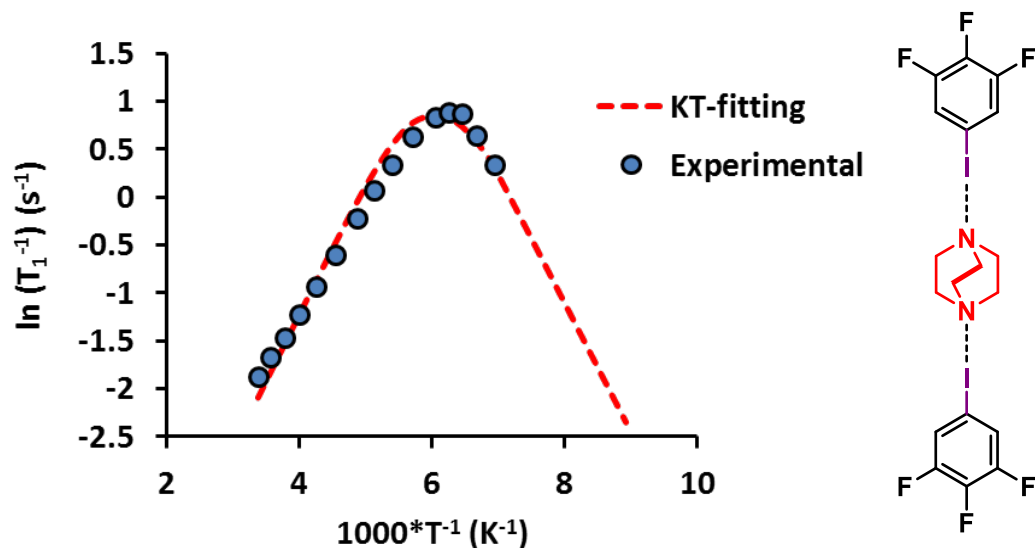
Figure 5.51 ^1H spin-lattice relaxation times (^1H T_1) measured on 3,4,5-F_3PhI·dabco (**r4**) from 296 K – 150 K at 300 MHz (solid blue circles). The plot ln (T_1^{-1}) *vs* 1000T⁻¹ shows a strong dependence of ^1H T_1 with the temperature displaying a maximum, that corresponds to the minimum ^1H T_1, at approximately 160 K. The red dotted line corresponds to the Kubo-Tomita fit for the process assuming an Arrhenius behavior with an E_a = 2.8 kcal·mol⁻¹ and τ_0^{-1} = 2.3x10¹² s⁻¹.
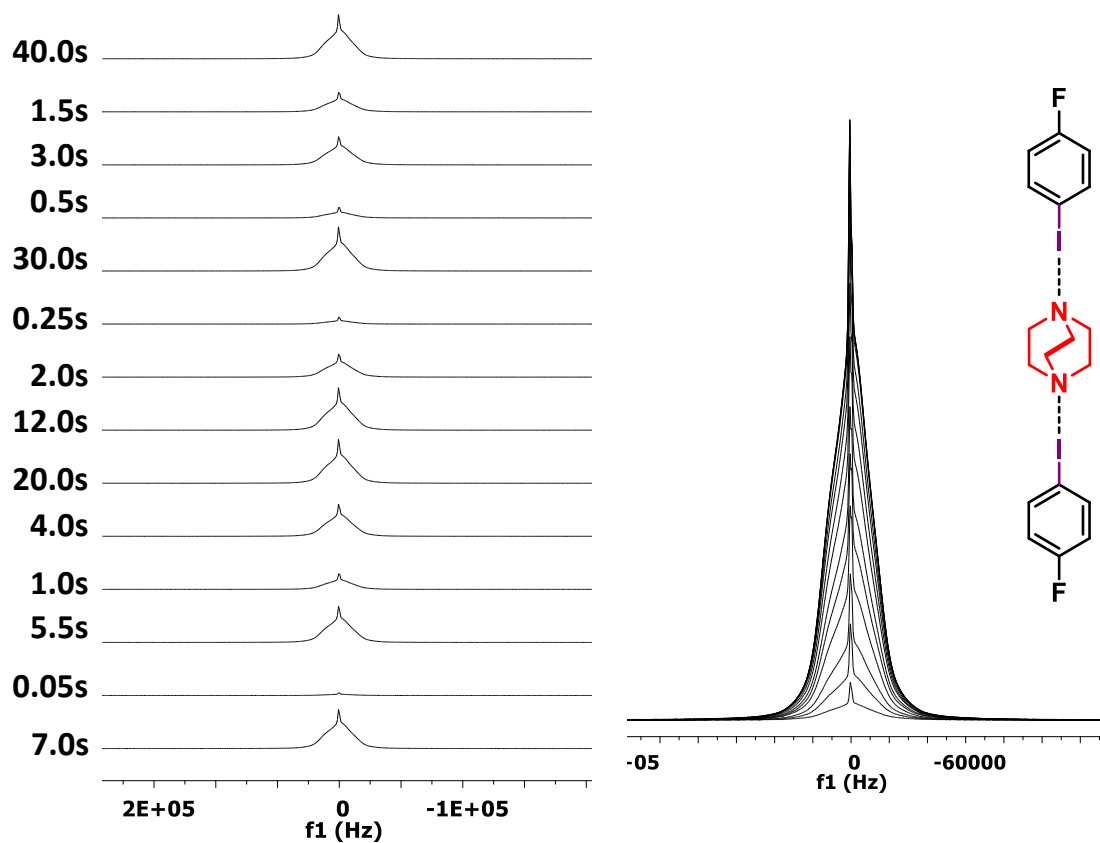
Figure 5.52 Representative ^{1}H wideline spin-lattice relaxtion (T$_1$) NMR measurement via the saturation-recovery method at 290 K: stacked spectra (left) and overlaid spectra (right).
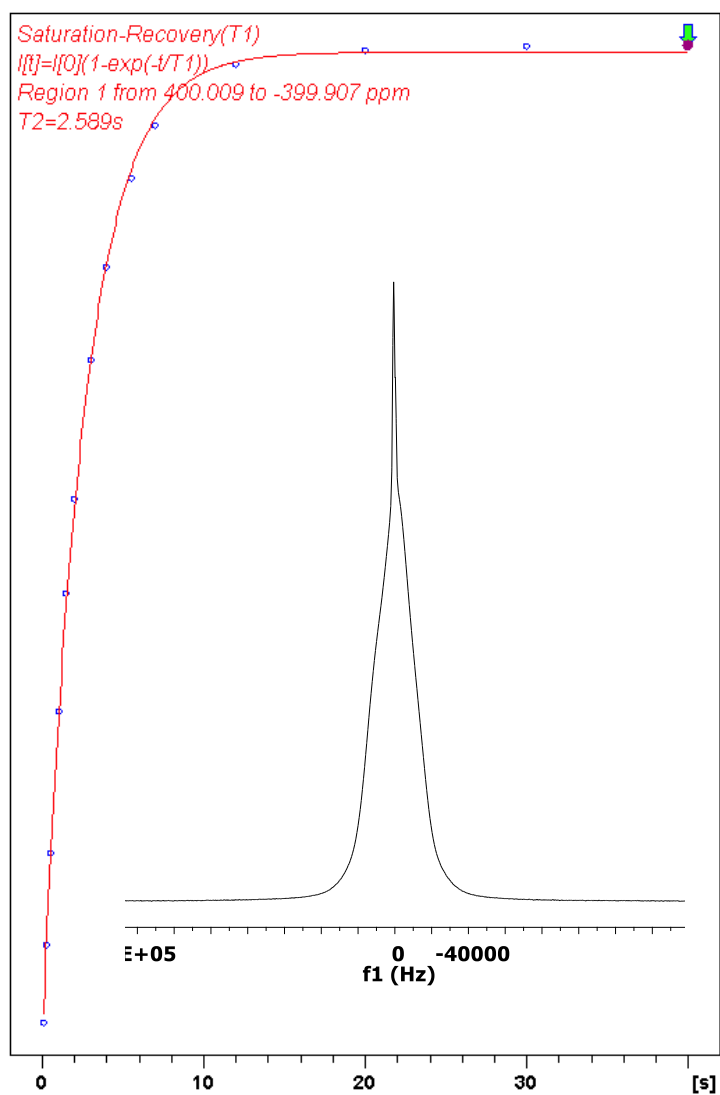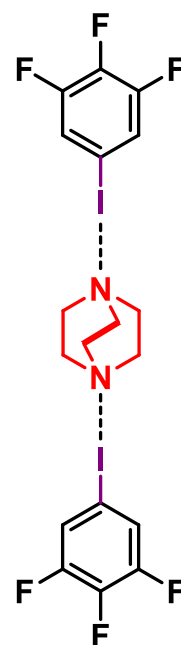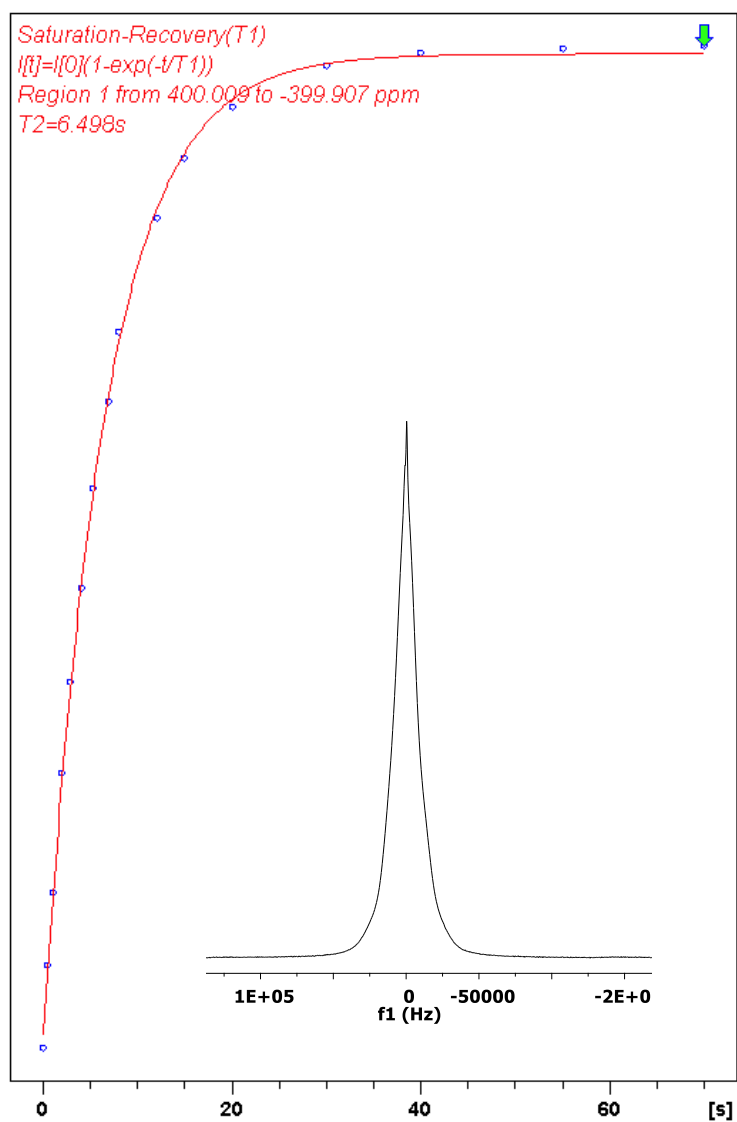
Figure 5.53 Representative example of the mono-exponential fit to representative ^{1}H wideline spin-lattice relaxation (T_1) saturation recovery data of complex **r1** at T= 290 K (T_1 = 2.589 s) with τ' values of 7s, 0.05s, 5.5s, 1s, 4s, 20s, 12s, 2s, 0.25s, 30s, 0.5s, 3s, 1.5s, 40s. The insert shows the recovery of the signal at 40s.
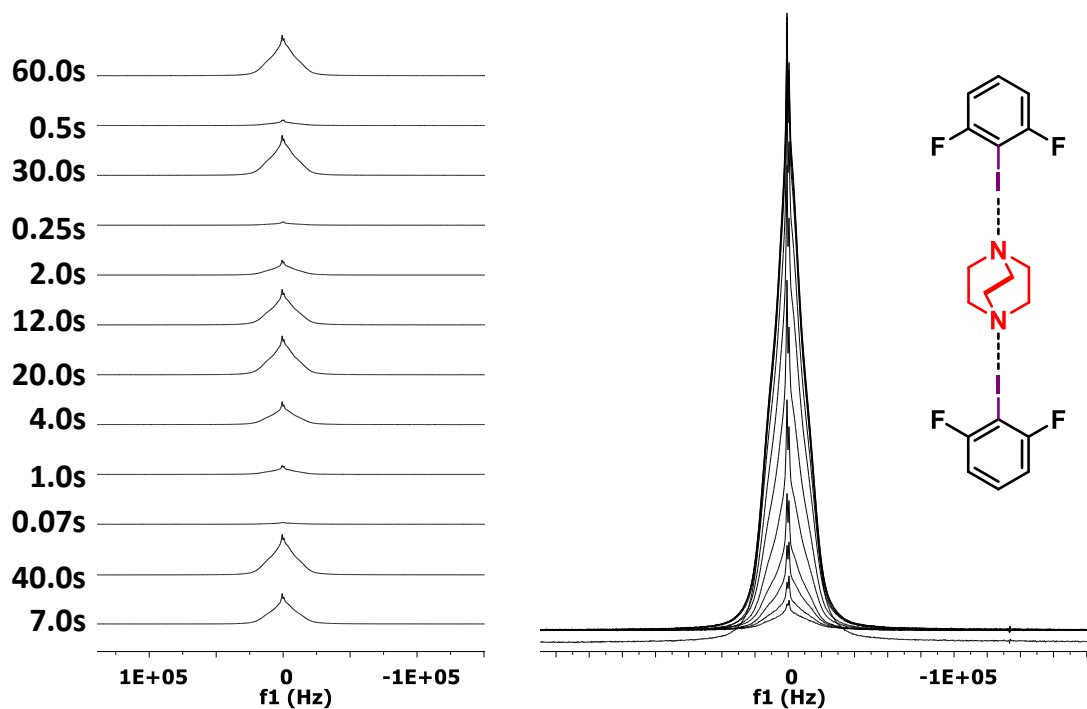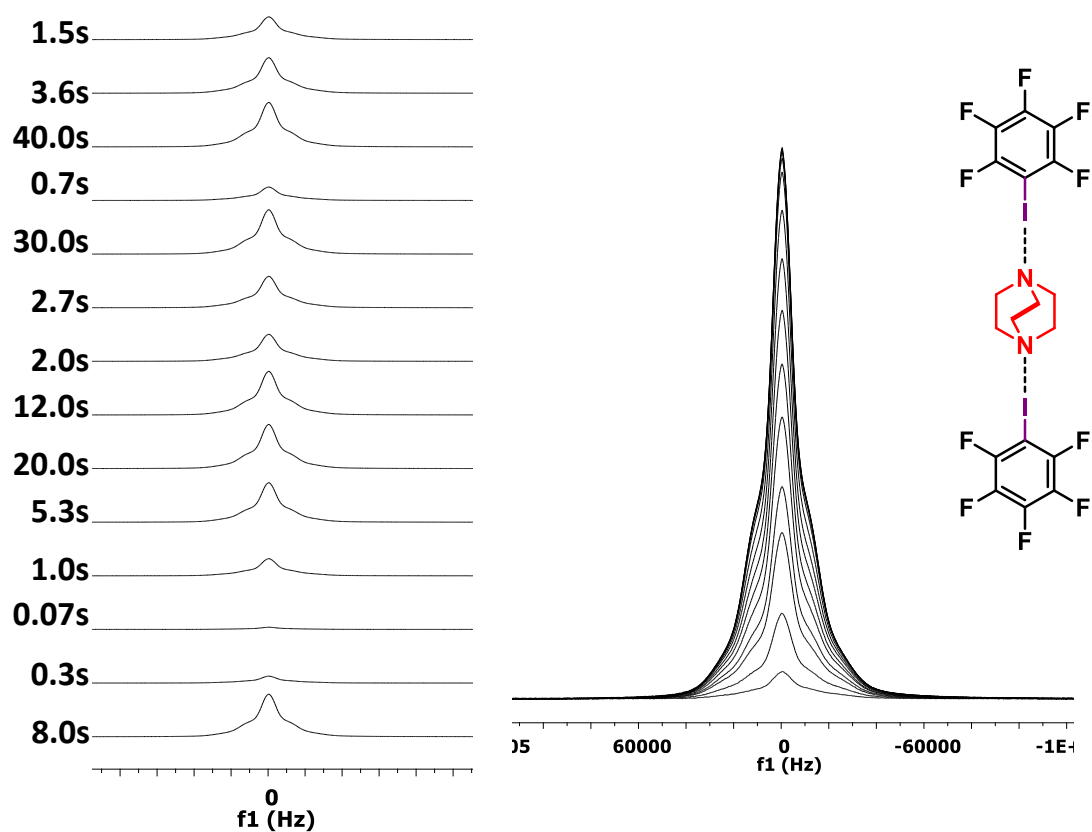
Figure 5.54 Representative ^{1}H wideline spin-lattice relaxtion (T_1) NMR measurement via the saturation-recovery method at 295 K: stacked spectra (left) and overlaid spectra (right).
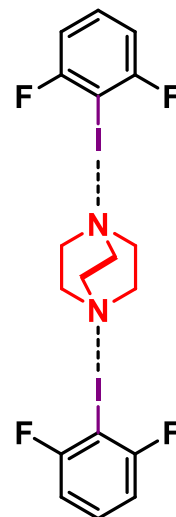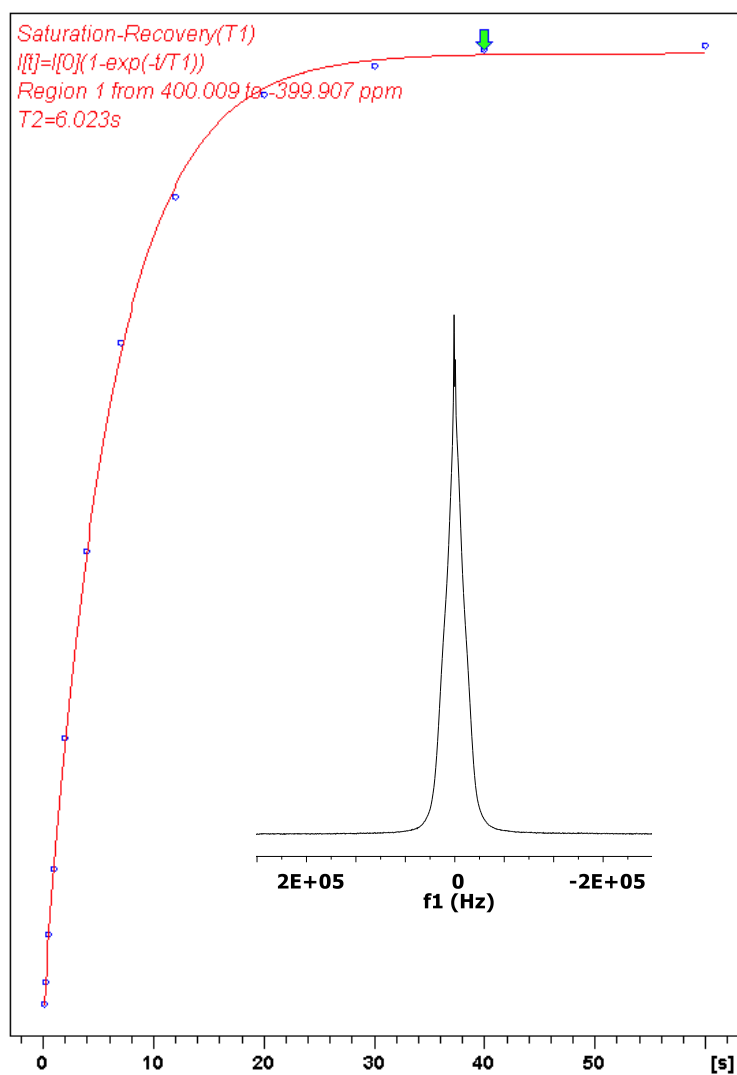
Figure 5.55 Representative example of the mono-exponential fit to representative ^{1}H wideline spin-lattice relaxation (T_1) saturation recovery data of complex **r2** at T= 295 K (T_1 = 6.0 s) with τ' values of 7s, 40s, 0.07s, 1s, 4s, 20s, 12s, 2s, 0.25s, 30s, 0.5s, 60s. The insert shows the recovery of the signal at 60s.
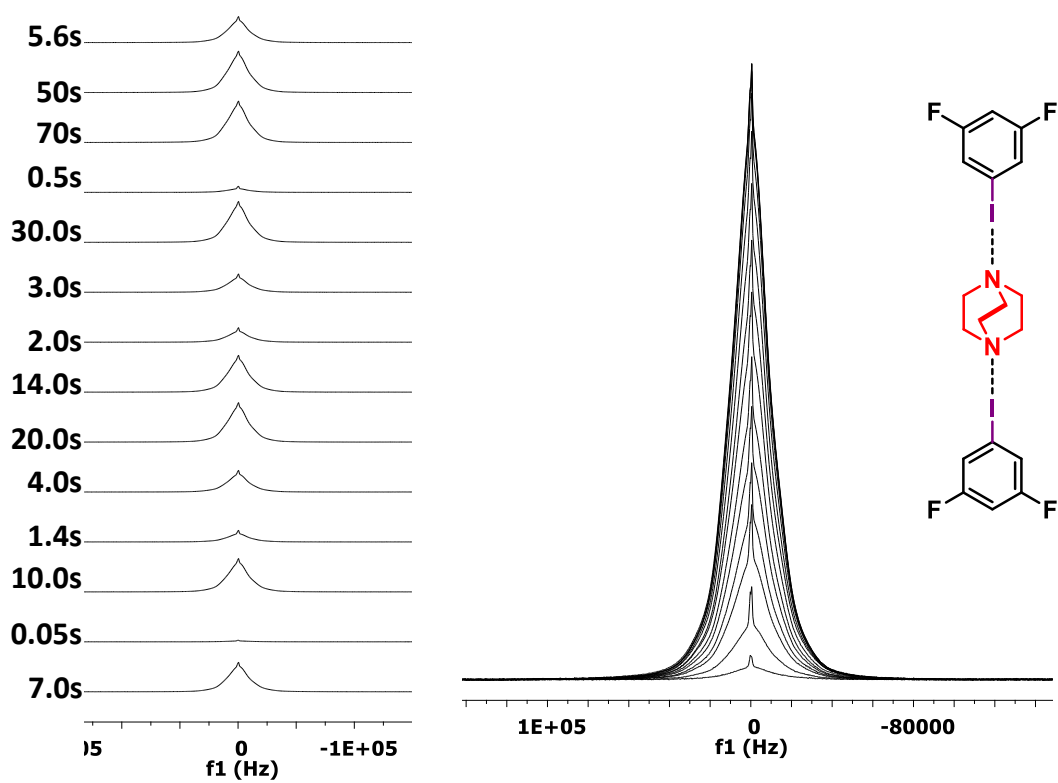
Figure 5.56 Representative ^1H wideline spin-lattice relaxtion (T_1) NMR measurement via the saturation-recovery method at 296 K: stacked spectra (left) and overlaid spectra (right).
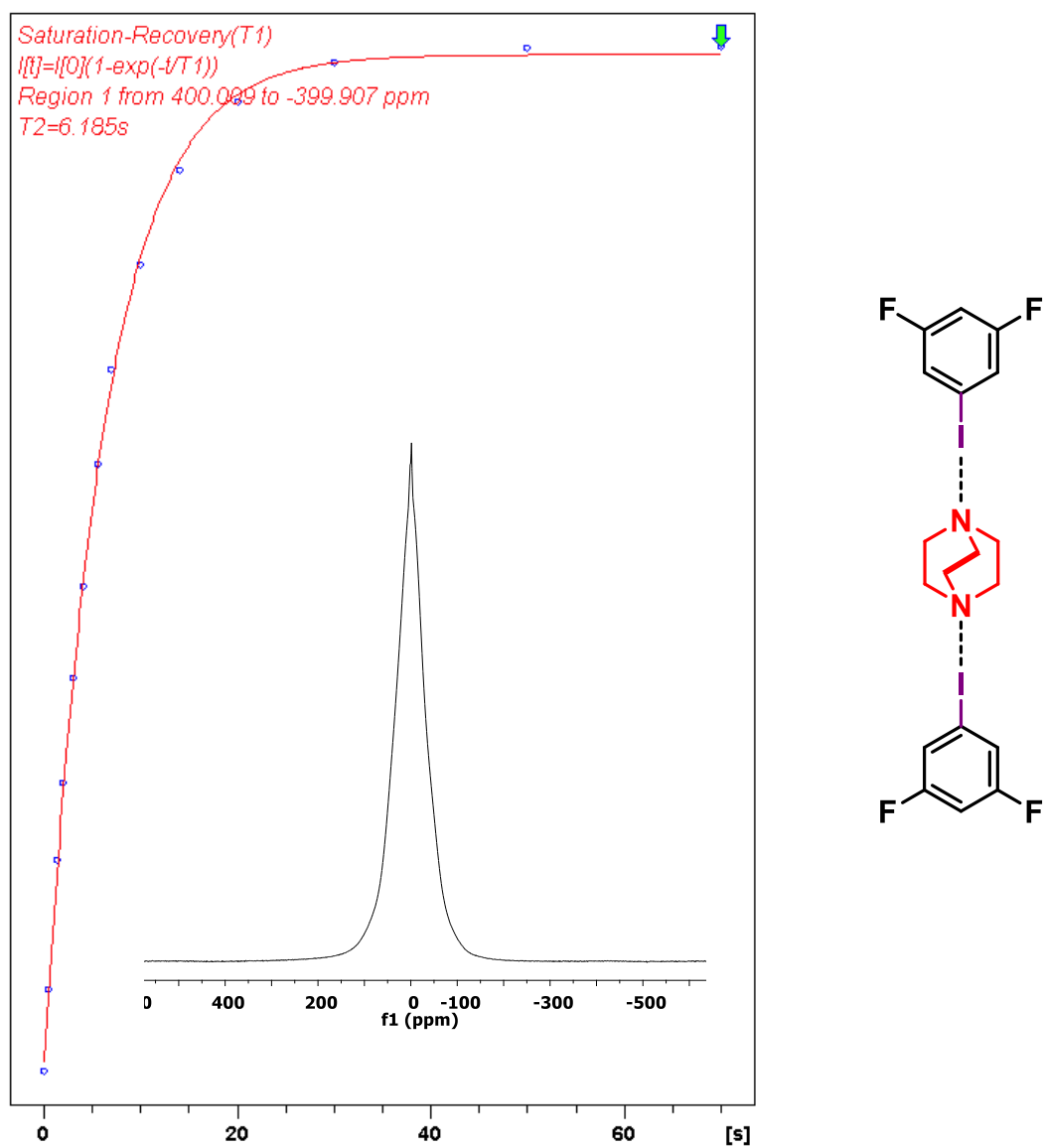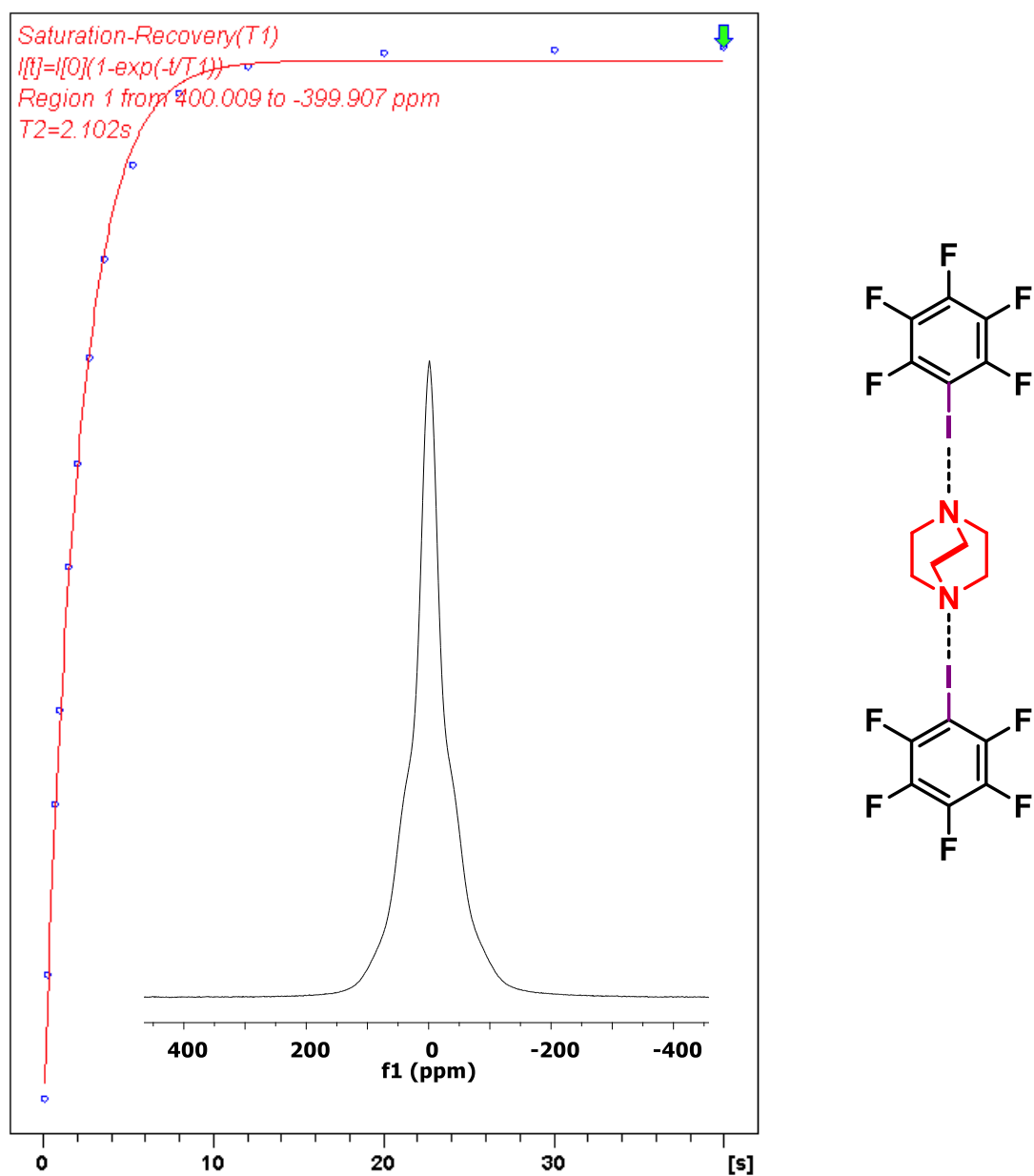
Figure 5.57 Representative example of the mono-exponential fit to representative ^{1}H wideline spin-lattice relaxation (T_1) saturation recovery data of complex **r3** at T= 296 K (T_1 = 6.185 s) with τ' values of 7s, 0.05s, 10s, 1.4s, 4s, 20s, 14s, 2s, 3s, 30s, 0.5s, 70s, 50s, 5.6s. The insert shows the recovery of the signal at 70s.
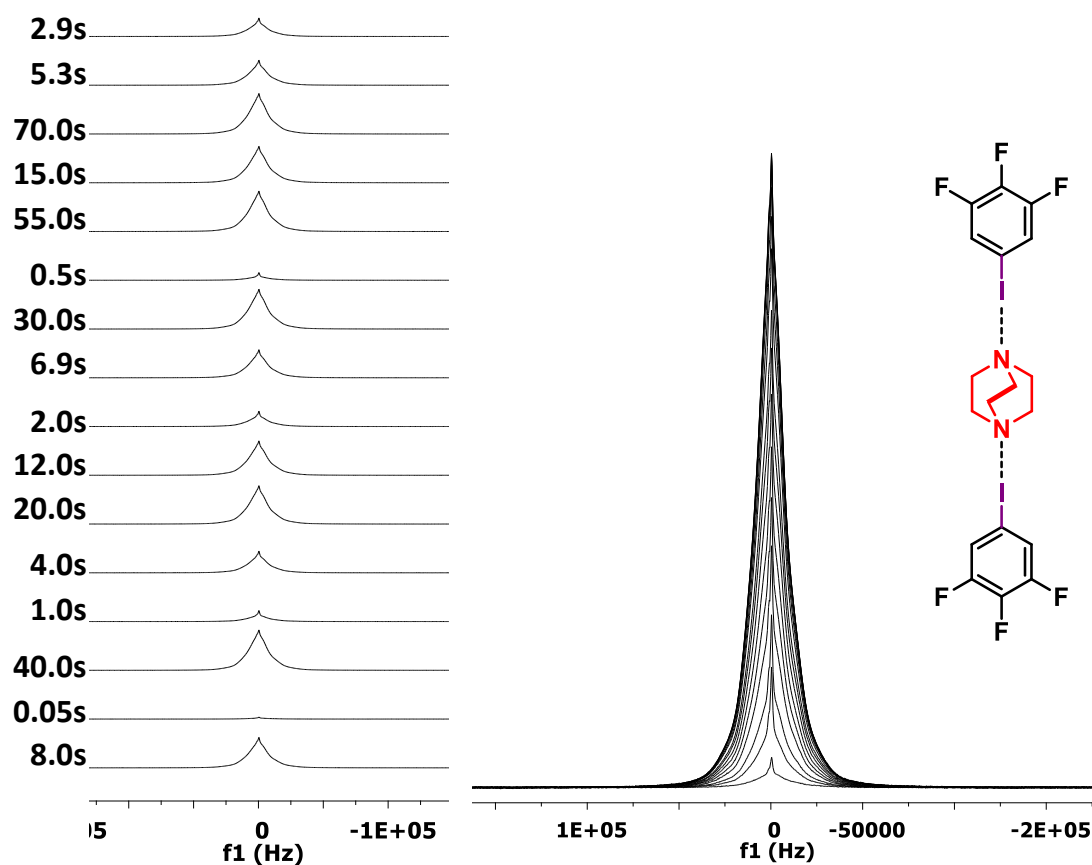
Figure 5.58 Representative ^{1}H wideline spin-lattice relaxtion (T_1) NMR measurement via the saturation-recovery method at 295 K: stacked spectra (left) and overlaid spectra (right).

Figure 5.59 Representative example of the mono-exponential fit to representative ^{1}H wideline spin-lattice relaxation (T_1) saturation recovery data of complex **r4** at T= 296 K (T_1 = 6.498 s) with τ' values of 8s, 0.05s, 40s, 1s, 4s, 20s, 12s, 2s, 6.9s, 30s, 0.5s, 55s, 15s, 70s, 5.3s, 2.9s. The insert shows the recovery of the signal at 70s.

Figure 5.60 Representative ^{1}H wideline spin-lattice relaxtion (T_1) NMR measurement via the saturation-recovery method at 275 K: stacked spectra (left) and overlaid spectra (right).

Figure 5.61 Representative example of the mono-exponential fit to representative ^1H wideline spin-lattice relaxation (T_1) saturation recovery data of complex **r5** at T= 275 K (T_1 = 2.102 s) with τ' values of 8s, 0.3s, 0.07s, 1s, 5.3s, 20s, 12s, 2s, 2.7s, 30s, 0.7s, 40s, 3.6s, 1.5s. The insert shows the recovery of the signal at 40s.

5.3.5 Synthesis of DABCO-*d₁₂*
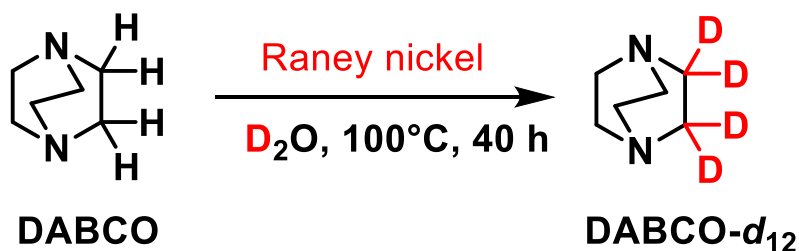
Step 1. Preparation of Raney-nickel containing active deuterium. A round bottom flask containing deuterium oxide (7.5 mL) was cooled on an iced bath, then while stirring, sodium metal (1.14 g) was carefully added in small portions so that the exothermic reaction can be safely controlled. After the addition of sodium was complete, the resulting solution was stirred at room temperature and then heated at 50 °C. Thereafter, nickel-aluminum alloy (Raney-nickel non-activated, 1,5 g) was added in small portions so that the temperature did not raise above 55°C with each addition. After the addition was complete, the resulting slurry was heated at 50°C for 1 h and the supernatant solution was decanted. Then the remaining solid was rinsed with deuterium oxide (5 x 3 mL).

Step 2. Hydrogen-deuterium exchange cycle. To the resulting black-gray slurry, 1,4-diazabicyclo[2.2.2]octane (409 mg) and deuterium oxide (1.5 mL) were added. The resulting mixture was heated at 100°C for 40 h and then cooled to room temperature. The liquid supernatant was then decanted and the solids were washed with water (3 x 10 mL). The organics were extracted from the aqueous residue with dichloromethane (4 x 15 mL). The combined organic layers were dried over $MgSO_4$ and the solvent was carefully evaporated at 30 °C under vacuum. The solid residue was sublimated under vacuum to afford dabco-*d₁₂* (ca. 100 mg, ca. 25%) as white crystals. m.p. 111-114 °C. MS(ESI): $[M+H]^+$: 123.17 (D_{10}, 1.9%), 124.18 (D_{11}, 28.2%), 125.18 (D_{12}, 100%), accounting for 88% deuterium atom content. IR (neat) v_{max}: 3397, 3236, 2229, 2121, 1678, 1165, 1135, 927, 882691. ^{13}C NMR (125 MHz, CDCl₃) δ 45.8 (pent, J_{CD} = 21.0 Hz).

5.3.6 ²H solid-state NMR analysis

²H NMR experiments were performed on polycrystalline samples of **r1**, **r2** and **r5** obtained from crystallization of a solution in acetone of the iodobenzene derivatives and DABCO-d_{12} in a 2:1 molar ratio. Solid-state ²H NMR experiments were recorded on a Bruker300 spectrometer operating at a frequency of 46.07 MHz, using a 4 mm wide-line probe with a 2/π pulse of 2.5 μs. A quadrupolar echo pulse sequence with phase-cycling along with an echo delay of 50 μs and recycle delay of 10 s was employed to acquire the ²H wide-line spectra. Variable temperature experiments were recorded in the range of 140 K – 295 K and the temperature inside the probe was calibrated by using the shift of ²⁰⁷Pb as reference. The spectra were acquired by averaging at least 32 scans and processed with a line broadening of 5 kHz.
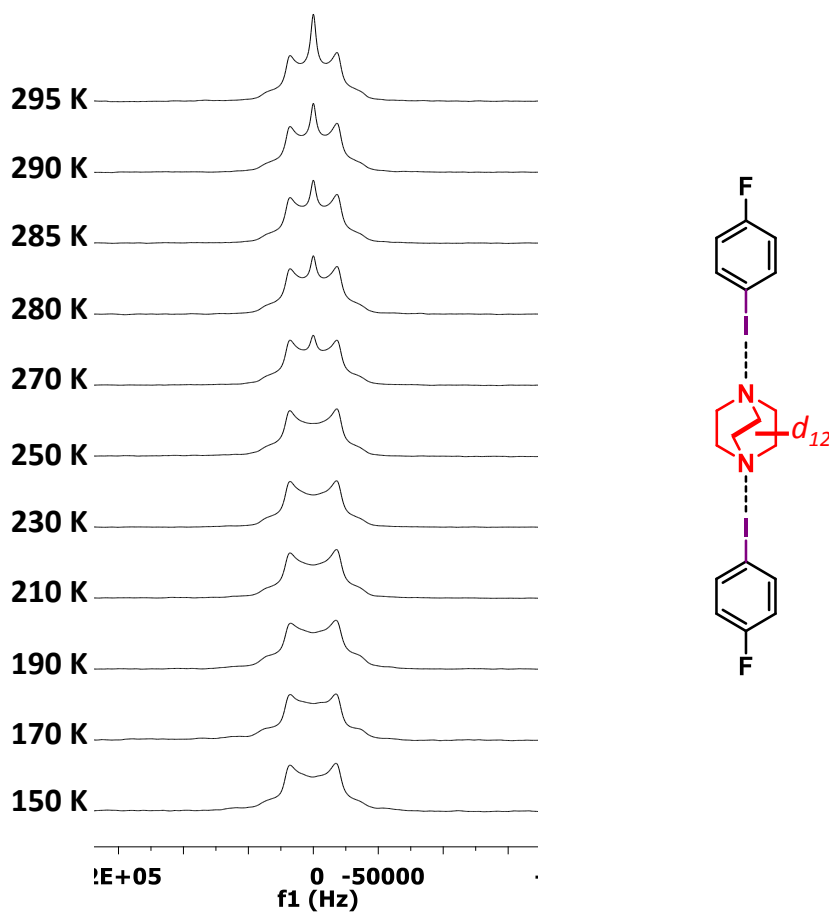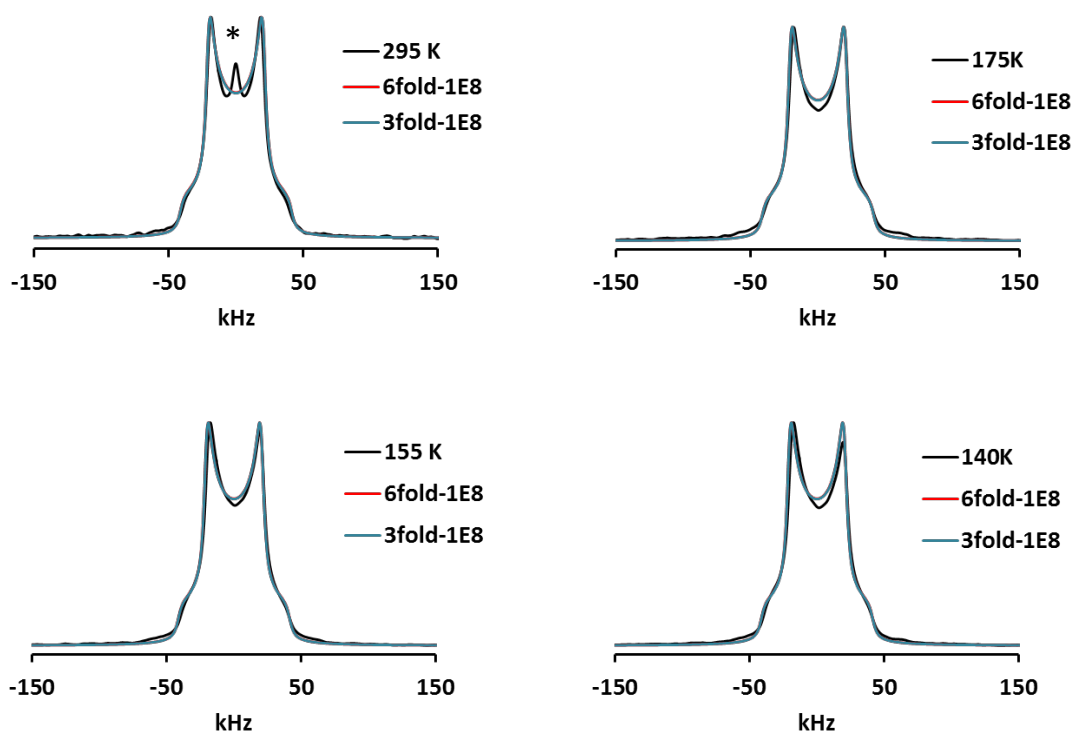

Figure 5.62 Variable temperature ²H NMR quadrupolar echo experiments for complex FPhI·DABCO-d_{12} (**r1-d_{12}**) from 295 K to 150 K.
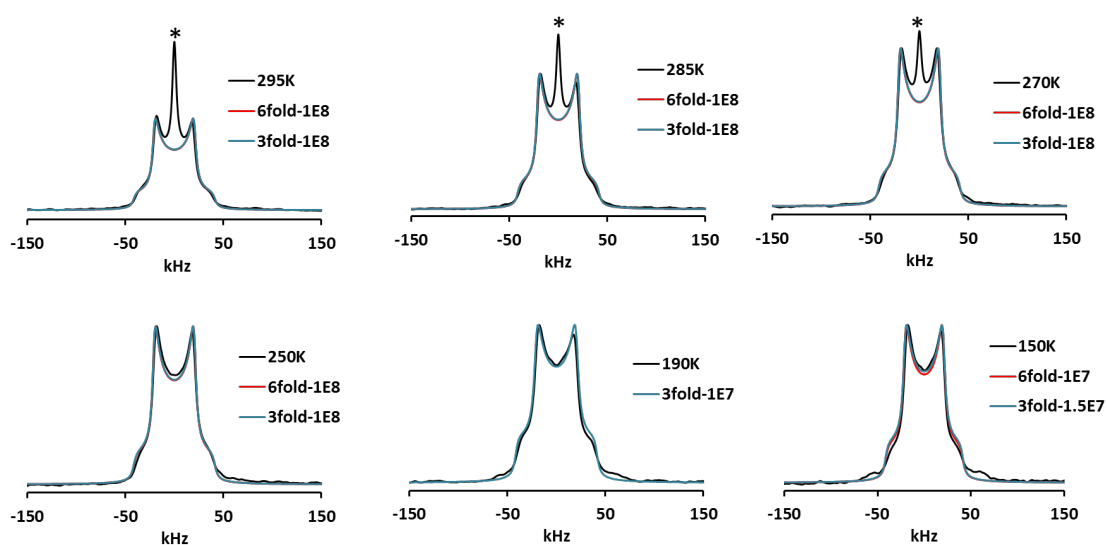
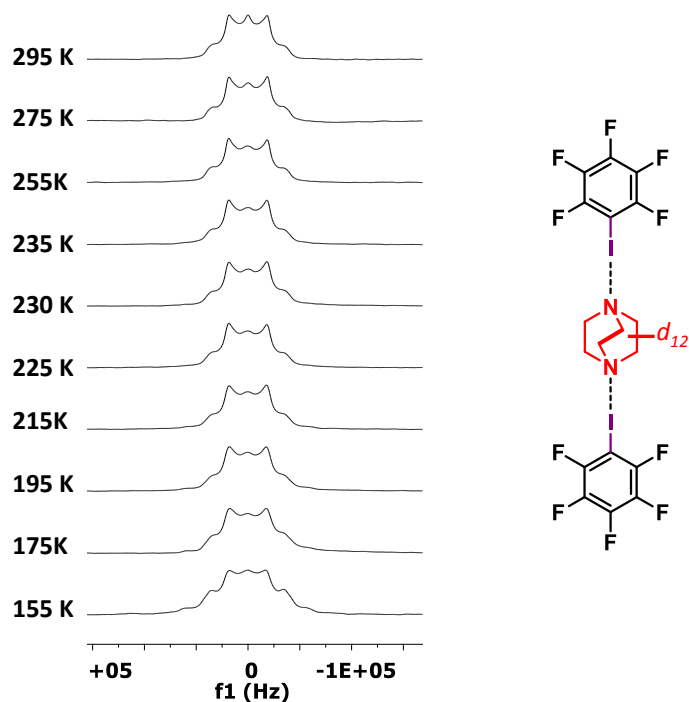**Figure 5.63** Experimental and simulated ^{2}H NMR quadrupolar echo spectra of **r1-** d_{12}. Simulations were carried out using the Nishikiori's program with a b angle of 70°, a QCC of 170 kHz, a line-broadening of 5 kHz and an echo delay (τ) of 50 msec. * The central peak was assigned to the isotropic peak of un-coordinated dabco.
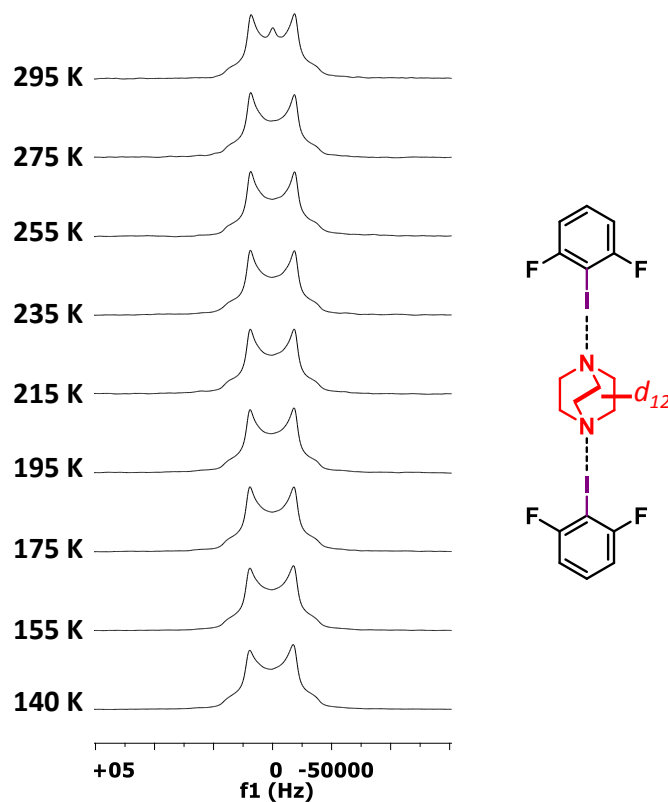

Figure 5.64 Variable temperature ^{2}H NMR quadrupolar echo experiments for complex F$_2$PhI·DABCO-d_{12} (**r2-**d_{12}) from 295 K to 140 K.

152

Figure 5.65 Experimental and simulated ^{2}H NMR quadrupolar echo spectra of **r2-d_{12}**. Simulations were carried out using the Nishikiori's program with a b angle of 70°, a QCC of 170 kHz, a line-broadening of 5 kHz and an echo delay (τ) of 50 msec.

Figure 5.66 Variable temperature ^{2}H NMR quadrupolar echo experiments for complex F$_5$PhI·DABCO-d_{12} (**r5-d_{12}**) from 295 K to 155 K.
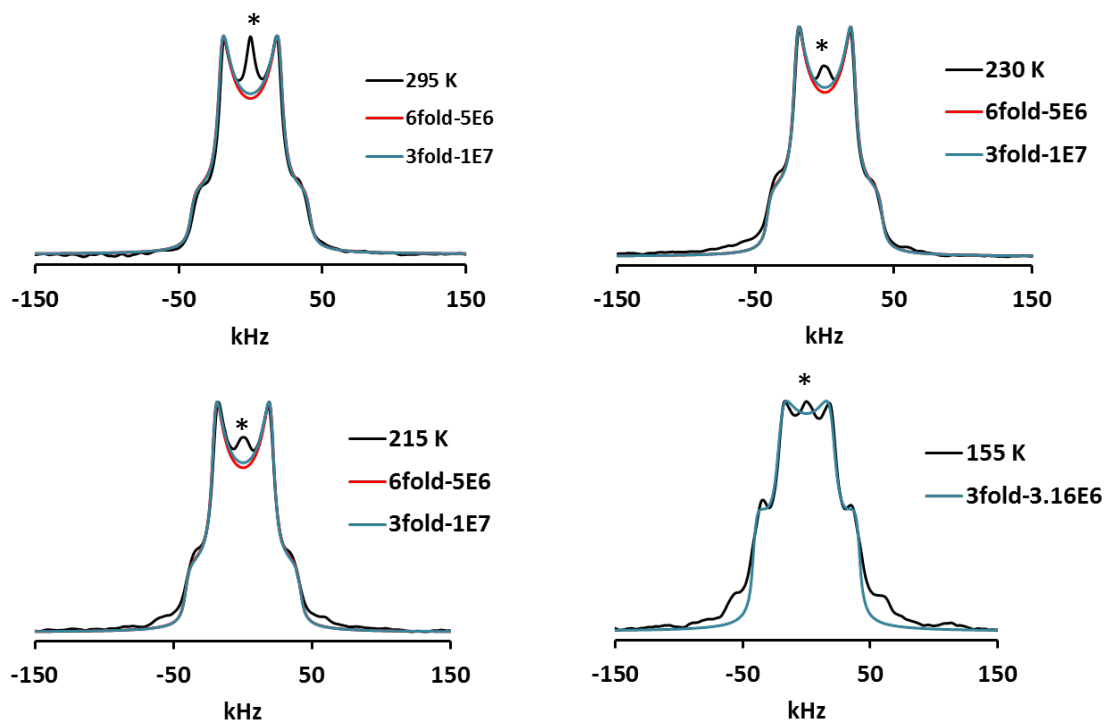
Figure 5.67 Experimental and simulated ^{2}H NMR quadrupolar echo spectra of **r5-d_{12}**. Simulations were carried out using the Nishikiori's program with a b angle of 70°, a QCC of 170 kHz, a line-broadening of 5 kHz and an echo delay (τ) of 50 msec.

5.4 Entropic and enthalpic effects in isomorphous halogen-bonded ampidynamic cocrystals

5.4.1 General information

All reactions were carried out under argon atmosphere in oven or flame-dried glassware, unless otherwise stated. All chemicals were purchased from commercial suppliers and used as received. 3,3,3-Triphenylprop-1-yne and 1,4-diazabicyclo[2.2.2]octane-d_{12} (dabco-d_{12}) were prepared according to reported literature procedures.[35,36] Tetrahydrofuran (THF) and dietylether (Et$_2$O) were dried by continuous distillation from sodium-benzophenone under argon atmosphere. Dichloromethane was dried by distillation from calcium hydride under argon atmosphere. Reactions at room temperature were carried out between 20-25 °C, reactions at 0 °C were performed on a water-ice bath and reactions at -40 °C were performed using an acetonitrile-dry ice bath. All reactions were monitored by thin layer chromatography (TLC) using TLC plates pre-coated with Silica Gel 60 F254 and visualized using UV, potassium permanganate (KMnO$_4$) and cerium molybdate (CAM) staining. Column chromatography was performed with silica gel (200-400 mesh) as the stationary phase. Characterization by nuclear magnetic resonance (NMR) was performed at 500 MHz for proton and 125 MHz for carbon-13. Chemical shifts are reported in ppm relative to TMS (d 0 ppm) using the residual solvent peaks as reference (CDCl$_3$ 7.26 and 77.16 ppm for ^{1}H and ^{13}C, respectively). Coupling constants *J* are reported in Hz. Multiplicities are reported as singlet (s), doublet (d), triplet (t), quartet (q), quintet (qnt), sextet (sxt), septed (spt) and multiplet (m). Uncorrected melting points were recorded on a melting point apparatus using sealed capillaries. IR spectra were recorded using an attenuated total reflectance (ATR) as the neat compound and units reported in cm^{-1}. Mass spectrometry data were collected on a Liquid Introduction Field Desorption Ionization mass spectrometer with a Time-of-Flight detector (LIFDI-TOF).

5.4.2 Synthetic procedures

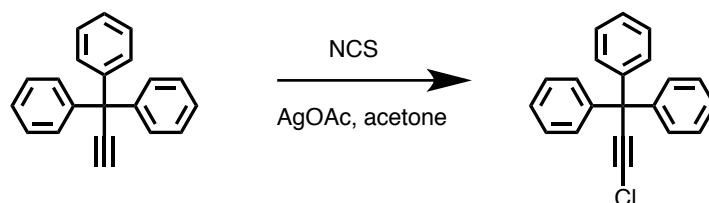**Scheme 5.1** Synthesis of 1,1,1-triphenyl-1-iodoprop-1-yne
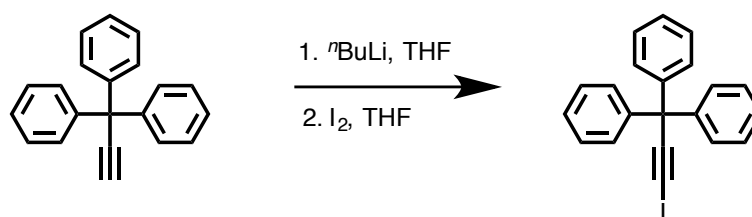
Synthesis of 1,1,1-triphenyl-1-iodoprop-1-yne. A solution of 1,1,1-triphenylprop-1-yne (256 mg, 0.96 mmol, 1.0 equiv) in dry THF (5 mL) at -40 °C was treated with nBuLi (1.6 M in hexanes, 0.5 mL, 1.24 mmol, 1.3 equiv). The reaction mixture was stirred at -40 °C under argon atmosphere for 2 h, then a solution of molecular iodine (257 mg, 1.01 mmol, 1.1 equiv) in dry THF (2 mL) was added. The reaction mixture was let to warm slowly to room temperature, then poured into a saturated aqueous solution of $NaHCO_3$ (30 mL) and the organics extracted with ethyl acetate (3x20 mL). The combined organic layers were washed with 10% aqueous $Na_2S_2O_3$ (30 mL), dried over Na_2SO_4 and concentrated to dryness under vacuum. The crude product was purified by column chromatography (20% dichloromethane-hexanes) to afford 380 mg (99% yield) of the desired compound as a white solid. m.p. 181-184 °C. IR (neat) v: 3058, 1594, 1489, 1445, 1031, 758, 697, 639 cm^{-1}. ^{1}H NMR (500 MHz, CDCl$_3$) δ 7.41-7.19 (15H, m, Ar). ^{13}C NMR (125 MHz, CDCl$_3$) δ 144.9 (Ci), 129.2 (Cm), 128.2 (Co), 127.1 (Cp), 100.0 (C-2), 57.8 (C-3), 0.3 (C-1). HRMS(DART) calcd. for [C$_{21}$H$_{15}$I+H]+: 395.02912, found: 395.02591.

Scheme 5.2 Synthesis of 1,1,1-triphenyl-1-bromoprop-1-yne

156
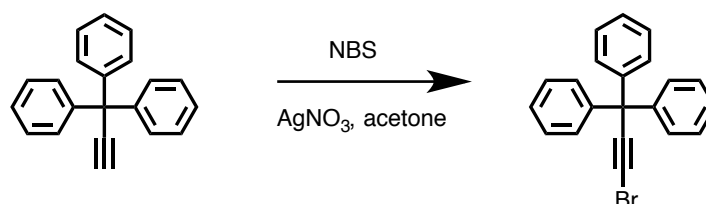
Synthesis of 1,1,1-triphenyl-1-bromoprop-1-yne. To a solution of 1,1,1-triphenylprop-1-yne (100 mg, 0.37 mmol, 1.0 equiv) in acetone (2 mL) were added N-bromosuccinimide (72 mg, 0.40 mmol, 1.1 equiv) and AgNO$_3$ (6 mg, 0.036mmol, 0.1 equiv). The reaction mixture was stirred overnight at room temperature, then the solvent was removed under vacuum and the crude product was purified by column chromatography (15% dichloromethane-hexanes) to afford 100 mg (78% yield) of the desired compound as a white solid. m.p. 148-151 °C. IR (neat) ν: 3058, 1594, 1489, 1445, 1031, 759, 699, 638 cm^{-1}. 1H NMR (500 MHz, CDCl$_3$) δ 7.39-7.21 (15H, m, Ar). ^{13}C NMR (125 MHz, CDCl$_3$) δ 144.7 (C*i*), 129.2 (C*m*), 128.2 (C*o*), 127.1 (C*p*), 85.8 (C-2), 56.8 (C-3), 44.4 (C-1). HRMS(DART) calcd. for [C$_{21}$H$_{15}$Br-H]+: 345.02734, found: 345.02600.

Scheme 5.3 Synthesis of 1,1,1-triphenyl-1-chloroprop-1-yne

Synthesis of 1,1,1-triphenyl-1-chloroprop-1-yne. To a solution of 1,1,1-triphenylprop-1-yne (100 mg, 0.37 mmol, 1.0 equiv) in acetone (3 mL) were added N-chlorosuccinimide (60 mg, 0.45 mmol, 1.2 equiv) and AgNO$_3$ (6 mg, 0.037mmol, 0.1 equiv). The reaction mixture was then heated to reflux overnight. The solvent was removed under vacuum and the crude product was purified by column chromatography (10% dichloromethane-hexanes) to afford 113 mg (99% yield) of the desired compound as a white solid. m.p. 132-134 °C. IR (neat) ν: 3058, 1594, 1489, 1445, 1032, 759, 738, 697, 638 cm^{-1}. ^{1}H NMR (500 MHz, CDCl$_3$) δ 7.40-7.21 (15H, m, Ar). ^{13}C NMR (125 MHz, CDCl$_3$) δ 144.8 (C*i*), 129.2 (C*m*), 128.2 (C*o*), 127.1 (C*p*), 75.2 (C-2), 63.2 (C-1), 56.0 (C-3). HRMS(DART) calcd. for [C21H15Cl-H]+: 302.08623, found: 302.08457.

Preparation of r7a and r7b cocrystals. In a typical procedure, the corresponding halo-alkyne (TrI or TrBr) and dabco were combined and ground in a mortar with addition of a few drops of acetone to make a slightly damp solid mixture. The solid mixture is ground and constantly added acetone until a single crystalline phase is obtained that matches that of the calculated from single crystal X-ray diffraction.

r7a: m.p. 157 – 160 °C. IR (neat) ν: 2930, 2866, 1489, 1447, 1057, 1031, 772, 766, 753, 699, 638 cm^{-1}.

r7b: m.p. 140 – 146 °C. IR (neat) ν: 2929, 2865, 1490, 1448, 1057, 1032, 756, 699, 637

cm^{-1}.

5.4.3 single crystal XRD analysis

Colorless needles of **r7a** and **r7b** co-crystals were grown from slow evaporation of acetone and they were used for intensity data collection without further manipulations.

The diffraction data were measured at 100(2) K and room temperature on an Bruker SMART Apex II single crystal X-ray diffractometer equipped with Mo-Kα radiation (λ = 0.71073 Å) and area detector. The structures were solved and refined using the SHELXTL software package.[3] Mercury package (version 3.5.1)[4] was used for analysis of crystalline packings. All atoms were refined anisotropically, and hydrogen atoms were placed at calculated positions.

**Table 5.11** Crystallographic details of **r7a** and **r7b** data collections at 2 different temperatures.

	r7a		r7b	
Formula	$C_{21}H_{15}I$. $C_6H_{12}N_2$	$C_{21}H_{15}I.C_6H_{12}N_2$	$C_{21}H_{15}Br$. $C_6H_{12}N_2$	$C_{21}H_{15}Br$. $C_6H_{12}N_2$
Temperature (K)	298 (2)	100(2)	296(2)	100 (2)
System	monoclinic	monoclinic	monoclinic	monoclinic
Space group	$P2_1/c$	$P2_1/c$	$P2_1/c$	$P2_1/c$
a (Å)	13.5312(6)	13.3106(19)	13.4442(16)	13.1901(12)
b (Å)	7.1004(3)	7.0791(10)	7.1664(9)	7.1685(7)
c (Å)	24.8852(11)	24.375(3)	24.537(3)	24.018(2)
α (°)	90.00	90	90.00	90.00
β (°)	100.2619(7)	100.278(2)	100.806(2)	101.2023(12)
γ (°)	90.00	90	90.00	90.00
V (Å^3)	2352.65(18)	2259.9(6)	2322.1(5)	2227.7(4)
Z	4	4	4	4
Collected I_o	37539	23056	38234	26964
Unique I_o	6288	5559	6610	5493
$I_o > 2\sigma(I_o)$	5203	4040	4799	4950
R_{ave}	0.0271	0.0578	0.0342	0.0182
Parameters	327	271	326	296
Restraints	369	0	294	0
$R_1 [I_o>2\sigma(I_o)]$	0.0258	0.0322	0.0378	0.0270
wR_2 (all)	0.0623	0.0557	0.1024	0.0747
G.o.f.	1.019	0.990	1.043	1.030
$\Delta\rho_{min}$ eÅ^{-3}	-0.401	-0.648	-0.528	-0.331
$\Delta\rho_{max}$ eÅ^{-3}	0.496	0.765	0.515	0.834

5.4.4 Powder XRD analysis

Crystalline samples of **r7a** and **r7b** were obtained by continuously grinding DABCO and the corresponding halo-tritylalkyne (TrI or TrBr) in a mortar in a 1:1 molar ratio and constant addition of a few drops of acetone to make a slightly damp solid; after the solvent evaporates out the crystal phase of the resulting material was checked by X-ray powder diffraction. Analyses were carried out using the Cu-Kα1 = 1.5406 Å radiation on a Bruker D8 Discover Powder X-ray diffractometer. Data were collected at room temperature in the range of 2Θ = 4-50° (step of 0.016°, step time 125 s).
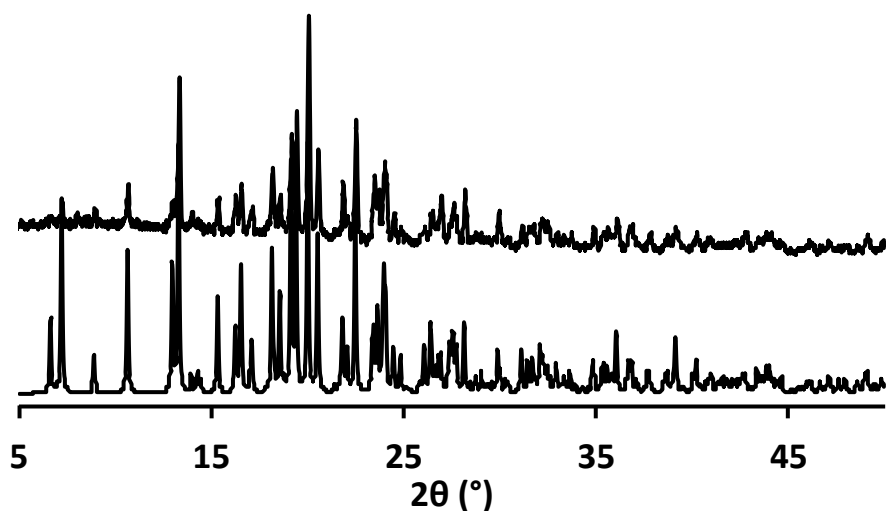
Figure 5.68 Calculated from single crystal X-ray diffraction (bottom) and experimental (top) powder X-ray diffraction patterns of **r7a** co-crystals.
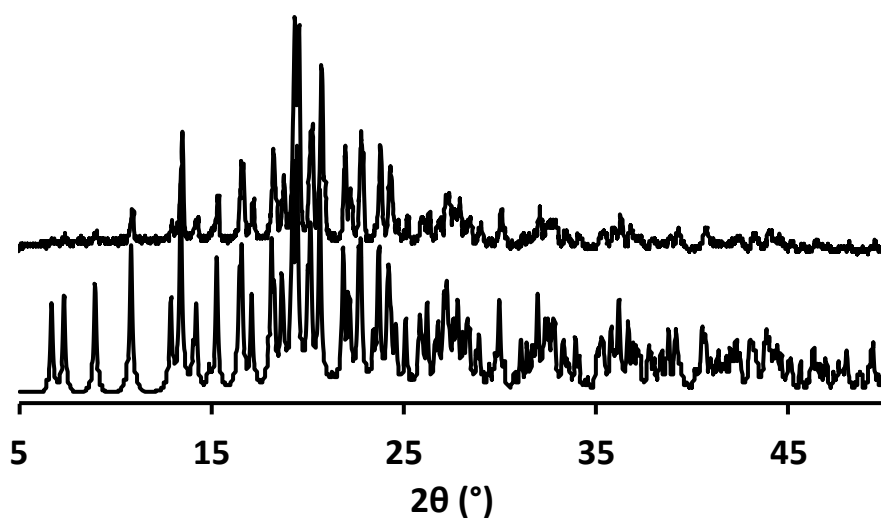

Figure 5.69 Calculated from single crystal X-ray diffraction (bottom) and experimental (top) powder X-ray diffraction patterns of **r7b** co-crystals.

5.4.5 ^{1}H spin-lattice relaxation solid-state NMR analysis

^{1}H T_1 measurements were carried out using a commercial magnet set at a magnetic field strength B_0 of 8.45 T, at which the proton frequency ($\nu_0 = \omega_0/2\pi$)

is 359.9 MHz. A tank circuit was built for this purpose using an inductor made of bare copper wire wound in a coil form. Polycrystalline samples of **r7a** and **r7b** cocrystals were packed in borosilicate glass tubes (5 mm diameter, 1.0 cm length) caped with Teflon tape plugs and placed in the copper coil. ^1H T_1 experiments were recorded using a saturation recovery pulse sequence combined with a spin-echo, the saturation state was attained with a pulse comb $(3*\pi/2)$ which was followed by a time recovery t. Saturation recovery traces were fitted to a single exponential function. ^1H T_1 experiments were recorded in the range of 80 K – 165 K and 40 K – 155 K for **r7a** and **r7b**, respectively.
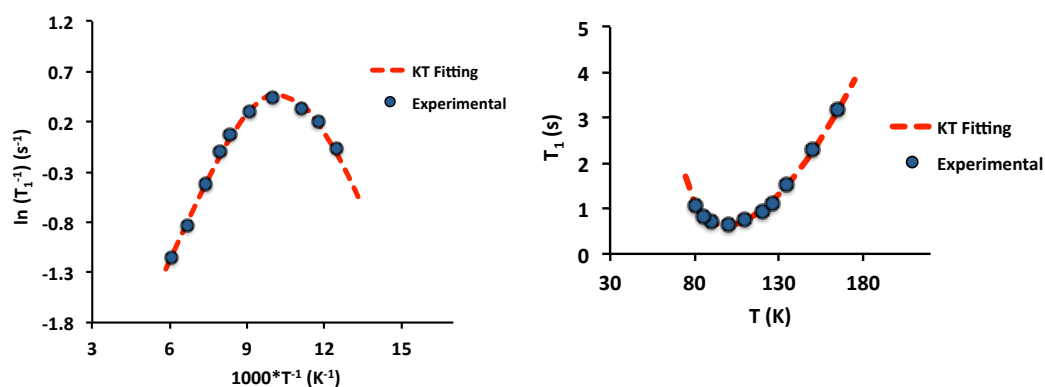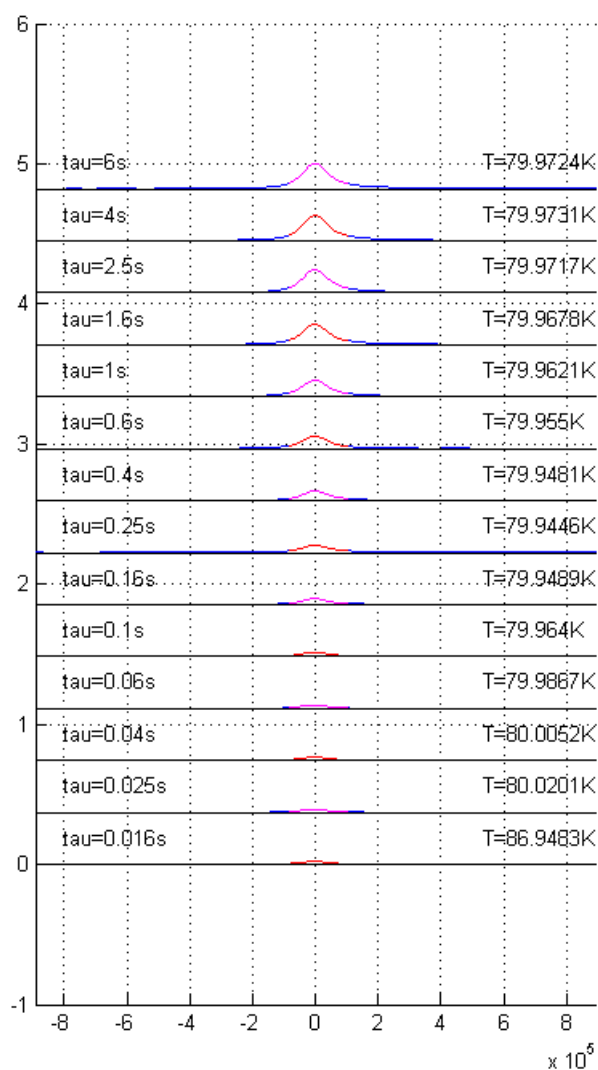

Figure 5.70 Temperature dependence of ^1H spin-lattice relaxation (T_1) on **r7a** cocrystals displaying the experimental data points and fitting to the Kubo-Tomita equation. Left: ln (T_1^{-1}) vs $1000*T^{-1}$ and right: T_1 vs T. The ^1H T_1 experiments were recorded on the range of 80 – 165 K. The plot on the right side shows that the minimum in T_1 occurs at 100 K. The fitting parameters found were: E_a = 1.15 kcal/mol, τ_0^{-1} = 1.3×10^{12} s^{-1} and C = 2.55×10^9 s^{-2}.
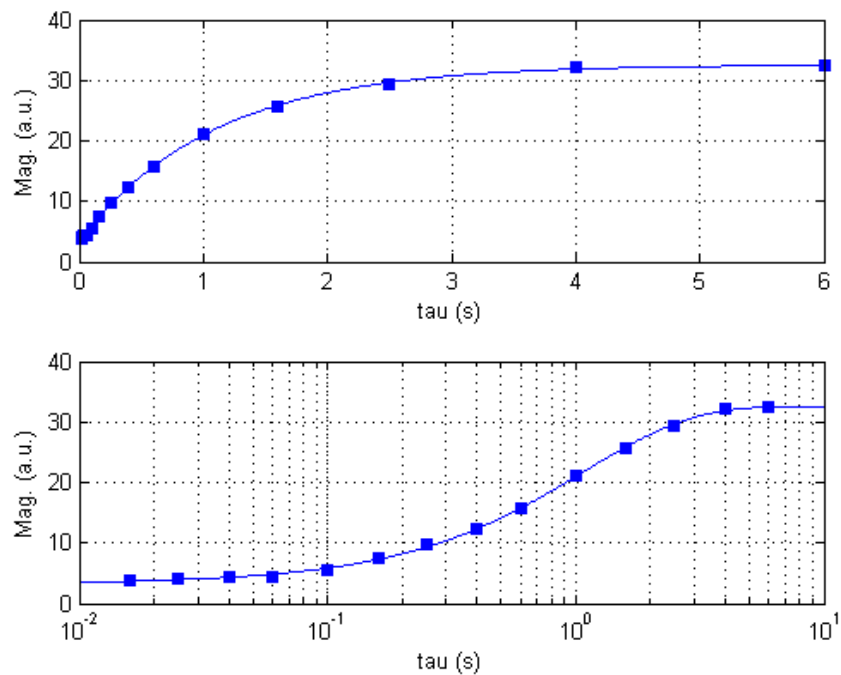
Figure 5.71 Representative example of a ^{1}H spin lattice relaxation experiment recorded at 80 K on a polycrystalline sample of **r7a** cocrystals, at 359.9 MHz using the saturation recovery pulse sequence. The delay times (tau) employed were 16 ms, 25 ms, 40 ms, 60 ms, 100 ms, 160 ms, 250 ms, 400 ms, 600 ms, 1 s, 1.6 s, 2.5 s, 4 s and 6 s. The data were fitted to a single exponential and the calculated T_1 was found to be 1.076 s.
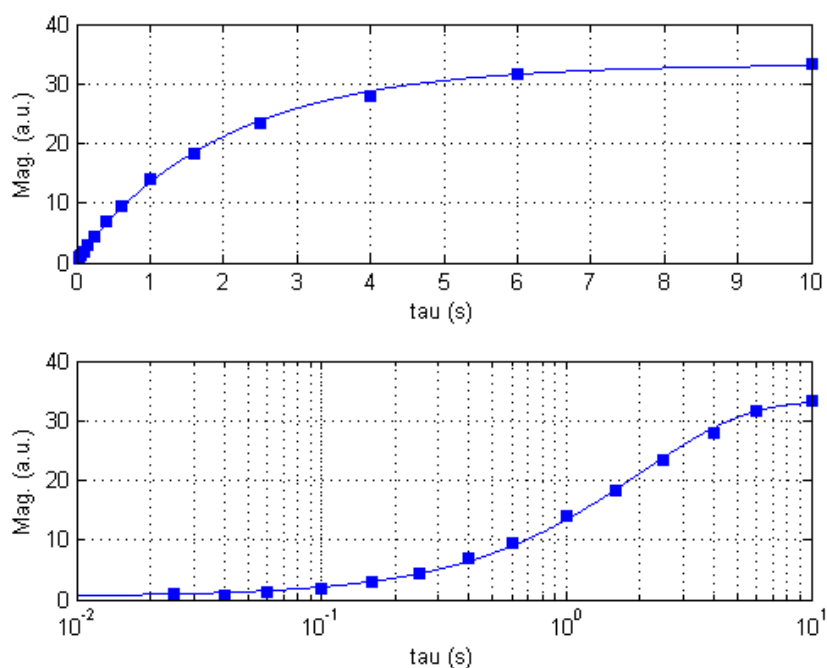
Figure 5.72. Set of spectra of a representative ^{1}H T[1] NMR experiment performed at 80 K on a polycrystalline sample of **r7a** cocrystals at a frequency of 359.9 MHz for proton. The spectra display different intensities obtained with the following tau delay times: 16 ms, 25 ms, 40 ms, 60 ms, 100 ms, 160 ms, 250 ms, 400 ms, 600 ms, 1 s, 1.6 s, 2.5 s, 4 s and 6 s.
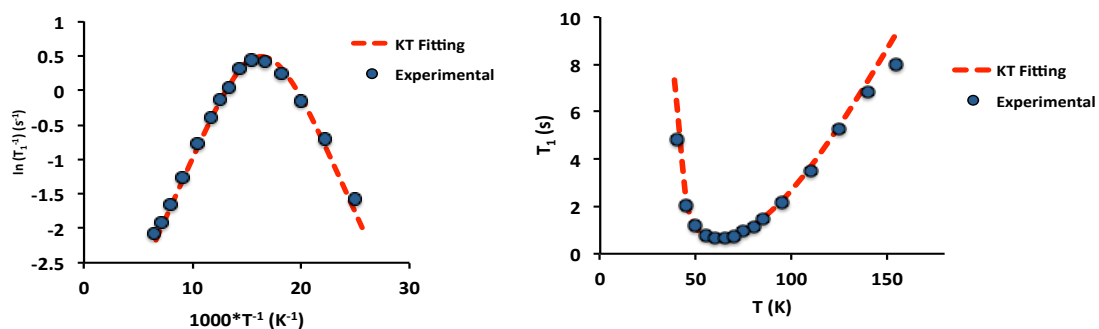
Figure 5.73. Temperature dependence of ^1H spin-lattice relaxation (T_1) on **r7b** co-crystals displaying the experimental data points and fitting to the Kubo-Tomita equation. Left: ln (T_1^{-1}) vs $1000*T^{-1}$ and right: T_1 vs T. The ^1H T_1 experiments were recorded on the range of 40 – 155 K. The right side plot shows that the minimum in T_1 occurs at 65 K. The fitting parameters found were: E_a = 0.71 kcal/mol, τ_0^{-1} = 1.2×10^{12} s^{-1} and C = 2.6×10^9 s^{-2}.

Figure 5.74. Representative example of a ^1H spin lattice relaxation experiment recorded at 45K on a polycrystalline sample of **r7b** cocrystals at a frequency of 359.9 MHz using the saturation recovery pulse sequence. The delay times (tau)

employed were 25 ms, 40 ms, 60 ms, 100 ms, 160 ms, 250 ms, 400 ms, 600 ms, 1 s, 1.6 s, 2.5 s, 4 s, 6 s and 10 s. The data were fitted to a single exponential and the calculated T_1 was found to be 2.04 s.
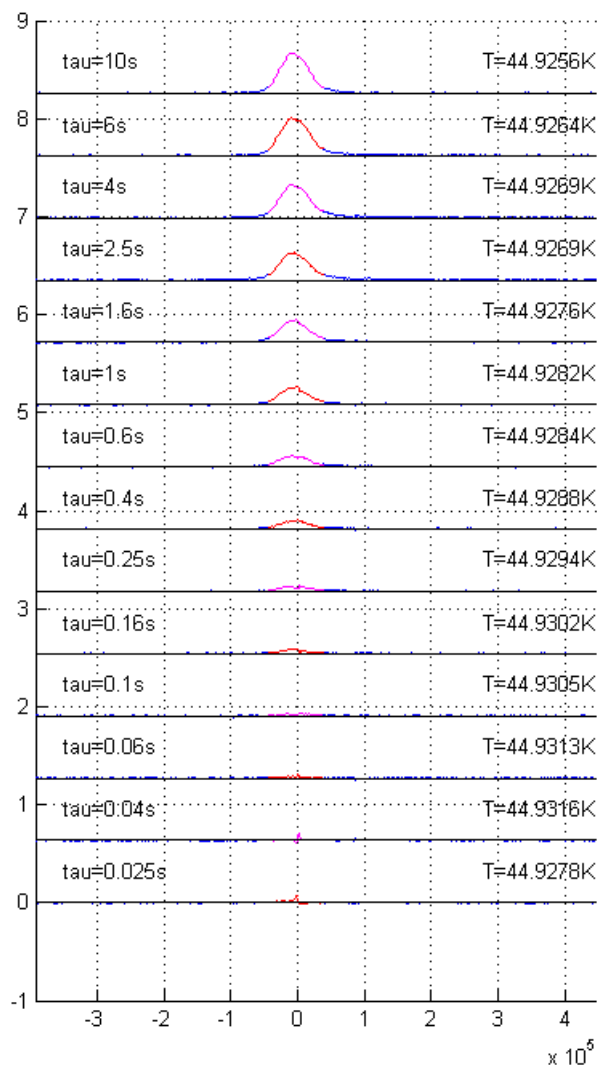
**Figure 5.75.** Set of spectra of a representative ^{1}H T[1] NMR experiment performed at 45K on a polycrystalline sample of **r7b** cocrystals at a frequency of 359.9 MHz for proton. The spectra display different intensities obtained with the following tau delay times: 25 ms, 40 ms, 60 ms, 100 ms, 160 ms, 250 ms, 400 ms, 600 ms, 1 s, 1.6 s, 2.5 s, 4 s, 6 s and 10s.
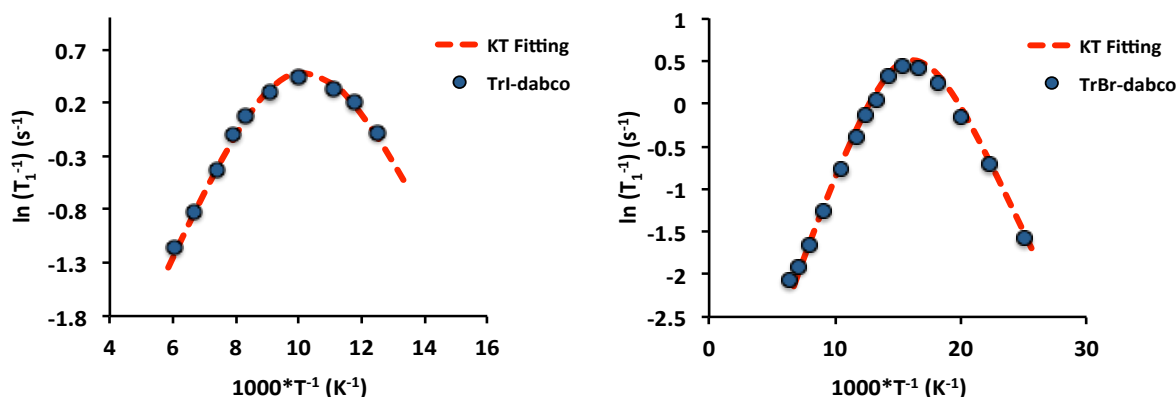
Figure 5.76. Fitting of the experimental ^1H spin-lattice relaxation (T_1) data to the Kubo-Tomita equation using τ_c in the form of the Eyring equation $\tau_c = h/k_BT$ exp($-\Delta S^{\neq}/R$) exp($\Delta H^{\neq}/RT$). The fitting traces shown in the figure were obtained using the following values of the adjustable parameters: for **r7a** $\Delta H^{\neq}$ = 0.95 kcal/mol, $\Delta S^{\neq}$ = -3.0 cal/mol*K and C = 2.55x10^9 s^{-2} and for **r7b** $\Delta H^{\neq}$ = 0.54 kcal/mol, $\Delta S^{\neq}$ = -3.0 cal/mol*K and C = 2.6x10^9 s^{-2}.

5.4.6 ^2H solid-state NMR analysis

Quadrupolar-echo ^2H NMR experiments were performed on polycrystalline samples of **r7b-d_{12}** obtained by solvent assisted mechanochemical crystallization using 1,1,1-triphenyl-1-bromoprop-1-yne and DABCO-d_{12} in a 1:1 molar ratio. Quadrupolar-echo ^2H NMR experiments were recorded on a spectrometer operating at a magnetic field of 7.0 Tesla, at which the ^2H nucleus resonates at 46.07 MHz ($\nu_0 = \omega_0/2\pi$). A 4 mm wide-line probe and a $\pi/2$ pulse of 2.5 ms pulse were used. A quadrupolar-echo pulse sequence with phase cycling, an echo delay of 50 ms and a recycle delay of 10 s was employed to acquire the ^2H wide-line spectra. Experiments at 150 K, 210 K and 296 K were recorded and the temperature inside the probe was calibrated using the shift of ^{207}Pb as reference. Spectra were acquired by averaging at least 32 scans and processed using a line broadening of 5 kHz.
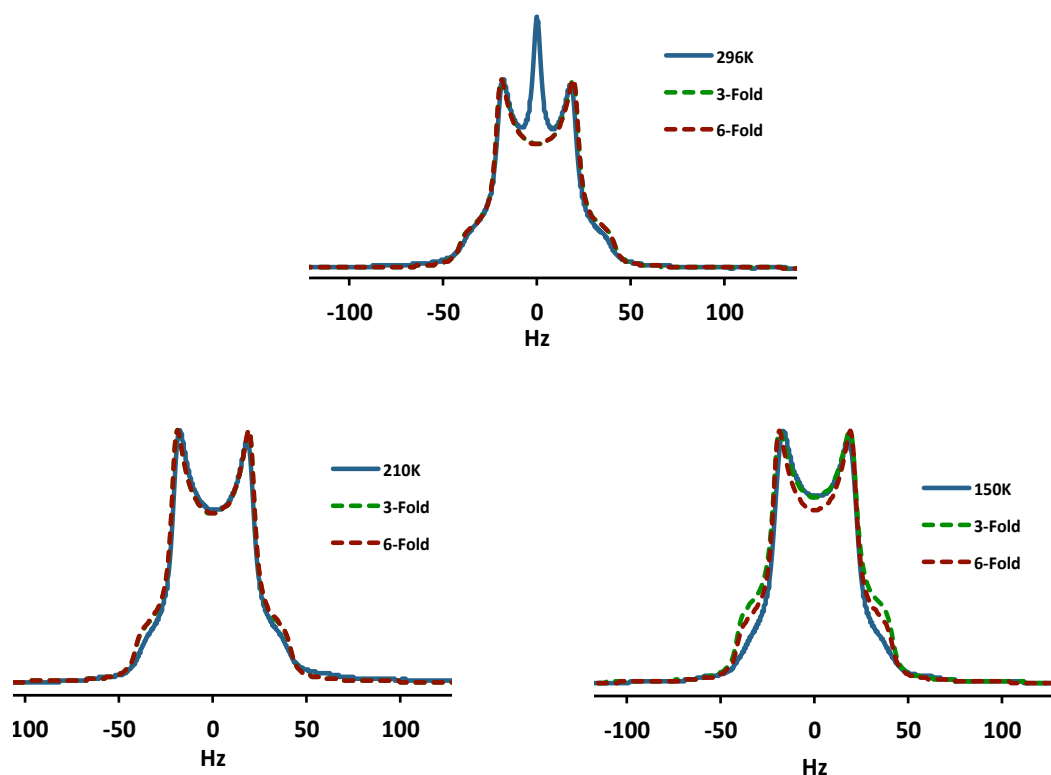
Figure S9. Experimental (blue solid lines) and simulated (green and red dashed lines) ^{2}H NMR wide line spectra of **r7b-d_{12}** cocrystals recorded at 296 K, 210 K and 150 K at a frequency of 46.07 MHz. The figure shows that at these three temperatures the experimental spectra are reproduced by considering 3-fold (120° jump angle) or 6-fold (60° jump angle) rotational symmetries. Simulations were carried out using the Nishikiosri's program with a β angle of 70°, a quadrupolar coupling constant (QCC) of 170 kHz, a line broadening of 5 kHz and an echo delay of 50 μs.

References:

1   R. Boese and M. Nussbaumer in *Organic Crystal Chemistry*, 1994, Oxford University Press, Oxford, 1994, 20.

2   A. Wasilewska, M. Gdaniec and T. Polonski, *CrystEngComm*, 2007, **9**, 203.

3   G. M. Sheldrick, *Acta Crystallogr. Sect. A.*, 2008, **64**, 112.

4   C. F. Macrae, I. J. Bruno, J.A. Chisholm, P. R. Edgington, P.McCabe, E. Pidcock, L. Rodriguez-Monge, R. Taylor, J. van de Streeka and P. A. Wood, *J. Appl. Cryst.* 2008, **41**, 466.

5   A. L. Spek, *Acta Crystallogr. Sect. D*, 2009, **65**, 148.

6   Gaussian 09, Revision C.01; Gaussian, Inc.: Wallingford CT, 2009.

7   A. D. Becke, *J. Chem. Phys.*, 1993, **98**, 5648.

8   C. Lee, W. Yang and R. G. Parr, *Phys. Rev. B: Condens. Matter*, 1988, **37**, 785.

9   P. J. Hay and W. R. Wadt, *J. Chem. Phys.*, 1985, **82**, 270.

10   C. E. Check, T. O. Faust, J. M. Bailey, B. J. Wright, T. M. Gilbert, L. S. Sunderlin, *J. Phys. Chem. A*, 2001, **105**, 8111.

11   S. F. Boys and F. Bernardi, *Mol. Phys.*, 1970, **19**, 553.

12   E. Corradi, S. V. Meille, M. T. Messina, P. Metrangolo and G. Resnati, *Angew. Chem. Int. Ed.*, 2000, **39**, 1782.

13   P. Cardillo, E. Corradi, A. Lunghi, S. V. Meille, M. T. Messina, P. Metrangolo and G. Resnati, *Tetrahedron*, 2000, **56**, 5535.

14   P. Metrangolo, W. Panzeri, F. Recupero and G. Resnati, *J. Fluorine Chem.*, 2002, **114**, 27.

15   A. De Santis, A. Forni, R. Liantonio, P. Metrangolo, T. Pilati and G. Resnati, *Chem. Eur. J.*, 2003, **9**, 3974.

16   P. Metrangolo, T. Pilati, G. Resnati, A. Stevanazzi, *Curr. Opin. Colloid. Interface Sci.*, 2003, **8**, 215.

17   M. T. Messina, P. Metrangolo, W. Panzeri, T. Pilati and G. Resnati, *Tetrahedron*, 2001, **57**, 8543.

18   E. Corradi, S. V. Meille, M. T. Messina, P. Metrangolo and G. Resnati, *Tetrahedron Lett.*, 1999, **40**, 7519.

19   P. Giannozzi, S. Baroni, N. Bonini, M. Calandra, R. Car, C. Cavazzoni, D. Ceresoli, G. L. Chiarotti, M. Cococcioni, I Dabo, A. Dal Corso, S. de Gironcoli, S. Fabris, G. Fratesi, R. Gebauer, U. Gerstmann, C. Gougoussis, A. Kokalj, M. Lazzeri, L. Martin-Samos, N. Marzari, F. Mauri, R. Mazzarello, R.; S. Paolini, A. Pasquarello, L. Paulatto, C. Sbraccia, S. Scandolo, G. Sclauzero, A. P. Seitsonen, A. Smogunov, P. Umari and R. M. Wentzcovitch, *J. Phys.: Condens. Matter*, 2009, **21**, 395502.

20   J. P. Perdew, K. Burke and M. Ernzerhof, *Phys. Rev. Lett.*, 1996, **77**, 3865.

21   J. P. Perdew and Y. Wang, *Phys. Rev. B*, 1986, **33**, 8800.

22   A. Otero-de-la Roza and E. R. Johnson, *J. Chem. Phys.*, 2013, **138**, 204109.

23   A. Otero-de-la Roza, E. R. Johnson and G. A. DiLabio, *J. Chem. Theory Comput.*,

2014, **10**, 5436.

24   G. Kresse and D. Joubert, *Phys. Rev. B*, 1999, **59**, 1758.

25   C. J. Pickard and F. Mauri, *Phys. Rev. B*, 2001, **63**, 245101.

26   C. J. Jameson, A. K. Jameson, D. Oppusunggu, S. Wille, P. M. Burrell and J. Mason, *J. Chem. Phys.*, 1981, **74**, 81.

27   H. J. Monkhorst and J. D. Pack, *Phys. Rev. B*, 1976, **13**, 5188.

28   F. Franco, M. Baricco, M. R. Chierotti, R. Gobetto and C. Nervi, *J. Phys. Chem. C*, 2013, **117**, 9991.

29   M. S. Solum, K. L. Altmann, M. Strohmeier, D. A. Berges, Y. Zhang, J. C. Facelli, R. J. Pugmire and D. M. Grant, *J. Am. Chem. Soc.*, 1997, **119**, 9804.

30   G. Metz, X. Wu and S. Smith, *J. Magn. Reson. Ser. A*, 1994, **110**, 219.

31   A: Bennett, C. Rienstra, M. Auger, K. Lakshmi and R. Griffin, *J. Chem. Phys.*, 1995, **103**, 6951.

32   R. S. Thakur, N. D. Kurur and P. K. Madhu, *Chem. Phys. Lett.*, 2006, **426**, 459.

33   A. Aliev, K. Harris, R. Harris, S. Carss and A. Olivieri, *J. Chem. Soc.-Faraday Trans.*, 1995, **91**, 3167.

34   C. Widdifield, G. Cavallo, G. A. Facey, T. Pilati, J. Lin, P. Metrangolo, G. Resnati and D. L. Bryce, *Chem. Eur. J.*, 2013, **19**, 11949.

35   B. Rodriguez-Molina, M. A. Ochoa, N. Farfan, R. Santillan and M. A. Garcia-Garibay, *J. Org. Chem.*, **2009**, *74*, 8554.

36   Please refer to section 5.3.5 in this Chapter.

37   S. I. Nishikiori, T. Soma and T. Iwamoto, *J. Inclusion Phenom. Mol. Recognit. Chem.*, 1997, **27**, 233.

Appendix

Crystal Engineering, a hystorical perspective

We can refer to crystal engineering as the design and synthesis of solids with desired physical and chemical properties. Specifically, it is focusing on the study of intermolecular interactions, molecular packing within crystalline lattices and the characterization and fine-tuning of crystals properties. However its principles and fundamental concepts can be applied to all intermolecular assemblies, thus embracing a wide range of disciplines, from pure crystallography to the study of complex biological assemblies, passing thorough materials and soft matter.[1]

Even though the term crystal engineering first appeared in 1955 during a meeting of the American Physical Society, proposed by R. Pepinsky,[2] the first unanimously recognised pioneer of the field has been G. M. J. Schimidt with his work, dated 1971, on photodimerization in crystals.[3] During the 1970s and 1980s the research of the newborn community mainly focused on photochemical reactivity, based on the topochemical principles proposed by Schmidt, and on the study of crystal packing to correlate size and shape of molecular building blocks to the final crystal structures; Kitaigorodskii's principle of close-packing was born.[4] Between the late 1980s and early 1990s, Gautam R. Desiraju understood that the deviations from the geometrical considerations of the close-packing principle, which are essentially related to strongly anisotropic non-covalent intermolecular interactions, are of extreme importance in order to engineer the crystal architectures.[5] Following this seminal work, Desiraju and Etter introduced the strong and directional hydrogen bond as a powerful tool in the hands of chemists to tune crystal packing motifs and hence crystal physico-chemical properties.[5,6] They also envisioned the potential of the Cambridge Structural Database (CSD) as a powerful and valuable support for the analysis and interpretation of non-covalent interactions networks in crystals.[7] In the same period, Robson and Ermer published the first works on metal-organic and fully organic intermolecular networks, respectively, attempting to establish

general designing principles for the construction of predictable crystalline structures.[8,9]

In the following decades, crystal engineering has been an evolving field of study, trying to address both fundamental and more practical issues. New supramolecular synthons[10] are continuously designed and discovered, based on an always wider gamut of anisotropic non-covalent interactions, not only hydrogen bond, but also halogen bond,[11] different kinds of π interactions (π-π, cation-π or anion-π interactions),[12-14] and, more generally, all the directional non-covalent interactions named from their electrophilic sites (*e.g.* chalcogen bond, pnictogen bond).[15] The expansion of crystal engineering is also due to the now available powerful computational platforms, which allow to perform sophisticated *ab-initio* calculations, which are trying to address Maddox's scandal of the impossibility to predict a crystal structure from first principles.[16,17] What is more, supramolecular isomerism and polymorphism, which are tipycal crystal engineer issues, are becoming more and more relavant problems to be solved for industries, especially pharmaceutical companies, attracting an increasing attention to the field. [18,19]

The quest of tailoring crystal structures from the knowledge of the starting molecular building blocks is still far from being fully accomplished and there is plenty of room for new ideas and concepts trying to address the future challenges of this multifaceted branch of science. These issues must be faced by who want to precisely engineer both crystal structures and their properties and, by doing so, to make the crystal engineers dream come true.

References:

1   G. R. Desiraju, *Angew. Chem. Int. Ed.*, **2007**, *46*, 8342.

2   R. Pepinsky, *Phys. Rev.*, **1955**, *100*, 971.

3   G. M. J. Schmidt, *Pure Appl. Chem.*, **1971**, *27*, 647.

4   A. I. Kitaigorodskii, *Molecular Crystals and Molecules*, Academic Press, New York, 1973.

5   G. R. Desiraju, *Crystal Engineering. The design of Organic Solids*, Elsevier, Amsterdam, 1989.

6   M. C. Etter, *Acc. Chem. Res.*, **1990**, *23*, 120.

7   F. H. Allen and O. Kennard, *Chem. Des. Autom. News* , **1993**, *8*, 31.

8   O. Ermer, *J. Am. Chem. Soc.*, **1988**, *110*, 3747.

9   B. F. Hoskins and R. Robson, *J. Am. Chem. Soc.*, **1989**, *111*, 5962.

10   G. R. Desiraju, *Angew. Chem. Int. Ed.*, **1995**, *34*, 2311.

11   G. Cavallo, P. Metrangolo, R. Milani, T. Pilati, A. Priimagi, G. Resnati and G. Terraneo, *Chem. Rev.*, **2016**, *116*, 2478.

12   C. A. Hunter and J. K. M. Sanders, *J. Am. Chem. Soc.*, **1990**, *112*, 5525.

13   J. C. Ma and D. A. Dougherty, *Chem. Rev.*, **1997**, *97*, 1303.

14   D.-X. Wang and M.-X. Wang, *Chem. Rev.*, **2013**, *135*, 892.

15   G. Cavallo, P. Metrangolo, T. Pilati, G. Resnati and G. Terraneo, *Cryst. Growth Des.*, **2014**, *14*, 2697.

16   J. Maddox, *Nature*, **1988**, *335*, 201.

17   S. M. Woodley and R. Catlow, *Nat. Mater.*, **2008**, *7*, 937.

18   B. Moulton and M. J. Zaworotko, *Chem. Rev.*, **2001**, *101*, 1629.

19   N. K. Duggirala, M. L. Perry, O. Almarsson and M. J. Zaworotko, *Chem. Commun.*, **2016**, *52*, 640.

Acknowledgements

List of Publications at NFMLab:

1) A. Bertolani, L. Pirrie, L. Stefan, N. Houbenov, J.S. Haataja, **L. Catalano**, G. Terraneo, G. Giancane, L. Valli, R. Milani, O. Ikkala, G. Resnati and P. Metrangolo, *Nat. Commun.*, 2015, **6**, 7574.

2) **L. Catalano**, S. Pérez-Estrada, G. Terraneo, T. Pilati, G. Resnati, P. Metrangolo and M. A. Garcia-Garibay, *J. Am. Chem. Soc.*, 2015, **167**, 49, 15386.

3) **L. Catalano**, G. Cavallo, P. Metrangolo, G. Resnati and G. Terraneo, *Top. Curr. Chem.*, 2016, **373**, 289.

4) V. Vasylyeva,* **L. Catalano**,* C. Nervi, R. Gobetto, P. Metrangolo and G. Resnati, *CrystEngComm*, 2016, **18**, 2247. (Front Cover). *these authors equally contributed.

5) **L. Catalano**, P. Metrangolo, T. Pilati, G. Resnati, G. Terraneo and M. Ursini, *J. Fluorine Chem.*, 2016, *ASAP*.

6) P. Cerreia-Vioglio, **L. Catalano**, V. Vasylyeva, M.R. Chierotti, C. Nervi, G. Resnati, R. Gobetto and P. Metrangolo, *Chem. Eur. J.*, 2016, **22**, 16819. (Inside Cover).

7) **L. Catalano**, S. Pérez-Estrada, H.-H. Wang, A. J.-L. Ayitou, S. Khan, G. Terraneo, P. Metrangolo, S. Brown and M.A. Garcia-Garibay, *J. Am. Chem. Soc.,* 2017, **139**, 843*.

8) V. Dichiarante, I. Tirotta, **L. Catalano**, G. Terraneo, G. Raffaini, M.R. Chierotti, R. Gobetto, F. Baldelli Bombelli and P. Metrangolo, *Chem. Commun.*, 2017, **53**, 621*.